MONASH University

Investigation of Microstructure and Compression Behaviour of Cemented Sand using X-Ray CT Imaging

by

Asheque al Mahbub

M.Eng.(Civil), NUS; B.Sc.Engg.(Civil), BUET

A thesis submitted for the degree of Doctor of Philosophy at
Department of Civil Engineering
Monash University, Australia

March 2019

COPYRIGHT NOTICE

To
my beloved wife and daughters

ABSTRACT

Understanding the mechanical behaviour of cemented soils has significant importance in geotechnical engineering. Most of the earlier research work on cemented soils were conducted at low stresses. Moreover, the complex interactions between the components of the grain-cement composite under progressive stresses at microscale level is poorly understood. This study with the aid of high-resolution X-ray Computed Tomography (CT) imaging technique aims to analyse the micromechanical behaviour of cemented sand up to high stress to explain their macroscale behaviour.

Artificially cemented sand specimens with varying degrees of cement contents were prepared and tested under incremental stresses within a custom built 1-D compression load cell. Imaging of the sample was performed at the end of each of the eight load stages and the corresponding microstructure was studied using high-performance image analysis software and in-house developed Matlab code. More specifically, this study analysed both 2-D and 3-D void fabrics for directional anisotropy and scalar parameters (e.g. void ratios, sphericity, anisotropy) with increased cement contents and progressive loading. However, for the sample with 0% cement content (uncemented) where significant crushing of particles under high stress took place, evolution of particle fabric (e.g., particle size distribution, relative breakage, particle anisotropy) in addition to void fabric was analysed.

Under compression, both cemented and uncemented sand as observed from e-logσ'_v plots exhibited an initial stiff response followed by yielding. However, for the cemented sand, the response was much stiffer without any clearly defined yield point for the stress range investigated as observed for the uncemented sand due to the initiation of particle crushing. Morphology of the void fabric for cemented sand was found to be isolated, dispersed and relatively regular in shape in contrast to the significantly interconnected and irregular shape for the uncemented sand. This is supported by increased values of average sphericity of voids for the cemented sand. With progressive loading, insignificant changes to void morphology and fabric

distributions for the uncemented sand were observed. However, relatively complex fabric distributions comprising both transversely-isotropic and orthotropic types were more appropriate to describe the evolution of fabric for the cemented sands investigated here.

For this first-of-its-kind study, observed findings are limited to the specific image processing and sample preparation methods used in this study. However, the study suggested a conceptual void-fabric based framework for seeking insightful explanation of the macro-scale behaviour of cemented sand subjected to 1D compression.

DECLARATION

This thesis contains no material which has been accepted for the award of any other degree or diploma at any university or equivalent institution and that, to the best of my knowledge and belief, this thesis contains no material previously published or written by another person, except where due reference is made in the text of the thesis.

Asheque al Mahbub

The 12th of March, 2019

LIST OF PUBLICATIONS

Al Mahbub, A., Haque, A., Bui, H.H. and Muhunthan, B. Evolution of fabric of cemented sands subjected to insitu X-ray CT imaging under one-dimensional compression. (in preparation).

Al Mahbub, A. and Haque, A., 2016. X-ray computed tomography imaging of the microstructure of sand particles subjected to high pressure one-dimensional compression. Materials, 9(11), p.890.

Al Mahbub, A. and Haque, A., 2016. Investigation of micro-mechanical behaviour of lime-slag treated soils using a high resolution X-Ray Computed Tomography. 24th Australian Conference on microscopy and microanalysis. Melbourne Exhibition Centre, 31st Jan-4 Feb 2016.

ACKNOWLEDGEMENTS

I am grateful to the Almighty, the All-knowing, and the Glorified God for His Mercy and Favours that brought me where I am today despite my countless limitations.

I would like to express my sincere gratitude and appreciation to my main Supervisor, Dr. Asadul Haque for his outstanding guidance, endless support, and assistance during the course of this research work. His encouraging advice and valuable feedback provided me with great insights into my research and kept me motivated in achieving my goals. I would also like to sincerely acknowledge my associate supervisor, Dr. Ha H Bui from Monash University and external supervisor Professor Dr. Balasingam Muhunthan from Washington State University, USA for their invaluable guidance and feedback to improve my research work. Special thanks to Dr. Yannis F. Dafalias, distinguished Professor from University of California, Davis, USA for his generous advice and supporting note.

I would like to sincerely acknowledge civil engineering laboratory staff members Mr. Long Goh, Mr. Zoltan Csaki, Mr. Michael Leach, and especially Mr. Sarvan Mani for their sincere support for making the experiments possible. I acknowledge the support of Australian Research Council funded X-ray CT facility at Monash University for providing me the access. My sincere appreciation goes to Monash University for providing financial support in the form of Research Training Program (RTP) scholarship to carry out this research work. Thanks to all the academic, research, administrative staff members of the Department of Civil Engineering, Monash University during my research period. I acknowledge Professor Nogami Toyoaki and Professor Chow Yean Khow from National University of Singapore for their support.

I am grateful to my parents and in-laws, my wife, my daughters, my sister, sister in law, my brothers in law, my nieces and nephew for their profound love, care and blessings that made it possible for me to reach the milestone. Heartiest appreciation to Dr. Muzharul Islam, Dr. Nilufar Talat, Engr. M A Awal, Dr. Iftekhar Anam, Dr. Mofakhar Hossain, Engr. Feroze Ahmed and especially Engr. Arshad Haque for their blessings and support. I am thankful to Dr. Rezaul Karim, Dr. Kamrul Ahsan, Dr. Bishwajit Chowdhury, Dr. Shahidul Islam, Engr. Masud Alam, Engr. M. Tarikul Islam and many others for their words of appreciation and encouragement.

I would like to acknowledge many brilliant people including post-doctoral fellows and fellow PhD students especially Dr. Daniel King, Dr. Louis King, Dr. Darshana Weerasinghe, Dr. Nhu Nguyen, Aamir Mahawish, Xue Le and Ferdous Alam whom I have been privileged to come across at the Monash University campus over the last few years.

Finally, I am deeply indebted to and proud of my beloved Country, Bangladesh where I was born and raised.

TABLE OF CONTENTS

LIST OF FIGURES

LIST OF TABLES

NOTATIONS AND ABBREVIATIONS

A	Anisotropy
Ap	Area of individual void
B_p	Breakage potential
B_t	Total breakage
B_r	Relative breakage
b_p	Potential for breaking
C_c	Compression Index
D	Particle diameter
D_{50}	Mean diameter of particles
$D_{i_1} \ldots \ldots D_{i_n}$	Deviator tensors
E	Void ratio
e_o	Initial void ratio
F_{ij}^{d}	Deviatoric component of second order fabric tensor of second kind
F_{ij}	Second order fabric tensor of second kind
F_{kk}	Trace of the fabric tensor
$f(n)$	Kanatani's density distribution function
G_s	Specific gravity of sand particles
M_s	Mass of sand particles
n_i	Deviatoric unit-norm loading direction
n^{α}	Component of the α^{th} unit vector
$N_{i_1 i_2 .. i_r}$	Tensorial product of unit vectors
Ω	Constant, values are 2π and 4π for 2-D and 3-D data distribution respectively

δ	Kronecker delta
σ'_v	Vertical effective stress
V_s	Total volume of sand particles
V_p	Volume of individual void
ρ_w	Density of water
ρ_i	Initial bulk density of sand
V_b	Bulk volume of sand
Ψ or S	Sphericity of individual void
ACST	Anisotropy critical state theory
C3A	Tricalcium aluminate
C2S	Dicalcium silicate
C3S	Tricalcium silicate
C4AF	Tetracalcium aluminoferrite
$C_3S_2H_x$	Calcium Silicate Hydrate
$FAV\ A$ or F	Fabric anisotropy variable

1 INTRODUCTION

1.1 Background

Cemented soils are widely found in nature around many parts of the world. In general, they demonstrate improved strength and stiffness characteristics compared to uncemented soil. One of the distinguishing characteristics of cemented soil is its ability of withstanding steep natural slope as can be observed from large deposits such as along the California coastline where the slopes of 60° or more reaches 100 m in heights whereas individual pieces of sand are very fragile (Clough et al., 1981). Formation of cement in natural soil, according to (Mitchell and Soga, 2005), is a combined result of mineralogy, particle size and shape, water chemistry during deposition, pressure, temperature and organic content. The basic mineral groups of cements are silica, carbonates, clay minerals, iron oxides and hydroxides, sulphates and zeolites.

Engineering properties of cemented soils have significant importance in geotechnical engineering projects e.g. slope stability, ground improvement, deep foundation etc.

This is not only because they are encountered by geotechnical engineers as natural deposits but also artificial mixing of cementitious additives (e.g., cement, lime, slag, fly ash) for soil stabilization is an economic and widely used method of ground improvement in various infrastructure projects like road, rail, embankment, dam etc. To meet safety and serviceability requirement of structures constructed over any type of cemented sand, there is a strong need among geotechnical engineers regarding proper understanding of the behaviour of this type of soil under infrastructure load.

Over the years, extensive research including laboratory compression testing have been conducted for naturally and artificially cemented soils of various types (Clough et al., 1981; Burland, 1990; Leroueil and Vaughan, 1990; Airey, 1993; Coop and Atkinson, 1993; Cuccovillo and Coop, 1999; Consoli et al., 2006). A comprehensive review of literature reveals, under compression cemented soils like uncemented soil exhibit an initially stiff elastic response followed by yielding (De Bono, 2013). However, for cemented sand, the mechanism is different owing to presence of adhesive resistance in addition to frictional resistance at particle contacts (Chang et al., 1990).

In the earlier studies on cemented sand, triaxial is the most commonly used test conducted due to the ability to control drainage and measure deformations. On most cases, those tests were conducted at low pressures (typically less than 1 MPa) where most geotechnical problems arise. However there are cases like high earth dams, deep well shafts which may subject soils to pressures upto 70 MPa (Yamamuro et al., 1996). Soils under tips of deep-driven pile foundations may experience pressure upto 350

MPa (Murphy, 1987). Under high pressures, the crushing behaviour of sand becomes prominent which influences macro-scale behaviour (Yamamuro et al., 1996). More recently, the study on cemented sand subjected to high-pressure triaxial testing (Marri, 2010) indicates significant effect of cement contents and confining pressures on the mechanical behaviour of cemented materials.

Earlier studies confirm that microstructure (fabric and bond) of soil in addition to its stress history significantly influences its mechanical behaviour for different range of strains (Leroueil and Vaughan, 1990; Cotecchia and Chandler, 1997). It is even suggested by (Cuccovillo and Coop, 1997) that structure should be considered as an element of the nature of a sand in addition to properties such as mineralogy, particle shape and grading. However, since interparticle cohesion forces for sands unlike structured clay are negligible, structure in sand can be simply identified with bonding which arises from interparticle cementing (Clough et al., 1981). Moreover, behaviour of cemented sands have been observed to resemble patterns of behaviour similar to structured clays which are related to the elements of the soil structure (Cuccovillo and Coop, 1999). However, significant number of pioneering experimental studies (Oda, 1972b; Oda, 1972c; Oda and Konishi, 1974; Oda, 1977; Konishi et al., 1982; Mehrabadi et al., 1982; Oda et al., 1982; Konishi et al., 1983; Oda et al., 1985; Oda and Nakayama, 1989; Oda, 1993) on fabric of granular soil were conducted without considering the influence of bond.

1.2 Statement of the Problem

One of the difficulty in working with microstructure of cemented sand is visualization and quantification of degeneration of cementation. This instigated development of various phenomenological method to be used in constitutive modelling without proper understanding of the micromechanics (Pekau and Gocevski, 1989; Lagioia and Nova, 1995; Desai and Toth, 1996; Abdulla and Kiousis, 1997; Nova et al., 2003; Haeri and Hamidi, 2009). However, many researchers with the aid of the Discrete Element Method (DEM), attempted to approximately simulate bonded material (Utili and Nova, 2008; Obermayr et al., 2013; Brown et al., 2014; Jiang et al., 2014; Bono et al., 2015) to investigate their micromechanical behaviour (Wang and Leung, 2008; de Bono and McDowell, 2014; Shen et al., 2016). But simulated behaviour may not be always true representative of the actual behaviour.

Rapid advancement in high-resolution X-ray CT imaging revolutionised the grain-scale investigation of soil fabrics (Alshibli et al., 2014; Al Mahbub and Haque, 2016; Druckrey et al., 2016; Alam and Haque, 2017; Karatza et al., 2017; Alam et al., 2018; Imseeh et al., 2018). In addition to quantification of fundamental properties (scalar and directional) of soil particles and voids like their morphology, coordination number, direction of long axis, direction of contact vector etc., this technology has been used for the quantification of microstructural evolution of granular soils and interparticle voids subjected to loads. X-ray CT technology offers the advantage of visualization of actual mechanism between particle-cement composite and voids and degeneration of bond, however, no such particle level studies on cemented soils using this technology

is available until a very recent one by Dadda et al. (2018a) which focused on contact properties (coordination number, contact surface area, contacts orientation and types of contact).

Bearing in mind the limited understanding of the microstructural behaviour of cemented sand, especially at high stress, a grain-scale investigation of the mechanical behaviour of cemented sands subjected to *insitu* X-ray CT imaging under one-dimensional compression is proposed in the current research.

1.3 Aims and Objectives

The principal aims of this research are to improve understanding micromechanics of cemented sand at high stress ultimately allowing better predictions of the behaviour of soil. The objectives of this research can be summarised as follows:

- To examine the microstructural evolution of cemented soils under *insitu* condition using high resolution X-ray CT imaging
- To evaluate the microstructural scalar properties (void ratio, particle size distribution, sphericity) of soils under one-dimensional compression loading
- To quantify directional properties of microstructure of cemented soils under one-dimensional compression loading
- To evaluate directional anisotropy based scalar parameter of voids to explain macro-scale behaviour of cemented sand.

1.4 Thesis Outline

This thesis consists of seven chapters. The following six chapters are organised as follows:

Chapter 2 provides a literature review, which covers experimental and numerical studies on microstructural behaviour of naturally and artificially cemented sand under compression. This is accompanied by a review on crushing behaviour of granular soil. Special attention was given on X-ray CT based studies for obvious reason.

Chapter 3 discusses the experimental setup and methodology. It describes X-ray CT technology, Monash X-ray CT facility, the materials and index properties, sample preparation, test setup, testing procedures, image acquisition, processing and analysing of images using image processing software and Matlab code, and relevant challenges encountered.

Chapter 4 presents and discusses the observed yielding and crushing behaviour and evolution of scalar and directional fabric of uncemented sand subjected to *insitu* X-ray CT under one dimensional compression test.

Chapter 5 explores observed behaviour and evolution of void fabric of cemented sand subjected to *insitu* X-ray CT under one dimensional compression test. With primary focus on the evolution of directional anisotropy of voids, changes in various scalar paramaters (sphericity, anisotropy) of voids with progressive loading were analysed and discussed.

Chapter 6 presents a conceptual framework for microstructural study of cemented sand.

Chapter 7 presents important conclusions of the research work with and provides recommendations for further research.

1.5 References

Abdulla, A. A. & Kiousis, P. D. 1997. Behavior of cemented sands—II. Modelling. *International Journal for Numerical and Analytical Methods in Geomechanics,* **21,** 549-568.

Airey, D. 1993. Triaxial testing of naturally cemented carbonate soil. *Journal of Geotechnical Engineering,* **119,** 1379-1398.

Al Mahbub, A. & Haque, A. 2016. X-ray computed tomography imaging of the microstructure of sand particles subjected to high pressure one-dimensional compression. *Materials,* **9,** 890.

Alam, M., Haque, A. & Ranjith, P. 2018. A Study of the Particle-Level Fabric and Morphology of Granular Soils under One-Dimensional Compression Using Insitu X-ray CT Imaging. *Materials (Basel, Switzerland),* **11**.

Alam, M. F. & Haque, A. 2017. A New Cluster Analysis-Marker-Controlled Watershed Method for Separating Particles of Granular Soils. *Materials,* **10,** 1195.

Alshibli, K. A., Druckrey, A. M., Al-Raoush, R. I., Weiskittel, T. & Lavrik, N. V. 2014. Quantifying morphology of sands using 3D imaging. *Journal of Materials in Civil Engineering,* **27,** 04014275.

Bono, J., McDowell, G. & Wanatowski, D. 2015. Investigating the micro mechanics of cemented sand using DEM. *International Journal for Numerical and Analytical Methods in Geomechanics,* **39,** 655-675.

Brown, N. J., Chen, J.-F. & Ooi, J. Y. 2014. A bond model for DEM simulation of cementitious materials and deformable structures. *Granular Matter,* **16,** 299-311.

Burland, J. 1990. On the compressibility and shear strength of natural clays. *Géotechnique,* **40,** 329-378.

Chang, C., Misra, A. & Sundaram, S. 1990. Micromechanical modelling of cemented sands under low amplitude oscillations.

Clough, G. W., Sitar, N., Bachus, R. C. & Rad, N. S. 1981. Cemented sands under static loading. *Journal of Geotechnical and Geoenvironmental Engineering,* **107**.

Consoli, N., Rotta, G. & Prietto, P. 2006. Yielding–compressibility–strength relationship for an artificially cemented soil cured under stress. *Geotechnique,* **56,** 69-72.

Coop, M. & Atkinson, J. 1993. The mechanics of cemented carbonate sands. *Geotechnique,* **43,** 53-67.

Cotecchia, F. & Chandler, R. 1997. The influence of structure on the pre-failure behaviour of a natural clay. *Géotechnique,* **47,** 523-544.

Cuccovillo, T. & Coop, M. 1997. Yielding and pre-failure deformation of structured sands. *Geotechnique,* **47,** 491-508.

Cuccovillo, T. & Coop, M. 1999. On the mechanics of structured sands. *Géotechnique,* **49,** 741-760.

Dadda, A., Geindreau, C., Emeriault, F., du Roscoat, S. R., Filet, A. E. & Garandet, A. 2018. Characterization of contact properties in biocemented sand using 3D X-ray micro-tomography. *Acta Geotechnica***,** 1-17.

De Bono, J. P. 2013. *Discrete element modeling of cemented sand and particle crushing at high pressures.* University of Nottingham.

de Bono, J. P. & McDowell, G. R. 2014. Discrete element modelling of one-dimensional compression of cemented sand. *Granular Matter,* **16,** 79-90.

Desai, C. S. & Toth, J. 1996. Disturbed state constitutive modeling based on stress-strain and nondestructive behavior. *International Journal of Solids and Structures,* **33,** 1619-1650.

Druckrey, A. M., Alshibli, K. A. & Al-Raoush, R. I. 2016. 3D characterization of sand particle-to-particle contact and morphology. *Computers and Geotechnics,* **74,** 26-35.

Haeri, S. & Hamidi, A. 2009. Constitutive modelling of cemented gravelly sands. *Geomechanics and Geoengineering: An International Journal,* **4,** 123-139.

Imseeh, W. H., Druckrey, A. M. & Alshibli, K. A. 2018. 3D experimental quantification of fabric and fabric evolution of sheared granular materials using synchrotron micro-computed tomography. *Granular Matter,* **20,** 24.

Jiang, M., Zhang, F. & Sun, Y. 2014. An evaluation on the degradation evolutions in three constitutive models for bonded geomaterials by DEM analyses. *Computers and Geotechnics,* **57,** 1-16.

Karatza, Z., Andò, E., Papanicolopulos, S., Ooi, J. & Viggiani, G. 2017. Evolution of deformation and breakage in sand studied using X-ray tomography. *Géotechnique,* **1,** 1-11.

Konishi, J., Oda, M. & Nemat-Nasser, S. 1982. Inherent anisotropy and shear strength of assembly of oval cross-sectional rods. *Deformation and failure of granular materials. AA BALKEMA/Rotterdam*.

Konishi, J., Oda, M. & Nemat-Nasser, S. 1983. Induced anisotropy in assemblies of oval cross-sectional rods in biaxial compression. *Studies in Applied Mechanics.* Elsevier.

Lagioia, R. & Nova, R. 1995. An experimental and theoretical study of the behaviour of a calcarenite in triaxial compression. *Géotechnique,* **45,** 633-648.

Leroueil, S. & Vaughan, P. 1990. The general and congruent effects of structure in natural soils and weak rocks. *Géotechnique,* **40,** 467-488.

Marri, A. 2010. *The mechanical behaviour of cemented granular materials at high pressures.* University of Nottingham.

Mehrabadi, M. M., Nemat-Nasser, S. & Oda, M. 1982. On statistical description of stress and fabric in granular materials. *International Journal for Numerical and Analytical Methods in Geomechanics,* **6,** 95-108.

Mitchell, J. K. & Soga, K. 2005. *Fundamentals of soil behavior*, John Wiley & Sons New York.

Murphy, D. J. 1987. Stress, degradation, and shear strength of granular material. *Geotech. Modeling and Applications, SM Sayed, Ed., Gulf Publishing Company, Houston, Tex***,** 181-211.

Nova, R., Castellanza, R. & Tamagnini, C. 2003. A constitutive model for bonded geomaterials subject to mechanical and/or chemical degradation. *International Journal for Numerical and Analytical Methods in Geomechanics,* **27,** 705-732.

Obermayr, M., Dressler, K., Vrettos, C. & Eberhard, P. 2013. A bonded-particle model for cemented sand. *Computers and Geotechnics,* **49,** 299-313.

Oda, M. 1972a. Initial fabrics and their relations to mechanical properties of granular material. *Soils and foundations,* **12,** 17-36.

Oda, M. 1972b. The mechanism of fabric changes during compressional deformation of sand. *Soils and foundations,* **12,** 1-18.

Oda, M. 1977. Fabrics and their effects on the deformation behaviors of sand. *埼玉大学工学部建設系研究報告***,** p1-59.

Oda, M. 1993. Inherent and induced anisotropy in plasticity theory of granular soils. *Mechanics of Materials,* **16,** 35-45.

Oda, M. & Konishi, J. 1974. Microscopic deformation mechanism of granular material in simple shear. *Soils and foundations,* **14,** 25-38.

Oda, M. & Nakayama, H. 1989. Yield function for soil with anisotropic fabric. *Journal of Engineering Mechanics,* **115,** 89-104.

Oda, M., Nemat-Nasser, S. & Konishi, J. 1985. Stress-induced anisotropy in granular masses. *Soils and foundations,* **25,** 85-97.

Oda, M., Nemat-Nasser, S. & Mehrabadi, M. M. 1982. A statistical study of fabric in a random assembly of spherical granules. *International Journal for Numerical and analytical methods in Geomechanics,* **6,** 77-94.

Pekau, O. & Gocevski, V. 1989. Elasto-plastic model for cemented and pure sand deposits. *Computers and Geotechnics,* **7,** 155-187.

Shen, Z., Jiang, M. & Thornton, C. 2016. DEM simulation of bonded granular material. Part I: contact model and application to cemented sand. *Computers and Geotechnics,* **75,** 192-209.

Utili, S. & Nova, R. 2008. DEM analysis of bonded granular geomaterials. *International Journal for Numerical and Analytical Methods in Geomechanics,* **32,** 1997-2031.

Wang, Y.-H. & Leung, S.-C. 2008. A particulate-scale investigation of cemented sand behavior. *Canadian Geotechnical Journal,* **45,** 29-44.

Yamamuro, J. A., Bopp, P. A. & Lade, P. V. 1996. One-dimensional compression of sands at high pressures. *Journal of geotechnical engineering,* **122,** 147-154.

2 LITERATURE REVIEW

2.1 Introduction

The primary objective of this current study is focused on understanding the grain-scale behaviour of cemented sand. In this context, it is quite reasonable to explore behaviour of uncemented sand for similar grain size and loading condition. So, quite understandably this chapter which reviews the previous studies, dedicates a substantial part on discussing the work on uncemented sand before moving on to cemented sand on which relatively limited microstructural work has been done.

In the next two sections, brief on fundamentals of fabric parameters and chemical cementation are presented which are followed by review of relevant literatures on microstructural behaviour of uncemented granular materials under compression. Finally, a comprehensive review of the literatures on behaviour of cemented sand under compression is presented. Among various experimental and numerical based studies, for obvious reason, particular focus was on X-Ray computed tomography (CT) based studies.

2.2 Microstructure of Soil

Behaviour of artificially cemented sand is typically affected by its internal structure consisting of both fabric and bonding. In absence of bond, fabric or internal structure is basically the arrangement of particles, particle groups, and associated pore spaces.

When sands are subjected to external loads, rearrangement of the particles take place as they move and rotate under the action of contact forces generated from the applied load. Thus progressive evolution of the fabric take place. To capture the initial fabric and their evolution, fabric can be quantified using scalar parameters (e.g. contact index, coordination number, void ratio distribution, vector magnitude) and directional parameters (e.g. particle orientation, void orientation, contact normal, branch vector) (Figure 2-1) and analysing them under statistical framework. For directional parameters, in particular, the effect of initial fabric orientation on the behaviour of soil under load and evolution of anisotropy in fabric orientation at different stages of loading have been the areas of significant interests among researchers (Arthur and Menzies, 1972; Oda, 1972b; Oda et al., 1985; Oda and Nakayama, 1989; Oda, 1993; Imseeh et al., 2018). Whereas suitability of scalar parameters to fit in existing or new soil models to explain the behaviour interests many researchers (Manahiloh and Muhunthan, 2012; Fonseca et al., 2013a; Fonseca et al., 2013b; Cil and Alshibli, 2014; Druckrey et al., 2016; Manahiloh et al., 2016).

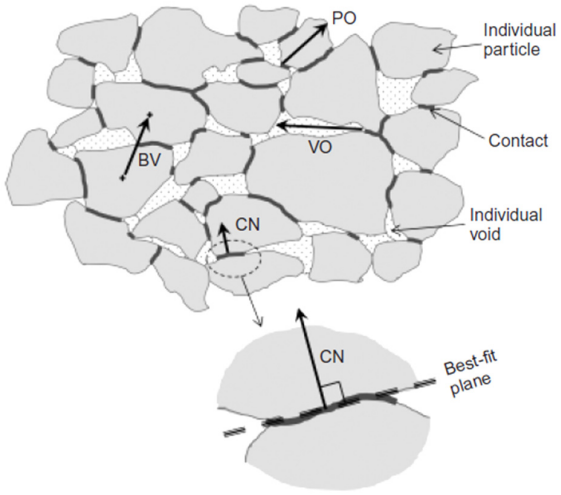

Figure 2-1: Schematic diagram of fabric for intact sample, with indication of main features and vectors used for fabric quantification: particle orientation (PO), void orientation (VO), contact normal (CN) and branch vector (BV). (from (Fonseca et al., 2013b)

The role of void shapes in determining granular material mechanical behaviour is less apparent (Fu and Dafalias, 2015). Since voids are simply the space that is not filled by the solid phase, the evolution of void spaces can be seen as a result of the evolution of the solid phase. Therefore, the relationship between the void space characteristics and material mechanical behaviour is somewhat indirect. However, an indirect relation could still result in a strong and definitive correlation, making void-based fabric tensor potentially useful, especially when it is convenient to measure (Manahiloh et al., 2016).

2.3 Hydration of Cement

Structured soil or cemented soil are widely available in nature. However, soil stabilization by artificially mixing cementitious additives (eg. Hydraulic cement, fly ash, lime etc.) with soil is a popular and economic method of ground improvement. Soil stabilization is based on the principle of producing high strength cementitious reaction products within soil mass through the introduction of different cementitious

additives. Different types of additives can be used for this purpose depending upon the type of soil, target strength and also the required rate of strength development. Portland cement, lime, and latent hydraulic or pozzalonic materials react with water under certain conditions forming similar reaction products (i.e. calcium silicate hydrate (C-S-H) gel, calcium aluminium silicate hydrates (C-A-S-H) gel) which possess high strength. Cement yields high-strength reaction products immediately on reacting with water. The most important constituents of cement are given in Table 2-1.

Table 2-1: Important constituents of cement (from Janz and Johansson, 2002)

Constituent	**Chemical formula**	**Abbreviation**
Tricalcium silicate	$3CaO.SiO_2$	C_3S
Dicalcium silicate	$2CaO.SiO_2$	C_2S
Tricalcium aluminate	$3CaO.Al_2O_3$	C_3A
Tetracalcium aluminoferrite	$4CaO.Al_2O_3.Fe_2O_3$	C_4AF

When water is added to cement, each of the compounds undergoes hydration and contributes to the final reaction product. Only the calcium silicates contribute to strength. Tricalcium silicate is responsible for most of the early strength (first 7 days). Dicalcium silicate, which reacts more slowly, contributes only to the strength at later times.

The reactions involving Tricalcium silicate, the major contributor of strength is given below(Bullard et al., 2011):

$$C_3S + H_2O \rightarrow C_3S_2H_x \text{ (Hydrated gel)} + Ca(OH)_2 \qquad (2.1)$$

Cementitious additives react with soil and improves engineering properties of treated soils (Ingles and Metcalf, 1972). In other way, additives impart structure (bond and fabric) to soils (Mitchell and Soga, 2005), and thus allows structured soils to exist at higher void ratios than their equivalent reconstituted counterparts (Burland, 1990; Leroueil and Vaughan, 1990).

2.4 Behaviour of Uncemented Sand

2.4.1 Phenomenological Studies

Under high stress, crushing of particles (Terzaghi and Peck, 1948) is a common phenomenon that takes place in granular soils. In fact, crushing is recognised by Coop and Lee (1993) as the principal mechanism for plastic volumetric compression of granular materials. A practical consequence of crushing which has fundamental importance especially in petroleum geology and reservoir mechanics is reduction of porosity and permeability (Chuhan et al., 2003).

With the objective of investigating the influence of sand characteristics like mineralogy, grain size, grain-size distribution, particle shape, sand density, and clay content on its mechanical compaction in terms of reduction of porosity, Chuhan et al. (2003) conducted a rigorous, systematic study on 22 naturally occurring wide range of sands by performing one-dimensional compression experiments (approx. 150 tests) at stresses up to 50 MPa. Chuhan et al. (2003) reported, at low stresses (<5 MPa), frictional slip and rotation - two irreversible micromechanical processes (Zhang et al., 1990a; Satake and Jenkins, 2013) were considered as the main mechanism of porosity

loss. In addition, at low stresses, initiation of early minor crushing of grain corners which increases with particle size and angularity as shown in Figure 2-2, were reported to contribute to the compression behaviour. From petrographic analyses, the study (Chuhan et al., 2003) at intermediate stress range (5–25 MPa) found increased grain crushing and reduced grain size (Chuhan et al., 2002) with an increasing stress. Stronger relationship between yield stress and porosity loss (Figure 2-3a) was observed in the intermediate stress interval (5-25 MPa). Therefore, the porosity values at 25 MPa are significantly affected by grain crushing (Figure 2-3b). Low yield stresses in coarser, angular, and dense sands are due to the initiation of marked grain crushing at relatively low stresses. This results in higher porosity loss over the intermediate-stress interval (5–25 MPa). Pre-existing fissures and crystal imperfections are explained as the result of positive correlation between increase in grain fracturing with an increase in grain size (Johnson and Johnson, 1987; Zhang et al., 1990b). In angular grains the contact forces are concentrated at smaller contact areas, which promotes grain crushing and increases porosity loss.

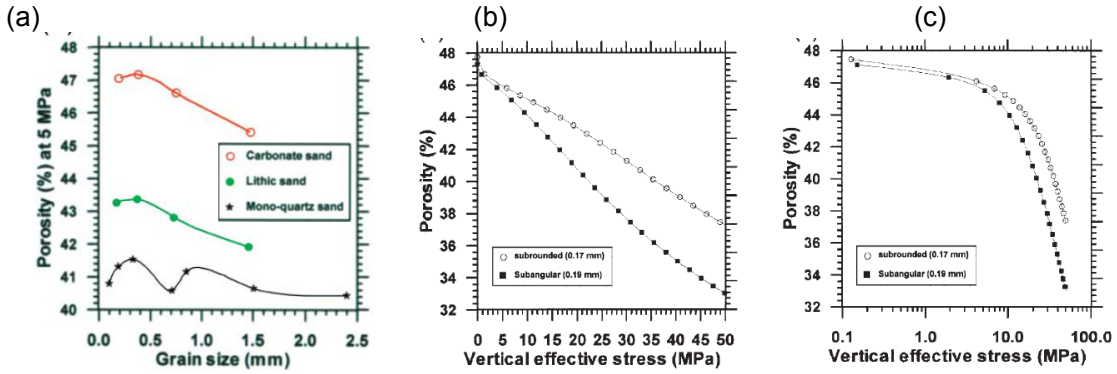

Figure 2-2: Effects of (a) grain-size variation in sand on porosities at 5 MPa vertical effective stresses (b) grain-shape variation for well-graded, fine-grained mono-quartz-rich sands on porosities. (from Chuhan et al. (2003))

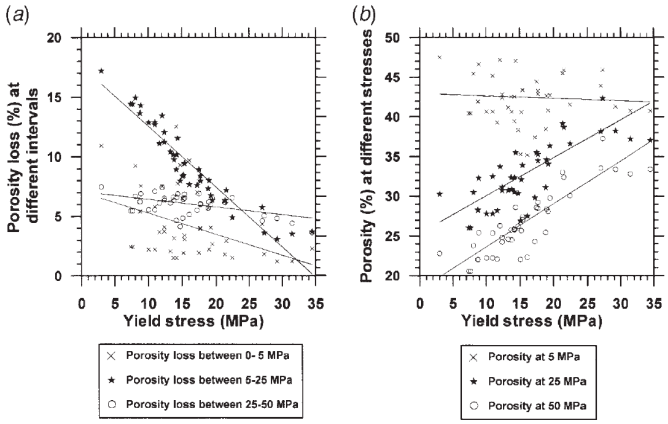

Figure 2-3: Yield stress (MPa) versus porosity and porosity loss at different stress levels: (a) porosity loss (%) over the stress intervals 0–5, 5–25, and 25–50 MPa; and (b) porosity values at 5, 25, and 50 MPa. (from Chuhan et al. (2003))

Rate of decrease of porosity loss after yield point as observed in compression curves suggest difficulty in further crushing of the smaller grains and their cushioning effect to the remaining coarser grains against crushing. Using petrographic analyses Chuhan et al. (2002) has shown (Figure 2-4) that grain crushing results in relatively more fine fragments in the lithic and carbonate sands than in the mono-quartz sand thus causing more rapid reduction in the post-yield compressibility. In terms of nature of grain crushing for mono-quartz sands, more brittle fracturing is common, and the fractures propagate into the grains. In lithic sands grains split along the sutures in the polycrystalline quartz grains, and grain crushing is more extensive than that in the mono-quartz sand. At stresses higher than 10 MPa the coarser carbonate sands become less compressible, maintaining higher porosities than the mono-quartz-rich sand. This is due to the fact that coarser carbonate sands have a relatively high angularity, and initially there is local grain crushing at grain contacts. This increases the area of the grain contacts, so the coarser carbonate sands become less compressible

at higher stresses. They (Chuhan et al., 2002) found it reasonable to conclude that the sands with the coarser and weaker grains are less compressible at stresses higher than 10 MPa. In the high-stress interval (25–50 MPa) differences in compressibility and porosity loss because of grain size, grain shape, uniformity coefficient, mineralogy, and clay content are significantly reduced. Grain crushing can thus be considered a part of the reorganisation process, where sand is adapting itself to higher stresses.

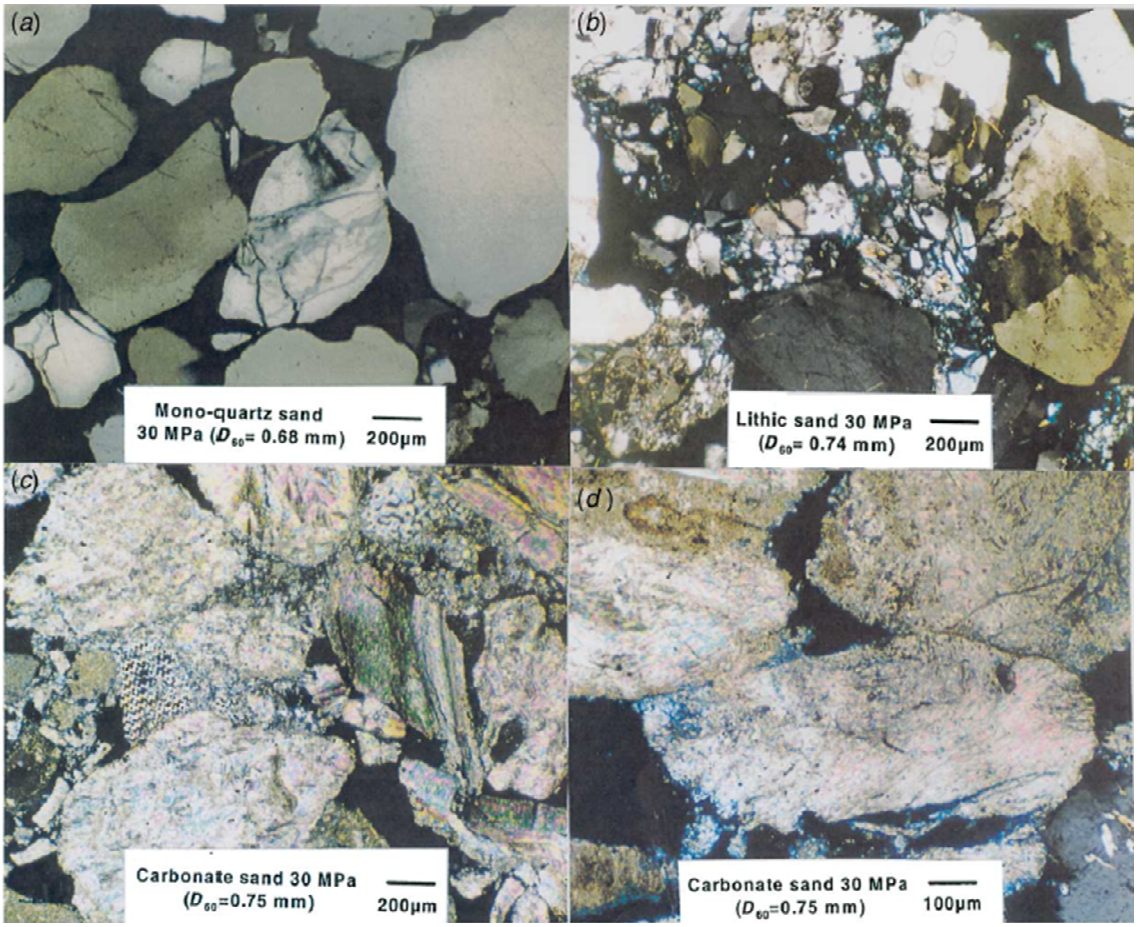

Figure 2-4: Microphotographs of medium-grained compacted sands of different compositions after an effective stress of 30 MPa: (a) mono-quartz-rich (D60 = 0.68 mm) sand, (b) lithic (D60 = 0.74 mm) sand, and (c, d) carbonate sand (D60 = 0.75 mm) (from Chuhan et al. (2003)).

Many other researchers have studied the crushing and yielding behaviour of granular soils subjected to one-dimensional compression loading (De Souza, 1958; Hendron Jr, 1963; Hardin, 1985; Hagerty et al., 1993; McDowell et al., 1996; Mcdowell and Bolton, 1998; Nakata et al., 2001; Soil and Rock, 2004; McDowell, 2005; Altuhafi and Coop, 2011). Nakata et al. (2001) conducted high pressure one-dimensional compression tests on silica sand seeded with marked particles to examine the relationship between the curvature and slope of the compression line and the statistics of individual particle crushing taking into account particle size and overall grading. It was observed that yielding characteristics significantly depends on the grading of particles with much more marked yielding occurring for uniformly graded sands. Figure 2-5a shows the relationship between void ratio and logarithm of vertical stresses for uniformly graded and well graded silica sand. The yield stresses marked by P is higher in well-graded sample (22 MPa) compared to that in uniformly graded one (14 MPa) and the maximum curvature is greater for uniformly graded material indicating higher degree of crushing (Hagerty et al., 1993) causing increase in compressibility which is supported by the initial larger rate of increase in vertical strain following the yield (Figure 2-5b). The marked peak value of the compression index, C_c observed from the plot of compression index curve vs. vertical stress (Figure 2-5c), represents the increase in the slope for e-logσ'_v occurring immediate after yielding. For the yield and $C_{cmax,}$ stress levels are different for each sand. The gradient C_c for uniformly graded sand decreases after the peak and approaches the same value as the well graded sand. Observation from the marked particles within uniformly graded sands show splitting of particles took place mainly between the yield stress and the point of C_{cmax}. Within

this stress zone, for well graded sample, breaking of asperities or grinding for large seeded particles and splitting for smaller particles were main reasons of crushing behaviour. As the material become better graded, nature of particle crushing changed from the sudden catastrophic onset of splitting to the gradual splitting of smaller size particles, breaking of smaller asperities and grinding of the surface. The similar cushioning effect of the smaller size particles as explained by Chuhan et al. (2003) may explain the gradual crushing behaviour of well graded sands. The effect of particle size distributions on the grain crushing under 1D compression were also studied by Nakata et al. (2001) and later by Altuhafi and Coop (2011). They concluded that a uniformly graded sand shows marked yielding compared to a well graded sand and they have related such differences with the nature of microscopic crushing of particles. Altuhafi and Coop (2011) concluded more breakage occurs in samples with higher initial void ratios. However, Nakata et al. (2001) found particles breakage alone as insufficient descriptor to explain overall compressibility of samples for changes observed of grain size distributions as presented in Figure 2-6.

The change of particle sizes with stresses affects many important properties of sands, such as the yield stress, compressibility, susceptibility to erosion, shear strength, and hydraulic conductivity. One of the earlier work by Hardin (1985) is highly recognised for the contribution it made defining degree of crushing or breakage of particles that is significant to soil behaviour. Hardin (1985) introduced new measures to account for particle breakage, called breakage potential, total breakage and relative breakage

which integrate the changes in the particle size distribution curve for all sizes greater than 0.074 mm caused by given loading of a given soil.

The potential for breakage, b_p of a particle of a given size D, may be represented by

$$b_p = \log_{10}\left[\frac{\text{D in mm}}{0.074\ \text{mm}}\right] \qquad \text{for D} \geq 0.074\ \text{mm} \qquad (2.2a)$$

$$b_p = 0 \qquad \text{for D} < 0.074\ \text{mm} \qquad (2.2b)$$

Breakage potential, B_p for the entire sample is

$$B_p = \int_0^1 b_p\, df \qquad (2.3)$$

df is a differential of "percent passing" divided by 100.

As shown in Figure 2-7a, B_p is equal to the area between the line defining the upper limit of the silt size, D>0.074 , and the part of the particle size distribution for which D>0.074 mm, where the unit area is the area of one log cycle as shown in the right most figure. Now, particle distribution curve after crushing will be shifted as shown in Figure 2-7b. The amount of crushing may be represented by

$$B_t = \int_0^1 (b_{p0} - b_{pl})df \qquad (2.4)$$

In which b_{p0} = the original values of b_p; and b_{pl} = the values of b_p after loading. B_t is called total breakage in Figure 2-7b. Relative breakage (B_r) is calculated as:

$$B_r = \frac{B_t}{B_p} \qquad (2.5)$$

All these equations (2.2 – 2.5), approximately independent of particle size distribution, greatly simplifies the analysis of the effects of state of effective stress and effective stress path, initial void ratios, particle shape and particle hardness.

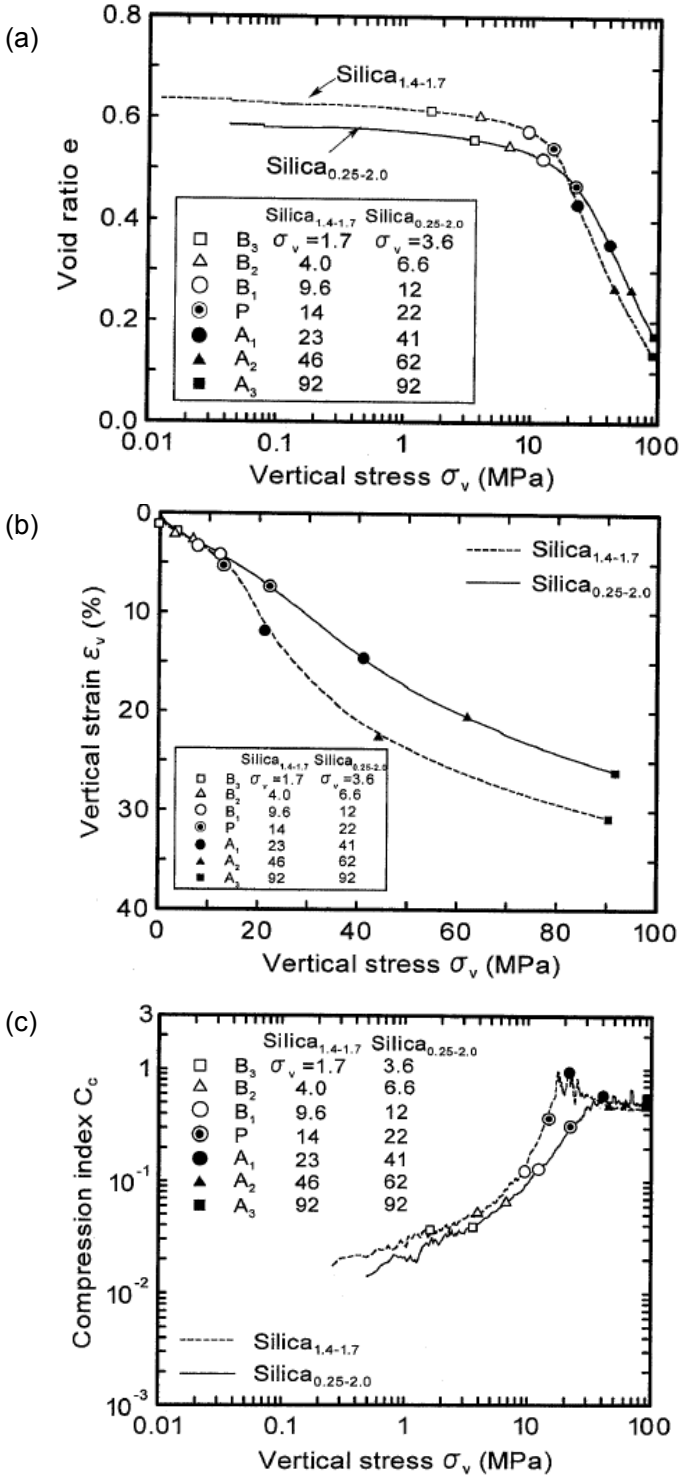

Figure 2-5: (a) One-dimensional compression curves (b) One-dimensional stress-strain curves (c) variations of compression index with vertical stress for uniformly and well-graded sands. (from Nakata et al. (2001))

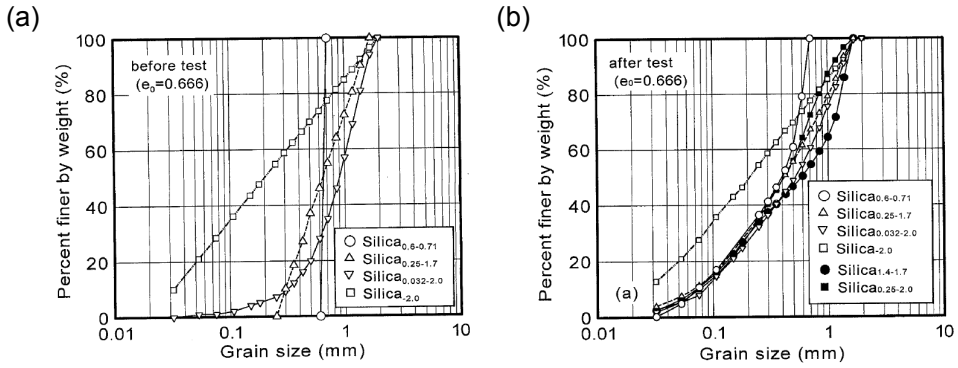

Figure 2-6: Grain size distributions for silica sands (a) before and (b) after testing (from Nakata et al. (2001))

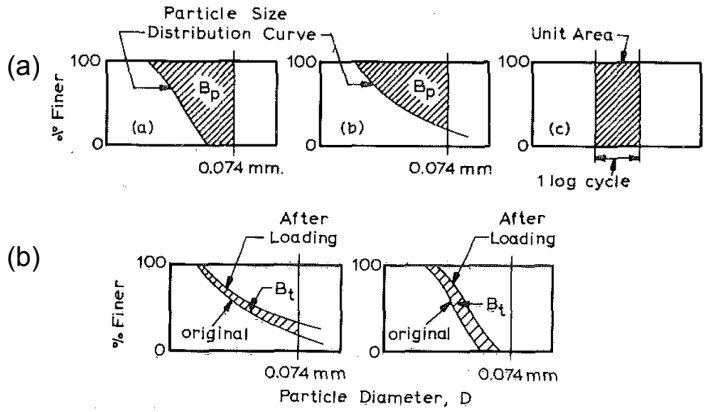

Figure 2-7: Definition of (a)breakage potential (b)total breakage (from Hardin (1985))

The above mentioned studies can be categorized as investigation of macro scale behaviour of granular material where influence of microstructure has been appreciated. However, due to highly invasive nature of these tests, they tend to disturb the fabric of the materials and failed to capture and explain the specific microstructural evolution of the material. In other words, it was not possible to examine non-destructively the micro-structural changes of soils subjected to an incremental stress regime. In addition, particles for observation had to be chosen randomly and in limited number which greatly influences the accuracy of the outcome.

2.4.2 Experimental Studies prior to advent of 3D grain-scale Imaging Technique

It has been recognised that microstructure (fabric only in absence of bond) of granular materials play crucial role in their mechanical behaviour (Satake and Jenkins, 2013). In the last few decades, numerous experimental studies have demonstrated that mechanical response of granular materials is significantly influenced by microstructural fabric and its evolution. Oda's pioneering work on soil fabric (Oda, 1972b; Oda, 1972c; Oda, 1972a; Oda and Konishi, 1974; Oda, 1977; Oda et al., 1982; Oda et al., 1985; Oda and Nakayama, 1989) for couple of decades have significantly contributed to the valuable understanding of behaviour of fabric. One of the fundamental objectives of fabric based study is to find correlation in fabric anisotropy with applied load or deformation. There are basically two types of fabric anisotropy which is of interest: initial or inherent anisotropy which is relevant to deposition of particles and induced anisotropy which is caused from modification of initial anisotropy on the application of load or deformation.

Oda's pioneering work (Oda, 1972b; Oda, 1972c; Oda, 1972a), with the aid of microscope and thin section method, quantified fabric anisotropy in terms of particle orientations. Those work suggested initial fabric which is dependent on particle shape and method of deposition, has great influences on the mechanical properties. Preferred alignment of particle long axes with the bedding plane is the primary source of inherent fabric anisotropy. However, it is not direct influence of orientation of particles rather it is the directional preference of the contact normal (with respect to loading direction (principal stress in triaxial test as performed in his studies) that

influences (Figure 2-8) the mechanical properties of soil. He also suggests, the process of fabric reconstruction from initial condition is continuous with increase of strain and is mostly due to preferred direction of sliding along the unstable contacts between grain particles and partly due to their rotation.

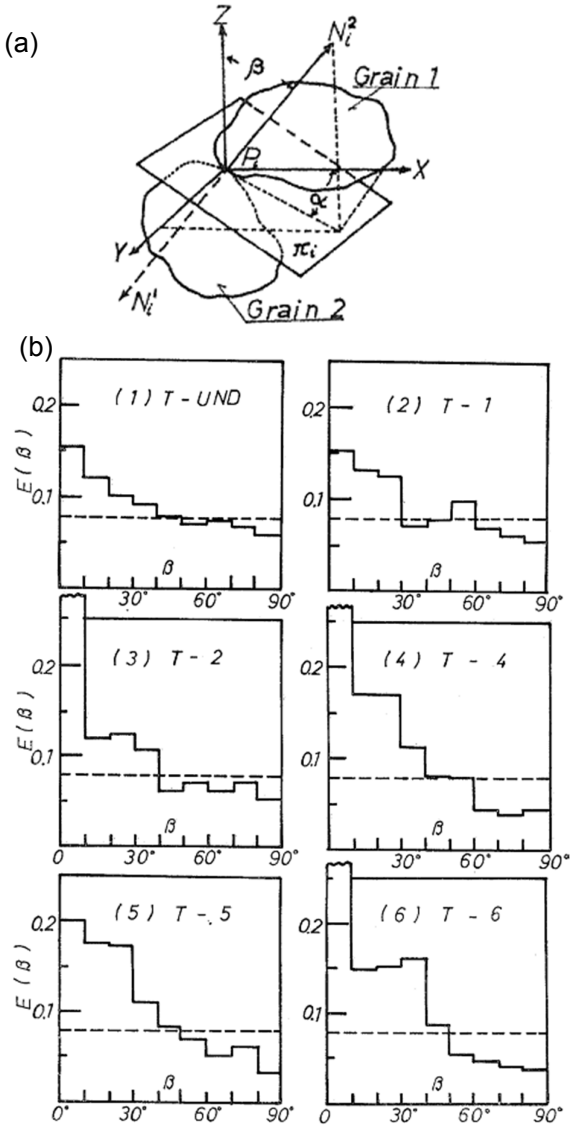

Figure 2-8: (a) Contact normal and orientation (from (Oda, 1972b)) (b) Evolution of probability density of point of contact, E with the increase of axial strain (from (Oda, 1972c)).

Oda et al. (1985) on the basis of biaxial compression tests on two-dimensional assemblies of oval cross sectional photoelastic rods, discussed the dependency of stress-induced anisotropy individually on the distribution shape of associated voids (Figure 2-9) in addition to contact normal and shape of particles, leading towards the introduction of second-rank tensors which measure the fabric anisotropy. Principal axes of these fabric tensors are shown to rotate toward the principal axes of the stress tensor (Figure 2-10). Generation of new contacts in the direction of maximum compression were found to be closely related to the formation of column-like load paths, and it is a major process which leads to the stress-induced anisotropy. Later Konishi and Naruse (1988) also proposed "mean void tensor" that could be a measure for the size, shape and orientation of local voids or void skeleton.

Later, Oda and Nakayama (1989) introduced a fabric tensor as an index for representing the anisotropy due to preferred orientation of three-dimensional particle assemblies. With the aid of this fabric tensor, they extended Drucker-Prager type yield function so as to take into account the anisotropic yielding behaviour of granular soils. Moreover, vector magnitude, Δ (introduced by (Curray, 1956)) an index measure to show the intensity of the preferred orientation of particles was found to be inversely related to the shape factor R (Figure 2-11).

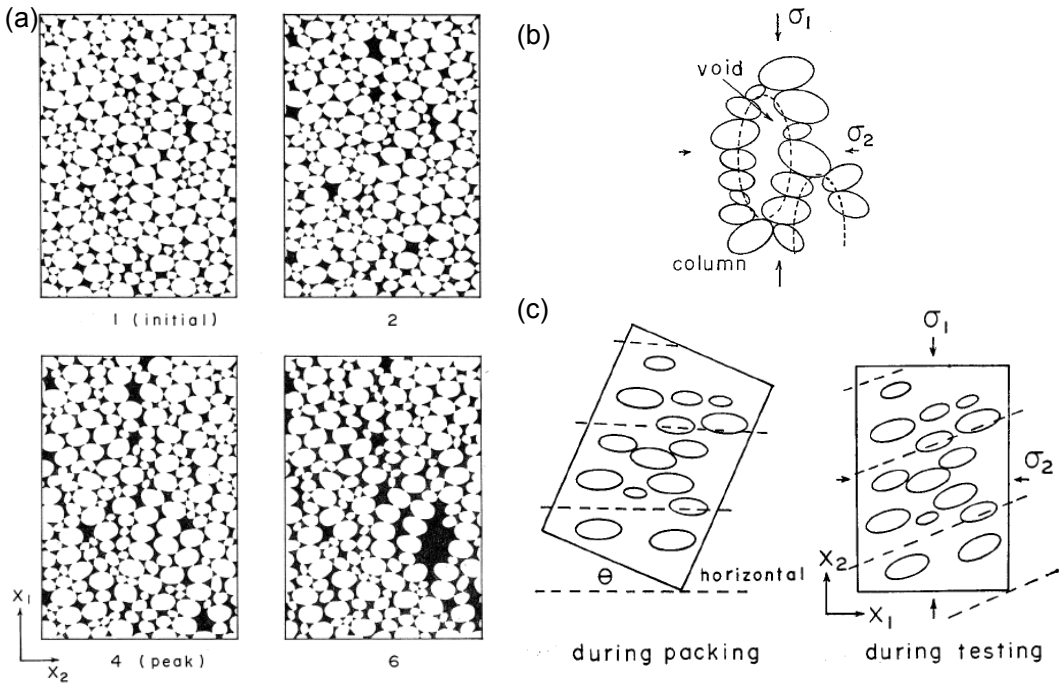

Figure 2-9: (a) Successive change of void fabric during axial compression (from (Oda et al., 1985)) (b)Mechanism of void elongation parallel to the direction of axial compression (c) Definition of bedding angle θ and of reference axes x_1 and x_2.

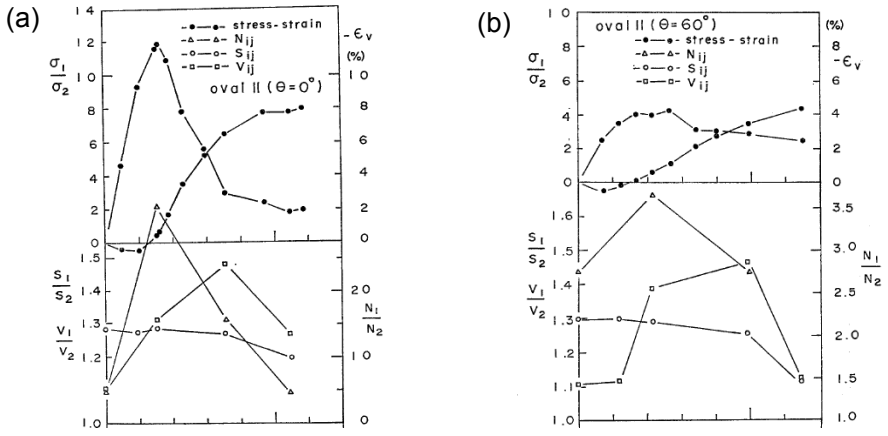

Figure 2-10: Successive change of fabric during axial compression (notations 1 and 2 are major and minor principal values for void size V, contact normal N, particle size S) for bedding plane (a) θ = 0° and (b) θ =60° (from (Oda et al., 1985))

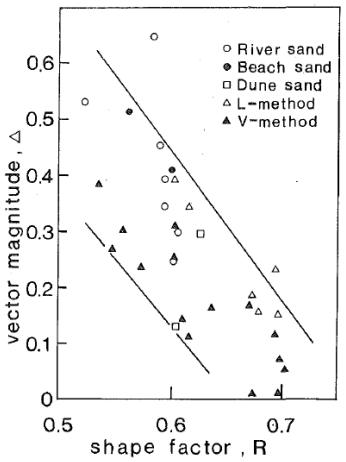

Figure 2-11: Effect of particle shape factor, R on intensity of particle anisotropy (from (Oda and Nakayama, 1989))

Jang and Frost (2000) conducted particle scale study with the aid of image analysis technique to investigate the behaviour of soil particles inside the shear zones. The methodology which includes specimen preservation by epoxy impregnation, coupon surface preparation, microscopy using bright-field illumination, and analysis of digital images (Jang, 1997; Jang, 1998). The sand particles in the shear band region was observed to demonstrate very strong alignment in the direction of shearing. For sand particles near the shear band, the contour plot of the anisotropy in Figure 2-12 shows that the sand particles are strongly oriented in the direction of the shear band. A zone about 5 mm wide of the highest anisotropy values in the range of 1.12–1.16 is shown cross-hatched.

The authors conclude, compared to global measurements of specimen response, localized behaviour state of a soil can be more correctly evaluated. However, this localized behaviour cannot be readily monitored by conventional testing methods. To quantify these localized soil structure attributes, new methodologies such as the

imaging methods described herein will be required for practical study of shear banding and other phenomena in sand specimens.

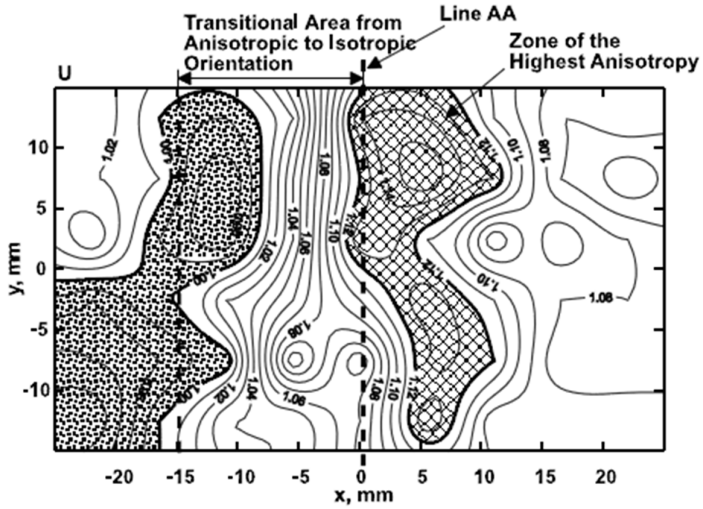

Figure 2-12: Particle orientations in the region of the shear band (from Jang and Frost (2000))

2.4.3 Discrete Element Method (DEM) based Studies

Due to the limitation in grain-scale investigation of microstructure, researchers have been relying on numerical tools predominantly DEM to investigate the material behaviour under different loading conditions (McDowell and Harireche, 2002b; Cheng et al., 2003; Cheng et al., 2004; Cheng et al., 2005; Wood, 2006; Bolton et al., 2008; Cil and Alshibli, 2014; Tengattini et al., 2016; Liu and Lok, 2018). These analyses, provided valuable understanding of the nature of compression in granular material.

By modelling each sand particle as an agglomerate of balls bonded together (as originally proposed by Robertson (2000)), McDowell and Harireche (2002b) through DEM simulations performed on one dimensional compression test on sand, showed that yielding coincides with the onset of bond breakage and yield stress reduces with

increasing agglomerates size as shown in Figure 2-13. To simulate flaws of particles, balls have been removed at random from each agglomerate to simulate flaws. The authors agree, the reason they obtained lower yield values than predicted from experiments were probably due mainly to differences in shape of real particles with the agglomerates. They also confessed that their suggested remedy by using smaller balls to obtain more angular agglomerates will make the computational time impractical.

However, in a recent study on one of the existing unresolved issue of soil mechanics - predicting the crushing strength of sand, Cavarretta et al. (2016), using a combination of physical experiments, as well as analytical and numerical simulations, claims particle size dependency of crushing failure is not necessarily due to the occurrence of material flaws but sensitive to the relative curvature of the contact. Their suggested new parameter, plastic flow ratio, is not size dependent but incorporates only the value of the crushing force as shown in Figure 2-14 and the main mechanical and shape properties of the contact. They suggest, this parameter could be used in particle-based models of granular material response, including the Discrete Element Method (DEM).

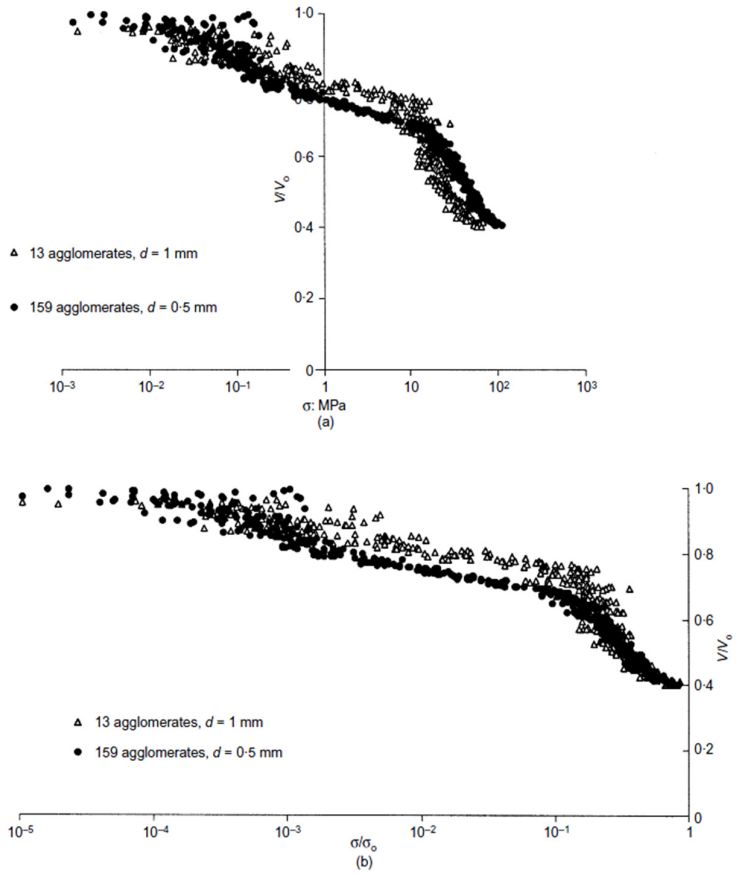

Figure 2-13: Compression curves for large and small agglomerates (from McDowell and Harireche (2002b))

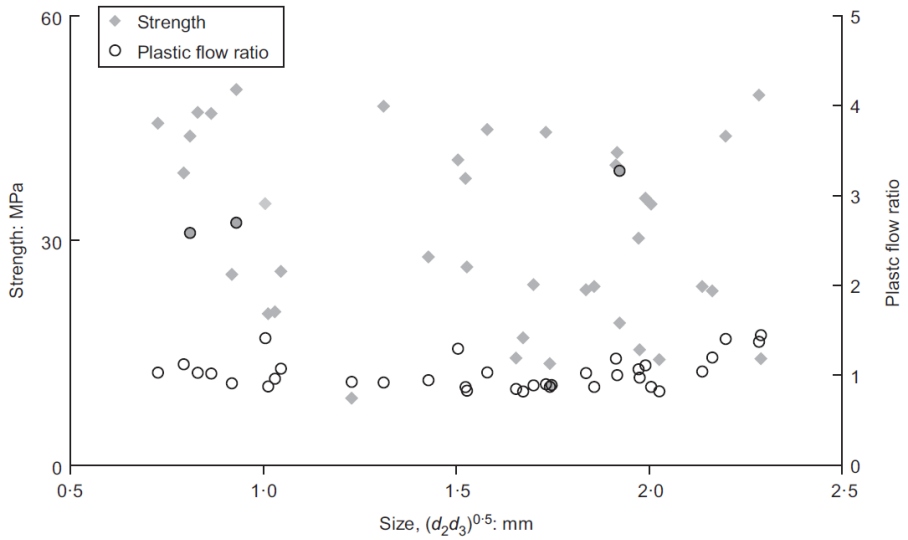

Figure 2-14: Results of crushing tests on single grains and Hime gravel (from Cavarretta et al. (2016))

Based on the results of DEM simulations, Bolton et al. (2008) discusses the possible micro-mechanical origins of soil behaviour for irregular agglomerates of bonded balls. Among various micro-mechanical processes that were examined in this study, the ratio of fragmentation before the 'yield point' in isotropic compression, was always small, corresponding in real grains with damage to asperities or by micro-cracking. An assembly of more perfect agglomerates yielded more suddenly, and exhibited unstable volume loss reminiscent of the phenomenon of 'destructuration'. After the 'yield point', when 'normal compression' on the e–logp plot gave a gradient $\lambda = 0.4$, the fragmentation ratio of smaller agglomerates was generally high, indicating splitting, whereas larger agglomerates continued to show asperity damage with small fragmentations. In the splitting events, the tensile bond breaking mode predominated. In triaxial compression, asperity damage led to reduced dilatancy on the 'dry' side of critical states, while grain splitting of the smaller fragments contributed to volume contraction during shearing on the 'wet' side. Average coordination number doubled as mean stress increased from 1 MPa to 100 MPa.

Yimsiri and Soga (2011) claims initial soil fabric has profound effects on the observed behaviours. Anisotropic characteristics of sand under isotropic stress condition are found to be a result of anisotropic soil fabric. For specimen with the contact normal concentrating in the vertical direction, the vertically-sheared (compression) specimen has higher stiffness and strength, and is more dilative than the horizontally sheared (compression) specimen. On the other hand, the results are opposite for specimen with contact normal concentrating in the horizontal direction.

DEM is a powerful tool for microstructural study. However, use of idealized digital particles may not truly represent the actual particle characteristics and behaviour in all cases. Therefore, to make the DEM more close to the reality, efforts have to be made to precisely characterize the micro-structure of soil through rigorous calibration.

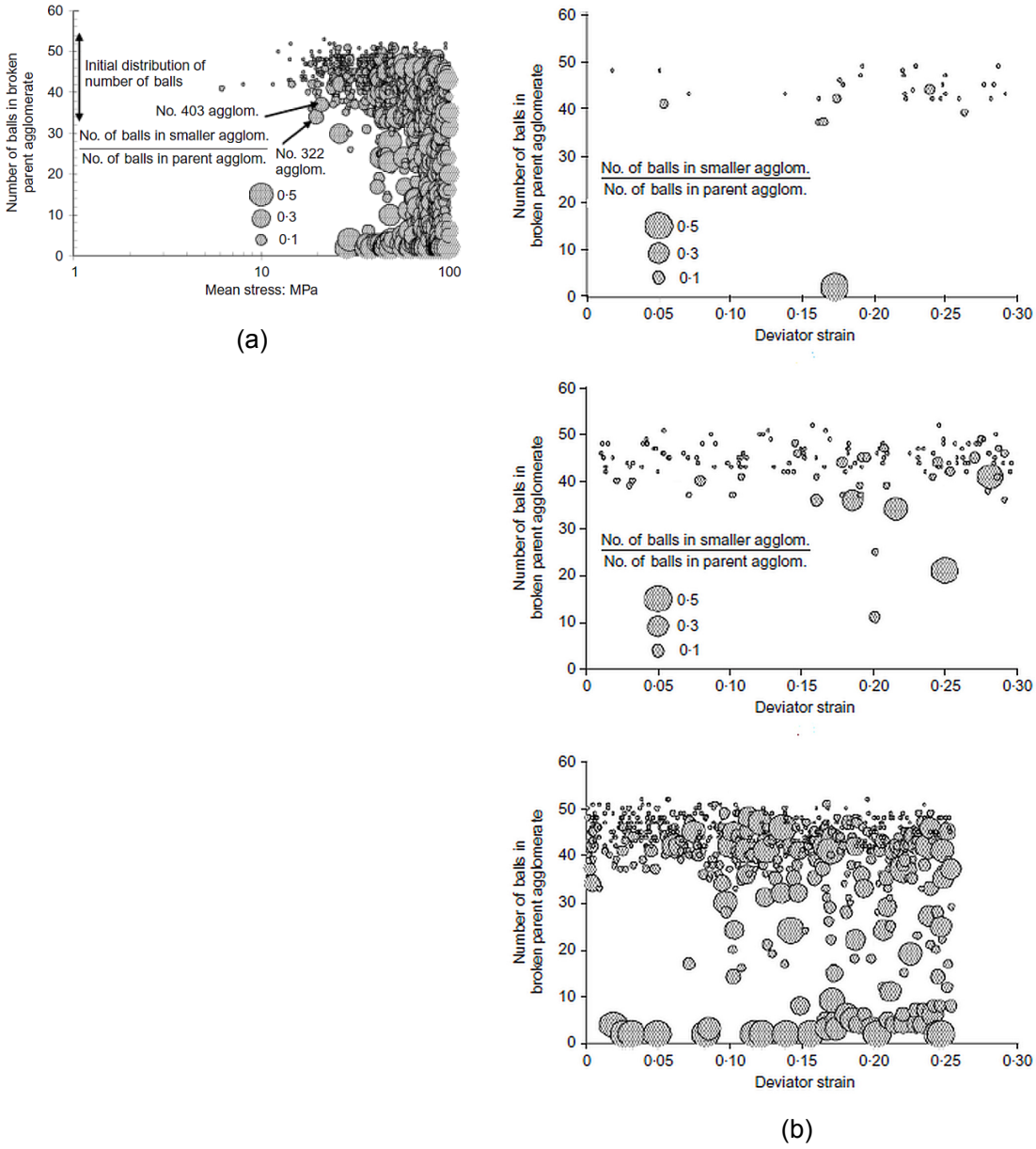

Figure 2-15: Degree of fragmentation during (a) isotropic compression: size of broken parent agglomerate against logarithm of mean stress (b) triaxial compression: 5MPa; 10 MPa; and 20 MPa (from Bolton et al. (2008)).

2.4.4 X-ray CT based grain-scale studies

Rapid advancement in high resolution imaging technology especially in last more than a decade, has greatly increased the scope for intensively studying the microstructural behaviour of geomaterials. Based on imaging techniques, experimental studies can be invasive like thin sectioning in Scanning Electron Microscopy (SEM) or non-invasive like using X-Ray radiography, ultrasonic testing, Neutron tomography, X-Ray computed tomography (CT) and Synchrotron microtomography (SMT).

High resolutions X-Ray computed tomography (X-Ray CT) is a robust non-destructive imaging technique, which can be used to overcome many difficulties through 3D visualization and quantification of many parameters closely describing the fabric of granular soils. Some researchers (Al-Raoush, 2007; Alshibli et al., 2014; Druckrey et al., 2016) used this technology for the quantification of fundamental particle characteristics, such as particle morphology, contact etc., while others (Hall et al., 2010; Fonseca et al., 2012; Higo et al., 2013; Karatza et al., 2015) used it for the quantification of the microstructural evolution of granular soils subjected to biaxial (Hall et al., 2010) and triaxial loading (Higo et al., 2013), where the focus was mainly on the development of shear bands (Jang and Frost, 2000). However, for better understanding of the response of soil, studying localized behaviour at grain-scale level is necessary.

However, with the advancement of laboratory-scale X-Ray CT technology and image segmentation techniques (Faessel and Jeulin, 2010; Hashemi et al., 2014; Alam and Haque, 2017), it is now possible to conduct investigation at grain-scale level (Fonseca et al., 2012; Druckrey et al., 2016; Alam et al., 2018).

Fonseca et al. (2012) used X-Ray CT to capture high-resolution grain-scale level images of intact and reconstituted sand samples undergoing compression and presented the challenge of recognising the effect of fabric on their mechanical behaviour. From the image analysis, breakage of fractured sand and subsequent change in particle size distribution (PSD) (Figure 2-16) during the process of reconstitution and shearing of the intact soil were observed. Such phenomenon of change of operational PSD which is impossible to obtain from invasive techniques like sieving or laser diffraction, indicates that fundamental differences exist between both materials and consequently different responses were to be expected between the intact and the reconstituted soil. Morever, the study reveals significant differences of the calculations of particle size and shape made by analysis of 2D binary images with 3D values. Furthermore, the study emphasizes on the soil models such as discrete element model, to use particle morphology obtained from 3D values instead of 2D images which is significantly less representative of the actual particle morphology.

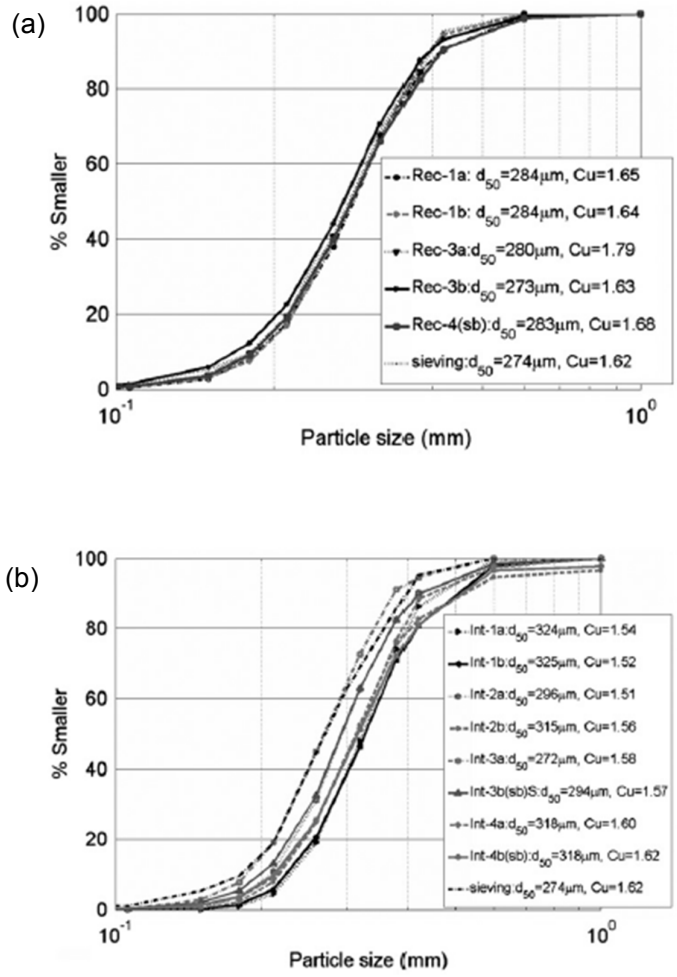

Figure 2-16: PSDs for the (a) reconstituted samples (b) intact samples (from Fonseca et al. (2012))

In recent times researchers (Cil and Alshibli, 2014; Cavarretta et al., 2016; Druckrey and Alshibli, 2016) are preferentially using integrated framework of experimental, analytical and numerical methods for investigation. Cil and Alshibli (2014) investigated evolution of particle fracture and deformation behaviour of a granular assembly subjected to one dimensional loading using 3D Synchrotron Microtomography (SMT) and discrete-element method (DEM). In this study, a series of actual laboratory one-dimensional compression experiments on sand sample of different aspect ratios (Height/Diameter) were simulated using 3D DEM model by

mapping particle positions from SMT images obtained from actual experiments. Crushable sand particles were modelled in DEM using agglomerates of spherical sub-particles as originally proposed by Robertson (2000) and Cheng et al. (2004). Under high compressive stress, inter-particle force chains that develops within granular material causes fracture of particles with subsequent effect on constitutive behaviour of the material. In granular materials, fabric which influence the force chains developed from compressive loading, is directly influenced by particle morphology (Tordesillas and Muthuswamy, 2009; Maeda et al., 2010; Wang et al., 2011). From the study, with the increase of aspect ratio, yielding point was observed to shift towards smaller strain levels Figure 2-17(a) and (b). *Insitu* SMT images reveals non-homogeneity in evolution of fractions within sample with more concentrations at certain locations near loading platen as shown in Figure 2-17c and the particles susceptible to fractures are those whose neighbouring particles have already experienced that. DEM allowed monitoring the formation of strong force chains by means of the generated contact force network as shown in Figure 2-17d and observation of subsequent breakage in agglomerates. Finally, the quantitative analysis of SMT images showed that sand fracture initiates with yielding and increases progressively as the compression continues.

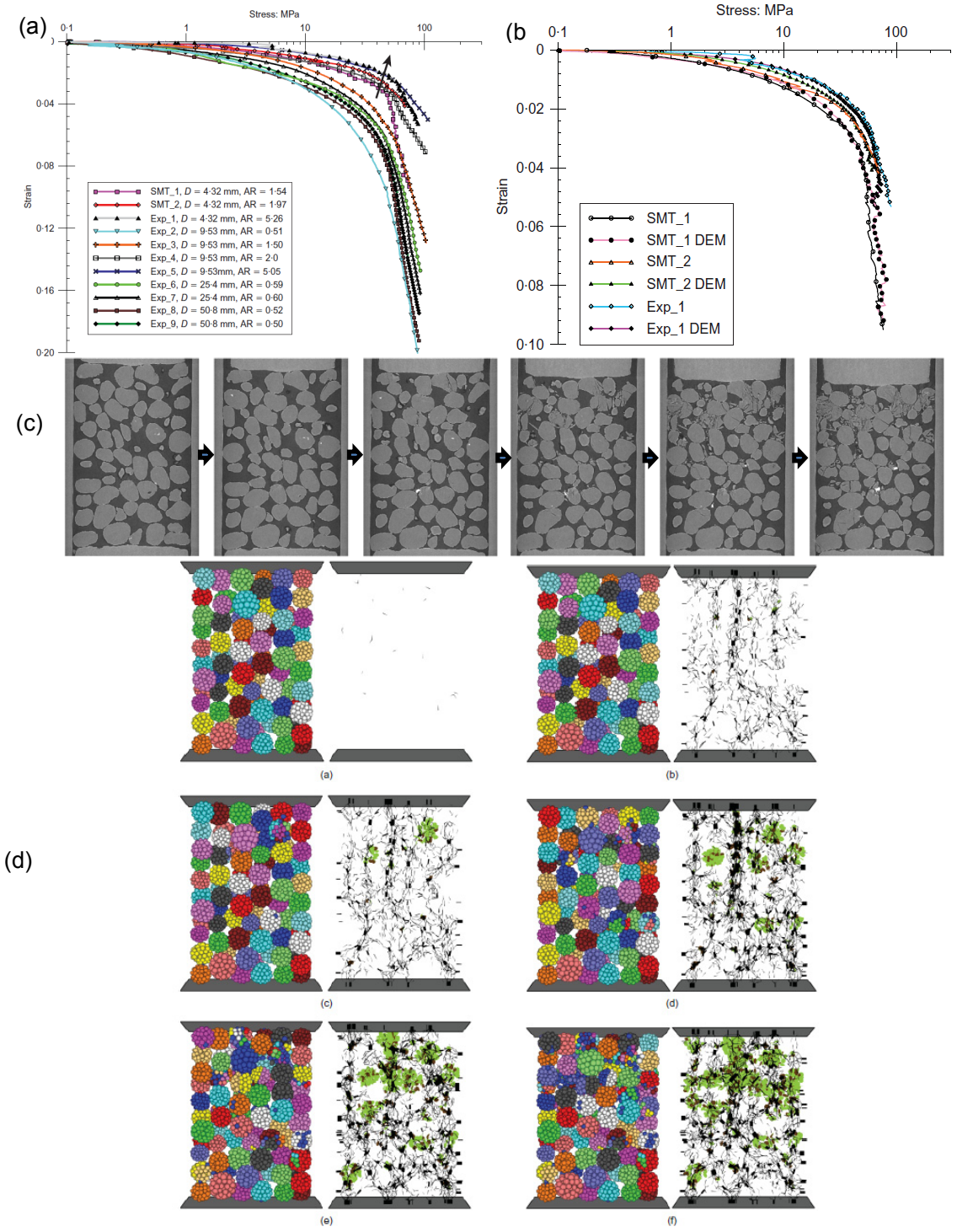

Figure 2-17: (a) Stress-strain relationships for 1D compression experiments on sand (AR=aspect ratio) (b) Comparison of laboratory experiments and DEM results (c) Axial cross-sectional images of SMT showing fractures near load platens with progressive strain levels (d) Development of force chains from contact force network at different strain level observed in DEM representation of particles. (from Cil and Alshibli (2014)).

Druckrey and Alshibli (2016) using synchrotron X-Ray radiography and 3D Synchrotron micro tomography (SMT) techniques collected images of fracture mode of individual particles of silica sand during in-situ unconfined compression experiments. Particle surfaces created from these images were transferred to finite element where the experimental loading setup was modelled using extended finite element software method (XFEM). The XFEM model analysis on the actual particle shape simulated fracture of the particle very similar to what was visualized using the radiograph images during compression as shown in Figure 2-18a and Figure 2-18b. With the assumed parameters, XFEM analysis on actual particle produced a load-displacement curve (Figure 2-18c) similar to the experimental curve.

Finally, the evidence on influence of particle shape on fracture behaviour observed in this study concludes the necessity of considering actual shape of the particles in modelling.

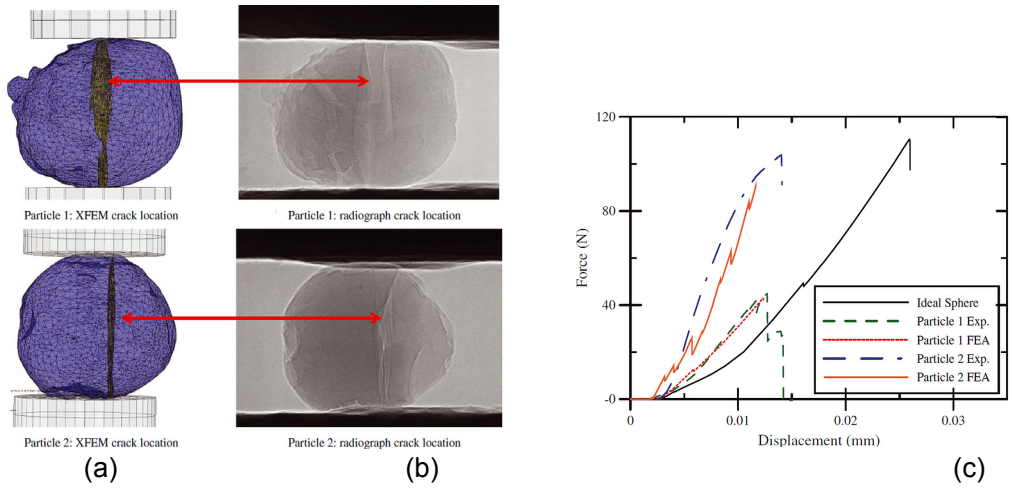

Figure 2-18: Crack locations of the two particles analysed from (a) XFEM results and (b) radiographs during experiments (c) Load-displacement relationships from experiments and FE model for ideal sphere and the two analysed particles. (from Druckrey and Alshibli (2016))

An important series of three studies on microstructural behaviour of sand was conducted using X-Ray CT technology (Fonseca et al., 2012; Fonseca et al., 2013a; Fonseca et al., 2013b). The studies investigated changes in Reigate sand morphology (size and shapes), and fabric under triaxial loading. Evolution of both directional and scalar fabric parameters were observed during the process of shear deformation in the latter studies consecutively. The first study has already been discussed.

In the second study (Fonseca et al., 2013b) for the same Reigate sand, quantified directional fabric in three dimensions and their evolution during shearing under triaxial loading for both intact and reconstituted samples. Statistical analyses of directional fabric data in terms of longest axis of particle, contact normal, branch vector and void orientation carried out at different stages of shearing. Based on the analyses, a conceptual model of the soil response to loading was proposed. At initial state, longest axis of the particles exhibited horizontal (perpendicular to the direction of deposition) preferences in general which was not affected by the shear band movement for reconstituted samples. But for intact samples at post-peak regions, the detached small fragments showed random orientation whereas large particles were horizontal. For intact and reconstituted soils, contact normal showed concentration along the direction of the major principal stress in the post peak regime which postulates the force chain (Tordesillas and Muthuswamy, 2009) theory. Initial slight biasness of the long axis of voids towards horizontal direction almost diminished upon shearing.

In the final study of the series Fonseca et al. (2013a), several scalar parameters like coordination number, contact index, and branch vector length were quantified using X-Ray CT imaging while undergoing compression and their relationships with the mechanical behaviour of both intact and reconstituted Reigate sand samples were analysed. Contact index was found to be more effective than coordination number in describing the evolution of contact densities. However, neither of the parameters alone appeared to be able to capture all of the important changes of the contacts during loading. However, dilation of soil was found to be closely related to scalar measurements of fabric.

In a recent study, Imseeh et al. (2018) has quantified 3D fabric and fabric evolution of sheared granular materials undergoing *insitu* conventional triaxial compression experiment using synchrotron X-ray CT tomography. The directional distribution of contact normals exhibited the highest degree of isotropy at initial state (i.e., zero global axial strain). As compression progressed, contact normals evolved in the direction of loading until reaching a constant fabric Fabric Anisotropy Variable ($FAV\ A$) approaching 1 (Figure 2-20) when experiments approached the critical state condition. Details on Fabric Anisotropy Variable A ($FAV\ A$), as introduced by (Li and Dafalias, 2011) which accounts for both magnitude of the fabric anisotropy and its orientation relative to loading direction, is provided in chapter 4. Moreover, relatively a higher applied confining pressure and a looser initial density state showed in a higher degree of fabric- induced internal anisotropy. Influence of particle-level morphology was also found to be significant particularly on fabric evolution.

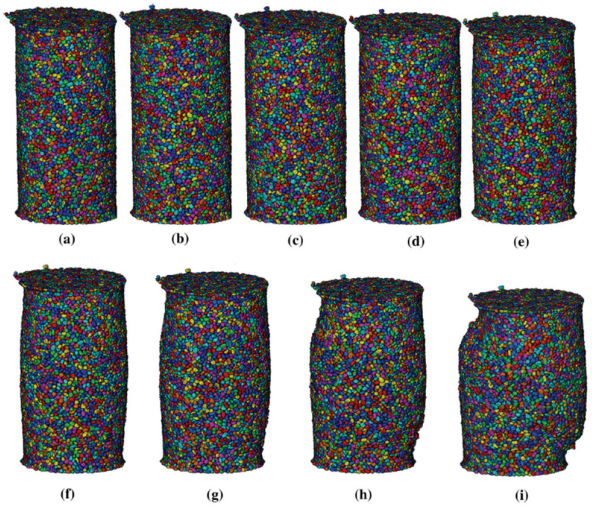

Figure 2-19: Processed 3D images of triaxial test at all loading stages. (from Imseeh et al. (2018))

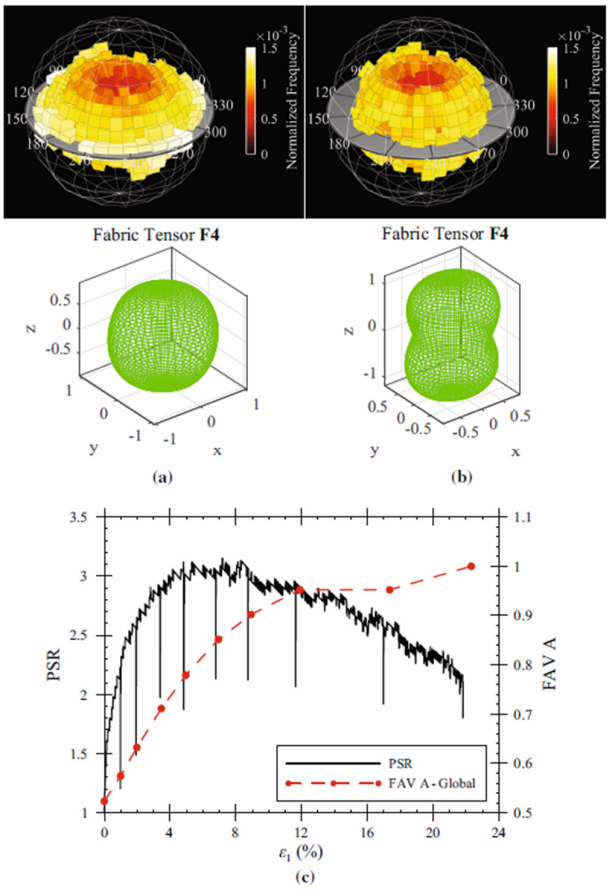

Figure 2-20: 3D spherical histogram with 4th order fabric tensor representation surface of global contact unit normal vectors at a initial and b last loading stage and c the evolution of Principal Stress Ratio (PSR) and global Fabric Anisotropy Variable A ($FAV\ A$) versus strain ε_1 (from Imseeh et al. (2018))

2.5 Behaviour of Cemented Sand

For geotechnical engineers and geologist, engineering properties of cemented soils have significant importance. It has been observed that presence of cementation can provide sand with a variety of mechanical behaviour such as increased stiffness (Leroueil and Vaughan, 1990; Coop and Atkinson, 1993; Huang and Airey, 1998; Cuccovillo and Coop, 1999). As a result, macroscopic behaviour of cemented soil is determined by the collaborative effect of the factors like cementation, fabric, density, and stress history and all these factors evolve in a coupled way during deformation (Shen et al., 2016).

2.5.1 Phenomenological Studies

Numerous studies have been carried out in the past emphasising the importance of understanding the effect of cementation on the strength and deformation characteristics of naturally cemented soils (Clough et al., 1981; Lade and Overton, 1989; Leroueil and Vaughan, 1990; Coop and Atkinson, 1993; Cuccovillo and Coop, 1997; Da Fonseca et al., 1998; Schnaid et al., 2001; Yu et al., 2007). In natural sands, silicates, amorphous silica, iron oxide, calcium carbonate and even clays are the common cementing agents (Clough et al., 1981; Santamarina et al., 2001; Mitchell and Soga, 2005).

But in addition to highly variable nature of density and cementation in naturally cemented soil attributing significant strength difference between adjacent and apparently similar core samples, difficulty in sampling without disturbing the

cementation makes it harder to study the fundamental behaviour of naturally cemented materials in the laboratory (Airey, 1993; Huang and Airey, 1998; Wang and Leung, 2008). Moreover, identical samples of natural cemented sand cannot be replicated for parametric studies. To overcome these difficulties artificially cemented soils have been used in many studies (Huang and Airey, 1998; Consoli et al., 2000; Schnaid et al., 2001; Ismail et al., 2002; Rotta et al., 2003; Consoli et al., 2006; Haeri et al., 2006; Rios et al., 2014; Islam et al., 2015).

Earlier studies confirm that the patterns of behaviour observed in naturally and artificially cemented soils are similar despite use of different processes of cementation (Marri et al., 2012). So, it is generally accepted assumption that artificially cemented materials simulate the stress-strain behaviour, volumetric change and strength characteristics of naturally cemented soils. Therefore, artificially cemented soils are frequently used in the laboratory to investigate behaviour of cemented soils.

One such landmark study by Coop and Atkinson (1993) explains how cementation in soil modifies its mechanical behaviour and complicates the interpretation of compression test results. In fact, two mutually complementing studies (Coop, 1990; Coop and Atkinson, 1993) were conducted on carbonated uncemented and cemented sands with the objectives of understanding the fundamental behaviour including stress-strain behaviour in triaxial tests. Indistinguishability of the breakage of cement bond and highly crushable carbonate sand particle within the same sample under high stress makes the interpretation of the effect of cement complicated or nearly impossible. To resolve the issue, the researcher conducted the test initially for

uncemented sand only(Coop, 1990) before conducting for naturally and artificially cemented sand(Coop and Atkinson, 1993). However, to balance the effect on behaviour due to change of void space and gradation in cemented sand compared to uncemented sand because of the presence of cementing materials, gypsum was used in cemented and powder form (Figure 2-21) in cemented and uncemented sand respectively.

The study on the behaviour of both naturally and artificially cemented carbonate sand observed to agree a general framework which the authors suggest is also likely to be applicable to other naturally cemented soils. Cementing introduced well defined yield point which is associated with breakage of the cement bonds and onset of particle fracture. Although the yielding for cemented sand under both compressive and shear stress occurred at states outside the boundary surface of the uncemented soil, but at large strains both samples reached essentially the same critical state lines. However, cementing caused increased peak strength by the reduction of void spaces (or specific volume) but the amount of cement used in this study was found to have hardly any influence on strength although influence on stiffness and stress-strain curve was apparent at higher confining pressures.

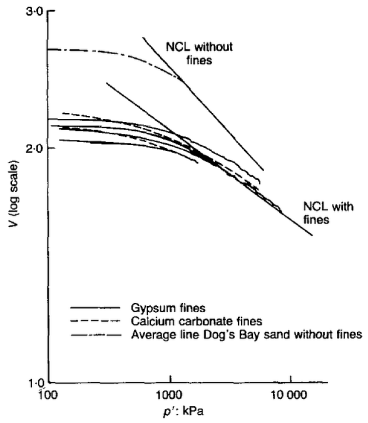

Figure 2-21: Isotropic compression of uncemented samples with and without fines (from Coop and Atkinson (1993))

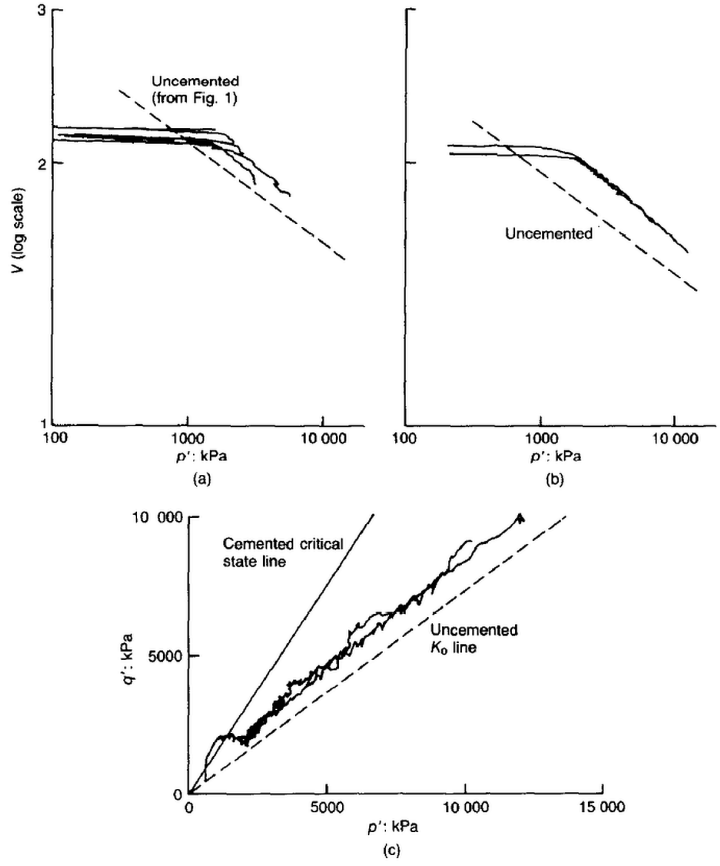

Figure 2-22: Compression of cemented samples: (a) isotropic (b) one-dimensional (c) one-dimensional (from Coop and Atkinson (1993)).

In another valuable study, Cuccovillo and Coop (1997) attempted to distinguish between the effects of inter-particle bonding and fabric. They studied two naturally

structured sands: a calcarenite consisting of a medium carbonate sand bonded by calcium carbonate, and a silica sand bonded by iron oxide. Based on their analysis of the shear behaviour under very small strain, they reported that yielding is noticeable by a rapid decrease in stiffness, degradation of bonding and the development of plastic strains. They claimed that for the carbonate sand the structure arises solely from bonding whereas for bonded silica sand, the structure predominantly arises from the interlocking soil fabric. For the bonded carbonate sand, they observed a progressive transformation of the bonded soil into a frictional material, with the shear stiffness becoming more controlled by state, rather than structure. For the silica sand, they observed that despite bond degradation, the influence of structure still persisted, giving higher values of shear stiffness at comparable strains. They concluded that the loss of bonding must precede any disruption to the fabric, i.e. particle arrangement.

Huang and Airey (1998) performed series of isotropic compression tests on a sand cemented with various gypsum cement contents (0–20%). They found that all the cemented soils demonstrated a stiff elastic response up to a well-defined yield stress, upon which the soils underwent large plastic strains following a normal compression line. They proposed that the slopes of the NCLs were independent of the cement content, and as the cement content increases, the NCL simply shifts to the right in a voids ratio–log stress plot. This shift was attributed to the change in grading caused by the addition of cement fines, and resulted in an increase in yield stress with cement content, which appeared to be a linear relationship.

Based on the interpretation of the results of unconfined compression test, drained triaxial compression tests and scanning electron microscopy in which the influence of both the degree of cementation and the initial mean effective stress was considered, an analysis of the mechanical behaviour of artificially cemented sand was attempted by (Schnaid et al., 2001). For cemented sandy soils, it was concluded that the unconfined compression resistance is a direct measurement of the degree of cementation (Figure 2-23). Consequently, the triaxial shear strength for cemented sand can be expressed as a function of only two variables: (1) the internal friction angle of the nonstructured material; and (2) the unconfined compression resistance.

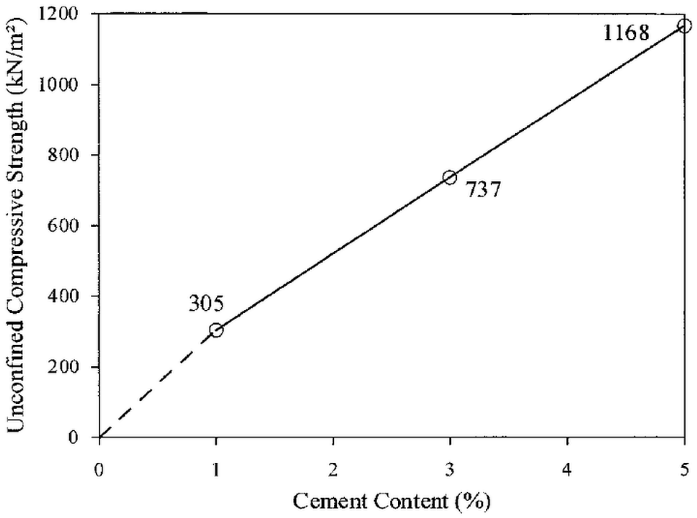

Figure 2-23: Effect of cement content on Unconfined Compressive Strength (from (Schnaid et al., 2001))

2.5.2 Micromechanics of Cemented Sand

In the earlier section, mechanical properties of cemented soil were studied based on their macroscale responses. However, it is widely recognised that the mechanical behaviour of sands can be directly related to its microstructure, i.e., the geometrical

arrangement of the grain particles including the forces acting between them. Microscopy analysis are generally undertaken in order to characterize the grain shapes of the hosting sand and identify (Figure 2-24) the nature of cement content due to calcite and the other particulate cementing agents.

Moreover, microscopy analysis is used to investigate the effect of compression and shearing on cement bonding and particles crushing. At high pressures, the crushing of sand particles is widely reported by many researchers as already discussed in the uncemented sand section.

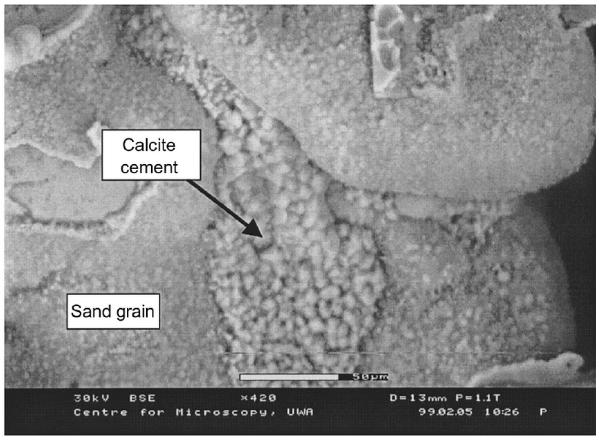

Figure 2-24: SEM micrograph of cemented sand (from Ismail et al. (2002))

For cemented sand, the amount, type, and location of inter-granular cements are primary factors influencing the strength of cemented materials. Small amounts of inter-granular cement can have profound effects on bulk mechanical behaviour of the material (Figure 2-23). However, the microscale interactions between different constituents of the grain-cement network combined with particle crushing and bond breakage is highly complicated phenomenon. Detailed grain scale investigation will

certainly improve the effect of such microscale interaction to explain macroscale behaviour. Due to difficulty in directly observing the complex interaction in cemented sand and quantifying degradation of cementation, many researchers with the aid of the Discrete Element Method (DEM), are attempting to approximately simulate bonded material (Utili and Nova, 2008; Obermayr et al., 2013; Brown et al., 2014; de Bono and McDowell, 2014; Jiang et al., 2014) to investigate their micromechanical behaviour (Wang and Leung, 2008; de Bono and McDowell, 2014; Shen et al., 2016). Few of such studies are discussed in the following section.

2.5.3 DEM based microstructural study for cemented soil

Using DEM, micromechanics of cemented sand under compression has been investigated by a group of researchers (de Bono and McDowell, 2014; Bono et al., 2015).

In the first study (de Bono and McDowell, 2014), show that the behaviour of cemented sand can be replicated using DEM. They incorporates soil structure in DEM model by simulating cemented sand and investigates the effects of interparticle bonding on the one-dimensional compression behaviour and evolving particle size distributions. The results show that bonding reduces particle crushing, and it is both the magnitude (Figure 2-25a,b)and distribution (Figure 2-25c)of bond strengths that influence the compression curve of the structured material.

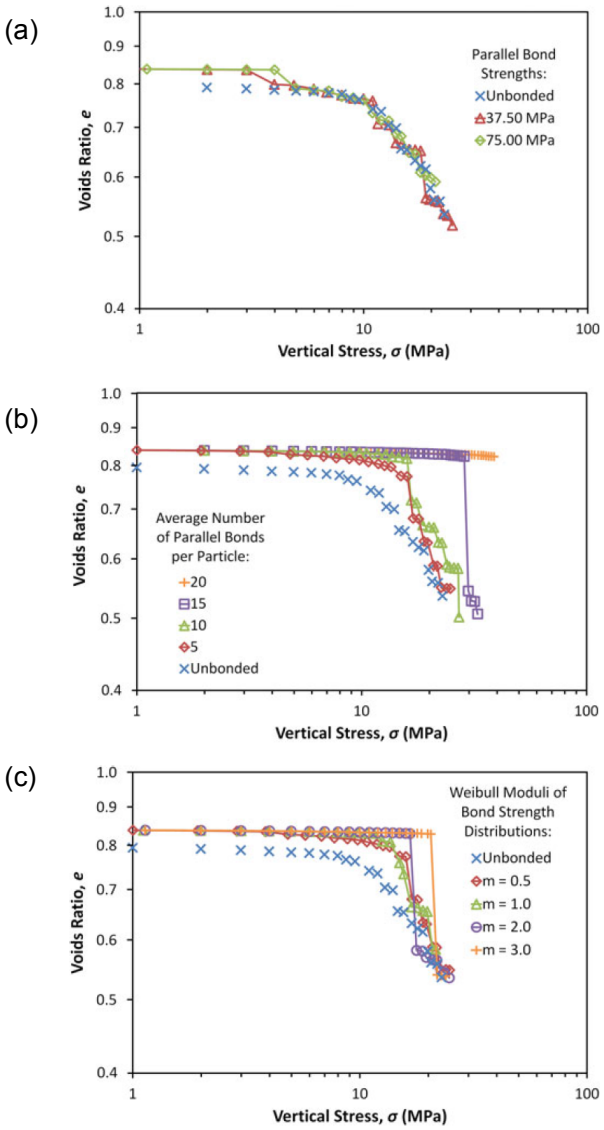

Figure 2-25: Compression lines showing effects of (a) increasing bond strength (b)increasing number of bonds (c) distribution of bond strength (from de Bono and McDowell (2014))

In the second study, Bono et al. (2015) modelled high pressure drained triaxial tests in 3D using a flexible membrane that allows the correct deformation to develop. A series of DEM simulations have been performed on cemented and uncemented materials.

The presence of bonds, which represent cementation, cause additional dilation (Figure 2-26(ii)) when compared with the uncemented simulations. The flexible membrane has allowed the correct failure modes to develop, allowing contrasting brittle and ductile failure modes caused by varying the cement content. It has been shown that for a given confining pressure, increasing the number of bonds (i.e. the degree of cementation) increases the strength and brittleness of the material (Figure 2-26(i)), with shear planes produced in the most highly cemented simulations. For a given cement content, increasing the confining pressure to 12 MPa suppresses the behaviour of the cementation, with no shear planes visible for even the most highly cemented samples. In between these pressures, 'transitional' behaviour of material neither completely brittle nor ductile was observed. DEM has therefore been shown to be able to capture the behaviour of cemented sand under a range of confining pressures and cement contents.

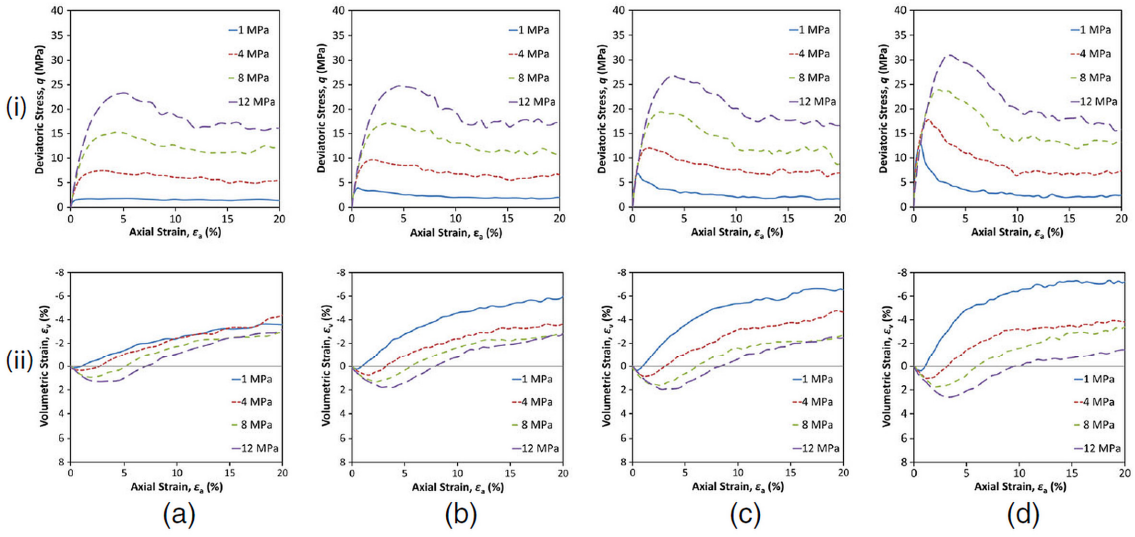

Figure 2-26: Triaxial behaviour of unbonded sample (a), and samples with an average of 5 (b), 10 (c) and 20(d) parallel bonds per particle, sheared across a range of high confining pressures (1–12 MPa): deviatoric stress (i) and volumetric strain (ii) versus axial strain. (from (Bono et al., 2015))

Wang and Leung (2008) with the combination of experimental triaxial tests and numerical simulations using DEM, investigated the underlying mechanisms of the unique behaviour of artificially cemented sands. In the simulations, the arrangement of the smaller cementing particles around the contacts between sand grains indicates the real features of cementation, and the use of flexible membrane boundaries improves the simulation of the deformation characteristics. The simulation results demonstrate that all of the particles in the bonding network jointly share the load and many micro force-chains (Figure 2-27) associated with cementation are generated. Compared with uncemented sand, a more stable and stronger force-chain network subjected to smaller force or stress concentrations is formed in cemented sand. The risk of force-chain buckling is therefore minimized and higher strength is measured. The simulation also reveals that intensive bond breakage, concentrated relative particle movement, column-like force chains (instead of a webbed pattern) with force concentrations, great particle rotation, and high local porosity can be found at similar locations in the sample, especially inside the shear band. The bonded cluster is essential to help stabilize the particle arch and maintain large voids for the volumetric dilation.

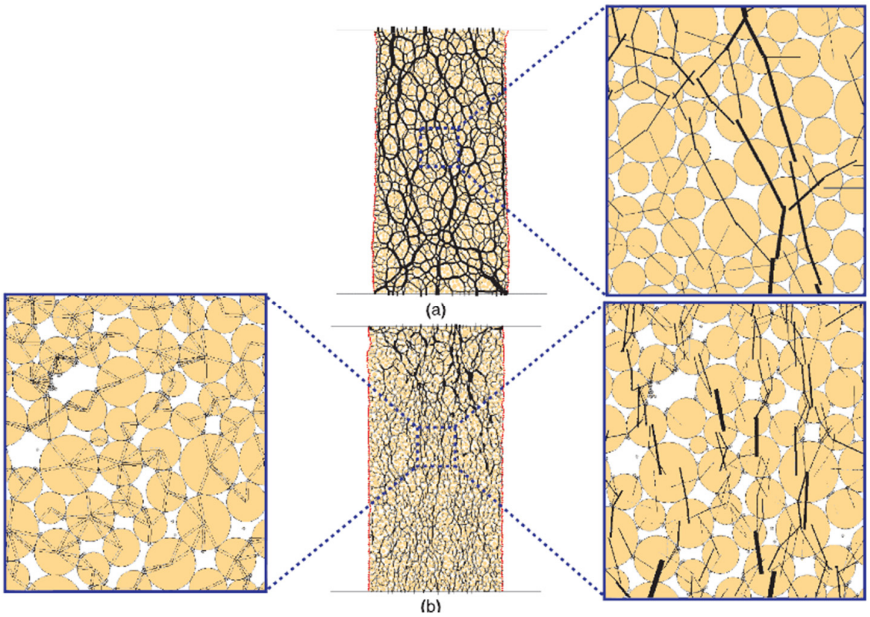

Figure 2-27: Force-chain distribution of the portland cement sample under the confining pressure of 50 kPa and axial strain of 1.76%: (a) uncemented sample; (b) 2% cement content sample. Note the force chain thickness represents the magnitude of contact normal forces. (from Wang and Leung (2008))

2.5.4 *X-ray CT based microstructure analysis for cemented sand*

This breakthrough technology is being extensively used to study microstructural behaviour of granular material. In earlier section on uncemented sand, many such studies have been discussed. Surprisingly, no grain-scale level study for cemented sand using this technology can be found. However, on bio-cemented material a particular group of researchers have recently published their work (Dadda et al., 2017; Dadda et al., 2018a; Dadda et al., 2018b). Considering somewhat similarity in the material characteristics and investigation methodology with this current work, a brief review of these papers are presented here.

Dadda et al. (2017) with the aid of high resolution images from X-Ray Synchotron microtomography, investigated the effect of the biocalcification process on the

microstructural and the physical properties of biocemented sand samples. From the computed microstructural properties (porosity, volume fraction of calcite, total specific surface area, specific surface area of calcite, etc.) and the physical properties (permeability, effective diffusion) of the biocemented samples indicates that all the properties are strongly affected by the biocalcification process. Finally, all these numerical results from 3D images and experimental data were compared to numerical values or analytical estimates computed on idealized microstructures. These comparisons show that these simple microstructures are sufficient to capture and to predict the main evolution of both microstructural and physical properties of biocemented sands for the whole range of volume fraction of calcite investigated.

In the second paper, micromechanical properties of biocemented sand such as the volume fraction of calcite, its distribution within the pore space and the contact properties: coordination number, contact surface area, contacts orientation and types of contact are computed with the objective of using them in the future as input parameters in micromechanical models (DEM simulations) in order to link these microstructural properties to the macroscopic effective properties (Young modulus and shear modulus) and strength properties (cohesion and friction angle). The coordination number, due to the creation of new contacts ('cemented' contacts), slightly increases when increasing the volume fraction of calcite. The orientation of contacts within the samples is isotropic before and after calcification. Three types of contact ('frictional,' 'mixed' and 'cemented' contacts) can be considered (Figure 2-28, Figure 2-29) after biocalcification. For a volume fraction of calcite lower than 3%, most

of the contacts remain 'frictional.' Beyond this value, most of the contacts are 'mixed' contacts. Whatever the value of fc, the number of new contacts ('cemented' contacts) created by the biocementation process remains quite small (less than 10% for fc = 14.8%) and the corresponding contact surface area is almost negligible. This evolution of the contacts, in terms of type, seems to be also related to the injection protocol of both the bacterial and calcification solutions.

In the final paper Dadda et al. (2018b) used the real microstructural properties (e.g. contact surface area, coordination number, and volume fraction of each phase) of biocemented sand computed on 3D X-Ray microtomography images as an input in current analytical models to estimate the evolution of the elastic and strength properties (Young and shear moduli, Coulomb cohesion) with the calcite content. They achieved good agreement between the experimental results of effective moduli and Poisson ratio and the Contact Cement Theory (CCT) model (proposed by Dvorkin et al. (1994)) for the whole range of volume fraction of calcite (Figure 2-30). Both results show that both moduli increase nonlinearly for low volume fraction of calcite and then increase linearly for larger volume fraction of calcite (Figure 2-31). This nonlinear increase is due to the nonlinear increase of the cohesive contact surface area between grains induced by the biocalcification process. Results point to importance of microstructural parameters on the effective parameters.

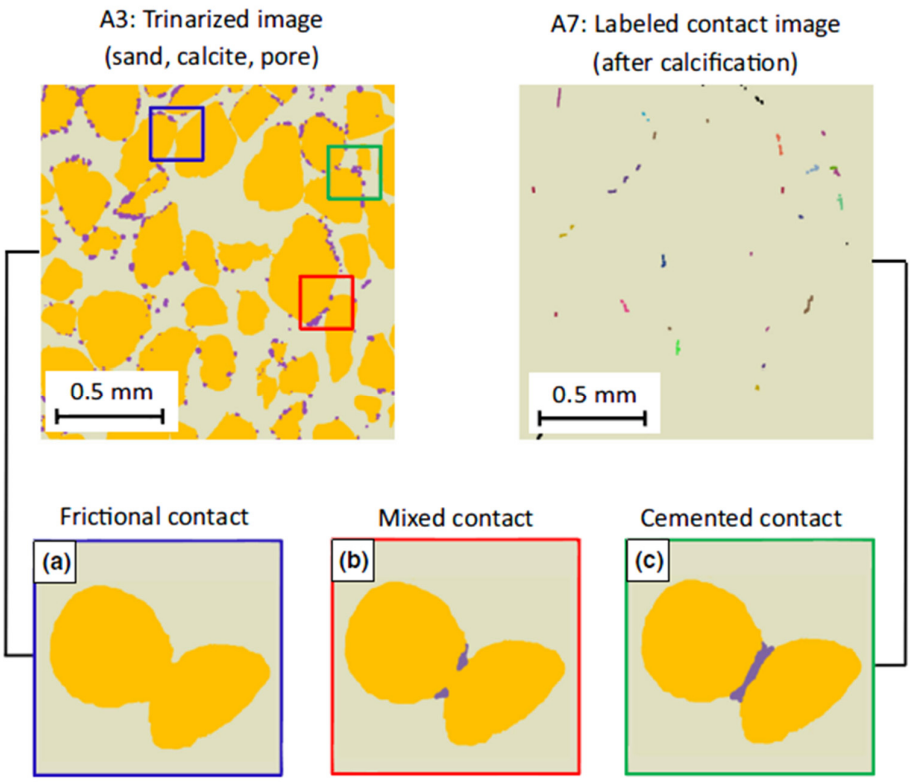

Figure 2-28: Definition of different types of contact

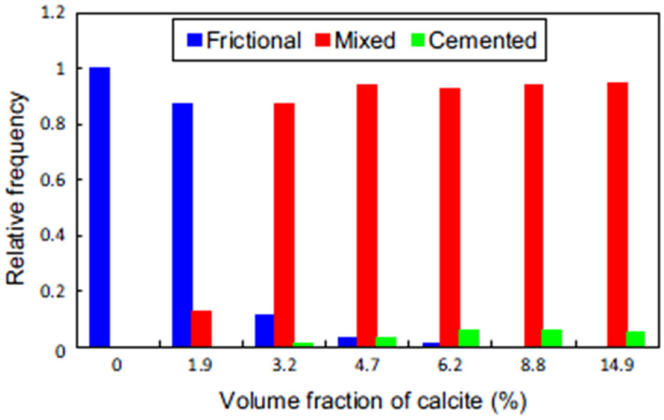

Figure 2-29: Evolution of the distribution of the different types of contact

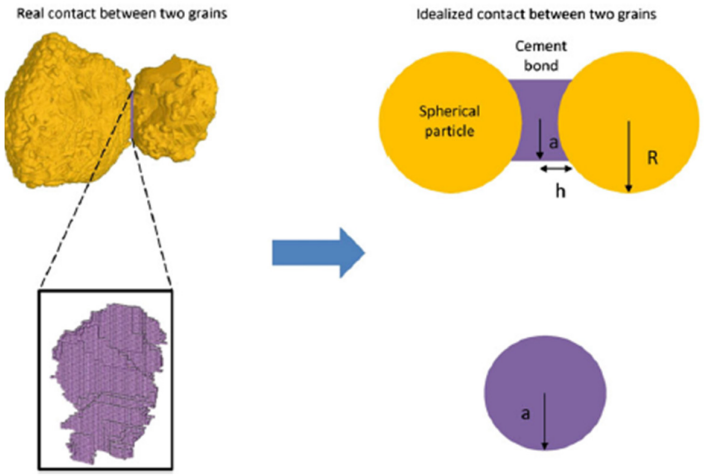

Figure 2-30: Contact between two grains deduced from 3D images and idealized contact used in the contact cement theory (CCT)

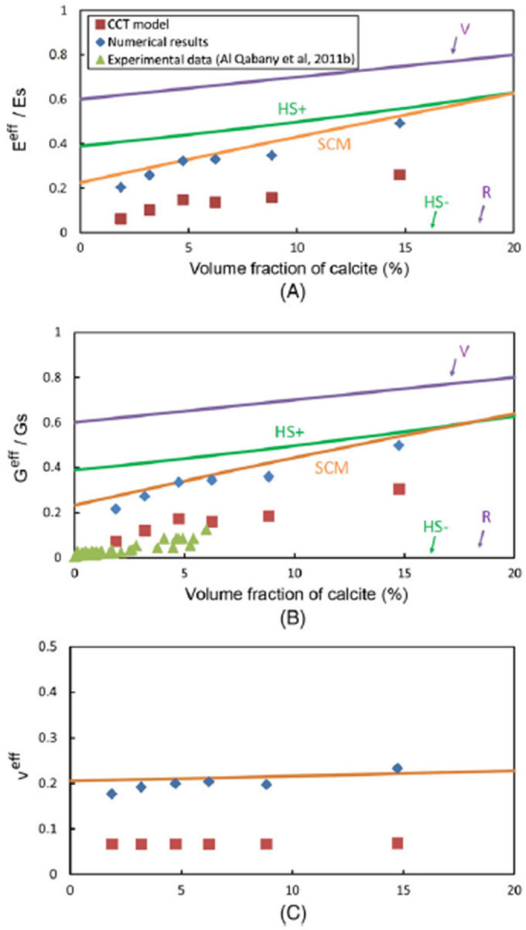

Figure 2-31: Evolution of the effective elastic properties of the biocemented sand: A, dimensionless Young modulus, B, dimensionless shear

2.6 Summary

For geotechnical engineers, understanding the compression behaviour of cemented sand both naturally occurring and artificially modified has significant importance for ensuring safety and serviceability requirements of infrastructure projects constructed over them. Many valuable phenomenological studies exist which attempt to explain the fundamental behaviour of such soil from macro perspective. However, numerous experimental studies suggest the strong influence of microstructural behaviour in shaping the macro scale behaviour.

Significant effort has been dedicated by using numerical tools especially discrete element method (DEM) to model cemented sand and to capture their microstructural behaviour under compression to explain macro behaviour. However, digital idealized particle, bond and the overall sand cement matrix may not be true representative of the actual behaviour in all cases.

The ground-breaking technology of 3D X-Ray CT imaging technology is highly recognised among the scientific world for microstructural investigation. In geotechnical engineering, the technology is being used for last few decades. However, rapid development in recent times regarding high-resolution 3D images and image analysis method, inspired particle level research of soil behaviour. Those valuable studies which contributed to significant understanding of microstructural behaviour are, however, limited to uncemented granular soil. Until now, no microstructural

investigation of cemented sand at grain-scale level is available. Just recently, a series publications on such area, however, on biocemented sand have been published.

In this study, with the objective of investigating microstructure and compression behaviour of cemented sand subjected to high pressure one-dimensional compression, *insitu* X-Ray CT imaging technology has been used for the first time at grain-scale level to study the evolution of various scalar and directional fabric parameters. The particular areas of focus of the study are to capture and explain the load dependent response of fabric, effect of cement content on fabric, and comparative evolution of the fabric anisotropy of the voids for cemented sand with reference to those for uncemented sand.

2.7 References

Airey, D. 1993. Triaxial testing of naturally cemented carbonate soil. Journal of Geotechnical Engineering, 119, 1379-1398.

Al-Raoush, R. 2007. Microstructure characterization of granular materials. Physica A: Statistical mechanics and its Applications, 377, 545-558.

Alam, M., Haque, A. & Ranjith, P. 2018. A Study of the Particle-Level Fabric and Morphology of Granular Soils under One-Dimensional Compression Using Insitu X-ray CT Imaging. Materials (Basel, Switzerland), 11.

Alam, M. F. & Haque, A. 2017. A New Cluster Analysis-Marker-Controlled Watershed Method for Separating Particles of Granular Soils. Materials, 10, 1195.

Alshibli, K. A., Druckrey, A. M., Al-Raoush, R. I., Weiskittel, T. & Lavrik, N. V. 2014. Quantifying morphology of sands using 3D imaging. Journal of Materials in Civil Engineering, 27, 04014275.

Altuhafi, F. & Coop, M. R. 2011. Changes to particle characteristics associated with the compression of sands. Géotechnique, 61, 459.

Arthur, J. & Menzies, B. 1972. Inherent anisotropy in a sand. Geotechnique, 22, 115-128.

Bolton, M., Nakata, Y. & Cheng, Y. 2008. Micro-and macro-mechanical behaviour of DEM crushable materials. Géotechnique, 58, 471-480.

Bono, J., McDowell, G. & Wanatowski, D. 2015. Investigating the micro mechanics of cemented sand using DEM. International Journal for Numerical and Analytical Methods in Geomechanics, 39, 655-675.

Brown, N. J., Chen, J.-F. & Ooi, J. Y. 2014. A bond model for DEM simulation of cementitious materials and deformable structures. Granular Matter, 16, 299-311.

Bullard, J. W., Jennings, H. M., Livingston, R. A., Nonat, A., Scherer, G. W., Schweitzer, J. S., Scrivener, K. L. & Thomas, J. J. 2011. Mechanisms of cement hydration. Cement and concrete research, 41, 1208-1223.

Burland, J. 1990. On the compressibility and shear strength of natural clays. Géotechnique, 40, 329-378.

Cavarretta, I., O'Sullivan, C. & Coop, M. 2016. The relevance of roundness to the crushing strength of granular materials. Géotechnique, 67, 301-312.

Cheng, Y., Bolton, M. & Nakata, Y. 2004. Crushing and plastic deformation of soils simulated using DEM. Geotechnique, 54, 131-141.

Cheng, Y., Bolton, M. & Nakata, Y. 2005. Grain crushing and critical states observed in DEM simulations. P&G05, 2, 1393-1397.

Cheng, Y., Nakata, Y. & Bolton, M. 2003. Discrete element simulation of crushable soil. Geotechnique, 53, 633-641.

Chuhan, F. A., Kjeldstad, A., Bjørlykke, K. & Høeg, K. 2002. Porosity loss in sand by grain crushing—Experimental evidence and relevance to reservoir quality. Marine and Petroleum Geology, 19, 39-53.

Chuhan, F. A., Kjeldstad, A., Bjørlykke, K. & Høeg, K. 2003. Experimental compression of loose sands: relevance to porosity reduction during burial in sedimentary basins. Canadian Geotechnical Journal, 40, 995-1011.

Cil, M. & Alshibli, K. 2014. 3D evolution of sand fracture under 1D compression. Géotechnique, 64, 351.

Clough, G. W., Sitar, N., Bachus, R. C. & Rad, N. S. 1981. Cemented sands under static loading. Journal of Geotechnical and Geoenvironmental Engineering, 107.

Consoli, N., Rotta, G. & Prietto, P. 2000. Influence of curing under stress on the triaxial response of cemented soils. Geotechnique, 50, 99-105.

Consoli, N., Rotta, G. & Prietto, P. 2006. Yielding–compressibility–strength relationship for an artificially cemented soil cured under stress. Geotechnique, 56, 69-72.

Coop, M. 1990. The mechanics of uncemented carbonate sands. Geotechnique, 40, 607-626.

Coop, M. & Atkinson, J. 1993. The mechanics of cemented carbonate sands. Geotechnique, 43, 53-67.

Coop, M. & Lee, I. 1993. The behaviour of granular soils at elevated stresses. Predictive soil mechanics, 186-198.

Cuccovillo, T. & Coop, M. 1997. Yielding and pre-failure deformation of structured sands. Geotechnique, 47, 491-508.

Cuccovillo, T. & Coop, M. 1999. On the mechanics of structured sands. Géotechnique, 49, 741-760.

Curray, J. R. 1956. The analysis of two-dimensional orientation data. The Journal of Geology, 64, 117-131.

Da Fonseca, A. V., FERNANDESĆ, M. M. & CARDOSOĆ, A. S. 1998. Interpretation of a footing load test on a saprolitic soil from granite. Pre-failure deformation behaviour of geomaterials, 247.

Dadda, A., Geindreau, C., Emeriault, F., du Roscoat, S. R., Filet, A. E. & Garandet, A. 2018a. Characterization of contact properties in biocemented sand using 3D X-ray micro-tomography. Acta Geotechnica, 1-17.

Dadda, A., Geindreau, C., Emeriault, F., du Roscoat, S. R., Garandet, A., Sapin, L. & Filet, A. E. 2017. Characterization of microstructural and physical properties changes in biocemented sand using 3D X-ray microtomography. Acta Geotechnica, 12, 955-970.

Dadda, A., Geindreau, C., Emeriault, F., Filet, A. E. & Garandet, A. 2018b. Influence of the microstructural properties of biocemented sand on its mechanical behavior. Int J Numer Anal Methods Geomech, 1, 10.

de Bono, J. P. & McDowell, G. R. 2014. Discrete element modelling of one-dimensional compression of cemented sand. Granular Matter, 16, 79-90.

De Souza, J. 1958. Compressibility of sand at high pressure. MS thesis, Massachusetts Institute of Technology, 63-64.

Druckrey, A. M. & Alshibli, K. A. 2016. 3D finite element modeling of sand particle fracture based on in situ X‐Ray synchrotron imaging. International Journal for Numerical and Analytical Methods in Geomechanics, 40, 105-116.

Druckrey, A. M., Alshibli, K. A. & Al-Raoush, R. I. 2016. 3D characterization of sand particle-to-particle contact and morphology. Computers and Geotechnics, 74, 26-35.

Dvorkin, J., Nur, A. & Yin, H. 1994. Effective properties of cemented granular materials. Mechanics of materials, 18, 351-366.

Faessel, M. & Jeulin, D. 2010. Segmentation of 3D microtomographic images of granular materials with the stochastic watershed. Journal of microscopy, 239, 17-31.

Fonseca, J., O'sullivan, C., Coop, M. & Lee, P. 2013a. Quantifying the evolution of soil fabric during shearing using scalar parameters. Géotechnique, 63, 818-829.

Fonseca, J., O'Sullivan, C., Coop, M. R. & Lee, P. 2013b. Quantifying the evolution of soil fabric during shearing using directional parameters. Géotechnique, 63, 487-499.

Fonseca, J., O'Sullivan, C., Coop, M. R. & Lee, P. 2012. Non-invasive characterization of particle morphology of natural sands. Soils and Foundations, 52, 712-722.

Fu, P. & Dafalias, Y. F. 2015. Relationship between void-and contact normal-based fabric tensors for 2D idealized granular materials. International Journal of Solids and Structures, 63, 68-81.

Haeri, S., Hamidi, A., Hosseini, S., Asghari, E. & Toll, D. 2006. Effect of cement type on the mechanical behavior of a gravely sand. Geotechnical & Geological Engineering, 24, 335.

Hagerty, M., Hite, D., Ullrich, C. & Hagerty, D. 1993. One-dimensional high-pressure compression of granular media. Journal of Geotechnical Engineering, 119, 1-18.

Hall, S. A., Wood, D. M., Ibraim, E. & Viggiani, G. 2010. Localised deformation patterning in 2D granular materials revealed by digital image correlation. Granular matter, 12, 1-14.

Hardin, B. O. 1985. Crushing of soil particles. Journal of geotechnical engineering, 111, 1177-1192.

Hashemi, M. A., Khaddour, G., François, B., Massart, T. J. & Salager, S. 2014. A tomographic imagery segmentation methodology for three-phase geomaterials based on simultaneous region growing. Acta Geotechnica, 9, 831-846.

Hendron Jr, A. J. (1963). The Behavior of Sand in One-Dimensional Compression. ILLINOIS UNIV URBANA.

Higo, Y., Oka, F., Sato, T., Matsushima, Y. & Kimoto, S. 2013. Investigation of localized deformation in partially saturated sand under triaxial compression using microfocus X-ray CT with digital image correlation. Soils and Foundations, 53, 181-198.

Huang, J. & Airey, D. 1998. Properties of artificially cemented carbonate sand. Journal of Geotechnical and Geoenvironmental Engineering, 124, 492-499.

Imseeh, W. H., Druckrey, A. M. & Alshibli, K. A. 2018. 3D experimental quantification of fabric and fabric evolution of sheared granular materials using synchrotron micro-computed tomography. Granular Matter, 20, 24.

Ingles, O. G. & Metcalf, J. B. (1972). Soil stabilization principles and practice.

Islam, S., Haque, A., Wilson, S. A. & Ranjith, P. 2015. Time-dependent strength and mineralogy of Lime-GGBS treated naturally occurring acid sulfate soils. Journal of Materials in Civil Engineering, 28, 04015077.

Ismail, M., Joer, H., Randolph, M. & Meritt, A. 2002. Cementation of porous materials using calcite. Geotechnique, 52, 313-324.

Jang, D.-J. 1997. Quantification of sand structure and its evolution during shearing using image analysis. Georgia Institute of Technology.

Jang, D.-J. Sand structure differences resulting from specimen preparation procedures. Proc. 1998 Conf. on Geotech. Earthquake Engrg. and Soil Dynamics, 1998. ASCE, 234-245.

Jang, D.-J. & Frost, J. D. 2000. Use of image analysis to study the microstructure of a failed sand specimen. Canadian geotechnical journal, 37, 1141-1149.

Jiang, M. & Shen, Z. Strength and fabric evolution of unsaturated granular materials by 3D DEM analyses. AIP Conference Proceedings, 2013. AIP, 273-276.

Jiang, M., Zhang, F. & Sun, Y. 2014. An evaluation on the degradation evolutions in three constitutive models for bonded geomaterials by DEM analyses. Computers and Geotechnics, 57, 1-16.

Johnson, K. L. & Johnson, K. L. 1987. Contact mechanics, Cambridge university press.

Karatza, Z., Andò, E., Papanicolopulos, S.-A., Ooia, J. Y. & Viggiani, G. 2015. Observing breakage in sand under triaxial and oedometric loading in 3D. Deformation Characteristics of Geomaterials, 431.

Konishi, J. & Naruse, F. 1988. A note on fabric in terms of voids. Studies in Applied Mechanics. Elsevier.

Lade, P. V. & Overton, D. D. 1989. Cementation effects in frictional materials. Journal of Geotechnical Engineering, 115, 1373-1387.

Leroueil, S. & Vaughan, P. 1990. The general and congruent effects of structure in natural soils and weak rocks. Géotechnique, 40, 467-488.

Li, X. S. & Dafalias, Y. F. 2011. Anisotropic critical state theory: role of fabric. Journal of Engineering Mechanics, 138, 263-275.

Liu, S. & Lok, T. M. H. Discrete Element Simulation of Particle Crushing in 1-D Compression. GeoShanghai International Conference, 2018. Springer, 140-147.
Maeda, K., Sakai, H., Kondo, A., Yamaguchi, T., Fukuma, M. & Nukudani, E. 2010. Stress-chain based micromechanics of sand with grain shape effect. Granular Matter, 12, 499-505.
Manahiloh, K. N. & Muhunthan, B. 2012. Characterizing liquid phase fabric of unsaturated specimens from X-ray computed tomography images. Unsaturated soils: Research and applications. Springer.
Manahiloh, K. N., Muhunthan, B. & Likos, W. J. 2016. Microstructure-based effective stress formulation for unsaturated granular soils. International Journal of Geomechanics, 16, D4016006.
Marri, A., Wanatowski, D. & Yu, H. 2012. Drained behaviour of cemented sand in high pressure triaxial compression tests. Geomechanics and Geoengineering, 7, 159-174.
McDowell, G. 2005. A physical justification for log e–log σ based on fractal crushing and particle kinematics. Géotechnique, 55, 697-698.
Mcdowell, G. & Bolton, M. 1998. On the micromechanics of crushable aggregates.
McDowell, G., Bolton, M. & Robertson, D. 1996. The fractal crushing of granular materials. Journal of the Mechanics and Physics of Solids, 44, 2079-2101.
McDowell, G. & Harireche, O. 2002. Discrete element modelling of yielding and normal compression of sand. Géotechnique, 52, 299-304.
Mitchell, J. K. & Soga, K. 2005. Fundamentals of soil behavior, John Wiley & Sons New York.
Nakata, Y., Hyodo, M., Hyde, A. F., Kato, Y. & Murata, H. 2001. Microscopic particle crushing of sand subjected to high pressure one-dimensional compression. Soils and foundations, 41, 69-82.
Obermayr, M., Dressler, K., Vrettos, C. & Eberhard, P. 2013. A bonded-particle model for cemented sand. Computers and Geotechnics, 49, 299-313.
Oda, M. 1972a. Deformation mechanism of sand in triaxial compression tests. Soils and Foundations, 12, 45-63.
Oda, M. 1972b. Initial fabrics and their relations to mechanical properties of granular material. Soils and foundations, 12, 17-36.
Oda, M. 1972c. The mechanism of fabric changes during compressional deformation of sand. Soils and foundations, 12, 1-18.
Oda, M. 1977. Fabrics and their effects on the deformation behaviors of sand. 埼玉大学工学部建設系研究報告, p1-59.
Oda, M. 1993. Inherent and induced anisotropy in plasticity theory of granular soils. Mechanics of Materials, 16, 35-45.
Oda, M. & Konishi, J. 1974. Microscopic deformation mechanism of granular material in simple shear. Soils and foundations, 14, 25-38.
Oda, M. & Nakayama, H. 1989. Yield function for soil with anisotropic fabric. Journal of Engineering Mechanics, 115, 89-104.
Oda, M., Nemat-Nasser, S. & Konishi, J. 1985. Stress-induced anisotropy in granular masses. Soils and foundations, 25, 85-97.

Oda, M., Nemat - Nasser, S. & Mehrabadi, M. M. 1982. A statistical study of fabric in a random assembly of spherical granules. International Journal for Numerical and analytical methods in Geomechanics, 6, 77-94.

Rios, S., Da Fonseca, A. V. & Baudet, B. A. 2014. On the shearing behaviour of an artificially cemented soil. Acta Geotechnica, 9, 215-226.

Robertson, D. 2000. Computer simulations of crushable aggregates. University of Cambridge.

Rotta, G., Consoli, N., Prietto, P., Coop, M. & Graham, J. 2003. Isotropic yielding in an artificially cemented soil cured under stress. Geotechnique, 53, 493-501.

Santamarina, J. C., Klein, A. & Fam, M. A. 2001. Soils and waves: Particulate materials behavior, characterization and process monitoring. Journal of Soils and Sediments, 1, 130-130.

Satake, M. & Jenkins, J. T. 2013. Micromechanics of Granular Materials: Proceedings of the US/Japan Seminar on the Micromechanics of Granular Materials, Sendai-Zao, Japan, October 26-30, 1987, Elsevier.

Schnaid, F., Prietto, P. D. & Consoli, N. C. 2001. Characterization of cemented sand in triaxial compression. Journal of Geotechnical and Geoenvironmental Engineering, 127, 857-868.

Shen, Z., Jiang, M. & Thornton, C. 2016. DEM simulation of bonded granular material. Part I: contact model and application to cemented sand. Computers and Geotechnics, 75, 192-209.

Soil, A. C. D.-o. & Rock 2004. Standard test methods for one-dimensional consolidation properties of soils using incremental loading, ASTM International.

Tengattini, A., Das, A. & Einav, I. 2016. A constitutive modelling framework predicting critical state in sand undergoing crushing and dilation. Géotechnique, 66, 695-710.

Terzaghi, K. & Peck, R. 1948. Soil mechanics in engineering practice. Soil mechanics in engineering practice. J. Wiley and Sons.

Tordesillas, A. & Muthuswamy, M. 2009. On the modeling of confined buckling of force chains. Journal of the Mechanics and Physics of Solids, 57, 706-727.

Utili, S. & Nova, R. 2008. DEM analysis of bonded granular geomaterials. International Journal for Numerical and Analytical Methods in Geomechanics, 32, 1997-2031.

Wang, Y.-H. & Leung, S.-C. 2008. A particulate-scale investigation of cemented sand behavior. Canadian Geotechnical Journal, 45, 29-44.

Wang, Z., Yang, X., Chen, Q., Zhang, Y. & Zhao, Y. Study of the contact forces and grain size distribution during grain crushing. Multimedia Technology (ICMT), 2011 International Conference on, 2011. IEEE, 2617-2622.

Wood, D. M. Geomaterials with changing grading: a route towards modelling. Int. Symp. on Geomechanics and Geotechnics of Particulate Media, IS-Yamaguchi, Ube, Japan, 12, 2006. 313-316.

Yimsiri, S. & Soga, K. 2011. Effects of soil fabric on behaviors of granular soils: microscopic modeling. Computers and Geotechnics, 38, 861-874.

Yu, H., Tan, S. & Schnaid, F. 2007. A critical state framework for modelling bonded geomaterials. Geomechanics and Geoengineering, 2, 61-74.

Zhang, J., Wong, T.-F., Yanagidani, T. & Davis, D. M. 1990a. Pressure-induced microcracking and grain crushing in Berea and Boise sandstones: Acoustic emission and quantitative microscopy measurements. Mechanics of Materials, 9, 1-15.

Zhang, J., Wong, T. F. & Davis, D. M. 1990b. Micromechanics of pressure - induced grain crushing in porous rocks. Journal of Geophysical Research: Solid Earth, 95, 341-352.

3 EXPERIMENTAL SETUP AND METHODOLOGY

3.1 Introduction

Under the current research scheme, a detailed plan was designed for smooth operation of this multi-tiered investigation on microstructural behaviour of cemented and uncemented sand subjected to *insitu* X-ray CT imaging under one-dimensional compression. The plan comprises one-dimensional load cell design, sample preparation for different cement contents, performing one-dimensional test, image acquisition and processing, image analysis using dedicated image analysis software Avizo and Matlab code.

In this study, the microstructural investigation was based on two distinct group of parameters: scalar (e.g. void ratio, particle size distribution, sphericity, anisotropy etc.) and directional (long-axis). Defining directional parameters on the void phase have a potential of avoiding the difficulty of defining contact normal, contact vector and thus offer a unified measure for all particulate media (Manahiloh et al., 2016). Accordingly, for sand fabric only scalar parameters were analysed whereas for void fabric both

scalar and directional parameters were analysed. Total 4 samples each for uncemented, 10, 20 and 30% cemented sand were investigated under one-dimensional compression subjected to *insitu* X-ray CT imaging.

3.2 Basics of X-Ray Computed Tomography (CT) Technology

Developed originally in early 70's, for use in medical-discipline, X-Ray CT is one of the widely used techniques on which substantial effort has been made in recent times to improve its performance. Unlike conventional medical CT scanning, today's high-resolution industrial or even more advanced laboratory grade X-Ray CT has its ability to resolve details as small as less than one micron in size, even when imaging objects are made of high density materials. This has provided the opportunity to the researchers in the field of geo-mechanics to work at grain-scale level with real 3-D microstructural image data of geomaterials. Unlike Scanning Electron Microscopy (SEM), X-Ray CT is a non-invasive technique that has offered immense opportunity to the researchers for advanced study in relating the microstructure of geomaterial to observed mechanical response.

Briefly industrial CT differs from medical CT in three important ways (Du Plessis et al., 2017): (i) in medical CT due to its application, the object is stationary and the X-Ray source and detector move around it, whereas in industrial CT, the X-Ray source and detector are fixed around a rotating sample. (ii) compared to medical CT, industrial CT is more flexible with regards to voltage and current modification, which allows for the setup to be modified to suit a range of materials (e.g., higher voltage for dense materials). (iii) image resolution of industrial CT scanners is often much higher

than that of medical CT scanners. Resolutions of industrial CT scanners are generally in the range of 5–150 µm, compared to medical CT scanners, which have best resolutions of 70 µm. In contrast, most nano-CT scanners have resolutions as low as to 0.5 µm.

Computed or computerized axial tomography involves the recording of two-dimensional (2D) X-Ray images from various angles around an object, followed by a digital three-dimensional (3D) reconstruction. The resultant 3D-rendered volume not only allows for the multidirectional examination of an area of interest, but also permits dimensional, volumetric, or other more advanced measurements to be made.

The principle of X-Ray CT is based on X-Ray radiography, in which the rays are attenuated as they traverse matter. Radiograms are acquired over a full rotation of the scanned sample and algorithmically reconstructed into a 3D X-Ray attenuation map of the sample (Cnudde and Boone, 2013). Intensity values are used to calculate the distribution of the linear attenuation coefficient to generate a map representing density at every point. Brighter regions correspond to dense objects such as grains, and dark regions correspond to low-density objects such as voids or pore-fluid. Sensitivity to density variations as low as 1% or smaller (Dennis, 1989) enables a wide spectrum of materials to be characterized, including bone, ceramic, metals, timber, asphalt, porous concrete and soft tissue.

3.3 X-Ray CT Facility at Monash University

3.3.1 High Resolution X-Ray CT Machine

Monash University in association with seven other Australian Universities was successful to establish an ARC-LIEF funded (LE130100006) X-Ray CT facility for imaging geo-materials. This unique facility as shown in Figure 3-1, which was commissioned in December 2013, is centred around Zeiss Xradia XRM520 Versa X-Ray (Zeiss Xradia, 2018). This high resolution (spatial resolution of 0.7 micron/voxel) CT machine is housed in one of the dedicated laboratory in civil engineering department (Figure 3-1). The unique proprietary interchangeable focusing optics (0.4X, 4X, 20X, 40X) of the XRM520 allows to locate and scan small sub-regions within a large specimen (maximum weight=15kg). The typical set up for high resolution X-Ray CT includes simple projection geometry with a high resolution imaging detector and a highly collimated beam. The VersaXRM520 is equipped with an X-Ray source of 160 kV and 10W.

This unique imaging facility has provided the researchers of the civil engineering department to advance scientific research in various branches including the geo-materials.

Figure 3-1: X-Ray CT machine housed in Geomechanics Laboratory of Monash University

3.3.2 CT5000 in-situ load stage for X-Ray CT applications

A purpose built *insitu* compression/tensile load stage as shown in Figure 3-2 designed by Deben(2018) in association with manufacturers of X-Ray CT systems was used to apply compressive load on the sample.

The compact design of this testing stage allow it to be used with the smallest high resolution micro CT system providing up to 5kN compression. System is controlled from the comprehensive MICROTEST (V6.13) software which provides a wide range of control functions and a live display of load versus extension.

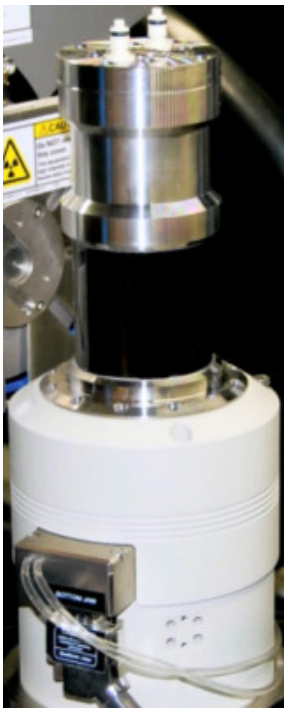

Figure 3-2: Deben CT5000 load stage (within the yellow box) designed for X-Ray CT application

Using the load stage with X-Ray CT provides a clear visual interpretation of how the properties of materials and composites change under different loading conditions. The load stage (Deben CT5000) is placed on the sample stage located between the X-Ray source and the detectors as shown in Figure 3-4 and it can be viewed from many different angles (an angular range of 180°) required for tomographic data collection for 2D imaging.

3.3.3 Custom built 1D compression load cell

A one-dimensional compression cell was designed in this study to specifically work with the CT5000 load stage and X-Ray CT facility. The cell comprises a 2 mm thick walled aluminium cylinder of 8.5 mm internal diameter and 10 mm height, two 2-mm

thick porous bronze filters and a 6-mm height stainless steel plunger with a 1-mm diameter stainless steel ball. A typical setup of the cell is shown in Figure 3-3. A sliding fit of filters and plunger were ensured. It is to be noted that the clearance between the top and the bottom platens of the CT5000 Deben load-stage is 15 mm, which restricted the height of the sample to be tested. The load cell is placed on the bottom platen as shown in Figure 3-4 of the load-stage which moves upward and compresses the sample against the top reaction platen. No lateral deformation of the cylinder was found.

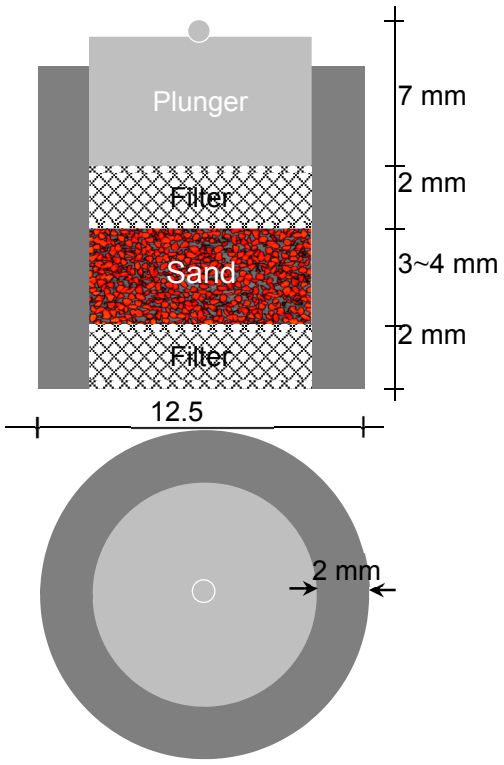

Figure 3-3: Custom-built 1D compression load cell

3.4 Materials and Sample Preparation

In this study, commercially available washed sand samples sourced from a natural deposit site located at Gippsland in Victoria, Australia was used. The sand particles are brown in colour and sub-angular in shape.

First, the sand particles were dried in an oven for 24 hours at 105±0.5°C. Second, the particles were sieved through 250, 212 and 150 microns sieves. In this study, sand particles passed through 250 microns and retained on 212 and 150 microns sieves were used. Image of the initial sand sample and its particle size distribution plot are shown in Figure 3-5 and Figure 3-6. The values of the coefficient of uniformity, C_u and the coefficient of curvature, C_c were 1.24 and 1.06 respectively and confirmed the sand to be uniformly graded as per Unified soil classification system. The mean diameter (d_{50}) including the minimum height to diameter ratio of sample to be tested under 1D compression with a full field of view imaging. X-Ray diffraction test showed that the sand particles comprised of quartz minerals. The specific gravity of sand particles were measured three times using a multipycnometer, which produced an average value of 2.68. For cementation, commercially available general purpose hydraulic cement was used.

The above sand was used for preparing both uncemented and cemented samples. For uncemented sample, a dry mass of 0.24 gm sand were placed in the load cell from a height of about 10 mm.

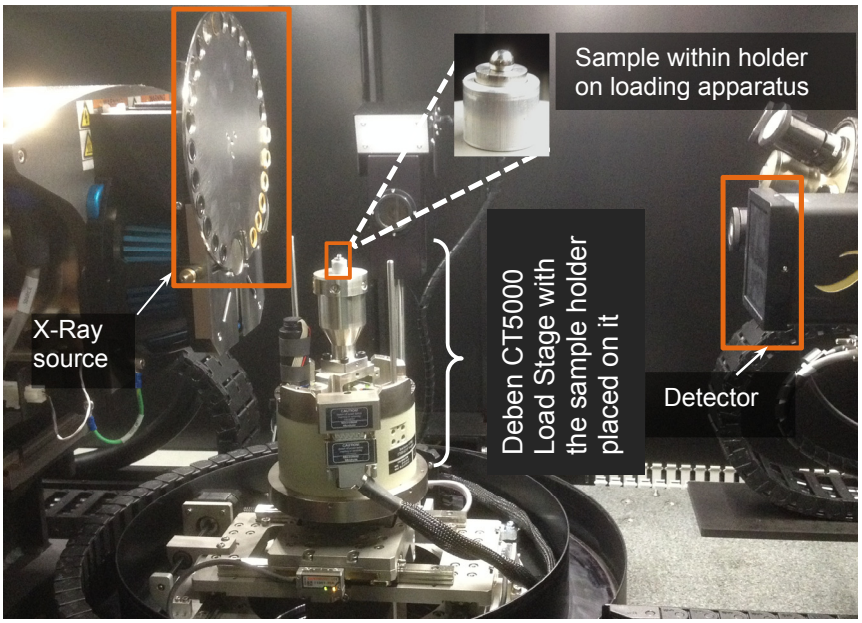

Figure 3-4: Experiment setup with 1D load cell placed on the Deben CT5000

However, for cemented sample, the dry sand was separately hand mixed with 10, 20 and 30% (by weight) of hydraulic cement. The sand-cement blend was mixed at 100% water/cement ratio using a spatula. Mix was laid in a rectangular (20 x 25 mm) acrylic mould of 3.7 mm height as shown in Figure 3-7 and the surface was levelled using an acrylic ruler. Then core was cut using sharp edged aluminium cylinder of 8.5 mm inside diameter. The sample cores were left in the box which was quickly wrapped up with cling wrap and left in curing room to avoid loss of moisture. One sample from each proportion were removed after 28 days and both surfaces of the samples were levelled using fine grained sand paper. However, the whole process of preparing such small cemented sample offered significant challenge.

Figure 3-5: Image of sand at initial condition

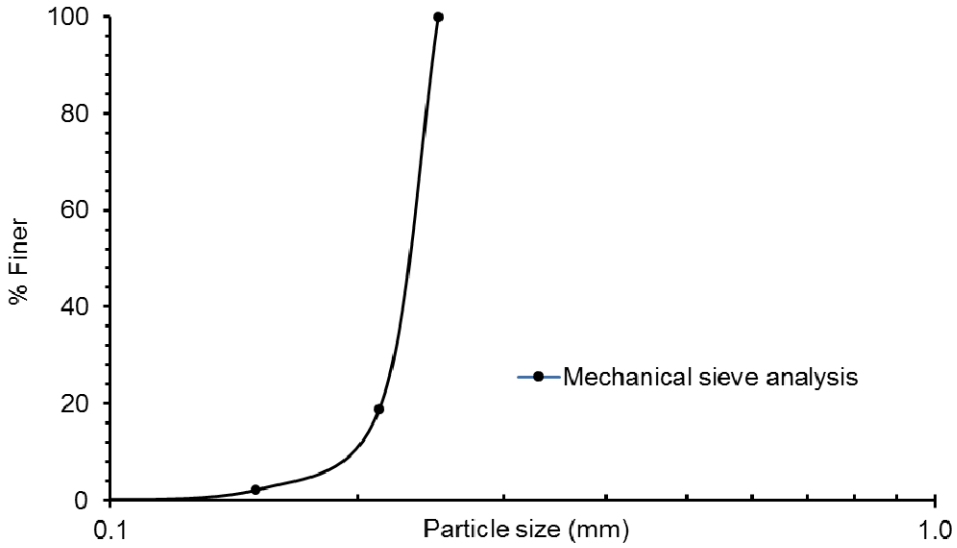

Figure 3-6: Initial particle size distributions from mechanical sieve analysis

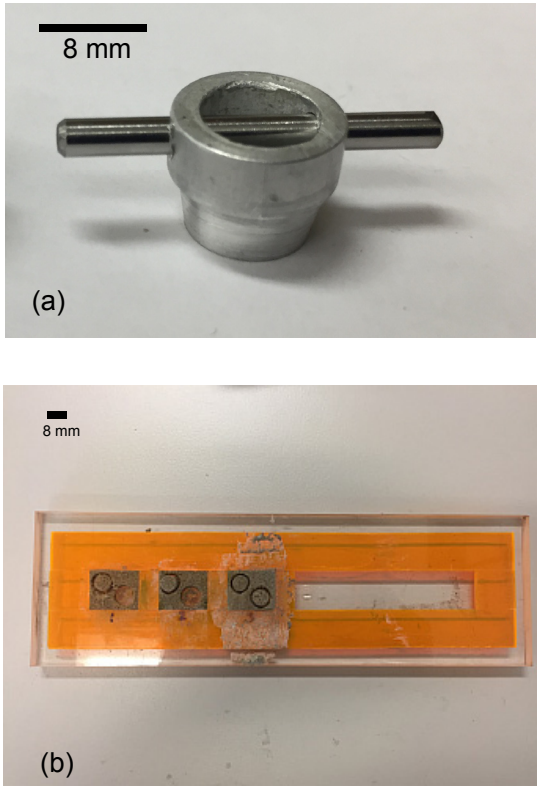

Figure 3-7: (a) Aluminium core cutter of 8.5 mm internal diameter and (b) typical samples in mould especially designed for this study to prepare cemented sample

Figure 3-8: A typical cemented sample marked by yellow circle

Despite several precautions, the consistency of the height of all samples could not be controlled using the methodology adopted. Physical properties of the samples are presented in Table 3-1.

Table 3-1: Physical properties of the samples

Sample ID	Cement Content (% by wt. of sand)	Height of sample (mm)	Diameter of sample (mm)	Mass of sample before test (gm.)
Uncem	0%	3.5	8.5	0.24
10C	10%	3.5	8.5	0.23
20C	20%	2.8	8.5	0.24
30C	30%	3.6	8.5	0.36

3.5 One-dimensional Compression Test

In the test, an initial load of 50 N was applied. Thereafter, the loads were doubled for the next five consecutive increments until they reached 3200 N. The final load after 3200 N was restricted to 4500 N due to the limitation of maximum capacity of the stage (5000 N). The vertical compressive stresses corresponding to the load cases were 1.8, 3.5, 7.0, 14.1, 28.2, 56.4, and 79.3 MPa. A target compressive load was achieved through the upward movement of the bottom platen at a rate of 0.1 mm/min. Once the load had reached a target value, sample was allowed to undergo complete deformation under constant load, which was monitored by reading axial deformation with time. It was found that about 30 to 60 minute was required to complete the immediate compression of the sample (i.e., the deformation-time plot reached an asymptotic value), where a higher time corresponded to a higher load. During imaging, movement of bottom platen was paused and final stress value at the end of imaging was recorded, which showed less than 5% stress relaxation. At the completion of

imaging which took approximately 40 minutes, the next level of load was applied and the whole process was repeated.

3.6 Image Acquisition

Image projections were acquired by rotating the load-stage 360° around its vertical axis. The frame size of the projections was 1024 × 1024 pixels. The scanning parameters used for all the scans are given in Table 3-2.

Table 3-2: Scanning parameters and values

Parameter	Value / Description
Source to sample distance	85 mm
Detector to sample distance	322 mm
Voltage	140 keV
Power	10 W
Exposure time	2.5 s
Camera binning	2
Lens	Macro (0.4x)

In this study, a total of 801 projections with a pixel size of 14.28 microns ($\approx 0.062 d_{50}$) was taken, which took about half an hour. The 2D projections were reconstructed to 3D volumes using XRM Reconstructor software.

3.7 Image Processing

The reconstructed raw images from X-Ray CT machine were post-processed using a commercially available image processing software, Avizo. Initially, images of sample were cropped from the whole apparatus assembly followed by removal of noises using appropriate filters. For noise reduction, the non-local means filter of Avizo was used in this study. Despite being GPU accelerated, the runtime of this filter was very high compared to other filters such as the 3D median filter. However, the non-local

filter was found to be highly effective in reducing noises while preserving the edges of particles which is critical for particle separation for uncemented sand.

After filtering, the greyscale image was transformed to binary image by applying the interactive thresholding module which prompts the user to set the grey level intervals manually with a visual feedback. As a preliminary identification of intensity ranges separating solids from voids, an intensity range partitioning tool was used which can automatically guess thresholds separating different densities of materials. Then by manually adjusting this preliminary threshold range in the interactive thresholding, voxels were defined as either solid (sand particle for uncemented sand and sand-cement matrix for cemented sand) or void by trial and error based on visual assessment (human judgement) (Hasan and Alshibli, 2010) of their intensities. However, to perform grain scale analysis, further segmentation was required to separate sand particles from each other which was perhaps the most challenging part of the image processing.

The morphological watershed algorithm module was applied to perform this task of separating individual sand particles. The procedure consisted of: (a) calculating the Euclidian distance map (EDM) on the solid phase of the binary image by applying fast yet accurate approximation based Chamfer metric considering 26-neighbourhood when propagating the distance value; (b) identifying the local maxima of the EDM with contrast value of 1; (c) labelling the local maxima as markers; and (d) applying marker based watershed with 3D interpretation and 26-neighbourhood connectivity.

In every load case, three to four iterations of watershed, depending on the extent of connected voxels resulting from increased loading, were found necessary to achieve the desired level (>90% particles separation) of segmentation. To avoid over segmentation, a subsequent run of the algorithm was conducted for only the particles which could not be separated in the previous instance. The overall methodology flowchart from sample preparation to image analysis is presented in Figure 3-9. The whole image processing method applied in this study for sand particles for uncemented sand is depicted briefly in the flowchart shown in Figure 3-10 (a). For processing the voids, the solid phase comprising the sand for uncemented sand and sand-cement matrix for cemented sand was separated from the void phase (Figure 3-10(b)). A sub-volume of the sample of size 6 mm x 6 mm and the thickness close to the thickness of the sample for uncemented and all cemented samples were extracted. Then non-local means filter was used to reduce noise from the image. Following similar procedure as above, binary image of void phase were obtained. On this image, watershed segmentation techniques was applied to separate the voids. No repetitive run of the watershed segmentation as were performed during the separation of particles, were done here for voids.

3.8 Image Analysis

Image analysis procedures followed in this study for obtaining evolution of various microstructural parameters, can be subdivided into two categories: analysis for microstructural scalar parameters and microstructural directional parameters.

For uncemented sand, scalar parameters like particle size distribution, anisotropy distribution, particle breakage, void size distribution, void ratio distribution were computed. For cemented sample scalar parameters like distribution of sphericity of voids, distribution of size anisotropy of voids, distribution of void volumes were computed. For computation of the scalar parameters, AVIZO software (V 9.1.1, V9.5) were used.

However, as directional parameter in this study, direction of the major axis of the separated void particles were considered for both uncemented and cemented sand. Image data from AVIZO were exported to MATLAB supported format. A MATLAB code was written based on Kanatani (1984)'s principle on two dimensional and three dimensional distribution of directional data and fabric tensors. The code is attached in appendix B. Using the code, distribution of fabric tensors of voids for both uncemented and cemented samples at different loading conditions were plotted. In addition, as a scalar parameter Fabric Anisotropy Variable A ($FAV\ A$) (Li and Dafalias, 2011) which accounts for both magnitude of the fabric anisotropy and its orientation relative to loading direction was computed for each loading case.

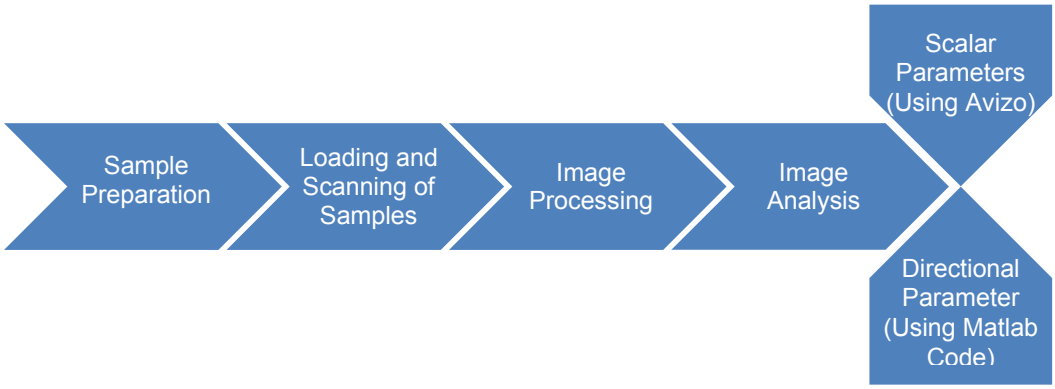

Figure 3-9: Methodology flowchart

(a)

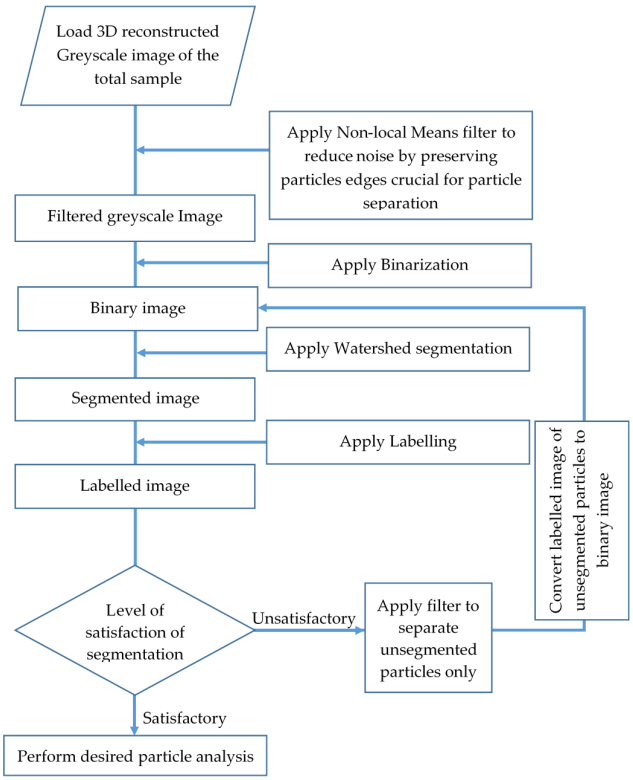

(b)

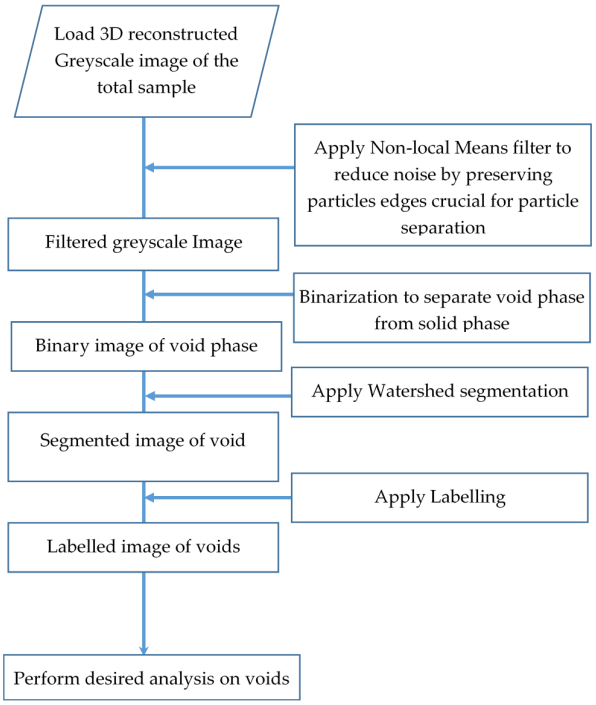

Figure 3-10: Flow chart depicting operations of image processing for (a) sand particles in uncemented sand (b) voids in uncemented and cemented sand

3.8.1 Brief on Kanatani's Framework for distribution of directional data

In Kanatani (1984)'s framework, the most fundamental fabric tensor is fabric of the first kind or moment tensor. This tensor which incorporates the relevant directional information in a tensorial structure is constructed by averaging the tensorial product of unit vectors:

$$N_{i_1 i_2 .. i_r} = \frac{1}{N} \sum_{\alpha=1}^{N} n_{i_1}^{\alpha} n_{i_2}^{\alpha} \dots n_{i_r}^{\alpha} \qquad (3.1)$$

The n^{α} is the component of the α^{th} unit vector, N is the number of contacts, and r is the order for the tensor. This symmetric moment tensor plays fundamental role in deriving further tensorial quantities that characterizes the directional data distribution.

The r[th] approximation of Kanatani (1984)'s proposed density distribution function is :

$$f(n) \sim \frac{1}{\Omega} F_{i_1 i_2 \dots i_r} n_{i_2} n_{i_2} \dots n_{i_r} \qquad (3.2)$$

Where, $F_{i_1 i_2 \dots i_r}$ is the fabric tensor of the second kind of rank r, also known as fabric tensor. Value of Ω is 2π for two-dimensional data distribution and and 4π for three-dimensional data distribution.

For the fabric tensor of the third kind the expansion of the distribution becomes as:

$$f(n) = \frac{1}{\Omega} \left[D + D_{ij} n_i n_{j+} D_{ijk} n_i n_j n_k n_l + \cdots \right] \qquad (3.3)$$

Value of $D_{i_1} \dots \dots . D_{i_n}$ is derived as deviator tensors. Value of D = 1.

The explicit expressions for the second and fourth order fabric tensors for two and three-dimensional data distributions can be expressed as below.

Fabric tensors of second kind of 2nd and 4th order for two-dimensional data distributions are:

$$F_{ij} = 4\left(N_{ij} - \frac{1}{4}\delta_{ij}\right) \tag{3.4}$$

$$F_{ijkl} = 16\left(N_{ijkl} - \frac{3}{4}\delta_{(ij}N_{kl)} + \frac{1}{16}\delta_{(ij}\delta_{kl)}\right) \tag{3.5}$$

Fabric tensors of second kind of 2nd and 4th order for three-dimensional data distributions are:

$$F_{ij} = \frac{15}{2}\left(N_{ij} - \frac{1}{5}\delta_{ij}\right) \tag{3.6}$$

$$F_{ijkl} = \frac{315}{8}\left(N_{ijkl} - \frac{2}{3}\delta_{(ij}N_{kl)} + \frac{1}{21}\delta_{(ij}\delta_{kl)}\right) \tag{3.7}$$

Fabric tensors of the third kind of 2nd and 4th order for three-dimensional data distributions are:

$$D_{ij} = \frac{15}{2}\left(N_{ij} - \frac{1}{3}\delta_{ij}\right) \tag{3.8}$$

$$D_{ijkl} = \frac{315}{8}\left(N_{ijkl} - \frac{6}{7}\delta_{(ij}N_{kl)} + \frac{3}{35}\delta_{(ij}\delta_{kl)}\right) \tag{3.9}$$

Where δ is the Kronecker delta.

For two dimensional data, distribution for each slice could be plotted. But to simulate the 3D behaviour of the distribution from the two-dimensional distribution, moment tensor for all the slices (in either XY, YZ or XZ plane whichever in applicable) were

averaged by dividing their respective summations by corresponding number of slices. These average moment tensor was used for the subsequent computations. Similar procedure was adopted by Manahiloh et al. (2016) for his two-dimensional distribution of directional data.

3.9 Additional Challenges

This X-Ray CT facility is a newly established facility at Monash University. This investigation was first of its kind in this facility. Several trial and error processes were followed with many abandoned or failed tests before achieving each successful test.

First hurdle was selecting suitable material for fabricating the one-dimensional load cell which is strong enough to withstand sufficient radial force generated from the test and at the same time allow least attenuation of X-Ray for generating sharp image of the sample material. After few trials with different materials such as steel, Perspex, Nylon, aluminium, finally aluminium cylinder of suitable diameter was chosen.

However, while preparing cemented sample within aluminium cylinder, the cement was found to react with aluminium wall and form bonds. This offered the challenge for preparing cemented sample of such small height (< 4 mm) and diameter (8.5 mm). As an alternative to preparing within aluminium cell, samples were prepared in Nylon cell of similar diameter. But after 28-day curing, removal of sample from Nylon cell and inserting in aluminium cell was impossible without causing substantial damage to the sample. At the end, an acrylic mould and a core cutter (Figure 3-7) was used to prepare the samples according to the procedure mentioned earlier.

Finally, one of the most challenging tasks was learning the image analysis software, Avizo. Unlike other image analysis software such as ImageJ, Avizo is more sophisticated and versatile and requires rigorous training. However, as the first and only user of this software in civil engineering department for the first two years, the author had to put significant time and effort to learn and develop expertise in this software on his own.

3.10 References

ASTM D2435 / D2435M-11, Standard Test Methods for One-Dimensional Consolidation Properties of Soils Using Incremental Loading, ASTM International, West Conshohocken, PA, 2011, www.astm.org.

Cnudde, V. & Boone, M. N. 2013. High-resolution X-ray computed tomography in geosciences: A review of the current technology and applications. Earth-Science Reviews, 123, 1-17.

Deben UK Ltd. CT5000; Deben UK Ltd.: Suffolk, UK, 2013.

Deben UK Ltd. MICROTEST (V6.13); Deben UK Ltd.: Suffolk, UK, 2013

Dennis, M. J. 1989. Industrial computed tomography. ASM Handbook., 17, 358-386.

Du Plessis, A., Broeckhoven, C., Guelpa, A. & Le Roux, S. G. 2017. Laboratory x-ray micro-computed tomography: a user guideline for biological samples. GigaScience, 6, 1-11.

Hasan, A. & Alshibli, K. 2010. Experimental assessment of 3D particle-to-particle interaction within sheared sand using synchrotron microtomography. Géotechnique, 60, 369.

Kanatani, K.-I. 1984. Distribution of directional data and fabric tensors. International Journal of Engineering Science, 22, 149-164.

Li, X. S. & Dafalias, Y. F. 2011. Anisotropic critical state theory: role of fabric. Journal of Engineering Mechanics, 138, 263-275.

Manahiloh, K. N., Muhunthan, B. & Likos, W. J. 2016. Microstructure-based effective stress formulation for unsaturated granular soils. International Journal of Geomechanics, 16, D4016006.

XMReconstructor-Cone Beam-10; Xradia: Pleasanton, CA, USA, 2011.

Zeiss Xradia 2018, Zeiss Xradia corporate website, viewed 18 Nov, 2018, https://www.zeiss.com/microscopy/int/products/x-ray-microscopy/zeiss-xradia-520-versa.html

4 MICROSTRUCTURAL ANALYSIS OF SAND

4.1 Introduction

Practical application of engineering mechanics on soils requires an in-depth understanding of their mechanical behaviour. In modelling soil behaviour, a soil mass has often been treated as a continuum, however, in reality it is composed of individual particles. The mechanical behaviour of soils (strength and deformation behaviour) is governed by the arrangement of soil particles (known as fabric) and the interparticle bonds, together they are known as soil structure (Mitchell, 1976). In the case of reconstituted soils or granular soils, where bond is negligible or even absent, its microstructure becomes the arrangements of particles and interparticle voids.

Granular soils such as sands under deep driven piles, deep well shafts, or large earth dams experience high stress. Under such high stresses in one-dimensional compression, crushing of granular materials (Terzaghi and Peck, 1948)which is linked with its yield stress(De Souza, 1958), causes large deformations associated with tight grain packing and reduction of void ratios. Although crushing of particles is strongly

associated with tensile strength of individual grains (McDowell and Harireche, 2002a), however, several studies have confirmed that other factors such as particle morphology and mineralogy, particle size distribution, contacts, orientations, and void ratio which contribute to the fabric of granular materials, significantly influence the complex micro-mechanical behaviour of granular materials. However, most of the past studies as presented in literature review chapter relied either on invasive tests or on numerical methods such as DEM. Invasive tests disturb the fabric and fail to capture the evolution of microstructure. On the other hand, DEM uses idealized digital particles, which may not truly represent the behaviour of actual particles. With the advancement of laboratory-scale X-Ray CT technology, it is now possible to conduct investigation at real particles at grain-scale level. Few such studies elaborated in the literature review chapter.

In this chapter, as part of the current study, microstructural behaviour of uniformly graded sand subjected to *insitu* X-ray CT imaging under one dimensional compression has been presented. A uniformly graded, sub-angular quartz sand passing through 250 microns and retained on 212 and 150 microns sieves was subjected to high-resolution X-Ray CT imaging while undergoing one-dimensional compression. The mean diameter (D50) of the sand particles was 230 microns. The selection of this size is important to achieve an acceptable representation of sand particles within the volume (Razavi et al., 2006) including the minimum height to diameter ratio of the sample to be tested under 1D compression with a full field of view imaging. Details about the sample, load cell, loading procedure, image acquisition and processing have

been mentioned in chapter 3. In brief, solid and void phases of 3D reconstructed images at the end of each applied load case were isolated and then sand particles were separated from each other up to desired level (> 90% particles separation) and labelled. Similarly, voids were separated and labelled. Then sand particles were analysed for evolution of various scalar parameters. Voids were analysed for both scalar and directional parameters.

4.2 Results and Discussion

4.2.1 Void ratio vs. logarithm of vertical stress (e-logσ'_v) plot

The experimental and physical measurements of the sand sample were utilised to calculate the void ratio at each load case. The variations of void ratio with the logarithm of vertical stress (e-logσ'_v) plot for the sand sample tested in this study is presented in Figure 4-1. The initial void ratio (e_0) of the sample was 0.60.

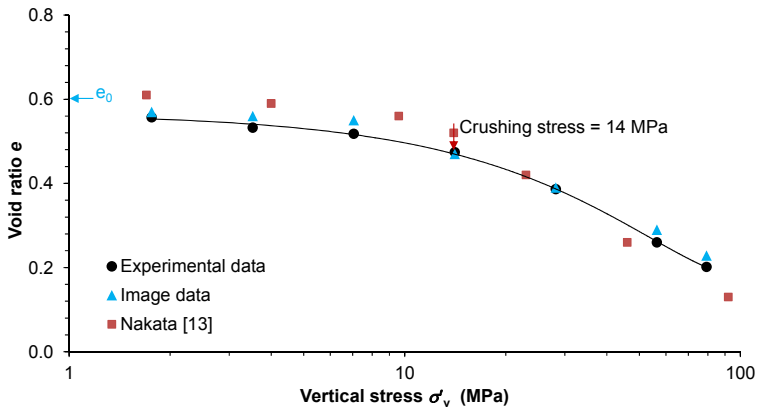

Figure 4-1: e-logσ'_v plot for the uniformly graded sand sample.

The e-logσ'_v plot shows a gradual change of slope up to 7 MPa stress followed by a significant change, which could be due to the crushing of particles. In this study, the crushing stress or yield stress is defined as the stress corresponding to the intersection

of two straight parts of the e-logσ'_v curve (Razavi et al., 2006; Zhao et al., 2015). The yield stress for the uniformly graded sands tested under 1D compression was found to be 14 MPa, which is denoted by the arrow sign in the above figure. The observed value is similar to that reported by Nakata et al. (2001) for uniformly graded quartz sand of relatively larger particle sizes but of almost similar uniformity coefficient (C_u) (1.1 vs. 1.24 of this study) and initial void ratio (e_0) of 0.6±0.03. This indicates that the small compression apparatus designed in this study is capable of producing an acceptable result when compared with the result obtained from a relatively large apparatus (50 mm diameter and 10 mm height) of Nakata et al. (2001).

The e-logσ'_v plot also shows that the decrease of void ratio in the post-yield stresses is higher, indicating a higher degree of particle crushing as claimed by (Hagerty et al., 1993) from his study. The slope of the e-logσ'_v curve in the post-yield region is reasonably in agreement with that of Nakata et al. (2001).

In order to explore the capability of 3D X-Ray CT imaging, only the greyscale images of vertical and horizontal sections through the centre of the whole sample under six load cases including the initial state are presented in Figure 4-2. It is evident from these images that with increased stresses, especially after the yield stress (14 MPa), a significant collapse of voids and crushing of particles were encountered. At the maximum vertical stress of 79.3 MPa, the void ratio was observed to decrease to 0.21, which is one-third of the initial value (0.60). A void ratio close to 0.19 was reported by Nakata et al. (2001).

4.2.2 Evolution of Scalar Fabric Parameters

4.2.2.1 Void Size Distributions with Vertical Stresses

The images acquired for each load case were thresholded to obtain the volume of solid and void phases. Subsequently, the void ratios were calculated for each load case and were plotted together with the experimentally obtained values (Figure 4-1). It can be seen that the void ratios calculated from the image analysis using the threshold intensities as shown in Figure 4-3 are in good agreement with the experimental data. An increasing trend of threshold intensity values as shown in Figure 4-3 could be associated with the increase of the fraction of fines and the bulk density of the sand sample subjected to increased compressive loads.

The void volume obtained by the thresholding was further processed using the watershed algorithm (Atwood et al., 2004; Fonseca et al., 2013b) to obtain the pore volume distributions. Figure 4-4 presents the distribution of pore volumes with increase in vertical stresses. Unlike particles, pores are interconnected and often form large volumes based on 26-neighbourhood connectivity. As anticipated, large pores were observed to reduce to small size pores with the increase of vertical stresses. Interestingly, not much difference between the pore size distribution plots for the final two load cases were observed, which is in-line with the relatively small change of void ratios experienced under these stresses (Figure 4-1).

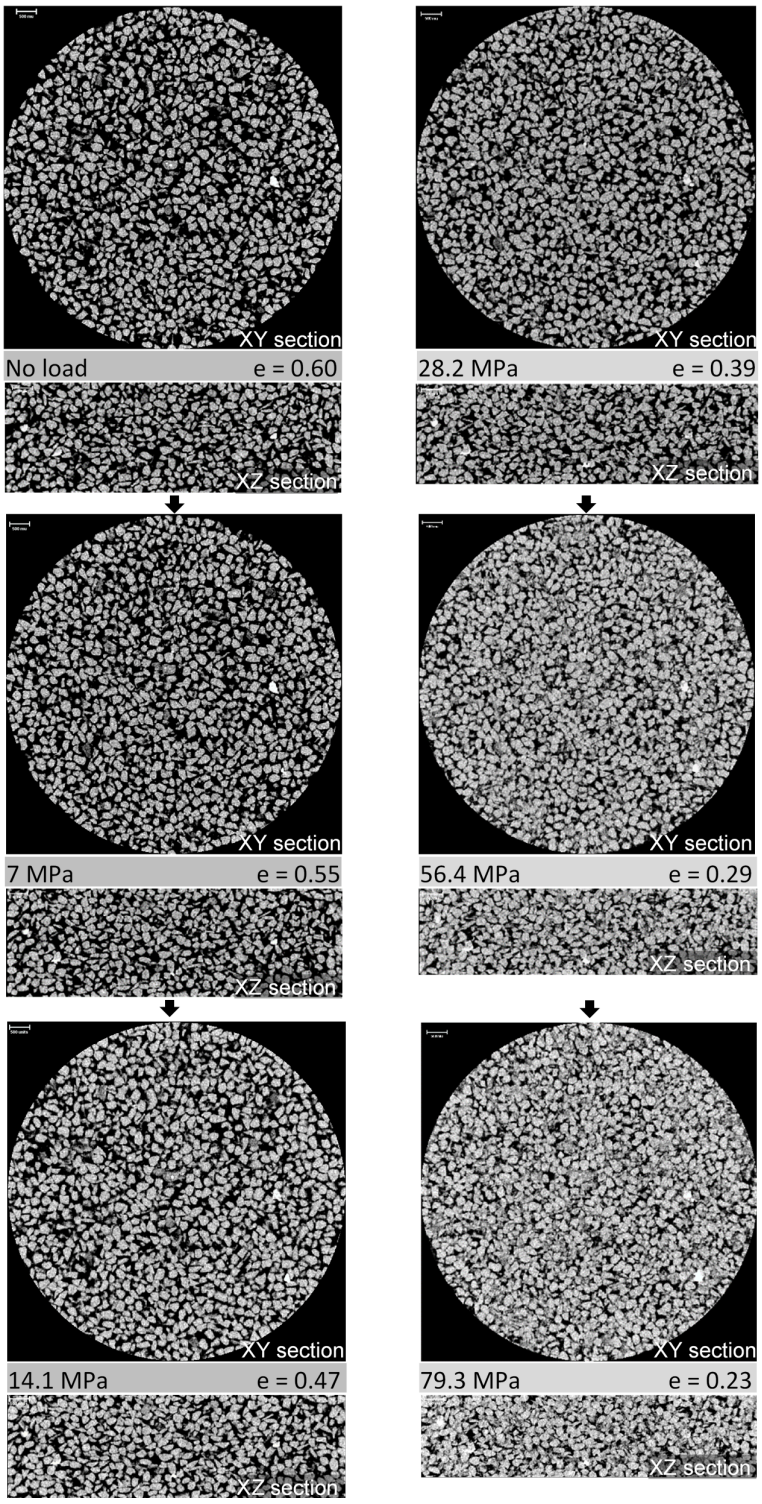

Figure 4-2: Horizontal and vertical image sections through the centre of sample at different vertical stresses.

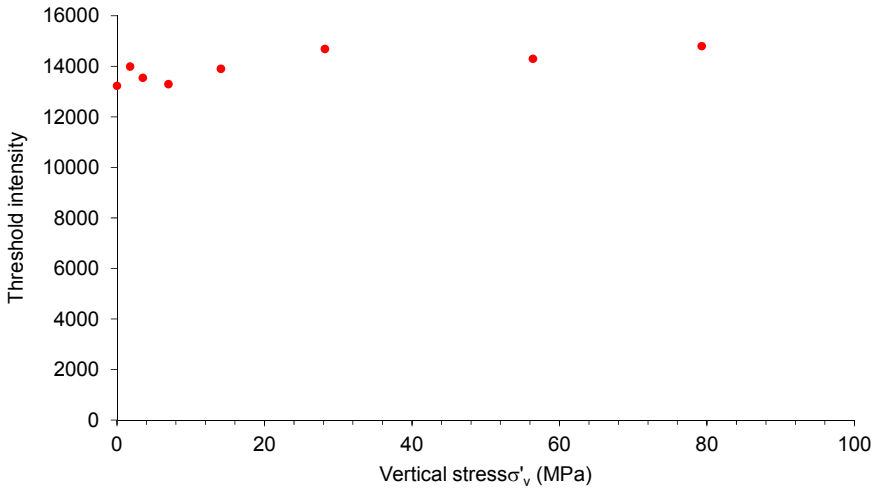

Figure 4-3: Threshold intensity values of grey scale images for different vertical stresses.

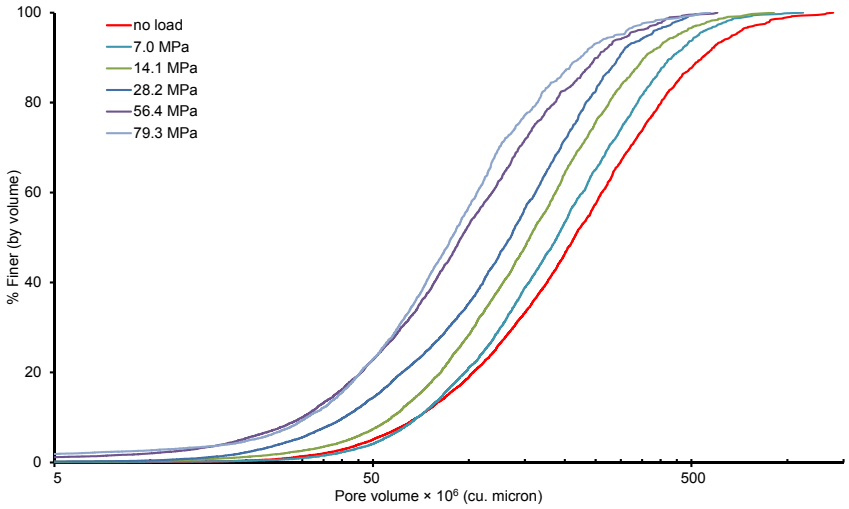

Figure 4-4: Pore volume distribution of samples tested under different vertical stresses.

4.2.2.2 Void Ratio Distributions

The 3D reconstructed slices of 8.5mm x 8.5mm x 0.14mm (600 x 600 x 1 voxels) size were analysed to determine the change of void ratios with the height of the sample for all the load cases (Figure 4-5a). A shift of the plot to the left indicates a reduction of

void ratio under the effect of vertical stress. Void ratios almost remained unchanged within the height of the sample for all the load cases except for the initial case where the top 100 microns of the sample had higher void ratios due to the uneven surface characteristics. Moreover, the change of void ratios with load cases up to the yield stress of 14 MPa were insignificant (0.6 at no load to 0.57 at 1.8 MPa to 0.55 at 7.0 MPa) compared to the values observed for higher stresses exceeding 14.1 MPa whereas crushing of particles were encountered. The crushing of particles resulted in a more uniform distribution of void ratios along the height of the sample (Figure 4-5a).

The spatial distribution of void ratios with the increase of vertical stresses was further investigated by selecting eight sub-volumes or representative elementary volume (REV) of 1.7mm x 1.7mm x 3.2mm (side length > $7D_{50}$) (Hasan and Alshibli, 2010) with a total voxels count of 3,175,873 (Figure 4-5b,c). It can be seen that the initial value of the void ratios for the REVs compared reasonable well with the initial void ratio of the whole volume (e_0=0.60). A wagon wheel plot of the void ratios calculated from the image analysis for the REVs under different load cases is shown in Figure 4-5d. As expected, the void ratio of the REVs decreases with the increase in pressure. Interestingly, the void ratio of the REVs under a given pressure are observed to be almost the same. Moreover, these values were very close to the values obtained along the full height of the sample (Figure 4-5a), indicating image analysis of a properly selected REV could produce meaningful outcomes of pressure-void ratio variations under very high pressure. Uniformity in distribution of void-ratios within the sample is a reflection of uniformly graded particles.

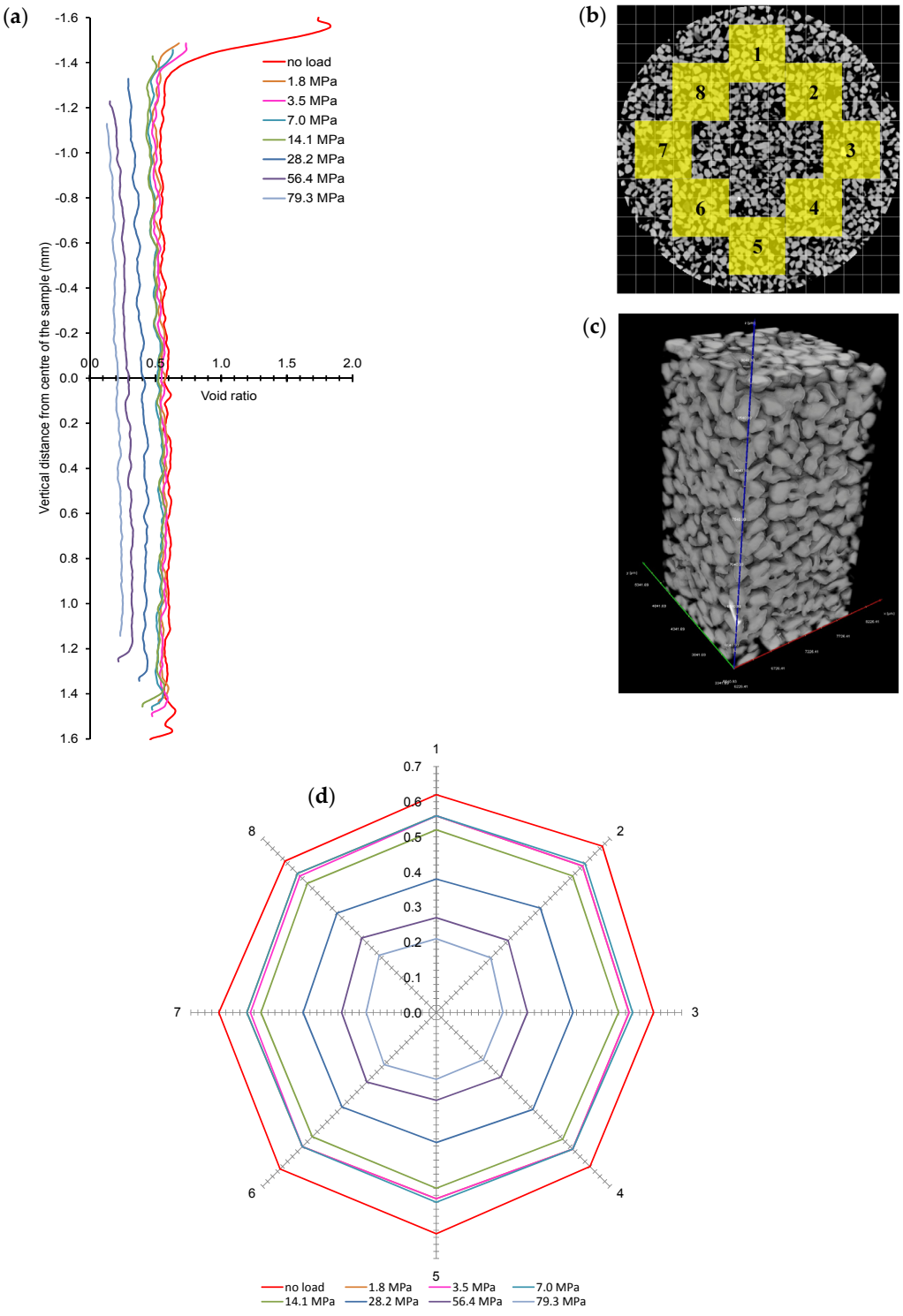

Figure 4-5: (**a**) Change of void ratios along the height of the sample with increased vertical stresses; (**b**) Locations of eight sub-volumes selected for spatial analysis; (**c**) 3D image of a sub-volume; (**d**) Spatial distribution of void ratios of sub-volumes with increased vertical stresses.

4.2.2.3 Particle Size Distributions

Initial Distributions

3D X-ray CT image of the initial sample was post-processed and particles were separated using the procedure mentioned in earlier chapter (Figure 3-9a). Two examples, one for no load and another for 14.1 MPa, of the process of separation are presented in Figure 4-6. The volume of particles obtained from the label analysis was used to calculate the equivalent sphere diameter of particles, which was then compared with the particle size distributions obtained from the sieve analysis (Figure 4-7). It is understood that different size descriptors (e.g., Feret diameter, equivalent sphere diameter) will have different degrees of success (Fonseca et al., 2014) when correlating with the particle size distributions curve obtained from the mechanical sieve analysis. In this study, equivalent sphere diameter of 3D volume of particles was considered due to its wide application in the laser particle size analysis. It can be seen that the particle size distribution curve obtained from the image analysis compares well with the sieve analysis curve for the uniformly graded sand particles tested in this study. Existence of insignificant percentage (<4%) of particles smaller than 150 microns (Figure 4-7) could be due to the tolerances permitted in the average opening of the testing sieves and abrasion of particles during sieving, which are usually less than 5% of the total sample (Carpenter and Deitz, 1950).

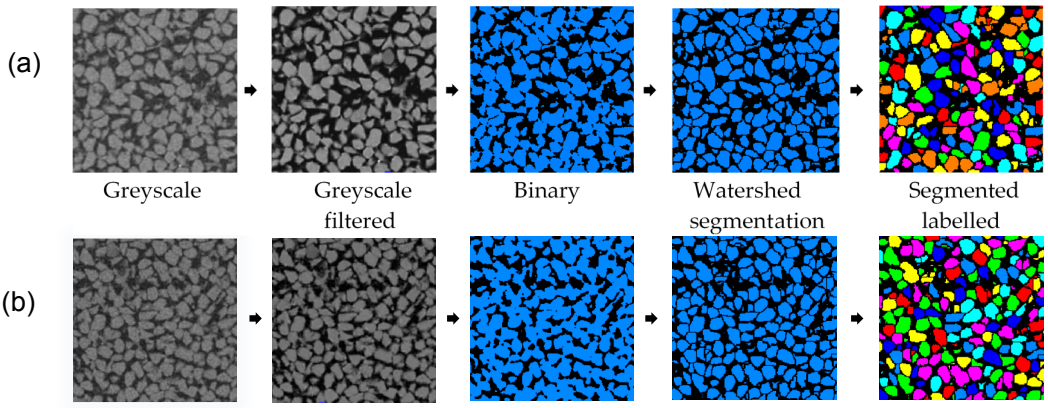

Figure 4-6: Examples of image processing depicting particle separation and identification for (a) no load, and (b) 14.1 MPa.

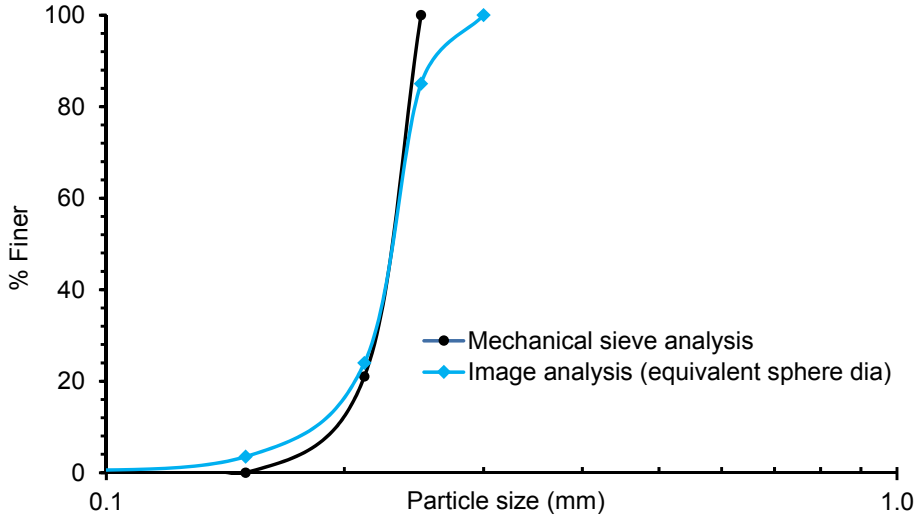

Figure 4-7: Initial grading obtained from mechanical sieving and image data.

Above 80% finer, the distribution obtained from the image analysis shows presence of particles of equivalent sphere diameters as large as 300 microns or even more. This value is some 20% higher than the opening size of the largest mesh (250 microns) used in this study. One of the most plausible explanations of relatively larger volume

particles to pass through smaller sieve size could be related to the large value of particle size anisotropy (discussed later section), and orientation. A further verification using the sand particles volume obtained from the image analysis confirms that the bulk density of the sample is in good agreement with the measured initial bulk density (Table 4-1).

Table 4-1: Calibration of image data with physical measurement.

Mass-Volume-Density Relationships	**Image Analysis**
Initial bulk density (ρ_i) = 1.62 g/cm^3	Total volume of sand particles (V_s) = 0.09 cm^3
	Specific gravity of sand particles (G_s) = 2.68
	Mass of sand particles (M_c) = $V_s G_s \rho_w$ = 0.24 gm
	Bulk volume (V_b) = 0.15 cm^3
	Bulk density=M_s/V_b=1.60 ≈ 1.62 g/cm^3

Load-Dependent Distributions

Figure 4-8 shows evolution of the particle size distribution with vertical stresses up to 79.3 MPa. For initial condition and subsequent stresses, images were analysed to obtain the particle size distributions (PSD). As there was very little change of particle size distributions up to a yield stress of 14 MPa, for the sake of clarity of the presentation only the evolution of PSD for stresses equal to or higher than the yield stress are presented. Both the 3D volume of particles and their equivalent sphere diameters were considered for plotting the PSD.

The nature of the gradual upward shifting of the PSD curves in Figure 4-8 from no load condition to subsequent higher loads indicates generation of smaller size particles due to particle crushing. The development of a pivot point around 250 microns equivalent sphere diameter and an upward shifting of PSD below this size indicate particle crushing predominantly at the pivot point and below. Similar observations were reported by (Nakata et al., 2001). However, this study finds relatively less breakage of particles in terms of increase of fines. The reason might be due to the smaller mean particle size (D_{50}=230 microns) in this study compared to a much higher value (D_{50}=1550 microns) of Nakata et al. (2001), which poses a higher potential to breakage (Hardin, 1985). On the other hand, particles above the 250 microns size showed an unexpected downward shift of the PSD curve compared to the no load curve. This could be related to the large equivalent diameter of small number of unseparated particles in the processed image. However, their influence on explaining the particle crushing behaviour of the sand sample can be considered relatively small.

In order to understand the evolution of PSD with increased loading, the frequency of a defined range of particles and their corresponding volume fraction with respect to the total volume of the sample were determined. A weighted frequency is calculated by multiplying the volume fraction of a range of particle size with its frequency i.e., weighted frequency = number of particles (%) x volume fraction. Figure 4-9 shows the change of weighted frequency of various particle ranges with increased stresses. It is evident from the plot that crushing of particles occurred predominantly within the

205 to 258 microns size. In particular, particles of size range between 225 and 243 microns showed a significant drop of weighted frequency with loading (5.5 for no load to 3 for 79.3 MPa), indicating a relatively high crushing of particles with sizes close to the mean particle diameter (D_{50}=230 microns). Interestingly, particle sizes close to 0.93D_{50} diameter (i.e., 205-225 microns) showed a very small change of the weighted frequency (5.5 for no load vs. 5 for 56.4 MPa) except for the 79.3 MPa, where a weighted frequency value of approximately 4.5 associated with a higher degree of crushing was observed. As expected, the weighted frequency of particles below 205 microns size was observed to increase with the increase of stress. This indicates the formation of new particles of smaller sizes at the expense of crushing of larger particles (>D_{50} size) with increased loading. This was also reflected in the rapid reduction of the effective particle diameter (D_{10}) with increased loading (Figure 4-8).

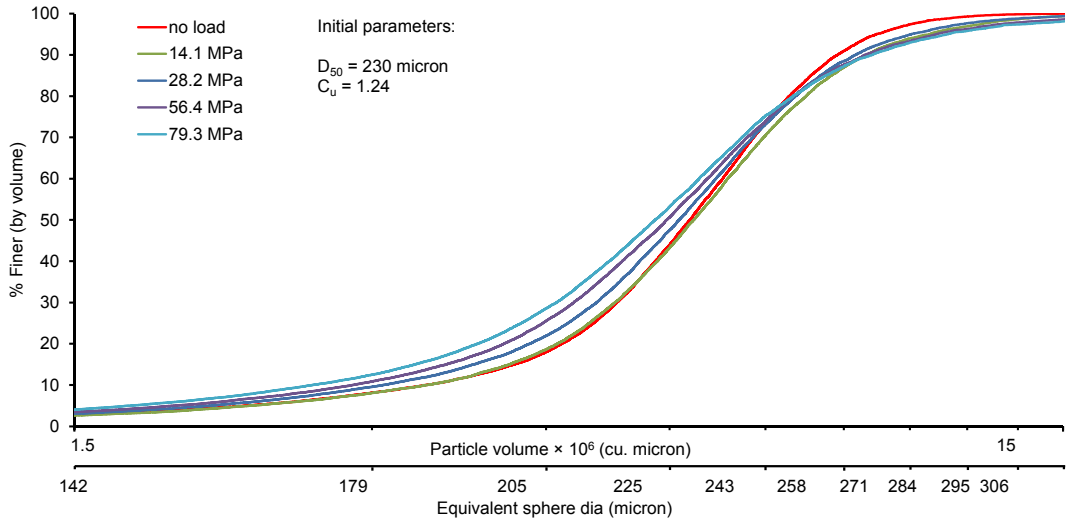

Figure 4-8: Evolution of particle size distribution from crushing at different loads.

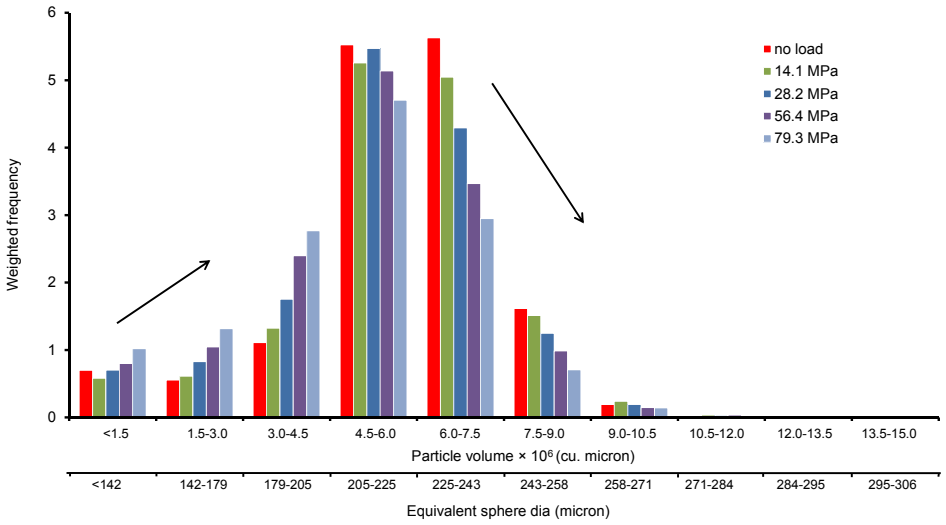

Figure 4-9: Particle size frequency distribution.

4.2.2.4 *Particle Breakage*

The relative breakage parameter (B_r), which is defined by Hardin (1985) as B_t/B_p where B_t = total breakage and B_p=breakage potential, was calculated for all load cases (Figure 4-10a). It can be seen that the values of B_r for stresses below the crushing stress (14 MPa) are insignificant (Br≈0). In the post-crushing stress range, a linear variation between B_r and stress can be approximated, which is in good agreement with Coop and Lee (1993). This linear variation of Br can be explained with the help of the gradual change of the slope of the e-logσ'_v plot in the post-crush region (Figure 4-1). It is believed that if applied stress is significantly higher than the presently used maximum stress (79.3 MPa), the value of B_r may reach an asymptotic value indicating no further breakage of particles. Figure 4-10b illustrates the breakage of particles at high stresses relative to no load condition. The breakage of particles under high stresses is marked by circles. The different colours of particles in Figure 4-10b indicate different intensity values.

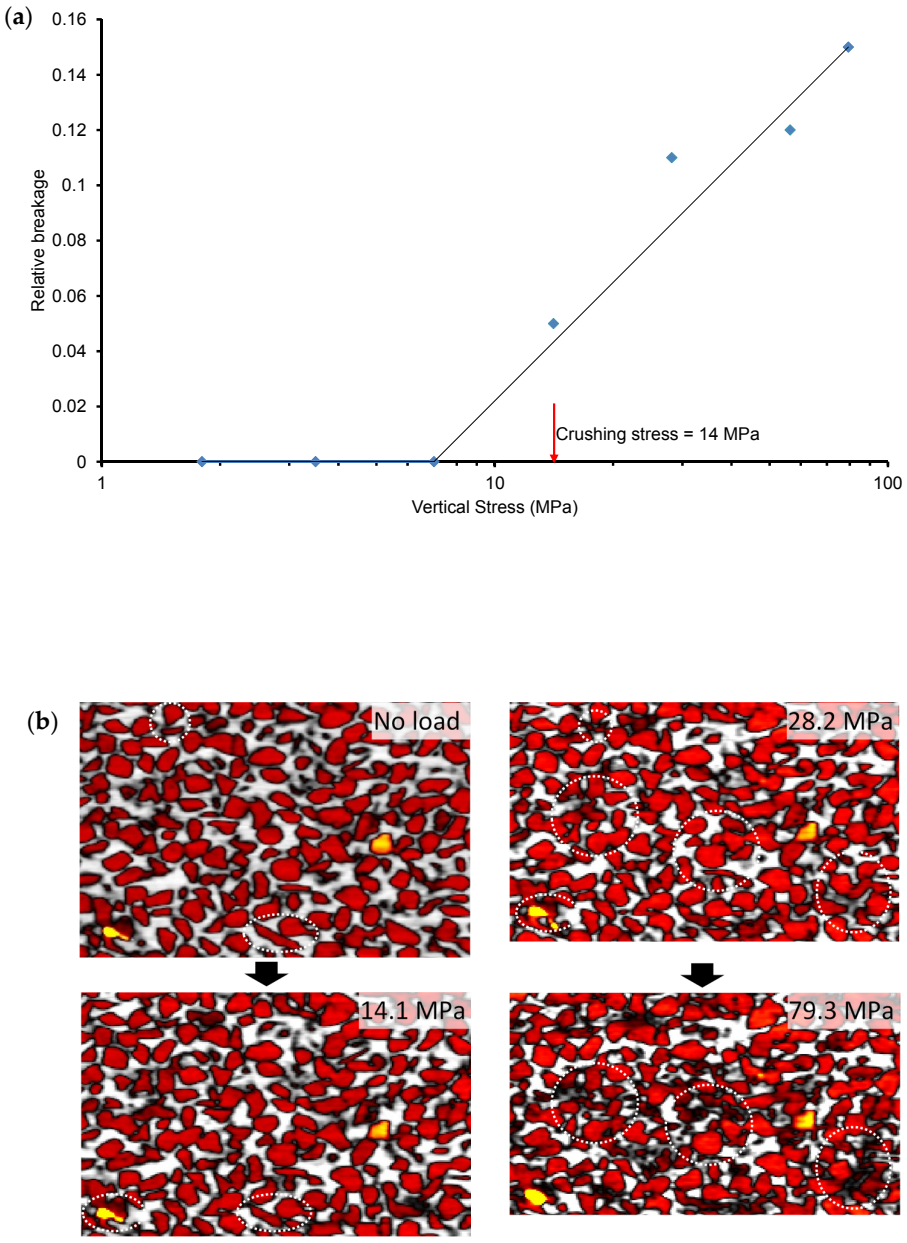

Figure 4-10: Particle breakage under different vertical stresses (a) relative breakage; (b) images showing breakage of particles.

4.2.2.5 *Particle Size Anisotropy*

Particle size anisotropy is defined as 1 minus the ratio of the smallest to the largest eigenvalue of the covariance matrix (Avizo.9.1.1, 2015). Anisotropy measures a

particle's deviation from a spherical shape with a value of 1 indicating highly non-spherical particle and a value of zero indicating a fully spherical particle.

Size anisotropy for all the particles under no load condition was determined from the labelled images and their distributions are plotted in Figure 4-11. It is clear that more than 80% particles had anisotropy values greater than 0.6. Therefore, it is likely, during mechanical sieving, that a particle with a given volume may pass a square mesh size, which is smaller than the equivalent sphere diameter at a suitable orientation as opposed to a particle with the same volume but with a lower anisotropy value. This phenomenon is illustrated in Figure 4-12, where thirteen particles of equal volume (6.3×10^6 cubic microns) are shown with varying anisotropy values (0.44 to 0.90). Due to the relatively large long-axis dimension of particles associated with high anisotropy values, these particles will have a greater chance of passing through sieve sizes smaller than their equivalent diameters.

With the increase of load, particles undergo more grinding and breakage leading to particles of more spherical in shape. This results in decrease of anisotropy (particles become more spherical) with an increase of loading which has been depicted from the inward shift of the anisotropy distribution curves (Figure 4-11).

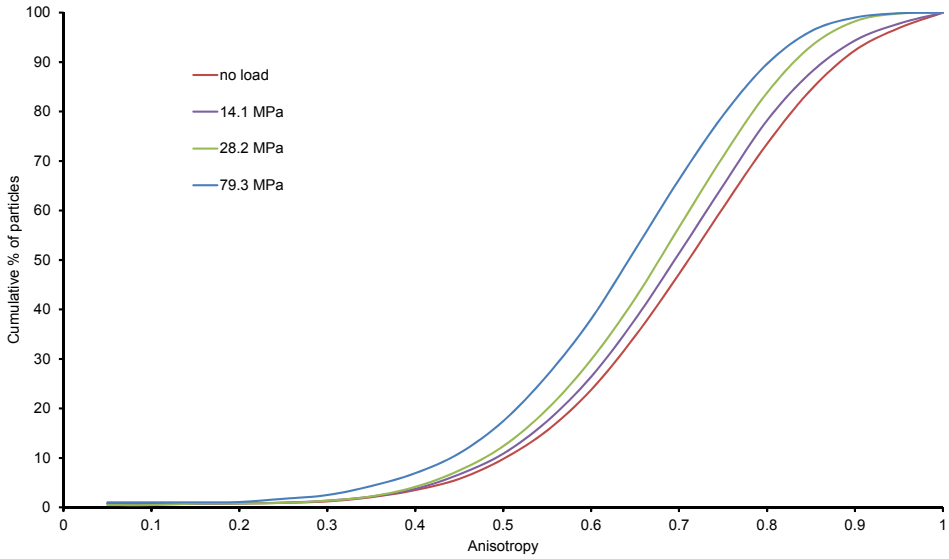

Figure 4-11: Anisotropy distributions of particles with vertical stresses.

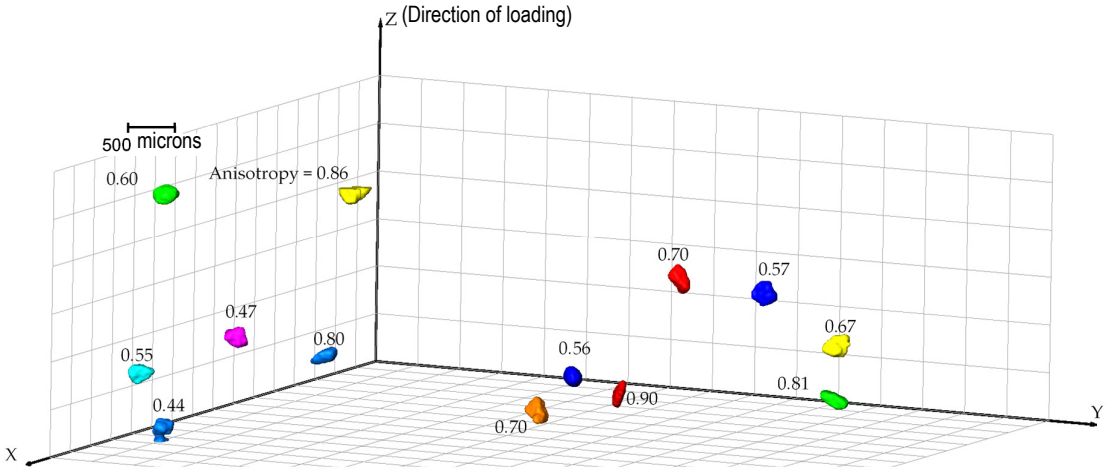

Figure 4-12: Variation of anisotropy of particles with equal volumes (6.3×10^6 cubic microns).

Figure 4-13 shows a bubble plot representing the frequency distribution of particles of various sizes and their anisotropy with different vertical stresses. It is observed that with the increasing load, anisotropy, in general, decreases and the bubble size representing the frequency of particles increases indicating formation of smaller size particles due to crushing.

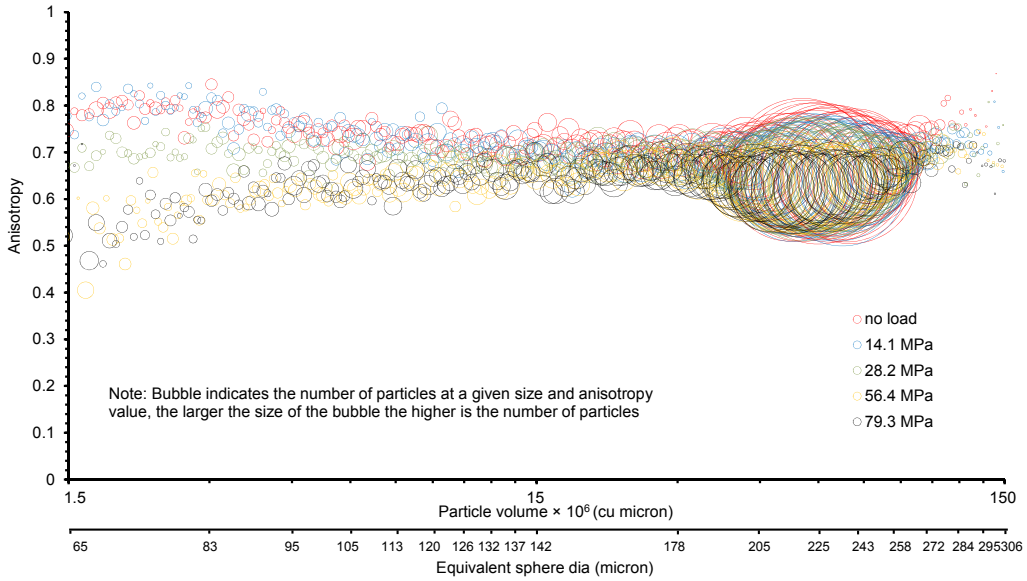

Figure 4-13: Particle anisotropy and frequency distributions with vertical stresses

4.2.3 Directional Fabric Analysis

When sands are subjected to external loads, rearrangement of the particles take place as they move and rotate under the action of contact forces generated from the applied load. Thus, progressive evolution of the fabric take place. To capture the initial fabric and their evolution, only scalar parameters such as void ratio, coordination number etc. are not sufficient (Oda et al., 1985; Muhunthan, 1991) . Therefore, researchers (Oda and Konishi, 1974; Oda, 1977; Christoffersen et al., 1981; Mehrabadi et al., 1982; Bathurst and Rothenburg, 1990) with the aid of various directional parameters (e.g.

contact normal vectors, particle long axis, void long axis and branch vectors) have tried to explain the macro behaviour of granular soil. In particular, the effect of initial fabric orientation on the behaviour of soil under load and evolution of anisotropic behaviour of fabric at different stages of loading have been the areas of significant interests among researchers (Arthur and Menzies, 1972; Oda, 1972b; Oda et al., 1985; Oda and Nakayama, 1989; Oda, 1993; Imseeh et al., 2018).

Among various directional parameters, shape and distribution of voids play an important role in defining the mechanical properties of a granular mass (Oda et al., 1985). However, the role of shape of voids are less apparent and indirect in determining granular material's mechanical behaviour because their evolution results from the evolution of the solid phase. Even then, an indirect relation could still result in a strong and definitive correlation, making void-based fabric tensor potentially useful, especially when it is convenient to measure (Fu and Dafalias, 2015). Moreover, tensor parameters on the void phase have a potential of delivering a unified measure for all particulate media (Manahiloh et al., 2016) by avoiding the difficulty of defining contact normal, contact vector and their distributions. The level of difficulty escalates significantly for cemented sand. Thus, void phase provides a suitable common platform for comparing microstructural evolution of directional parameters for uncemented sand with those of cemented sand as analysed in chapter 5.

In addition to graphical representation of the distribution, to represent the distribution by a scalar quantity is important for inclusion of the influence of the fabric in

modelling especially in DEM. Such a scalar quantity, Fabric Anisotropy Variable A, $FAV\ A$, proposed by Li and Dafalias (2011) under anisotropic critical state theory (ACST) framework, and further clarified by Dafalias (2018) (attached in Appendix A), was employed to study the phenomenon of fabric evolution (Equation 3). Where non-transversely isotropic fabric tensors are encountered, $FAV\ A$ was still calculated based on the assumption of transverse isotropy.

$$FAV\ A = \pm F_{ij}^{d} : n_i \delta_{ij} \tag{3}$$

Where F_{ij}^{d} is deviatoric component of second order fabric tensor of second kind F_{ij} as expressed by Equation 4, n_i is the deviatoric unit-norm loading direction.

$$F_{ij}^{d} = F_{ij} - \frac{1}{3} F_{kk} \delta_{ij} \tag{4}$$

Where F_{kk} is trace of the fabric tensor.

4.2.3.1 Directional Distribution of voids

In this study, the directional distribution of the interparticle void long axis has been studied at initial condition and over the course of progressive loading. A Matlab code based on Kanatani (1984)'s principle on 2D and 3D directional data has been developed. Details on Kanatani (1984)'s framework is discussed in chapter 3. For 2D analysis to ensure equal cross sectional area along any plane (XY, XZ or YZ) a square area of 6x6 sq. mm. in XY plane for the thickness the sample were analysed for all load cases. For consistency, the same subvolume has been analysed for 3D distribution as well. Figure 4-14 shows the marked subvolume and corresponding voids in binary and 3D labelled image.

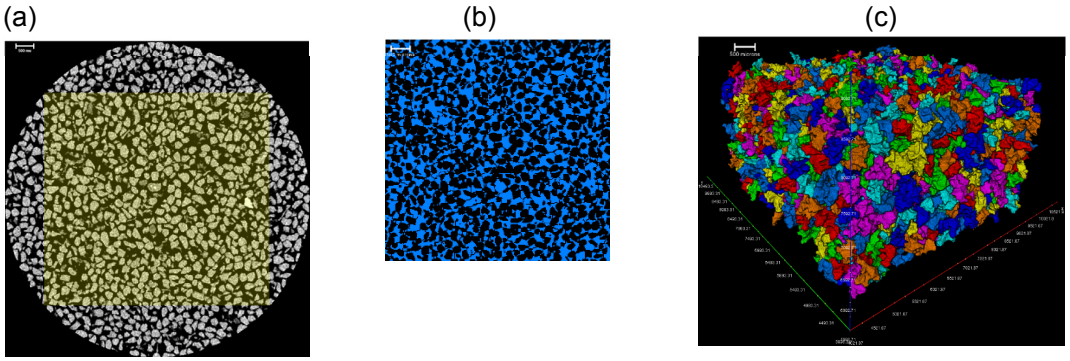

Figure 4-14: (a) 6x6 sq. mm. subvolume (light yellow) marked in XY plane of the whole sample (b) corresponding voids within subvolume (c) 3D labelled image of voids

Evolution of directional distribution of long axis of 3D voids is presented as 3D surface plot in Figure 4-15. Kanatani (1984)'s 4th order distribution of third kind has been used to capture the distribution. In general, the distribution as observed from the perspective view, reflects biasness at the right angle to the direction of applied pressure (which is along Z axis). With progressive loading, the intensity of the directional biasness seems to become higher especially for the final two stress levels. Similar observation for voids orientation, however for kaolin clay, was also claimed by McConnachie (1974). In addition, the transverse isotropy of the distribution at initial stages started to concentrate more along two major axis (x and y) in yield and post yield stages. Perhaps, breakage of particles might have influenced the reorientation of the void fabric towards such distribution.

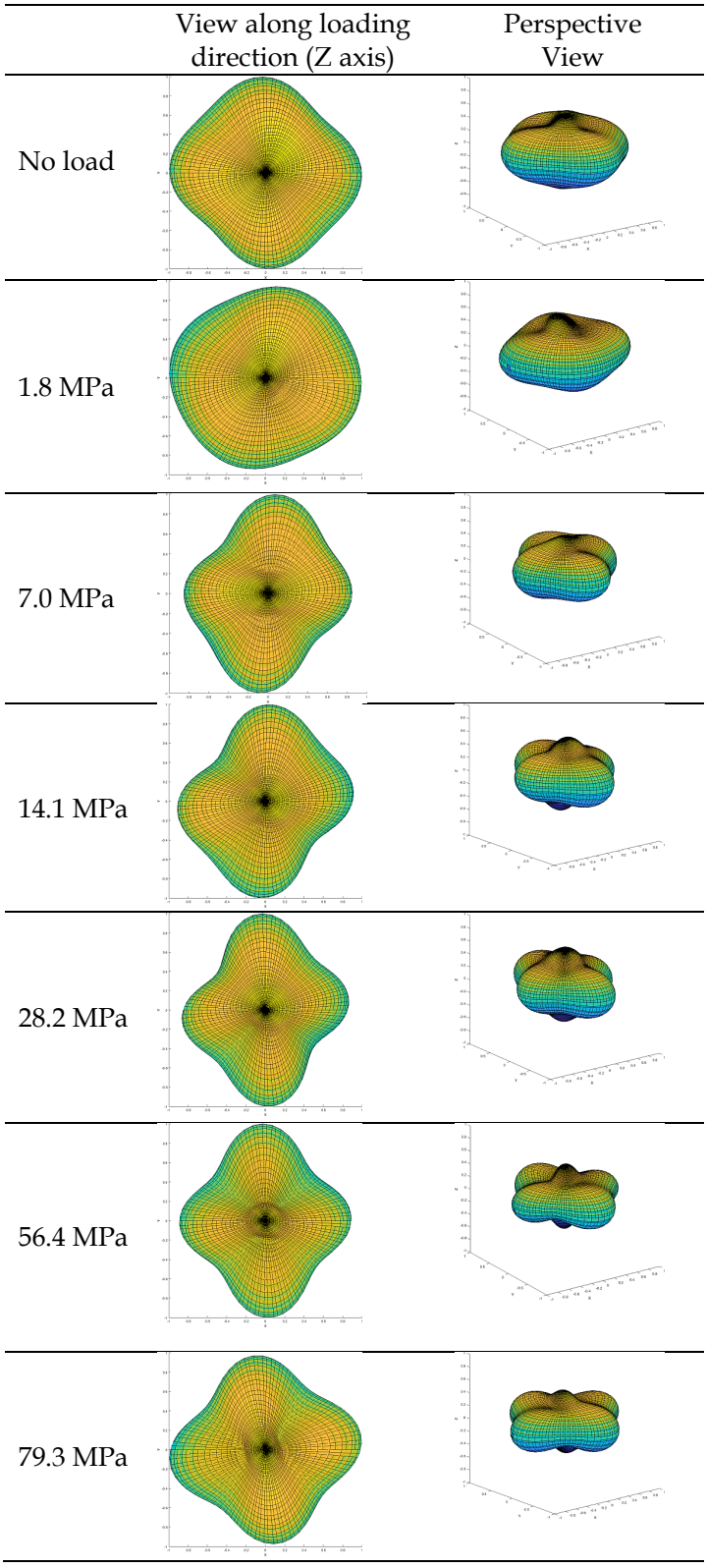

Figure 4-15: 3D surface plot of density distribution for the voids

Voids are 3D objects. However, due to limitation of suitable technology, earlier researchers (McConnachie, 1974; Oda and Nakayama, 1989; Oda, 1993) frequently used 2D slices to study fabric and their evolution. However, those studies being invasive, number and orientation of slices were limited. Moreover, different sample for each load increment had to be used to capture the evolution, which cannot be representative in true sense. With the aid of non-invasive X-ray CT technology, numerous number of slices of the samples in each plane can be analysed with progressive loading. Using (Kanatani, 1984)'s 2nd order (blue coloured) and 4th order (red coloured) distribution of second kind for 2D data, the distribution in all three planes are presented in Figure 4-16. To represent 3D nature of the distribution from the two-dimensional slices, moment tensor for all the slices (in either XY, YZ or XZ plane) were averaged by dividing their respective summations by corresponding number of slices. These average moment tensor was used for the subsequent computations of the distribution. Similar procedure was adopted by (Manahiloh et al., 2016) for his two-dimensional distribution of directional data. In addition, rose diagrams, as an additional representation of the distribution of 2D data are also presented. For rose diagram plot, number of vectors in corresponding angular ranges (15°), for all slices, were summed up. Among all representation of 2D, Kanatani's 4^{th} order distribution more represents the 3D distribution. However, in general, other two representation were found sufficiently capable of reflecting the actual distributions.

Finally, for 3D data, $FAVA$ (Figure 4-17) with their increased values especially for two final loads cases, are in agreement with the change of observed graphical distribution.

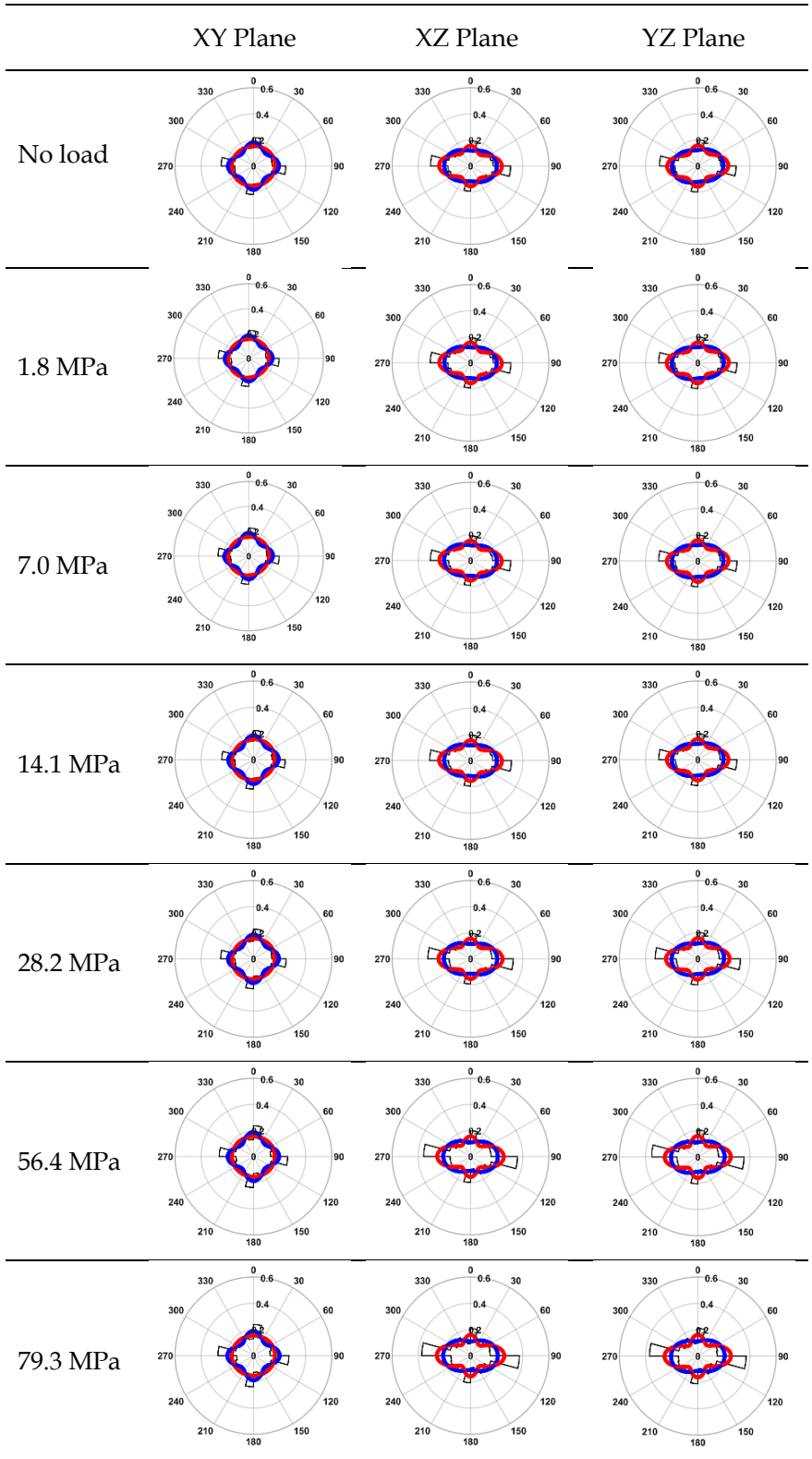

Figure 4-16: Rose diagram, and 2nd order (blue) and 4th order (red) density distribution of direction of voids long axis

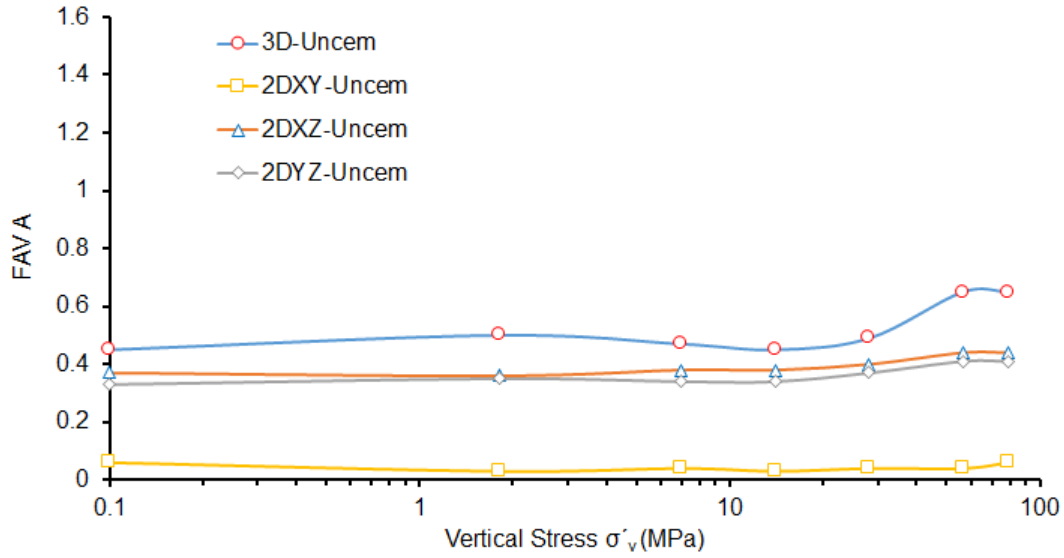

Figure 4-17: *FAV A* vs. Vertical stress, σ'_v

4.3 Summary

High-resolution *insitu* X-Ray CT imaging of microstructure of sand particles subjected to high pressure one-dimensional compression leading to particle crushing was conducted. The images taken at different load stages have been analysed to capture the micro-structural characteristics including the void and particles volumes distributions, change of void ratios, range of particles undergoing crushing, distribution of particle size anisotropy, and directional distribution of void long-axis. The outcomes of this study are summarised below:

- The small-scale 1D compression apparatus setup designed for *insitu* X-Ray CT imaging was found to produce comparable results for *e*-logσ'v variations including the yield strength obtained from the lab-scale 1D compression test performed by Nakata et al. (2001) on uniformly graded sand particles of similar uniformity coefficients. The void ratios calculated for each load cases from the

image analysis were in good agreement with the experimental data, including the initial bulk density of the sand particles tested. Thus provides a platform of conducting high-resolution CT imaging and associated analyses.

- The increase of loads resulted in decreased global void ratios and pore volume sizes. Moreover, the void ratio variations along the height of the sample showed a gradual decrease until the yield stress and thereafter a significant decrease instigated by marked particles crushing. With the increase of stresses, the sinusoidal variations of void ratios encountered along the height of the sample under low stresses were observed to diminish. A more uniform change of void ratio of sub-volumes (REV) located at peripheral positions was also observed.
- The initial particle size distributions of sand particles obtained from mechanical sieve analysis and that obtained from image analysis using equivalent sphere diameter were in reasonably good agreement. The evolution of particle size distributions resulting from crushing of particles under incremental stresses could be captured using the non-destructive X-Ray CT *insitu* imaging. Moreover, the specific size group of particles predominantly subjected to crushing or forming under different stresses could be identified. With increased stresses, the creation of more fine particles associated with reduced values of size anisotropy was evident.
- The crushing of sand particles in the pre-yield stress region was insignificant as supported by the near zero values of the relative breakage parameter. The value of the relative breakage parameter was found to increase at the onset of

yielding and thereafter a linear variation with logarithm of vertical pressure could be approximated.

- The directional distribution of the voids long-axis, in general, shows anisotropy perpendicular to the loading direction. With increased stresses the increased intensity of anisotropy especially for the final two load cases were captured from both graphical distribution and values of $FAVA$. Such behaviour support similar claim by McConnachie (1974). However, the graphical distribution shows shift from more transverse isotropic distribution at initial stages towards concentrated distribution along two major axes (x and y) in yield and post yield stages. Reorientation of the newly generated smaller particles from crushing and grinding action is believed to have contributed to such reoriented void structure.

The non-destructive X-Ray CT imaging of micro-structure and analysis of image data for sand particles subjected to high pressure one dimensional compression are believed to add significant insight into the development of robust soil models using the discrete element modelling technique, where the particles can be modelled as crushable with the capacity of accommodating microstructural evolution. The outcomes will serve as the basis for X-Ray CT investigation of cemented sand, which are currently underway, on cemented sand particles subjected to one-dimensional compression.

4.4 References

Arthur, J. & Menzies, B. 1972. Inherent anisotropy in a sand. *Geotechnique,* **22,** 115-128.

Atwood, R., Jones, J., Lee, P. & Hench, L. 2004. Analysis of pore interconnectivity in bioactive glass foams using X-ray microtomography. *Scripta Materialia,* **51,** 1029-1033.

Avizo.9.1.1 2015. FEI Visualizations Sciences Group: Hillsboro, OR, USA, 2015.

Bathurst, R. J. & Rothenburg, L. 1990. Observations on stress-force-fabric relationships in idealized granular materials. *Mechanics of materials,* **9,** 65-80.

Carpenter, F. G. & Deitz, V. 1950. Methods of sieve analysis with particular reference to bone char. *Journal of Research of the National Bureau of Standards,* **45**.

Christoffersen, J., Mehrabadi, M. & Nemat-Nasser, S. 1981. A micromechanical description of granular material behavior. *Journal of applied mechanics,* **48,** 339-344.

Coop, M. & Lee, I. 1993. The behaviour of granular soils at elevated stresses. *Predictive soil mechanics***,** 186-198.

De Souza, J. 1958. Compressibility of sand at high pressure. *MS thesis, Massachusetts Institute of Technology***,** 63-64.

Fonseca, J., O'Sullivan, C., Coop, M. R. & Lee, P. 2013. Quantifying the evolution of soil fabric during shearing using directional parameters. *Géotechnique,* **63,** 487-499.

Fonseca, J., Sim, W., Shire, T. & O'sullivan, C. 2014. Microstructural analysis of sands with varying degrees of internal stability. *Géotechnique,* **64,** 405-411.

Fu, P. & Dafalias, Y. F. 2015. Relationship between void-and contact normal-based fabric tensors for 2D idealized granular materials. *International Journal of Solids and Structures,* **63,** 68-81.

Hagerty, M., Hite, D., Ullrich, C. & Hagerty, D. 1993. One-dimensional high-pressure compression of granular media. *Journal of Geotechnical Engineering,* **119,** 1-18.

Hardin, B. O. 1985. Crushing of soil particles. *Journal of geotechnical engineering,* **111,** 1177-1192.

Hasan, A. & Alshibli, K. 2010. Experimental assessment of 3D particle-to-particle interaction within sheared sand using synchrotron microtomography. *Géotechnique,* **60,** 369.

Imseeh, W. H., Druckrey, A. M. & Alshibli, K. A. 2018. 3D experimental quantification of fabric and fabric evolution of sheared granular materials using synchrotron micro-computed tomography. *Granular Matter,* **20,** 24.

Kanatani, K.-I. 1984. Distribution of directional data and fabric tensors. *International Journal of Engineering Science,* **22,** 149-164.

Li, X. S. & Dafalias, Y. F. 2011. Anisotropic critical state theory: role of fabric. *Journal of Engineering Mechanics,* **138,** 263-275.

Manahiloh, K. N., Muhunthan, B. & Likos, W. J. 2016. Microstructure-based effective stress formulation for unsaturated granular soils. *International Journal of Geomechanics,* **16,** D4016006.

McConnachie, I. 1974. Fabric changes in consolidated kaolin. *Geotechnique,* **24,** 207-222.

McDowell, G. & Harireche, O. 2002. Discrete element modelling of soil particle fracture. *Géotechnique,* **52,** 131-135.

Mehrabadi, M. M., Nemat-Nasser, S. & Oda, M. 1982. On statistical description of stress and fabric in granular materials. *International Journal for Numerical and Analytical Methods in Geomechanics,* **6,** 95-108.

Muhunthan, B. 1991. Micromechanics of steady state, collapse and stress-strain modeling of soils. PhD dissertation, Perdue University, West Lafayette.

Mitchell, J. 1976. Fundamentals of Soil Behaviour" John Wiley. *New York*.

Nakata, Y., Hyodo, M., Hyde, A. F., Kato, Y. & Murata, H. 2001. Microscopic particle crushing of sand subjected to high pressure one-dimensional compression. *Soils and foundations,* **41,** 69-82.

Oda, M. 1972. Initial fabrics and their relations to mechanical properties of granular material. *Soils and foundations,* **12,** 17-36.

Oda, M. 1977. Fabrics and their effects on the deformation behaviors of sand. *埼玉大学工学部建設系研究報告*, p1-59.

Oda, M. 1993. Inherent and induced anisotropy in plasticity theory of granular soils. *Mechanics of Materials,* **16,** 35-45.

Oda, M. & Konishi, J. 1974. Microscopic deformation mechanism of granular material in simple shear. *Soils and foundations,* **14,** 25-38.

Oda, M. & Nakayama, H. 1989. Yield function for soil with anisotropic fabric. *Journal of Engineering Mechanics,* **115,** 89-104.

Oda, M., Nemat-Nasser, S. & Konishi, J. 1985. Stress-induced anisotropy in granular masses. *Soils and foundations,* **25,** 85-97.

Razavi, M. R., Muhunthan, B. & Al Hattamleh, O. 2006. Representative elementary volume analysis of sands using X-ray computed tomography. *Geotechnical Testing Journal,* **30,** 212-219.

Terzaghi, K. & Peck, R. 1948. Soil mechanics in engineering practice. *Soil mechanics in engineering practice.* J. Wiley and Sons.

Zhao, B., Wang, J., Coop, M., Viggiani, G. & Jiang, M. 2015. An investigation of single sand particle fracture using X-ray micro-tomography. *Géotechnique,* **65,** 625-641.

5 MICROSTRUCTURAL ANALYSIS OF CEMENTED SAND

5.1 Introduction

Engineering properties of cemented soils have significant importance for geotechnical engineers and geologists. This is because many natural soils like carbonate soils can be moderately to even highly cemented (Airey, 1993; Huang and Airey, 1998). Moreover, soil stabilization by mixing cementitious additives (e.g. hydraulic cement, lime, slag, flyash etc.) with soil is an economic and eco-friendly method of ground improvement, which is increasingly being used worldwide in foundation engineering, road and railway platform construction, and other geotechnical engineering applications. Thus, there is a strong need to improve the understanding of the behaviour of naturally and artificially cemented soils for geotechnical engineering applications.

Researchers have carried out several studies on both naturally and artificially cemented soils. However, most of those studies were based on their macroscale

responses whereas microstructure has significant influences on their mechanical responses (Leroueil and Vaughan, 1990; Cotecchia and Chandler, 1997; Cuccovillo and Coop, 1997). Existing microstructural studies based on phenomenological and discrete element methods are not sufficient to capture and understand the actual mechanics. State-of-the-art X-Ray CT technology offers wide opportunity to conduct such grain-scale studies of soils. However, almost all of the existing studies using X-Ray CT technology are on uncemented geomaterials as explained in the literature review chapter. In those studies, microstructural changes under applied stresses are captured by measuring various scalar (void ratio, particle size distribution, coordination number etc.) and directional parameters (particle long axis, contact normal, void long axis etc.) to understand the macro behaviour. In this chapter, behaviour of void fabric for cemented sand undergoing one-dimensional compression have been studied with the aid of X-Ray CT technology.

5.2 Results and Discussions

5.2.1 Microstructure under no load condition

The reconstructed images of the samples were post-processed and images of the samples were extracted from the load cell assembly. Volumetric and cross-sectional close-up views (horizontal and vertical, XZ plane only) of the samples at no load conditions are shown in Figure 5-1 and Figure 5-2.

.

Three phases of the sample i.e., sand, cement and void are visible from the images. However, due to proximity of material density of sand and cement, subtle difference in their image threshold intensity makes it difficult to identify them for separation. However, as this study is concerned about the void spaces only, that was not a matter of concern.

5.2.1.1 Void Volume Distribution

As discussed earlier, as a microstructural component, characteristics of evolution of void is of primary concern of this study. Following the similar procedure as conducted for images of uncemented sand sample, images of the voids for three cemented sand samples have been extracted from the complex greyscale image before they can be analysed. The solid (sand-cement) phase and void phase of the sample were separated. As a quick comparison, cross sections of the subvolumes (as marked in Figure 5-2) of the samples at initial condition are presented in Figure 5-3. Voids show interconnectivity which decreases with increased cement quantity and thus produces higher quantity of smaller voids. Interestingly, few unusual large voids were observed for 30% cement content. For better visualization and understanding of the void structure, 3D labelled image of the separated voids are presented in Figure 5-4. The labelled image clearly depicts the differences in the nature of connectivity of the voids and their morphology based on the degree of cementation.

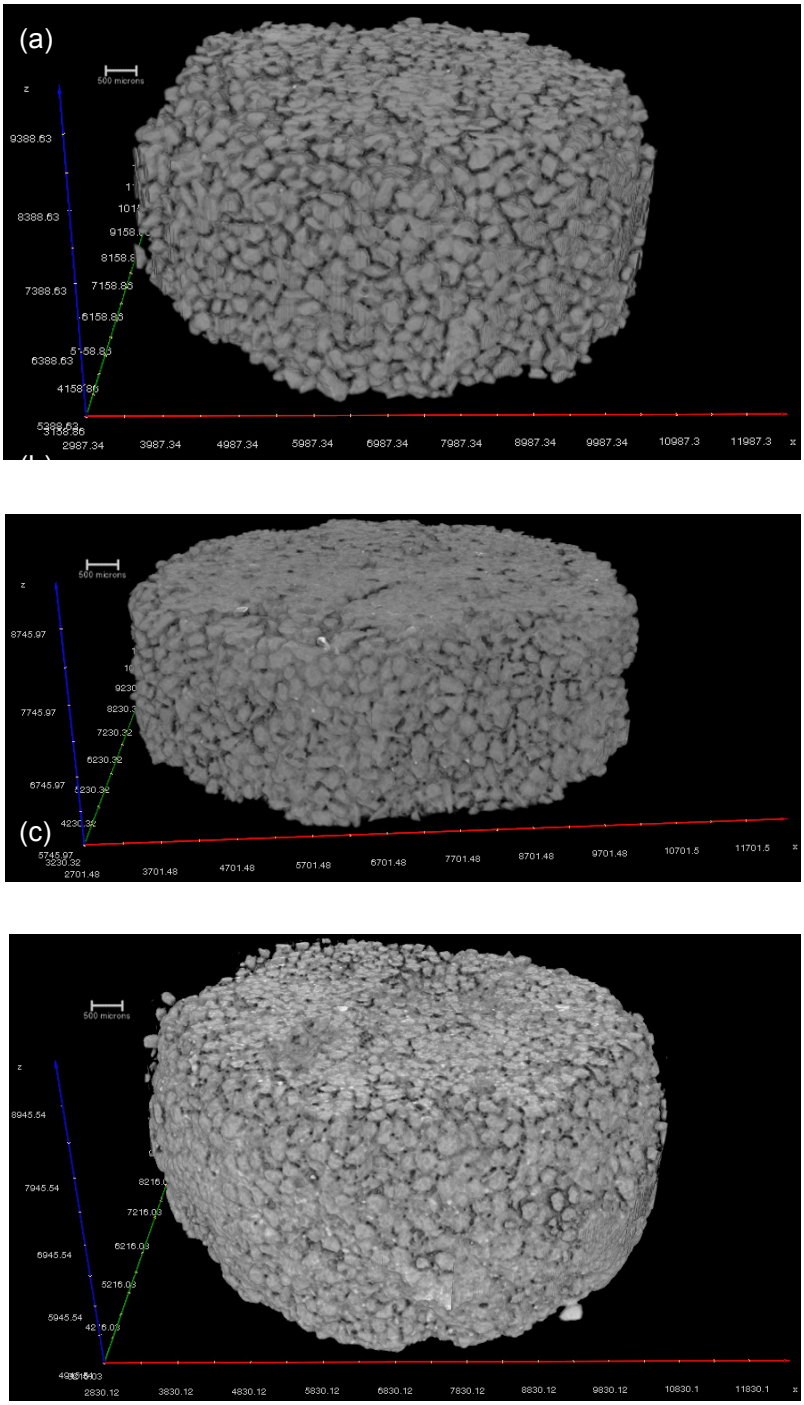

Figure 5-1: 3D Volumetric Image of samples with (a) 10, (b) 20 and (c) 30% cement content

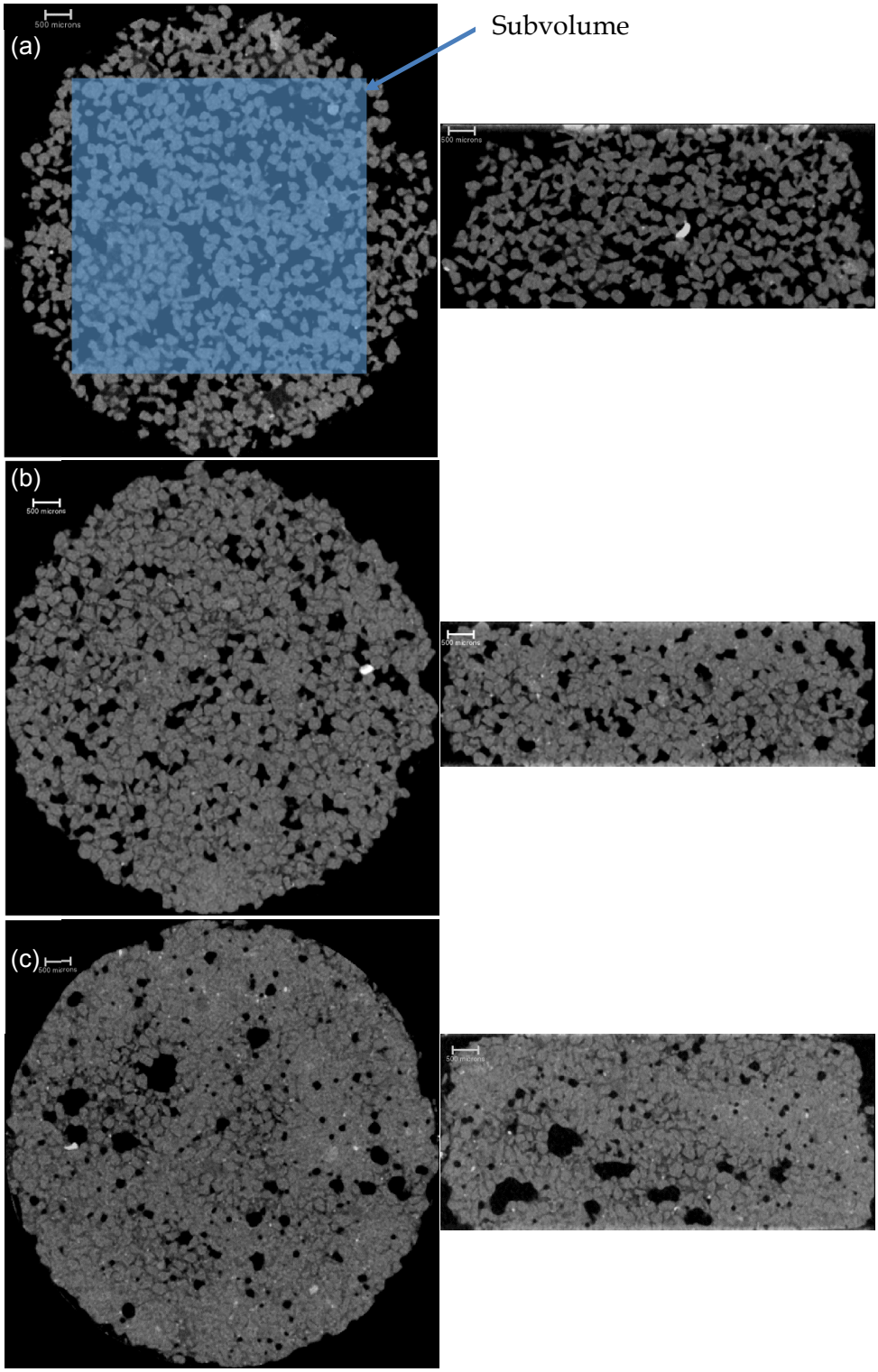

Figure 5-2: Horizontal and vertical (XZ plane only) cross sections through the centre of the samples with (a) 10, (b) 20 and (c) 30 % cement content.

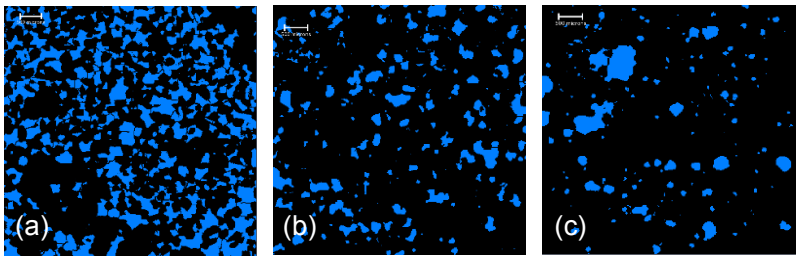

Figure 5-3: Cross section of samples (along centre of XY plane) showing void structure for (a) 10, (b) 20 and (c) 30% cemented sand samples

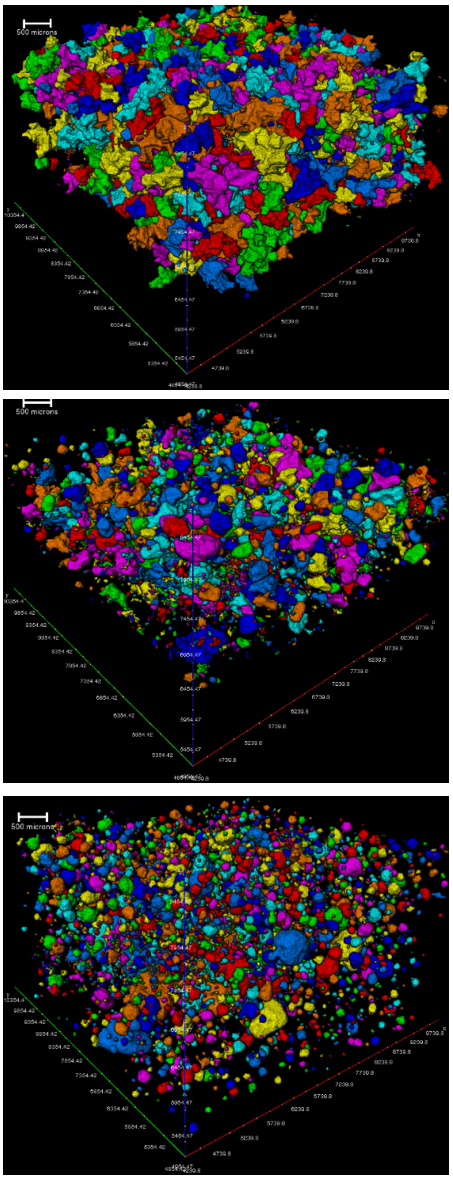

Figure 5-4: Labelled 3D image of voids for 10, 20 and 30% cemented sand respectively at initial conditions

From the frequency distribution of the void volumes as shown in Figure 5-5, it is reflected that for samples without or with low degree of cementation, void volumes are more widely distributed. With increasing cement content, voids fillup with cement and range of distribution of void volumes becomes narrower. In addition, average volume of the voids decreases with increasing cement content as shown in this figure.

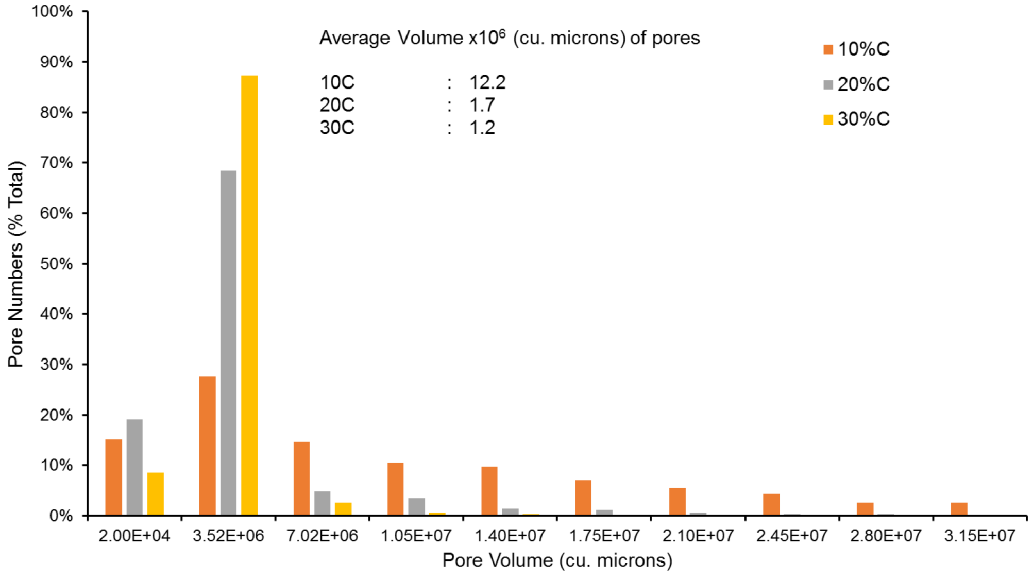

Figure 5-5: Void volume frequency distribution for all samples at initial condition

Again, 3D labelled voids in Figure 5-4 also shows that increased degree of cementation changes the morphology of the voids. Voids seem to become more regular in shape with increased cementation. As a measure of this characteristic, sphericity of the voids were computed for all cemented samples.

5.2.1.2 Sphericity Distribution

Sphericity is the measure of how closely the shape of an object approaches that of a mathematically perfect sphere. Defined by Wadell in 1935 (Wadell, 1935) the

sphericity of a particle is the ratio of the surface area of a sphere (with the same volume as the given particle) to the surface area of the particle.

$$\text{Sphericity, } \Psi = \frac{\pi^{\frac{1}{3}}(6V_p)^{\frac{2}{3}}}{A_p}$$

Where Vp is volume of the particle (or void in this case) and Ap is the surface area of the particle. The sphericity of a sphere is unity by definition and, by the isoperimetric inequality, any particle that is not a sphere will have sphericity less than 1.

Frequency distribution of sphericity values of voids for all samples are presented in Figure 5-6. The table on the figure shows the average sphericity of the voids increases significantly with increased degree of cementation which supports the earlier claim that was made based on visualization of Figure 5-4.

Distribution of sphericity of voids for 10% cemented sand shows relatively wider spread and two distinct peaks with the higher one within low sphericity range. This indicates insufficiency in cement to cause more convincing spherical distribution. With increased cement content, the dual peaks disappears and the distribution becomes increasingly narrower.

Further increase in cement (20%) caused the peaks to merge and move to the right towards higher sphericity. The spread also became narrower. This distribution was left-skewed which indicates gradual movement (started from earlier mix, 10%) of biasness towards higher sphericity.

With 30% cementation, the distribution showed the sharpest pick compared to other distributions with a convincing shift towards the higher sphericity.

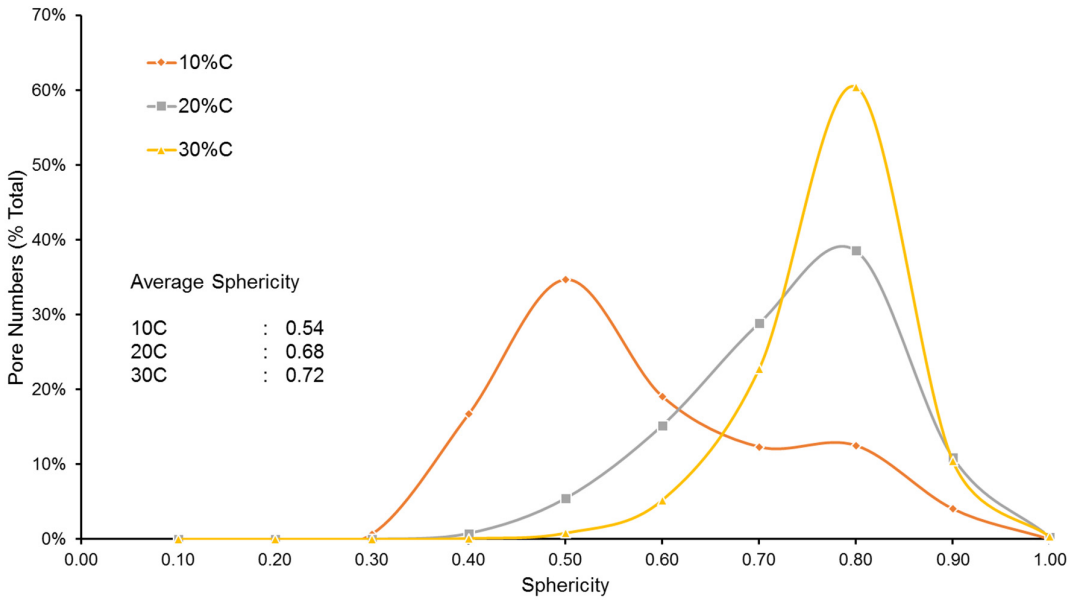

Figure 5-6: Evolution of sphericity of voids with degree of cementation

5.2.2 *Microstructure evolution under compression*

At the end of scanning all the samples at no-load condition, an initial load of 5.67 N (equivalent to 100 kPa stress) was applied on the first sample (10% cemented sand). At the end of full deformation of the sample on the application of the load, the sample was scanned. Subsequent loading and corresponding scanning were conducted as per Table 5-1. Similar procedure was repeated for the two other samples. Details on loading, scanning and image processing have been elaborated in Chapter 3. Although similar rate of loading (0.1 mm/min) was used for all the three samples but for the sample with 10% cement content, relatively smaller incremental loads were applied in anticipation of capturing early bond breakage (if any) of this relatively weaker sample. The scanned image of the sample at initial no-load condition shows only a

few sparingly present cement bonds in the sample. This was due to non-uniform mix resulting from insufficient cement quantity. In addition, as this sample looked fragile while handling, smoothening of the top and bottom surface using fine sand paper could not be done properly as can be seen in Figure 5-1 and Figure 5-2.

Table 5-1: Applied incremental Stresses (marked by dot) on all cemented samples

Sample	Initial	0.1 MPa	0.15 MPa	0.2 MPa	0.4 MPa	0.88 MPa	1.8 MPa	7.0 MPa	14.1 MPa	28.2 MPa	56.4 MPa	79.3 MPa
10C	•	•	•	•	•	•	•	•	–	–	–	–
20C	•	•	•	•	•	•	•	•	•	•	•	–
30C	•	•	–	•	•	•	•	•	•	•	•	•

As a result, few sharp peaks from those surfaces touched the loading plate initially and resulted some early minor localized collapse without almost any drop of void ratio. However, only significant collapse of bond and reduction of void ratio was observed on application of 7.0 MPa load. Interestingly, careful observations of the scanned images at the end of this load showed no traces of any cement bond indicating, at least visually, complete collapse of all the bonds. At this stage, the particles were observed in direct contact with each other. Reduction of void ratio on further application of stresses may misrepresent collapse of bond whereas they may be actually due to crushing of sand particles. As such, no further loading was applied on this sample. However, in contrast, for sample with 20% and 30% cement contents, existence of cement were visible even at higher stresses. Evolution of overall fabric for all three samples with increasing stresses are presented in Figure 5-9, Figure 5-10 and Figure 5-11 for 10, 20 and 30% cemented sand, respectively.

5.2.2.1 Void ratio vs. Logarithm of vertical stress (e-logσ'_v) Plot

From image analysis, the void ratio of the samples for each load cases were calculated and their variations with the logarithm of vertical stress (*e*-logσ'_v plot) are presented in Figure 5-7.

The *e*-logσ'_v plots in Figure 5-7 shows almost no change in void ratio up to 1.8 MPa, 7 MPa and 14.1 MPa for 10, 20 and 30% cemented sand samples respectively. Their initial void ratio was around 0.6, 0.17 and 0.14 respectively. However, some irregularity in behaviour showing increase in void ratio during initial loading stages is due to micro adjustments that the samples had to make with increased loading until they came into full contact with the cylinder wall.

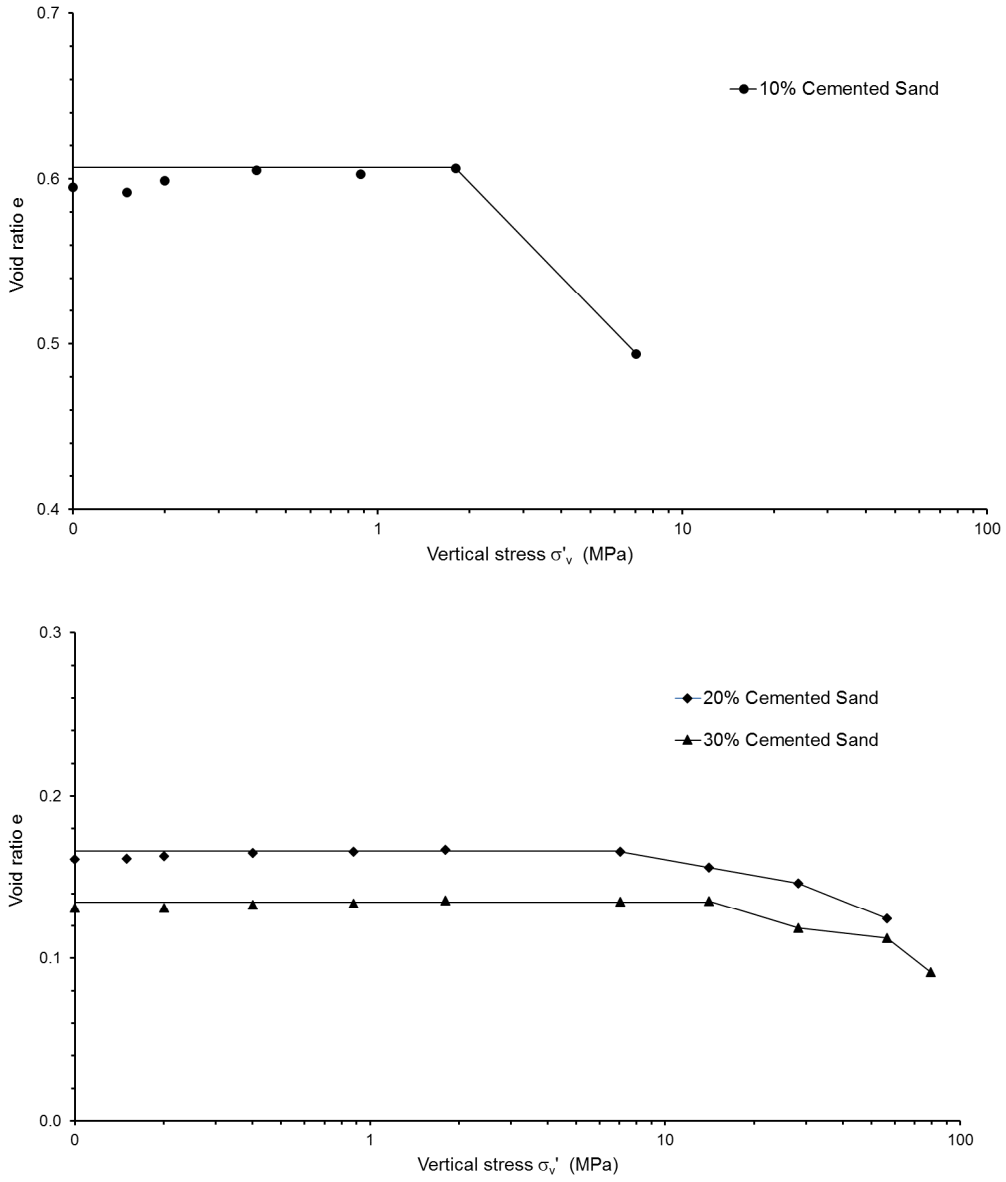

Figure 5-7: *e*-logσ'_v plot for cemented sand (a) 10 (b) 20 and 30% cemented sample

For 10% cemented sand, application of 7 MPa load caused significant deformation which is reflected by almost of 18.6% drop of void ratio at the rate of 3.5% per 1 MPa as shown in Figure 5-8. As explained earlier, at the end of this deformation, total collapse of all bonds was assumed as no more traces of cements were visible from observing the greyscale image. Moreover, the value of initial void ratio for this

cemented sample is almost similar to that of uncemented sand sample (0.61 vs. 0.60) and this is also an indication of insignificance of quantity of cementing material in this sample. As a result, no further load was applied for this sample. Figure 5-9 illustrates the change of overall fabric for this sample upon application of incremental stresses.

For the next sample with 20% cemented sand, first noticeable or measureable deformation was observed at 14.1 MPa which is double the stress that was able to cause deformation of the earlier sample with 10% cementation. However, even doubling the stress could cause only about 5.9% drop in void ratio compared to 18.6% drop of the earlier sample as can be observed from Figure 5-8. Rate of decrease of void ratio dropped significantly from 3.5% to 0.8% per 1 MPa of stress. This can be attributed to the increased stiffness of sample due to higher degree of cementation. The rate of decrease of void ratio plunged to 0.5% with the stress being doubled to 28.2 MPa, although decrease in void ratio remained nearly the same as earlier, 6.0%. However, on further doubling the stress, decrease in void ratio (%) doubled causing total drop of void ratio by 25.1% with slightly higher rate of change, 0.5% per 1 MPa of stress.

For the final sample of 30% cemented sand, no change of void ratio was observed until 28.2 MPa where void ratio dropped by 12.5% at the rate of 0.9% per 1 MPa of stress which is close to the rate of first void ratio change for 20% cemented sand. However, the rate for 30% cemented sand dropped significantly to 0.2% with total decrease of void ratio to 16.9% for 56.4 MPa stress. This increased stiffness of the sample due to

higher cement content perhaps jointly resulted from higher bond strength and additional cushioning phenomenon. However, the largest drop in void ratio for this sample was observed at 79.3 MPa stress. The drop of overall void ratio doubled to 32.4% for only nearly 40% increase of stress. Moreover, the rate of decrease of void ratio jumped to 0.7% from earlier 0.2% as well. At this final stress, significant bond breakage followed by collapse of few large voids as observed in Figure 5-11 have resulted such elevated values.

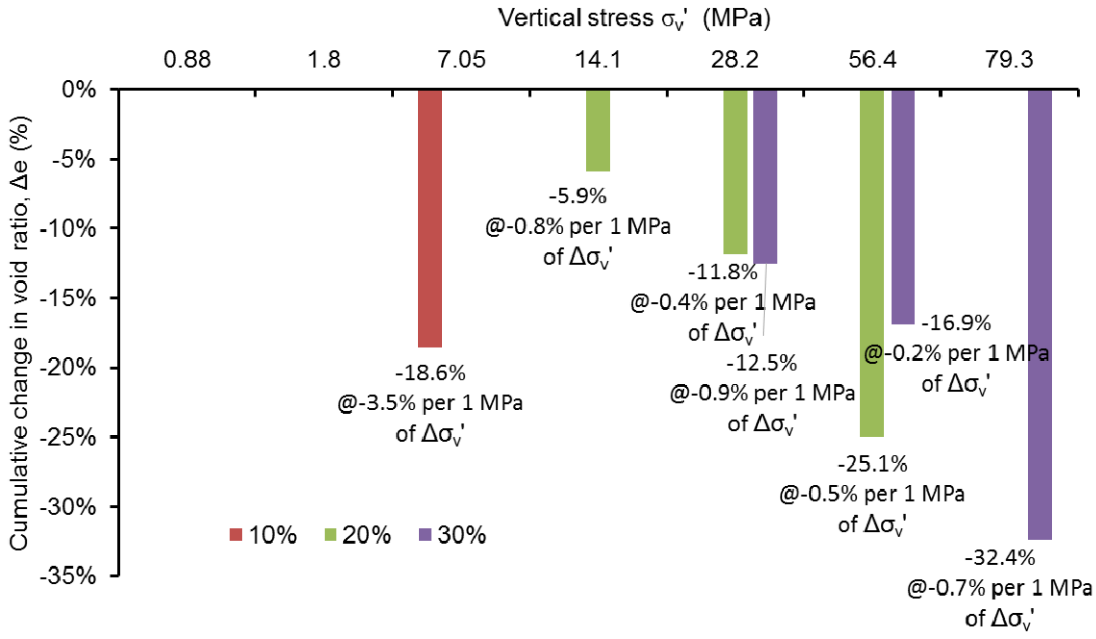

Figure 5-8: Cumulative change (%) of void ratio with loads and rate of change of void ratio (%) for incremental loads.

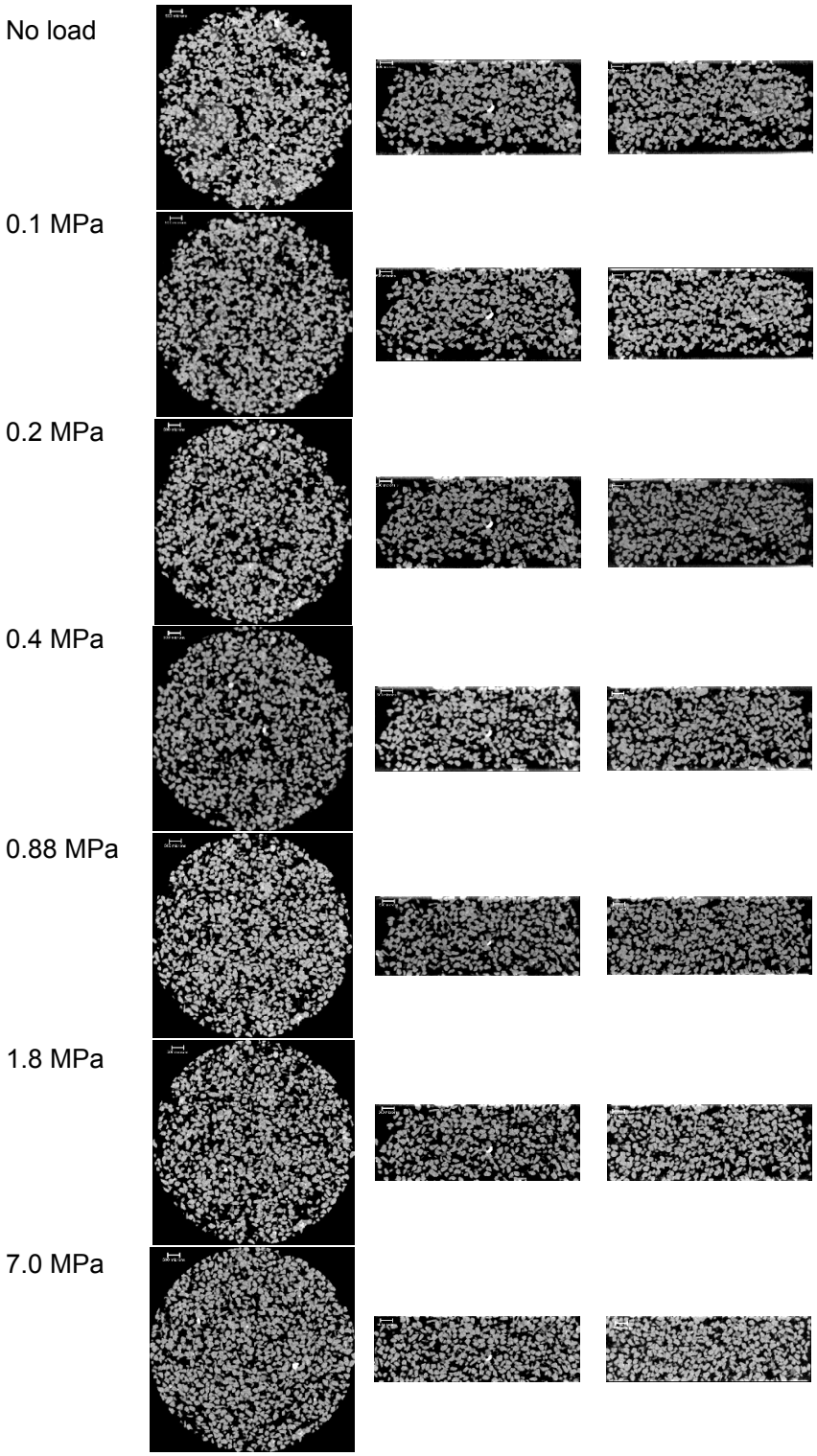

Figure 5-9: Evolution of fabric in central XY, XZ and YZ slices for cemented (10%) sand under loadings.

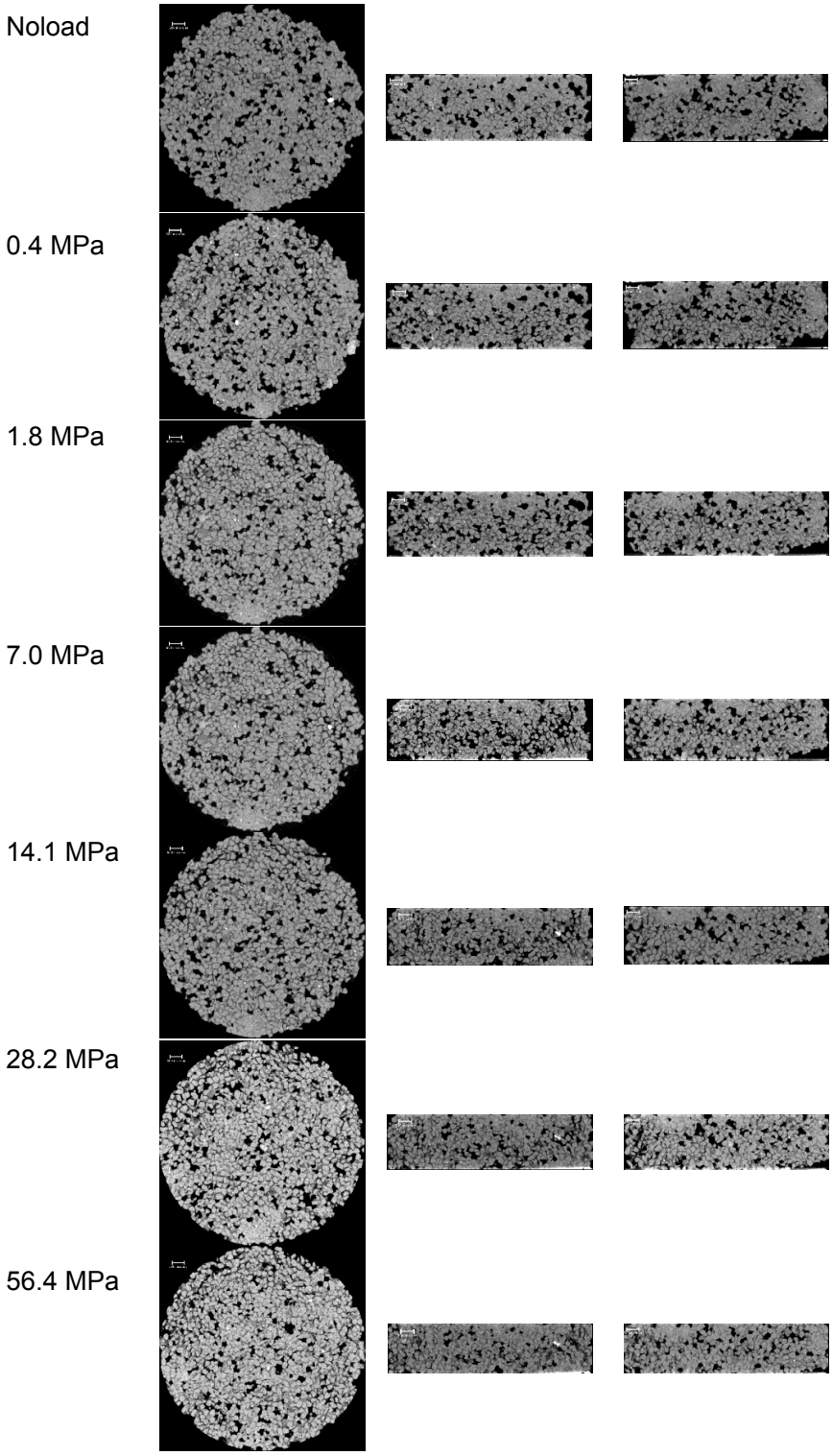

Figure 5-10: Evolution of fabric in central XY, XZ and YZ slices cemented (20%) sand under loadings.

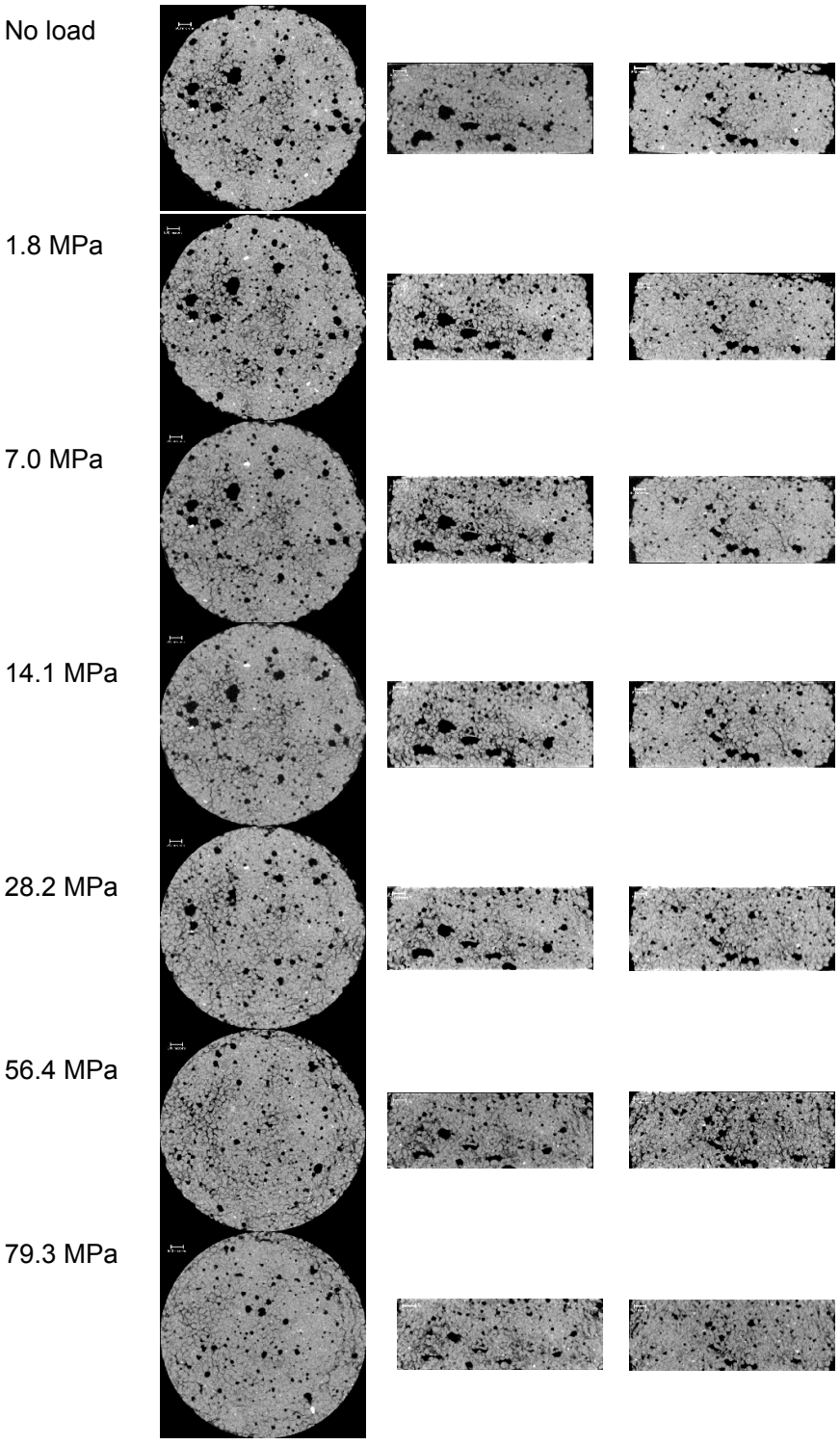

Figure 5-11: Evolution of fabric in central XY, XZ and YZ slices for cemented (30%) sand under loadings.

5.2.2.2 Evolution of Void Fabric with incremental stresses

Load-induced evolution of voids will be analysed to explain macroscale behaviour of the cemented sand. As explained earlier, for the initial no load condition, the voids of the sample in image were separated from the solid (sand and cement) and then the connected voids were segmented using the watershed segmentation method. Similar procedure was followed at the end of each applied stress for all three samples of cemented sand. In Figure 5-12, Figure 5-15, and Figure 5-18 evolution of voids in their binary images are represented with the increasing stresses.

However, visualization of neither 2D sections nor even 3D planar view is sufficient to recognise the true mechanics happening inside. Quantification of relevant parameters and their evolution with load is necessary for this purpose. Required parameters have been divided into two distinct classes: Scalar and directional. In the next two sections, void volume, sphericity and anisotropy will be discussed for each of the cemented samples.

Analysis of Scalar Parameters: void volume and sphericity

From e-logσ'_v plot for 10% cemented sand in Figure 5-7, only stress causing the effective change of void ratio was 7 MPa. It appears from the 2D sections in Figure 5-12 that with applied stress some smaller voids disappears and few larger voids breaks into smaller ones. In general, as expected, size of the voids decreased. Computed void volume distribution for initial, and final stress is presented in Figure 5-13(a). The

upward shift of the distribution curve indicates generation of smaller size voids upon collapse of bonds.

To further understand the nature of void evolution, frequency of different size ranges of voids were computed for no stress and 7 MPa and presented in Figure 5-13(b). As expected disappearance of smallest voids is indicated by decrease of frequency in the first group of voids, followed by an increase of frequency for the next couple of ranges. These new voids are result of collapse or suppression of larger size voids which is reflected by the decrease of larger voids in the later part of the graph.

Decrease in sphericity by almost 17% due to collapse or squizzing of voids is reflected by leftward shifting of the solid lines in Figure 5-13(c). The dotted line on the plot suggests that smaller voids are more spherical than their larger counterpart and upon application of stress sphericity of the larger voids drops more rapidly than smaller ones.

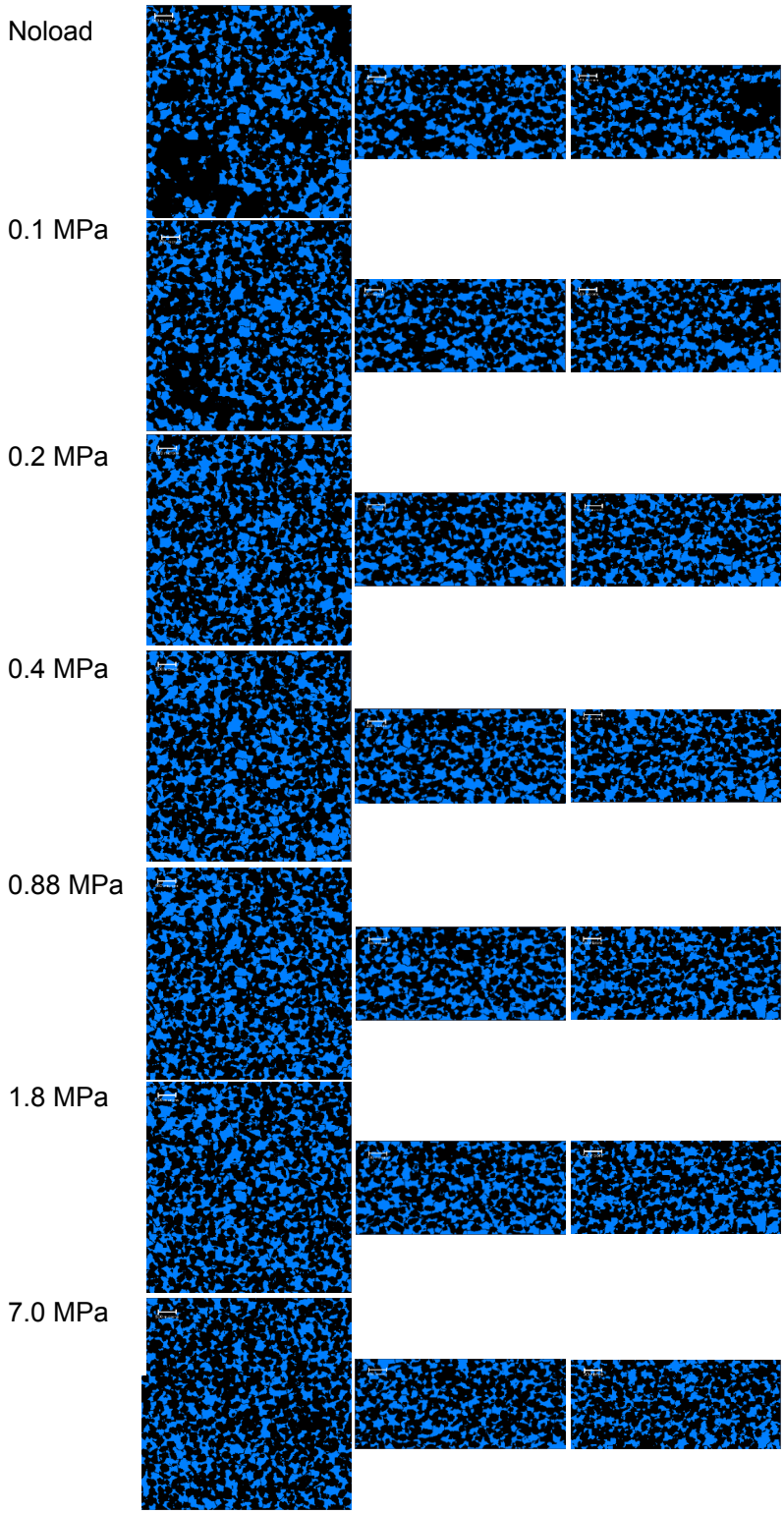

Figure 5-12: Evolution of void fabric in central XY, XZ and YZ slices of subvolume for cemented (10%) sand under loadings.

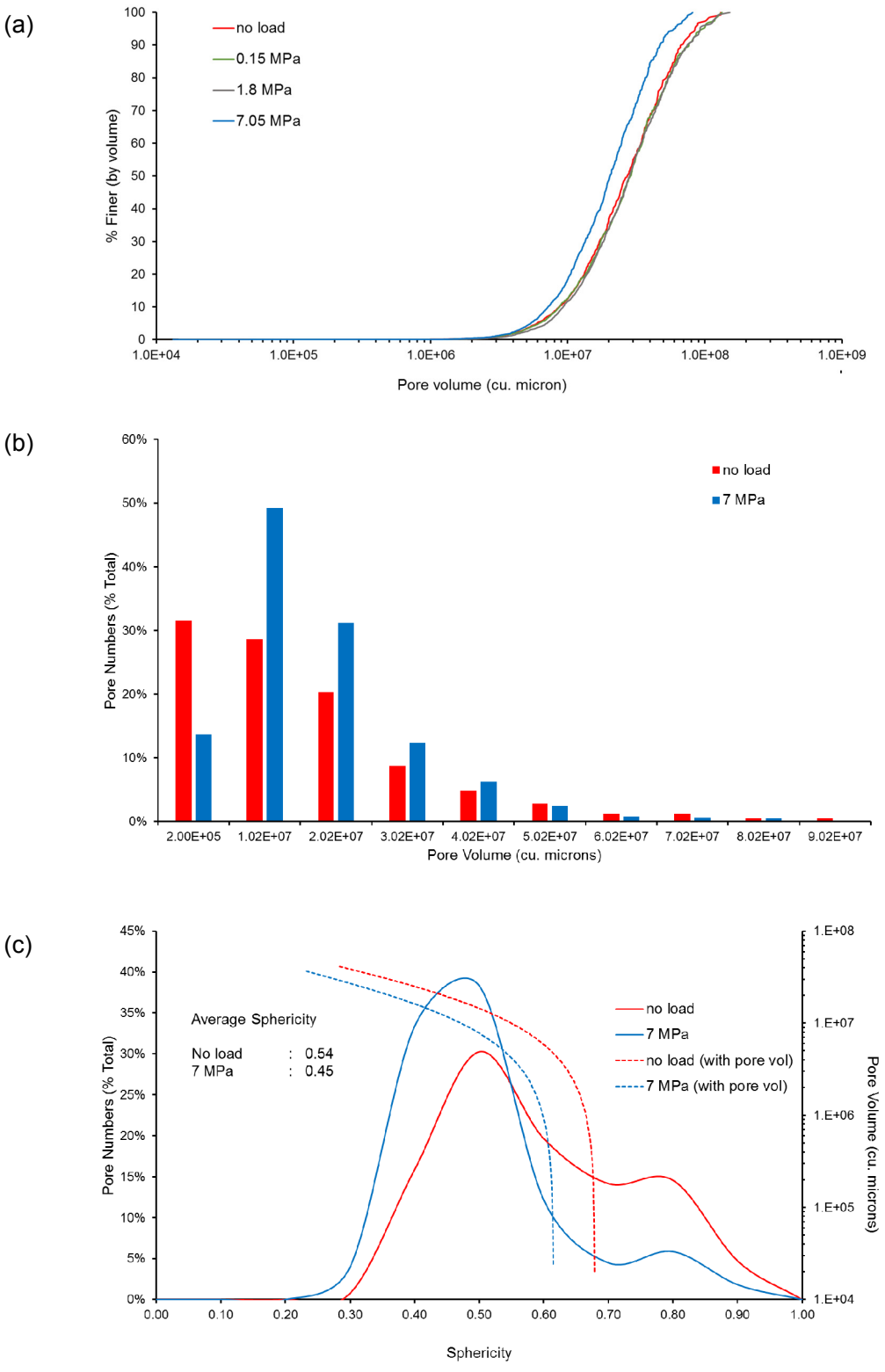

Figure 5-13: Evolution of voids on application of load for 10% cemented sand (a) void volume distribution (b) void volume frequency distribution (c) sphericity distribution with frequency and volume of voids.

From e-logσ'_v plot for 20% cemented sand sample in Figure 5-7, the first stress causing the effective change of void ratio was 14.1 MPa. However, a very little change in void size distribution was observed under this stress. Increased stiffness of this sample due to double cement content restricted the deformation. By further doubling the stress, visible upward shift of the void size distribution could be attained as shown in Figure 5-16(a), which indicates formation of smaller size voids. From Figure 5-15, formation of new larger voids by connecting 2 or more smaller voids at higher stress followed by their splitting in further higher stress due to void collapse was an interesting phenomenon that was observed in this sample.

Distribution of number of voids over their volume for all three samples as shown in in Figure 5-14 shows presence of significantly higher number of smaller voids with increased cement content. Unlike earlier sample, frequency distribution of the void sizes for this sample shows increase rather than decrease of the smallest size voids as presented in Figure 5-16(b).

Distribution of sphericity in Figure 5-16(c) indicates relatively higher stiffness of the sample and smaller void volumes resulted in marginal drop of sphericity with again accelerated drop in larger voids than smaller voids.

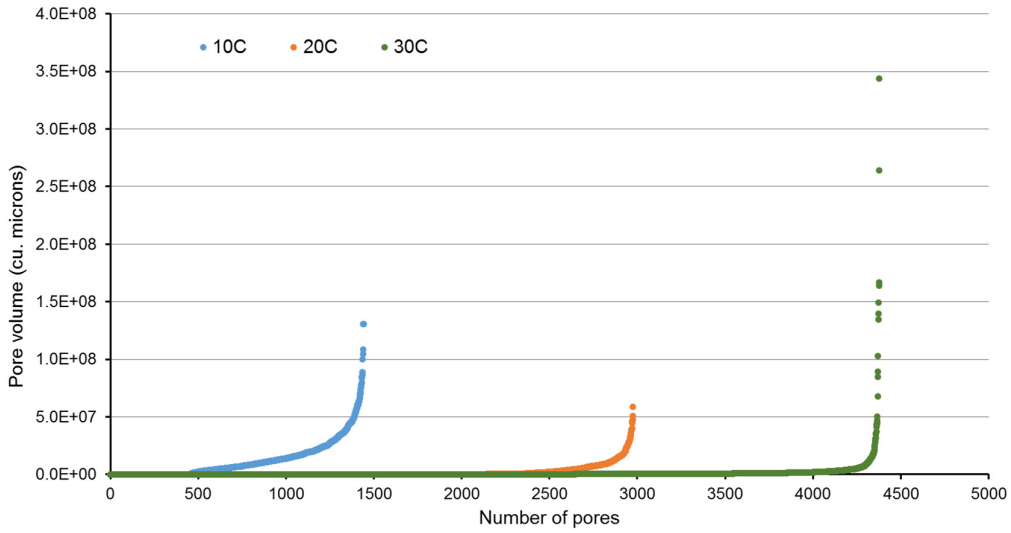

Figure 5-14: Number of voids over volume range for all cemented samples

Highest stiffness as expected was observed in the sample with 30% cemented sand with first drop in void ratio at stress 28.2 MPa. Images in Figure 5-17 show presence of few unusually large voids along with very large number of small voids. With elevated stresses, generation of larger voids from accumulation of smaller ones followed by their degeneration with further increase of stress was observed as before. However, once the bond started breaking, the rapid upward shift of the void size distribution in Figure 5-18(a) indicates relatively low stiffness of the sample compared to that with 20% cement content. This may be attributed to collapse of few unusually large voids present in this sample. From Figure 5-18(b), gradual rise in frequency of smaller voids and subsequent fall for larger voids up to 56.4 MPa was reverted at 79.3 MPa. Similar trend was observed for sphericity in Figure 5-18(c) which drops significantly at the initiating stress then continued decreasing slowly until 56.4 MPa, then it reversed at 79.3 MPa showing increase of sphericity.

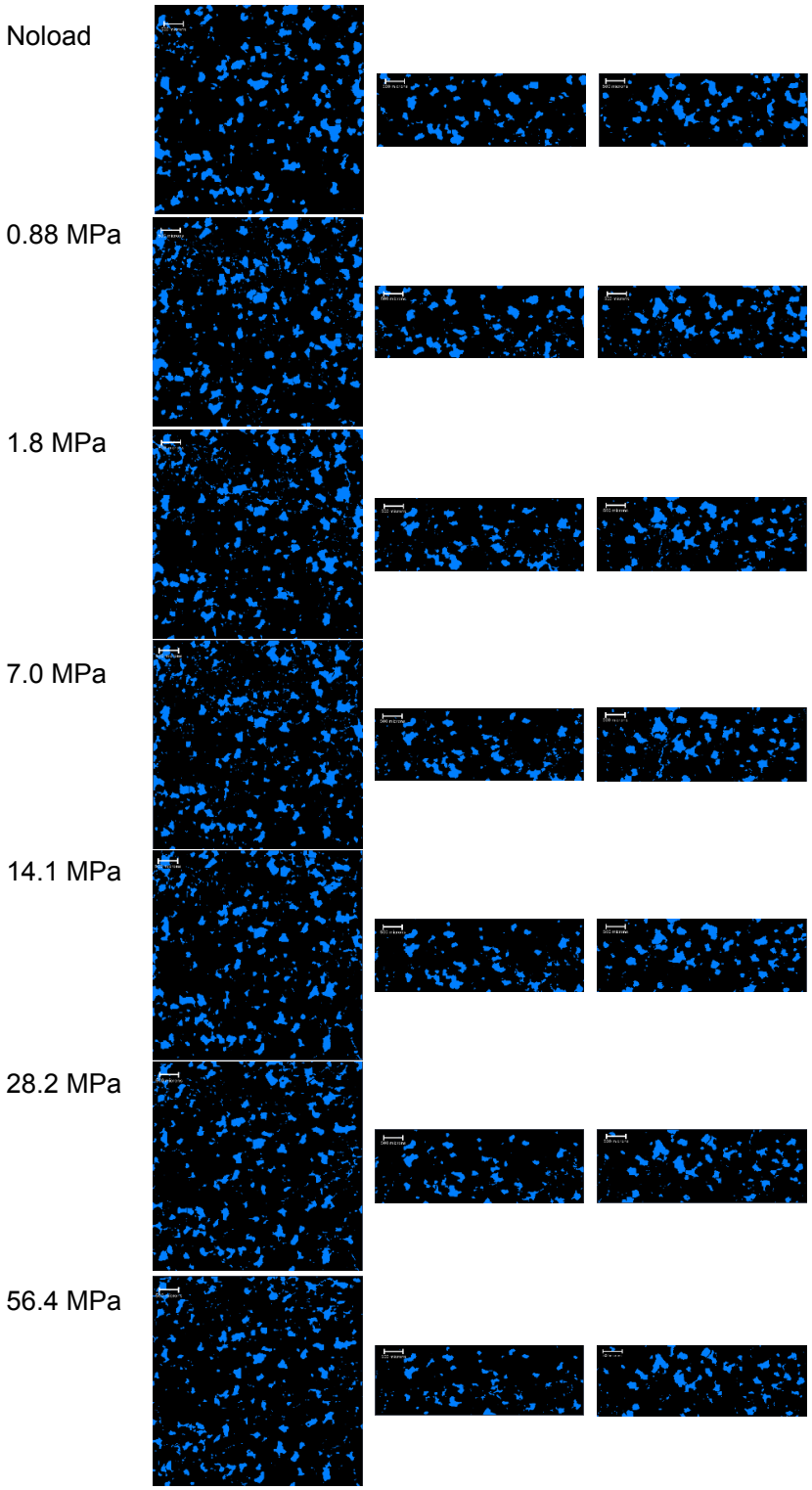

Figure 5-15: Evolution of void fabric in XY, XZ and YZ planes for cemented (20%) sand under loadings.

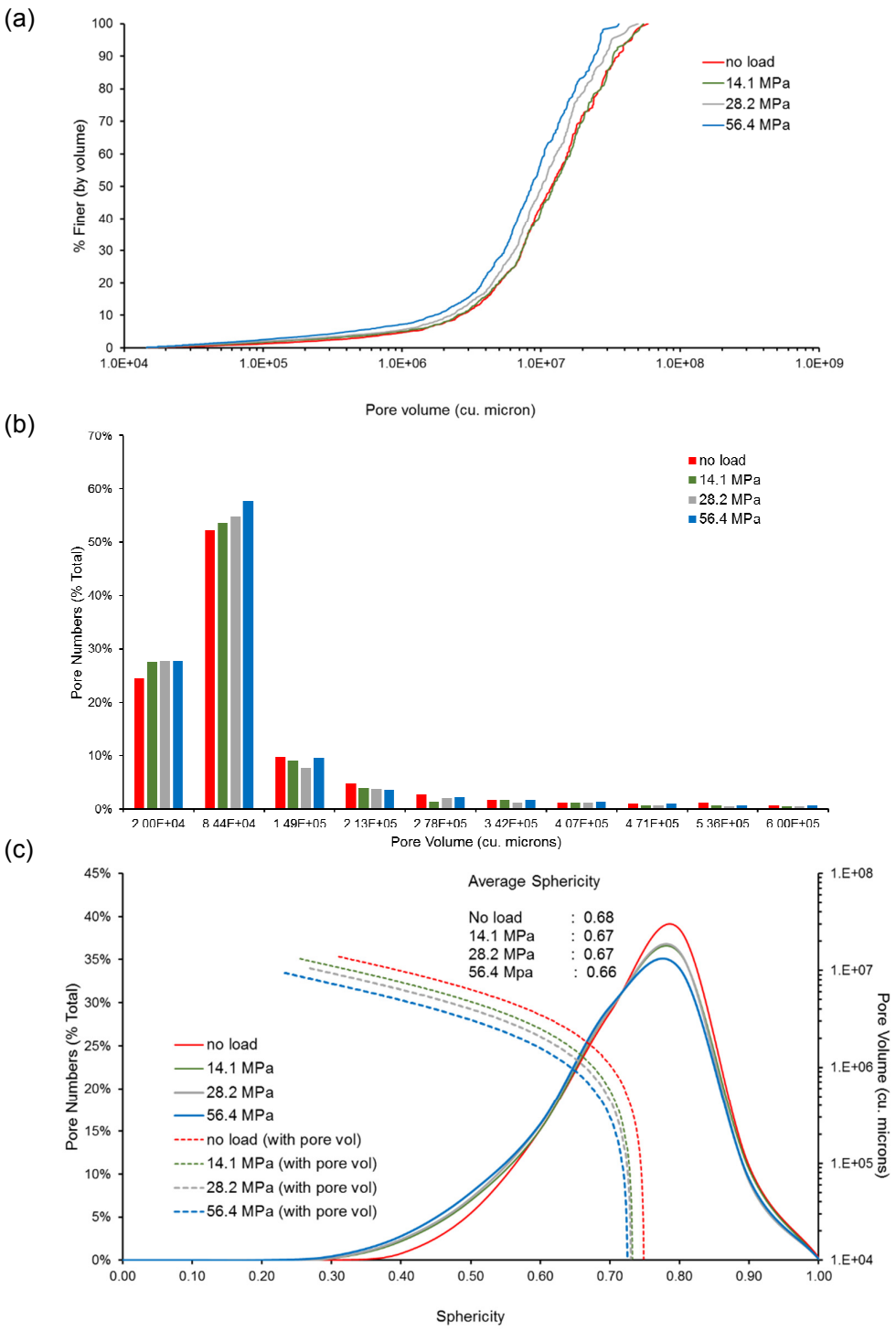

Figure 5-16: Evolution of voids on application of load for 20% cemented sand (a) void volume distribution (b) void volume frequency distribution (c) sphericity distribution with frequency and volume of voids.

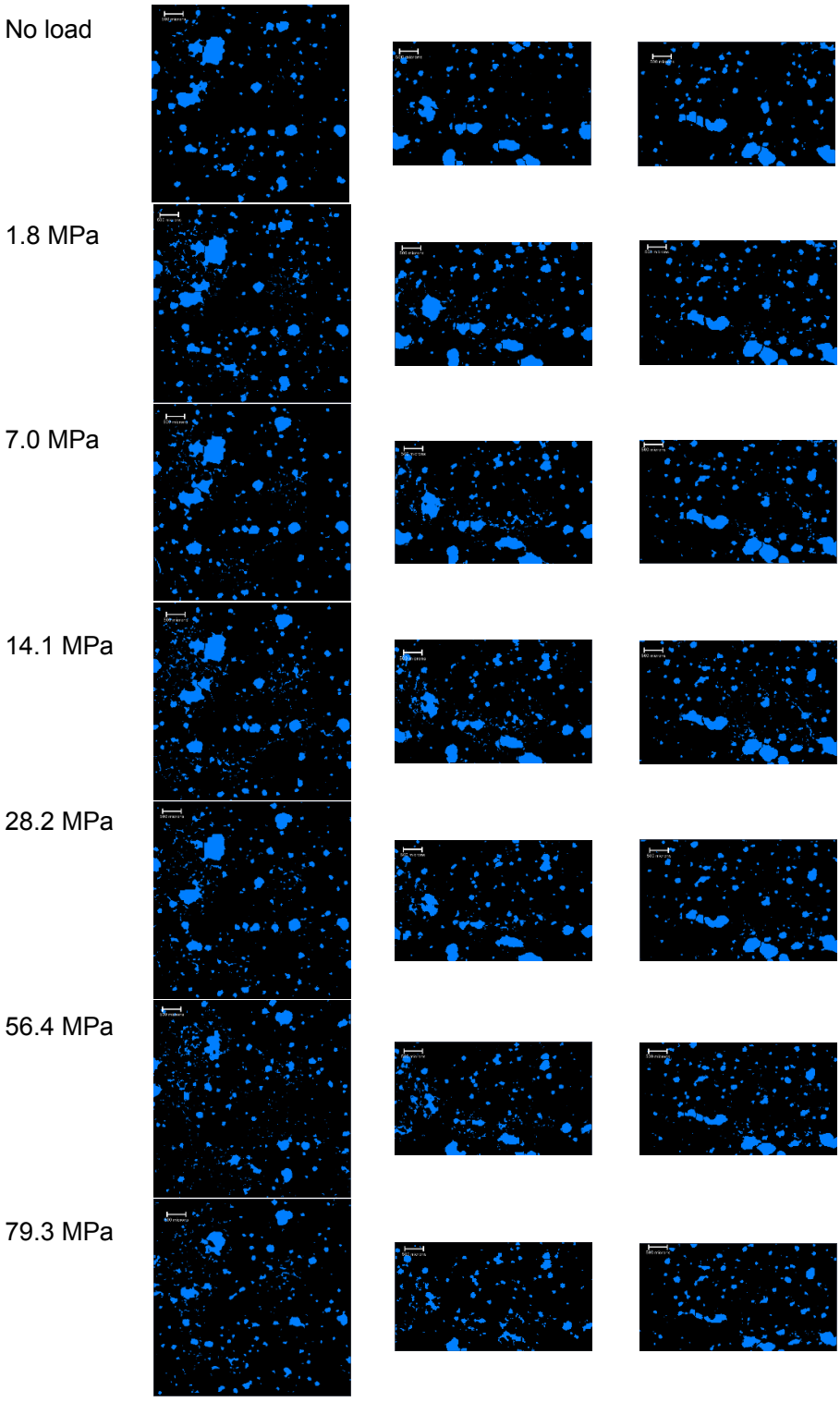

Figure 5-17: Evolution of void fabric in XY, XZ and YZ planes for cemented (30%) sand under loadings.

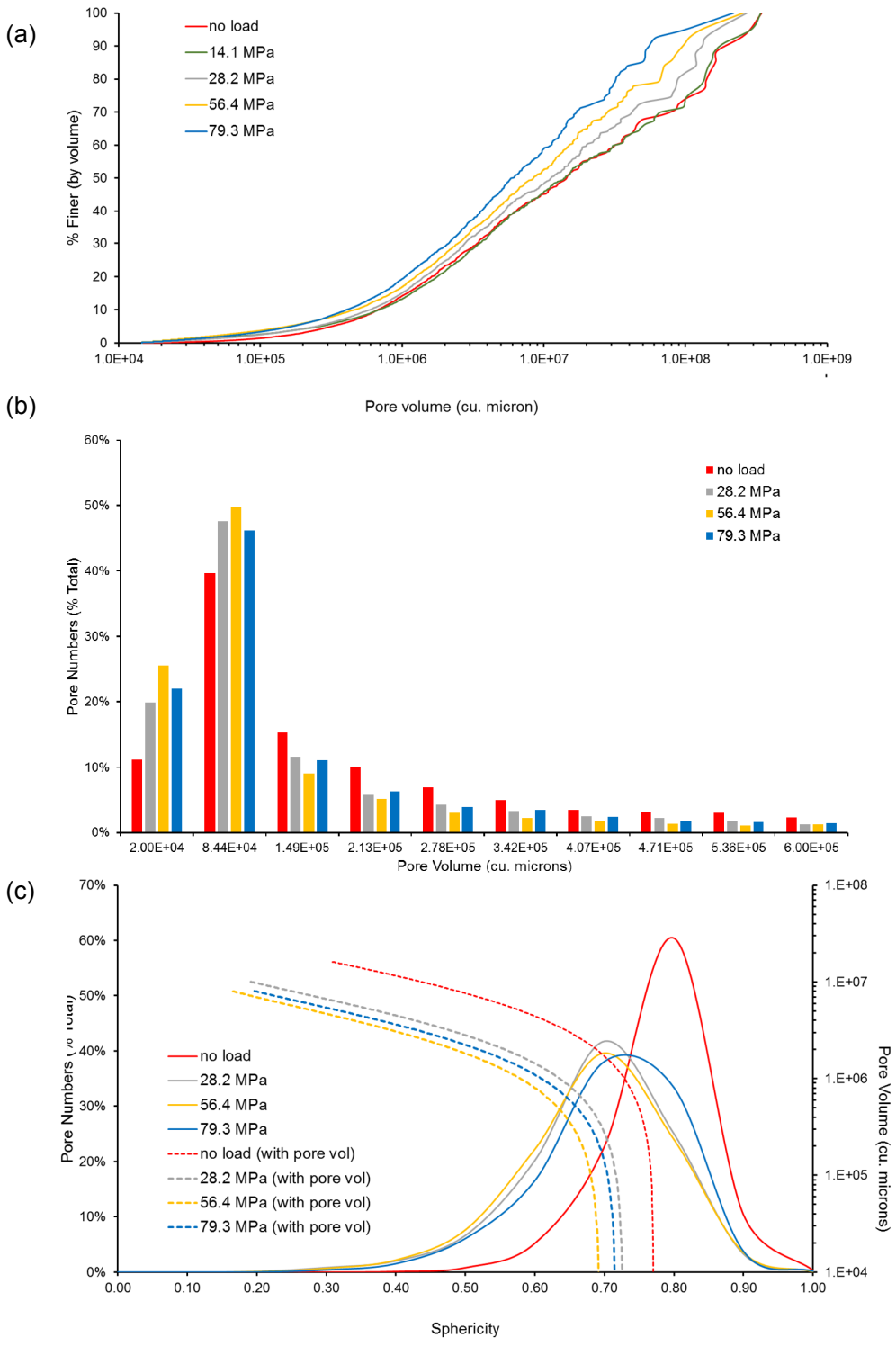

Figure 5-18: Evolution of voids on application of load for 30% cemented sand (a) void volume distribution (b) void volume frequency distribution (c) sphericity distribution with frequency and volume of voids.

Analysis of Scalar Parameters: anisotropy

Anisotropy as described for all voids of three different cemented sand samples at different stress conditions including initial no stress condition were determined from the labelled images and their distributions are plotted in Figure 5-19. For 10% cemented sand it is clear that at initial condition more than 85% voids had anisotropy values of 0.6 or above. With increased cement content, the anisotropy goes down. For 20% cemented sand, anisotropy value 0.6 or above drops to 75% whereas for 30% cemented sand the drop is far higher, 40%. The average values of anisotropy of these samples respectively are 0.77, 0.73 and 0.63. The more is the cement content, the more is its accumulation at particle contact, and interparticle void throats and thus more regular the shape of the voids become.

Average values of anisotropy for different size ranges of voids are presented in Figure 5-20 (a), (b) and (c) for all three cemented samples. Insignificant variation (Standard Deviation, SD=0.02) among different size ranges at initial state for 10% cemented sample, compared to higher variation (SD=0.09 and 0.10) for other two samples is another indication of insignificant cementation for this sample.

However, with progressive stresses, anisotropy shows somewhat mixed behaviour for different sample or even in the same sample under different stresses. For 10% cemented sample, Figure 5-19(a) shows anisotropy distribution shifts leftward indicating decreasing value, which is also reflected in the slight decrease in average value of anisotropy. Average values of anisotropy for different size ranges of voids

are shown in Figure 5-20(a). Average anisotropy for almost all size groups, show decrease by 4-7%.

Unlike 10% cemented sand, anisotropy distribution of voids for 20 and 30% cemented sand up to 56.4 MPa as shown in Figure 5-19 (b) and Figure 5-19 (c) respectively, show rightward movement indicating overall increase in anisotropy. Average values of anisotropy as shown on the above figures reflects similar behaviour. Average anisotropy based on different size ranges as shown in Figure 5-20(b) and Figure 5-20(c) for 20 and 30% cemented sand, show increased values by different percentage up to 37%. Larger voids, compared to smaller ones show significant increase which indicates larger voids experienced higher deformation.

For 30% cemented sand up to 56.4 MPa stress level as shown in Figure 5-20(c), shows significant increase 11%, 26% and 29% for the first three size ranges where again most of the void (as high as 86% at 56.4 MPa) exist (Figure 5-18(b)). However, with further increase of stress to 79.3 MPa, anisotropy decreases as reflected by leftward movement of the distribution (Figure 5-19(c)). Average anisotropy of voids of different size ranges (Figure 5-20(c)) show decreased anisotropy within 1-3% and that was mostly within smaller size range of voids.

Interestingly, at 79.3 MPa which is the highest stress for any cemented sample, the distribution of anisotropy shifts towards lowers anisotropy (Figure 5-19(c)). This reduction of anisotropy of voids may be hypothesized as resulting from surface

smoothness of the particles or sand-cement composite from grinding action under extreme pressure.

Evolution of these complex phenomena of the voids are further investigated by analysing their directional parameters in the next section.

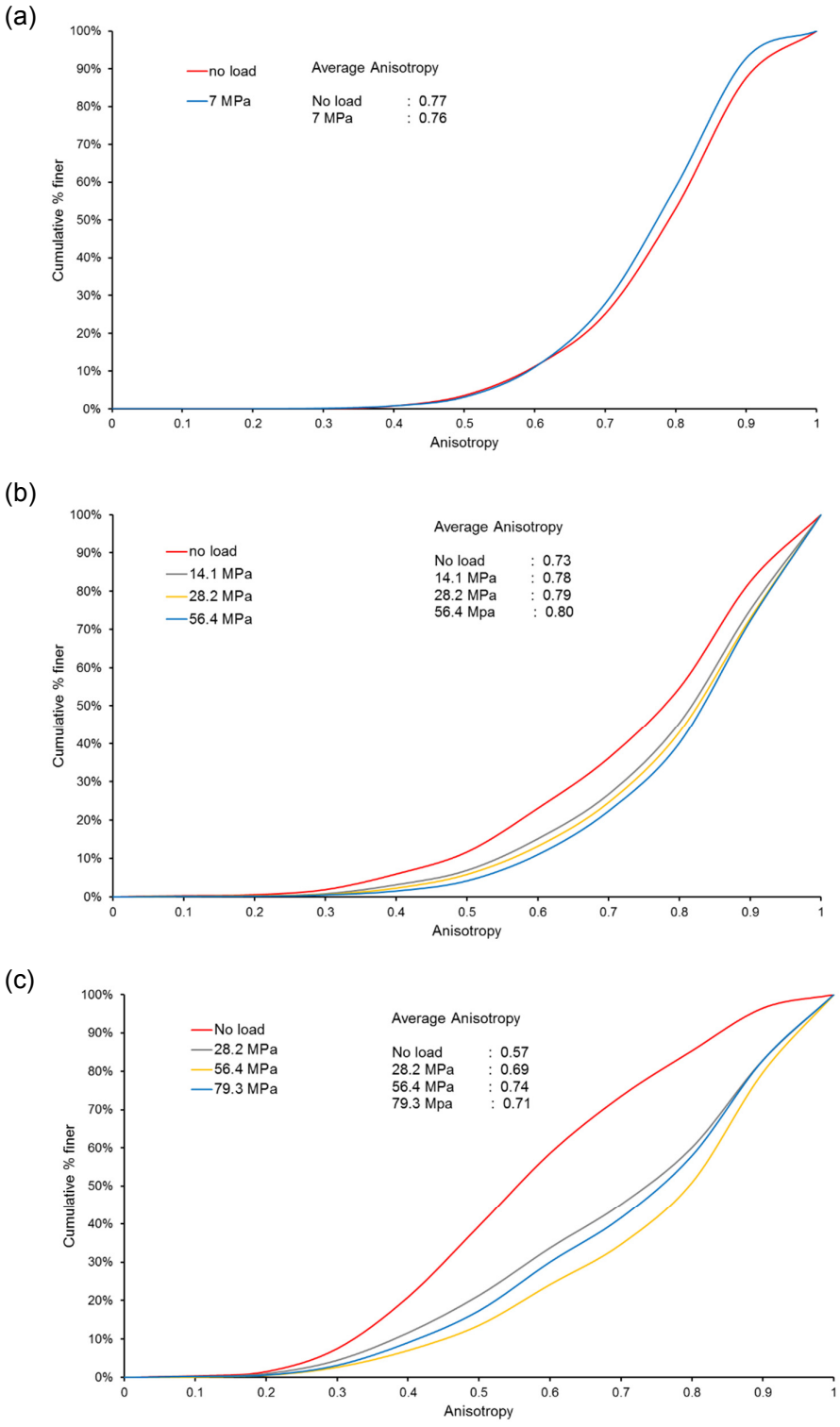

Figure 5-19: Evolution of anisotropy distributions of void particles for (a) 10 (b) 20 and (c) 30% cemented sand samples with progressive vertical stresses

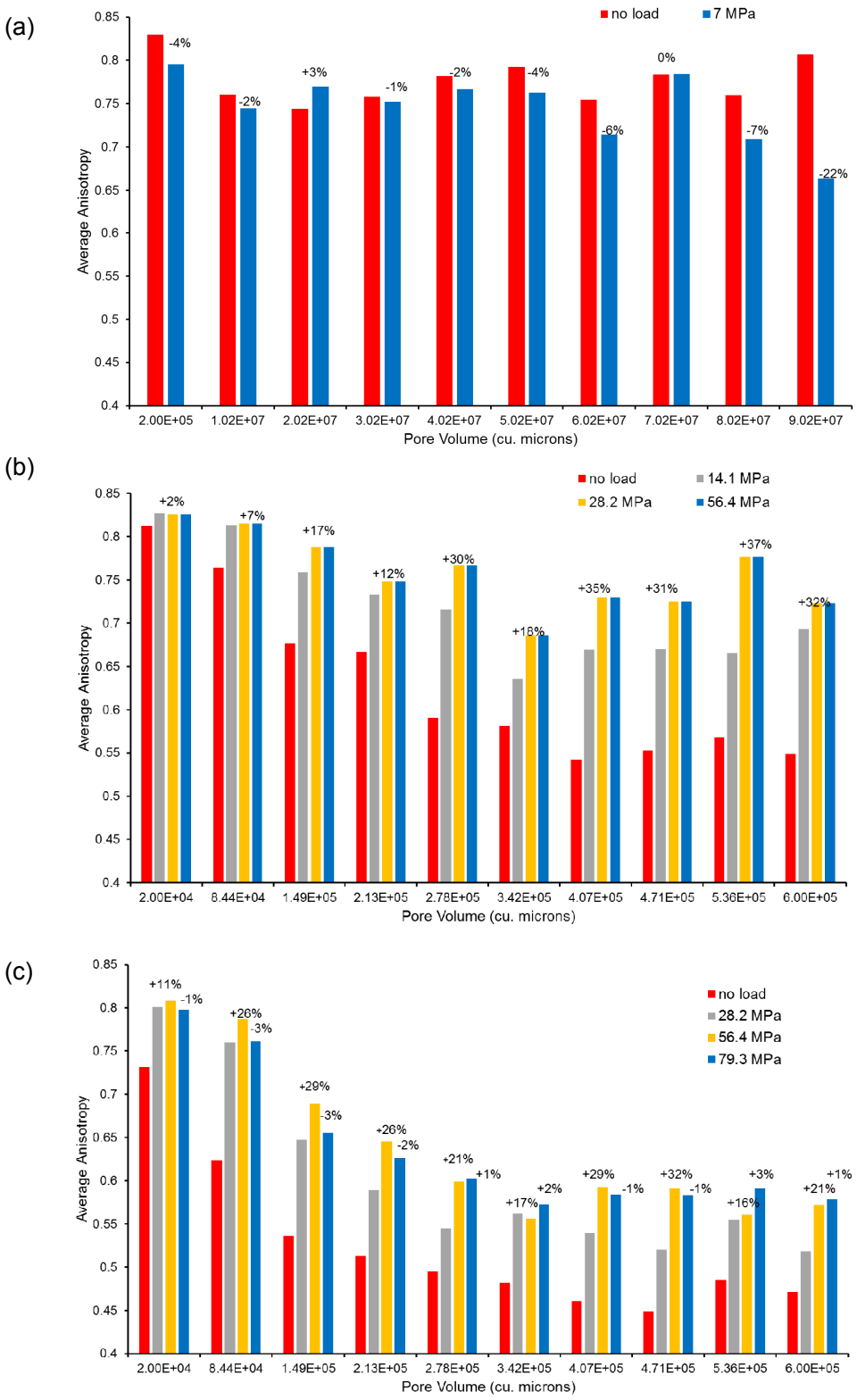

Figure 5-20: Average anisotropy values of void particles of different size ranges of particles for (a) 10 (b) 20 and (c) 30% cemented sand samples with stresses

Analysis of Directional Parameter: Void long axis

Considering lack of sufficient data points that may contribute to understanding of the evolution of directional fabric, 10% cemented sand has not been considered any further. Only 20 and 30% cemented sand has been analysed and described henceforth.

Distribution of 3D fabric tensors are represented by surfaces plots (Figure 5-21 and Figure 5-24) whose shape in a specific direction gives an immediate indication of the preference of the voids' long-axis. Whereas, 2D representation (Figure 5-22 and Figure 5-25, red for 4th order and blue is the 2nd order of second kind) indicates the preference of the void fabric on a planar view. In addition, 2D rose diagram was plotted in Figure 5-22 and Figure 5-25. Moreover, $FAV\ A$ values with incremental stresses have been plotted as well (Figure 5-23 and Figure 5-26).

The initial 3D fabric tensors for all samples show transversely isotropic distributions (i.e., rotational symmetry along the vertical loading axis). For 20% cemented sand, $FAV\ A$ (3D) value of 0.82 indicates strong biasness of fabric distribution perpendicular to the loading direction which is also reflected by the surface presentation. However, with increased cement content of 30%, the 3D fabric tensor almost became spherical indicating absence of directional bias as observed from near zero value of $FAV\ A$ (3D). A possible explanation of the no directional fabric for the high cement content (30%) sample is formation of more uniform-shaped voids due to accumulation of excess cement at the particle contacts and inter-particle void throats. Interestingly, the 2D

tensors and rose diagrams at initial state for the samples sufficiently represented the bias of fabric orientations as observed in the 3D distributions.

Under progressive loading, for 20% cemented sand, $FAVA$ (3D) value is observed to increase marginally which indicates stronger horizontal preference of void fabric. However, despite having rotational symmetry of fabric at initial state with $FAVA$ (3D) of 0.82, fabric distributions with progressive loading show orthotropic distributions. These distributions were also captured by the 2D fabric tensors and $FAVA$ (2D) values. The rotation of preferred fabric directions on the XY and YZ planes for 20% cemented sand are particularly interesting. This notion can be explained with the closure and subdivided nature of 3D void volumes with loading and their rotational shift of long-axis. On the other hand, the 3D void tensors for 30% cemented sand which started with an initial no-directional fabric ($FAVA$ (3D)=0.07) state to a transverse isotropy at 14.1 MPa followed by repetitive and complex fabric distributions of orthotropic and transversely isotropic types with increased loading up to 79.3 MPa. Similar to previous cases, 2D fabric tensors and rose plots for all planes are capable of sufficiently describing the observed 3D fabric distributions (Figure 2c) of 30% cemented sand with progressive loading.

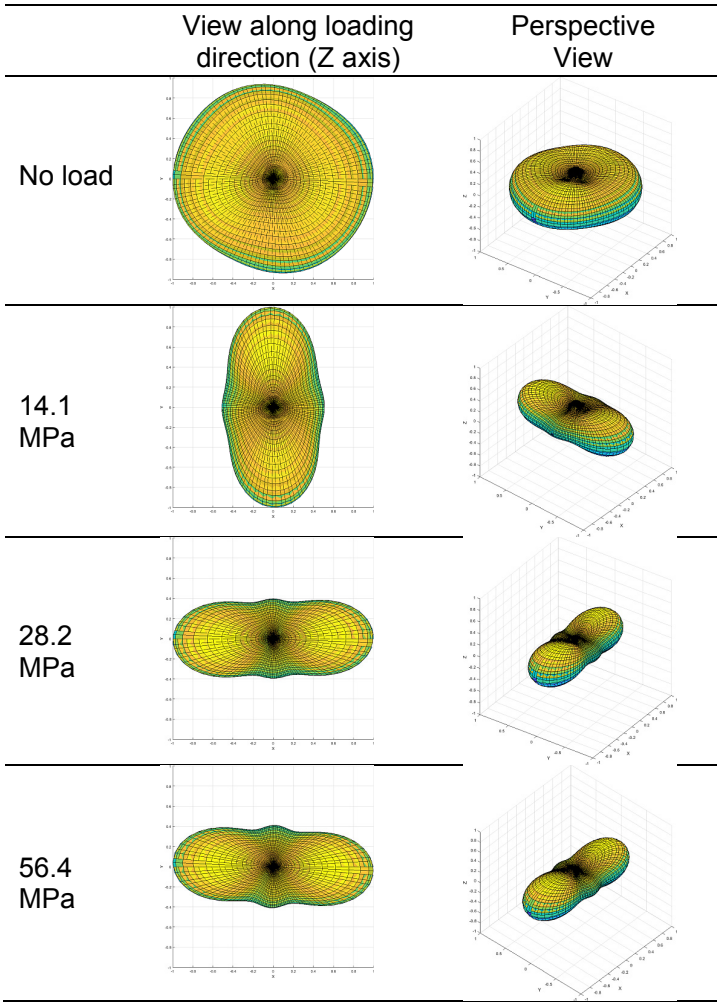

Figure 5-21: Surface plot representing distribution of 3D void fabric tensor of 20% cemented sand

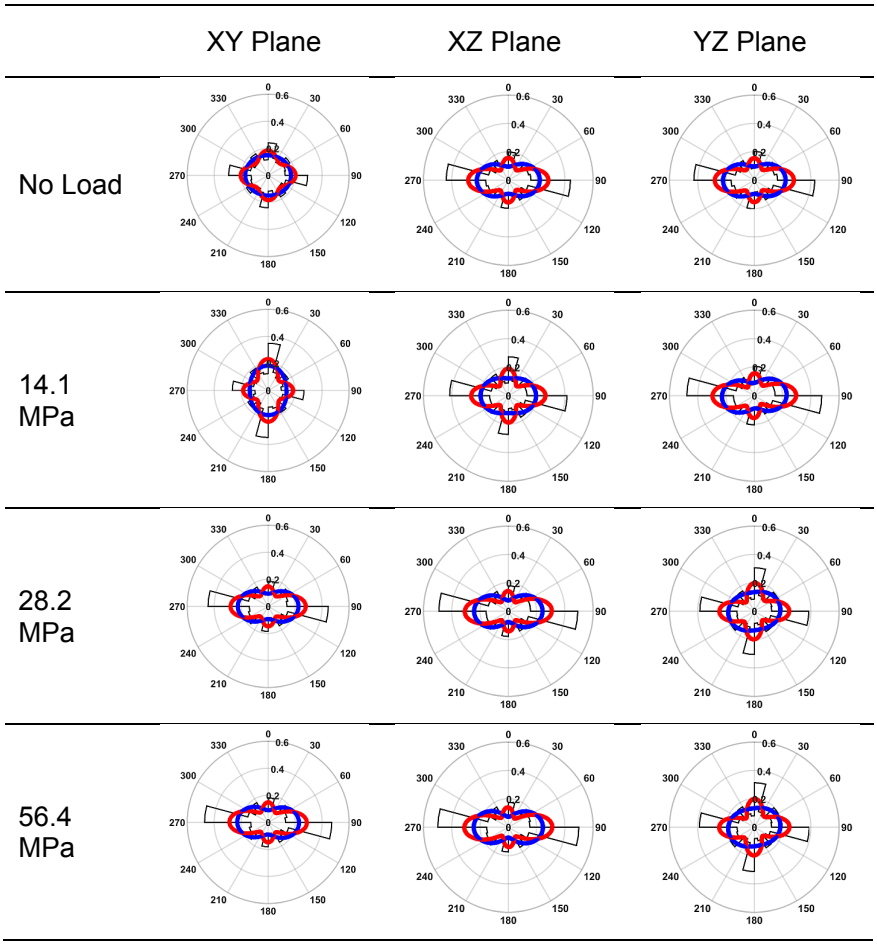

Figure 5-22: Rose diagram, and 2nd (blue) and 4th order (red) density distribution curve for the voids of 20% cemented sand

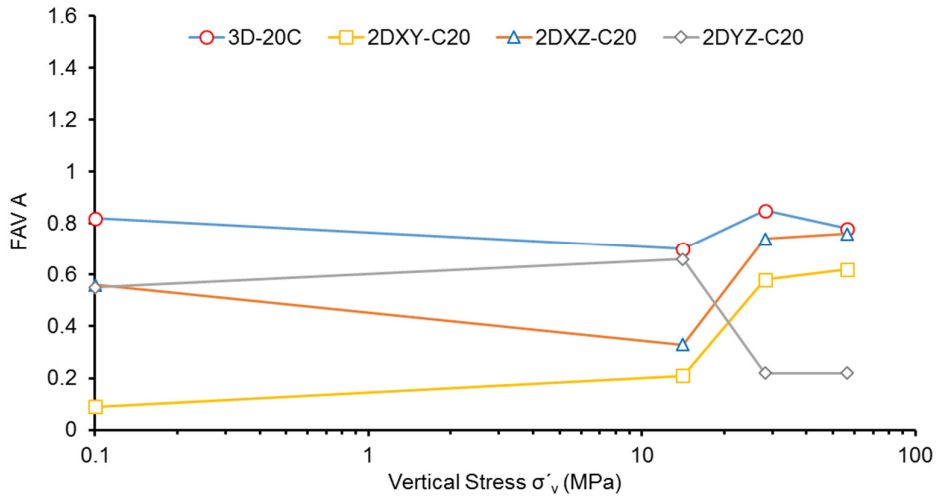

Figure 5-23: *FAV A* vs. Vertical Stress for 20% cemented sand

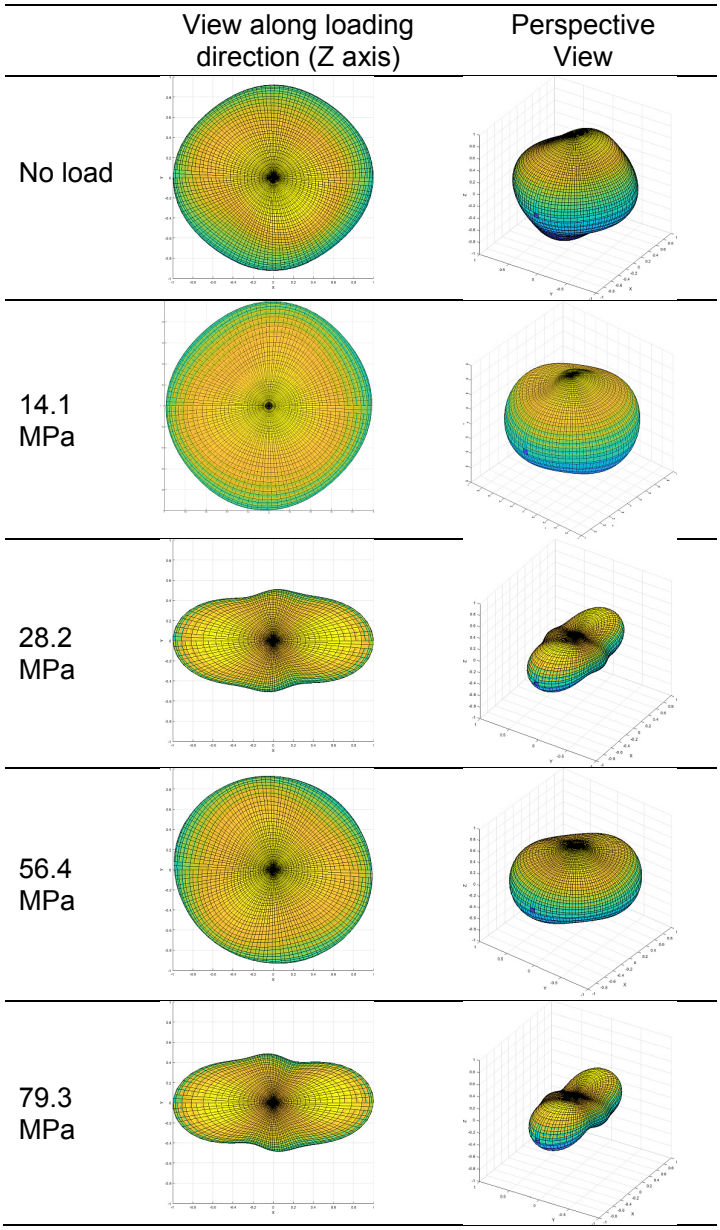

Figure 5-24: Surface plot representing distribution of 3D void fabric tensor of 30% cemented sand

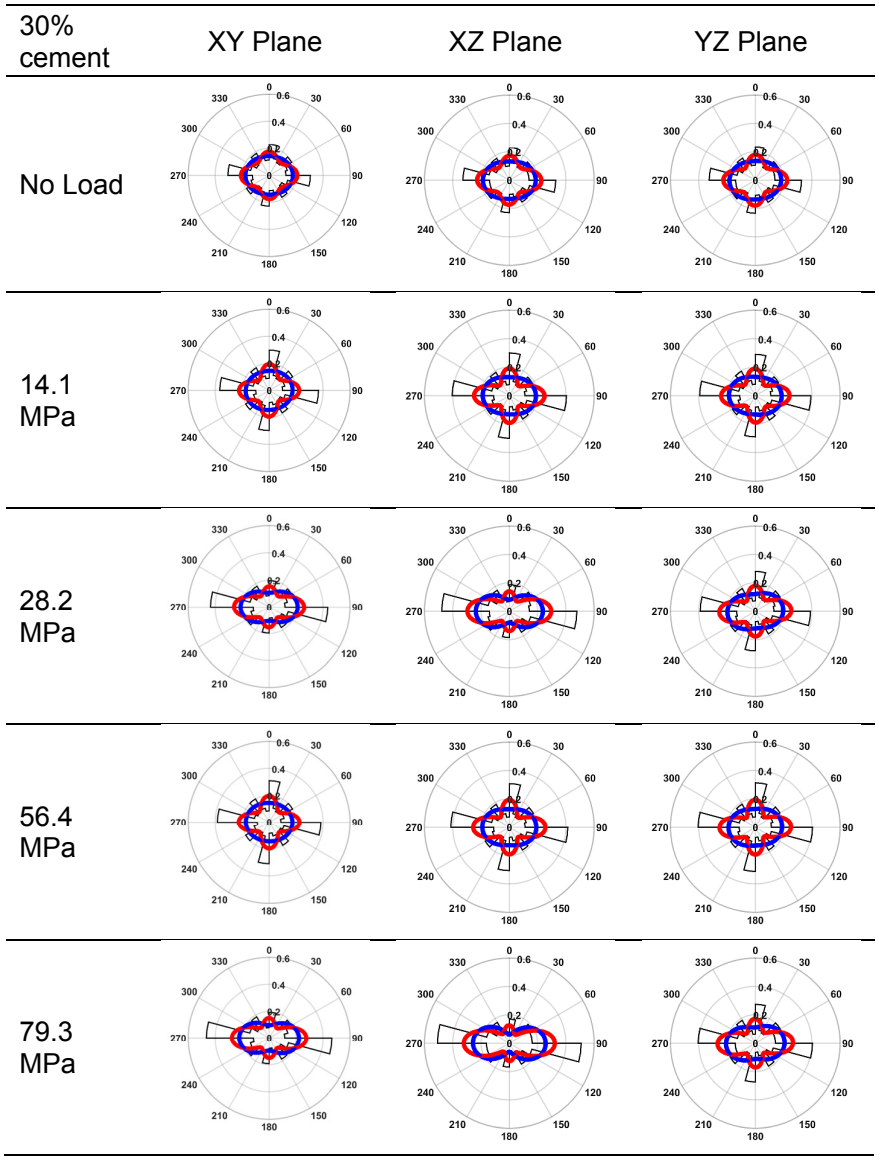

Figure 5-25: Rose diagram, and 2nd order and 4th order density distribution curve for the voids of 30% cemented sand

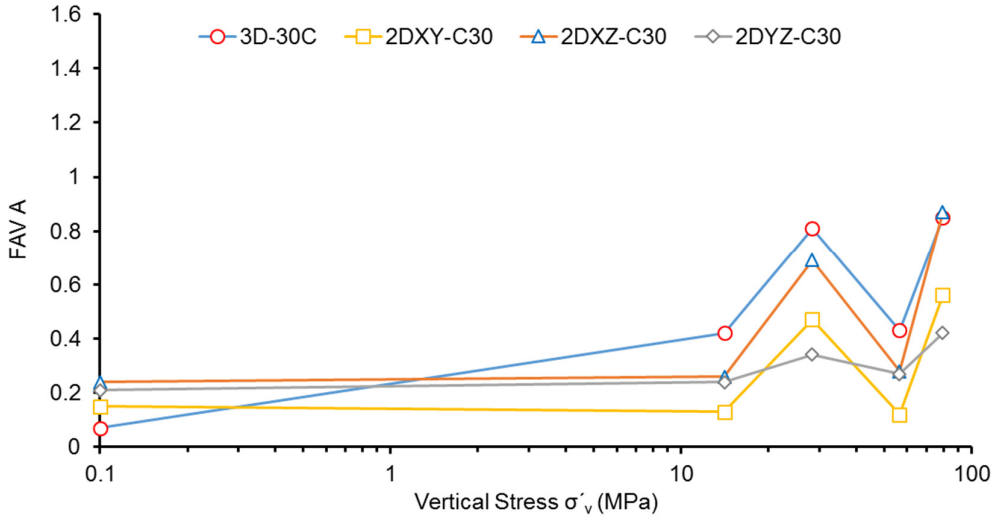

Figure 5-26: *FAV A* vs. Vertical Stress for 30% cemented sand

5.3 Summary

Evolution of the void fabric for cemented sand undergoing one-dimensional compression was investigated with the aid of *insitu* X-ray CT imaging technique. Three samples, prepared by mixing of 10, 20 and 30% cement content with quartz sand (median size 230 μm) were tested. Various scalar parameters (e.g. sphericity, void volume, anisotropy) and directional parameters (e.g. void long-axis) have been investigated in relation to their evolution with incremental stresses. The findings of this study on cemented sand are summarized below:

- Cementation results in generation of disconnected voids, which increases with the increase of cement content. Accumulation of cement at particle contacts and interparticle void throats are the possible reason of such void structure. Moreover, with increased cement quantity, interparticle voids fill up with cement and causes the voids to become increasingly dispersed. In addition, due to this obvious reason, average volume of the voids significantly decreases with the increased cement contents.

- Increased quantity of cement causes the morphology of voids change from irregular to more regular shapes. This is exhibited by the gradual shift of distribution of sphericity curve towards higher values. For 10% cemented sand, relatively wider spread in distribution with dual peaks was observed. Dual peaks indicate non-homogeneous mix of sand and cement or insufficiency of cement in the mix. With increased cement content, the dual peaks disappears and the distribution becomes increasingly narrower.
- With increased cement content, average anisotropy of voids, significantly decreases. However, with incremental stresses, insignificant change in anisotropy was observed. Larger voids, compared to smaller ones show much higher increase in anisotropy values.
- The initial 3D fabric tensors for all samples show transversely isotropic distributions (i.e., rotational symmetry along the vertical loading axis). For 20% cemented sand, strong biasness of fabric distribution perpendicular to the loading was observed whereas for 30% cemented sand, any directional biasness was absent.
- Under progressive loading, directional biasness for 20% cemented sand intensified. However, orthotropic distributions with rotational shift in orthogonal directions were observed. This notion can be hypothesized with the closure and subdivision of voids resulting rotational shift of long-axis. For 30% cemented sand, a relatively complex fabric distributions comprising alternating transversely isotropic and orthotropic types were observed. Interestingly, the 2D tensors and rose diagrams sufficiently represented the

fabric orientations as observed in the 3D distributions. Fabric anisotropy variable ($FAV\ A$) were consistent with the graphical representation of the anisotropy.

5.4 References

Abdulla, A. A. & Kiousis, P. D. 1997. Behavior of cemented sands—II. Modelling. *International Journal for Numerical and Analytical Methods in Geomechanics,* **21,** 549-568.

Airey, D. 1993. Triaxial testing of naturally cemented carbonate soil. *Journal of Geotechnical Engineering,* **119,** 1379-1398.

Al-Raoush, R. 2007. Microstructure characterization of granular materials. *Physica A: Statistical mechanics and its Applications,* **377,** 545-558.

Al Mahbub, A. & Haque, A. 2016. X-ray computed tomography imaging of the microstructure of sand particles subjected to high pressure one-dimensional compression. *Materials,* **9,** 890.

Alam, M., Haque, A. & Ranjith, P. 2018. A Study of the Particle-Level Fabric and Morphology of Granular Soils under One-Dimensional Compression Using Insitu X-ray CT Imaging. *Materials (Basel, Switzerland),* **11**.

Alam, M. F. & Haque, A. 2017. A New Cluster Analysis-Marker-Controlled Watershed Method for Separating Particles of Granular Soils. *Materials,* **10,** 1195.

Alshibli, K. A., Druckrey, A. M., Al-Raoush, R. I., Weiskittel, T. & Lavrik, N. V. 2014. Quantifying morphology of sands using 3D imaging. *Journal of Materials in Civil Engineering,* **27,** 04014275.

Altuhafi, F. & Coop, M. R. 2011. Changes to particle characteristics associated with the compression of sands. *Géotechnique,* **61,** 459.

Arthur, J. & Menzies, B. 1972. Inherent anisotropy in a sand. *Geotechnique,* **22,** 115-128.

Atwood, R., Jones, J., Lee, P. & Hench, L. 2004. Analysis of pore interconnectivity in bioactive glass foams using X-ray microtomography. *Scripta Materialia,* **51,** 1029-1033.

Avizo.9.1.1 2015. FEI Visualizations Sciences Group: Hillsboro, OR, USA, 2015.

Bathurst, R. J. & Rothenburg, L. 1990. Observations on stress-force-fabric relationships in idealized granular materials. *Mechanics of materials,* **9,** 65-80.

Bolton, M., Nakata, Y. & Cheng, Y. 2008. Micro-and macro-mechanical behaviour of DEM crushable materials. *Géotechnique,* **58,** 471-480.

Bono, J., McDowell, G. & Wanatowski, D. 2015. Investigating the micro mechanics of cemented sand using DEM. *International Journal for Numerical and Analytical Methods in Geomechanics,* **39,** 655-675.

Brown, N. J., Chen, J.-F. & Ooi, J. Y. 2014. A bond model for DEM simulation of cementitious materials and deformable structures. *Granular Matter,* **16,** 299-311.

Bullard, J. W., Jennings, H. M., Livingston, R. A., Nonat, A., Scherer, G. W., Schweitzer, J. S., Scrivener, K. L. & Thomas, J. J. 2011. Mechanisms of cement hydration. *Cement and concrete research,* **41,** 1208-1223.

Burland, J. 1990. On the compressibility and shear strength of natural clays. *Géotechnique,* **40,** 329-378.

Carpenter, F. G. & Deitz, V. 1950. Methods of sieve analysis with particular reference to bone char. *Journal of Research of the National Bureau of Standards,* **45**.

Cavarretta, I., O'Sullivan, C. & Coop, M. 2016. The relevance of roundness to the crushing strength of granular materials. *Géotechnique,* **67,** 301-312.

Chang, C., Misra, A. & Sundaram, S. 1990. Micromechanical modelling of cemented sands under low amplitude oscillations.

Cheng, Y., Bolton, M. & Nakata, Y. 2004. Crushing and plastic deformation of soils simulated using DEM. *Geotechnique,* **54,** 131-141.

Cheng, Y., Bolton, M. & Nakata, Y. 2005. Grain crushing and critical states observed in DEM simulations. *P&G05,* **2,** 1393-1397.

Cheng, Y., Nakata, Y. & Bolton, M. 2003. Discrete element simulation of crushable soil. *Geotechnique,* **53,** 633-641.

Christoffersen, J., Mehrabadi, M. & Nemat-Nasser, S. 1981. A micromechanical description of granular material behavior. *Journal of applied mechanics,* **48,** 339-344.

Chuhan, F. A., Kjeldstad, A., Bjørlykke, K. & Høeg, K. 2002. Porosity loss in sand by grain crushing—Experimental evidence and relevance to reservoir quality. *Marine and Petroleum Geology,* **19,** 39-53.

Chuhan, F. A., Kjeldstad, A., Bjørlykke, K. & Høeg, K. 2003. Experimental compression of loose sands: relevance to porosity reduction during burial in sedimentary basins. *Canadian Geotechnical Journal,* **40,** 995-1011.

Cil, M. & Alshibli, K. 2014. 3D evolution of sand fracture under 1D compression. *Géotechnique,* **64,** 351.

Clough, G. W., Sitar, N., Bachus, R. C. & Rad, N. S. 1981. Cemented sands under static loading. *Journal of Geotechnical and Geoenvironmental Engineering,* **107**.

Cnudde, V. & Boone, M. N. 2013. High-resolution X-ray computed tomography in geosciences: A review of the current technology and applications. *Earth-Science Reviews,* **123,** 1-17.

Consoli, N., Rotta, G. & Prietto, P. 2000. Influence of curing under stress on the triaxial response of cemented soils. *Geotechnique,* **50,** 99-105.

Consoli, N., Rotta, G. & Prietto, P. 2006. Yielding–compressibility–strength relationship for an artificially cemented soil cured under stress. *Geotechnique,* **56,** 69-72.

Coop, M. 1990. The mechanics of uncemented carbonate sands. *Geotechnique,* **40,** 607-626.

Coop, M. & Atkinson, J. 1993. The mechanics of cemented carbonate sands. *Geotechnique,* **43,** 53-67.

Coop, M. & Lee, I. 1993. The behaviour of granular soils at elevated stresses. *Predictive soil mechanics*, 186-198.

Cotecchia, F. & Chandler, R. 1997. The influence of structure on the pre-failure behaviour of a natural clay. *Géotechnique,* **47,** 523-544.

Cuccovillo, T. & Coop, M. 1997. Yielding and pre-failure deformation of structured sands. *Geotechnique,* **47,** 491-508.

Cuccovillo, T. & Coop, M. 1999. On the mechanics of structured sands. *Géotechnique,* **49,** 741-760.

Curray, J. R. 1956. The analysis of two-dimensional orientation data. *The Journal of Geology,* **64,** 117-131.

Da Fonseca, A. V., FERNANDESĆ, M. M. & CARDOSOĆ, A. S. 1998. Interpretation of a footing load test on a saprolitic soil from granite. *Pre-failure deformation behaviour of geomaterials***,** 247.

Dadda, A., Geindreau, C., Emeriault, F., du Roscoat, S. R., Filet, A. E. & Garandet, A. 2018a. Characterization of contact properties in biocemented sand using 3D X-ray micro-tomography. *Acta Geotechnica***,** 1-17.

Dadda, A., Geindreau, C., Emeriault, F., du Roscoat, S. R., Garandet, A., Sapin, L. & Filet, A. E. 2017. Characterization of microstructural and physical properties changes in biocemented sand using 3D X-ray microtomography. *Acta Geotechnica,* **12,** 955-970.

Dadda, A., Geindreau, C., Emeriault, F., Filet, A. E. & Garandet, A. 2018b. Influence of the microstructural properties of biocemented sand on its mechanical behavior. *Int J Numer Anal Methods Geomech,* **1,** 10.

Dafalias, Y. F. 2016. Must critical state theory be revisited to include fabric effects? *Acta Geotechnica,* **11,** 479-491.

De Bono, J. P. 2013. *Discrete element modeling of cemented sand and particle crushing at high pressures.* University of Nottingham.

de Bono, J. P. & McDowell, G. R. 2014. Discrete element modelling of one-dimensional compression of cemented sand. *Granular Matter,* **16,** 79-90.

De Souza, J. 1958. Compressibility of sand at high pressure. *MS thesis, Massachusetts Institute of Technology***,** 63-64.

Dennis, M. J. 1989. Industrial computed tomography. *ASM Handbook.,* **17,** 358-386.

Desai, C. S. & Toth, J. 1996. Disturbed state constitutive modeling based on stress-strain and nondestructive behavior. *International Journal of Solids and Structures,* **33,** 1619-1650.

Druckrey, A. M. & Alshibli, K. A. 2016. 3D finite element modeling of sand particle fracture based on in situ X-Ray synchrotron imaging. *International Journal for Numerical and Analytical Methods in Geomechanics,* **40,** 105-116.

Druckrey, A. M., Alshibli, K. A. & Al-Raoush, R. I. 2016. 3D characterization of sand particle-to-particle contact and morphology. *Computers and Geotechnics,* **74,** 26-35.

Du Plessis, A., Broeckhoven, C., Guelpa, A. & Le Roux, S. G. 2017. Laboratory x-ray micro-computed tomography: a user guideline for biological samples. *GigaScience,* **6,** 1-11.

Dvorkin, J., Nur, A. & Yin, H. 1994. Effective properties of cemented granular materials. *Mechanics of materials,* **18,** 351-366.

Faessel, M. & Jeulin, D. 2010. Segmentation of 3D microtomographic images of granular materials with the stochastic watershed. *Journal of microscopy,* **239,** 17-31.

Fonseca, J., O'sullivan, C., Coop, M. & Lee, P. 2013a. Quantifying the evolution of soil fabric during shearing using scalar parameters. *Géotechnique,* **63,** 818-829.

Fonseca, J., O'Sullivan, C., Coop, M. R. & Lee, P. 2013b. Quantifying the evolution of soil fabric during shearing using directional parameters. *Géotechnique,* **63,** 487-499.

Fonseca, J., O'Sullivan, C., Coop, M. R. & Lee, P. 2012. Non-invasive characterization of particle morphology of natural sands. *Soils and Foundations,* **52,** 712-722.

Fonseca, J., Sim, W., Shire, T. & O'sullivan, C. 2014. Microstructural analysis of sands with varying degrees of internal stability. *Géotechnique,* **64,** 405-411.

Fu, P. & Dafalias, Y. F. 2015. Relationship between void-and contact normal-based fabric tensors for 2D idealized granular materials. *International Journal of Solids and Structures,* **63,** 68-81.

Haeri, S. & Hamidi, A. 2009. Constitutive modelling of cemented gravelly sands. *Geomechanics and Geoengineering: An International Journal,* **4,** 123-139.

Haeri, S., Hamidi, A., Hosseini, S., Asghari, E. & Toll, D. 2006. Effect of cement type on the mechanical behavior of a gravely sand. *Geotechnical & Geological Engineering,* **24,** 335.

Hagerty, M., Hite, D., Ullrich, C. & Hagerty, D. 1993. One-dimensional high-pressure compression of granular media. *Journal of Geotechnical Engineering,* **119,** 1-18.

Hall, S. A., Wood, D. M., Ibraim, E. & Viggiani, G. 2010. Localised deformation patterning in 2D granular materials revealed by digital image correlation. *Granular matter,* **12,** 1-14.

Hardin, B. O. 1985. Crushing of soil particles. *Journal of geotechnical engineering,* **111,** 1177-1192.

Hasan, A. & Alshibli, K. 2010. Experimental assessment of 3D particle-to-particle interaction within sheared sand using synchrotron microtomography. *Géotechnique,* **60,** 369.

Hashemi, M. A., Khaddour, G., François, B., Massart, T. J. & Salager, S. 2014. A tomographic imagery segmentation methodology for three-phase geomaterials based on simultaneous region growing. *Acta Geotechnica,* **9,** 831-846.

Hendron Jr, A. J. (1963). The Behavior of Sand in One-Dimensional Compression. ILLINOIS UNIV URBANA.

Higo, Y., Oka, F., Sato, T., Matsushima, Y. & Kimoto, S. 2013. Investigation of localized deformation in partially saturated sand under triaxial compression using microfocus X-ray CT with digital image correlation. *Soils and Foundations,* **53,** 181-198.

Huang, J. & Airey, D. 1998. Properties of artificially cemented carbonate sand. *Journal of Geotechnical and Geoenvironmental Engineering,* **124,** 492-499.

Imseeh, W. H., Druckrey, A. M. & Alshibli, K. A. 2018. 3D experimental quantification of fabric and fabric evolution of sheared granular materials using synchrotron micro-computed tomography. *Granular Matter,* **20,** 24.

Ingles, O. G. & Metcalf, J. B. (1972). Soil stabilization principles and practice.

Islam, S., Haque, A., Wilson, S. A. & Ranjith, P. 2015. Time-dependent strength and mineralogy of Lime-GGBS treated naturally occurring acid sulfate soils. *Journal of Materials in Civil Engineering,* **28,** 04015077.

Ismail, M., Joer, H., Randolph, M. & Meritt, A. 2002. Cementation of porous materials using calcite. *Geotechnique,* **52,** 313-324.

Jang, D.-J. 1997. *Quantification of sand structure and its evolution during shearing using image analysis.* Georgia Institute of Technology.

Jang, D.-J. Sand structure differences resulting from specimen preparation procedures. Proc. 1998 Conf. on Geotech. Earthquake Engrg. and Soil Dynamics, 1998. ASCE, 234-245.

Jang, D.-J. & Frost, J. D. 2000. Use of image analysis to study the microstructure of a failed sand specimen. *Canadian geotechnical journal,* **37,** 1141-1149.

Jiang, M., Zhang, F. & Sun, Y. 2014. An evaluation on the degradation evolutions in three constitutive models for bonded geomaterials by DEM analyses. *Computers and Geotechnics,* **57,** 1-16.

Johnson, K. L. & Johnson, K. L. 1987. *Contact mechanics*, Cambridge university press.

Kanatani, K.-I. 1984. Distribution of directional data and fabric tensors. *International Journal of Engineering Science,* **22,** 149-164.

Karatza, Z., Andò, E., Papanicolopulos, S.-A., Ooia, J. Y. & Viggiani, G. 2015. Observing breakage in sand under triaxial and oedometric loading in 3D. *Deformation Characteristics of Geomaterials***,** 431.

Karatza, Z., Andò, E., Papanicolopulos, S., Ooi, J. & Viggiani, G. 2017. Evolution of deformation and breakage in sand studied using X-ray tomography. *Géotechnique,* **1,** 1-11.

Konishi, J. & Naruse, F. 1988. A note on fabric in terms of voids. *Studies in Applied Mechanics.* Elsevier.

Konishi, J., Oda, M. & Nemat-Nasser, S. 1982. Inherent anisotropy and shear strength of assembly of oval cross-sectional rods. *Deformation and failure of granular materials. AA BALKEMA/Rotterdam*.

Konishi, J., Oda, M. & Nemat-Nasser, S. 1983. Induced anisotropy in assemblies of oval cross-sectional rods in biaxial compression. *Studies in Applied Mechanics.* Elsevier.

Lade, P. V. & Overton, D. D. 1989. Cementation effects in frictional materials. *Journal of Geotechnical Engineering,* **115,** 1373-1387.

Lagioia, R. & Nova, R. 1995. An experimental and theoretical study of the behaviour of a calcarenite in triaxial compression. *Géotechnique,* **45,** 633-648.

Leroueil, S. & Vaughan, P. 1990. The general and congruent effects of structure in natural soils and weak rocks. *Géotechnique,* **40,** 467-488.

Li, X. S. & Dafalias, Y. F. 2011. Anisotropic critical state theory: role of fabric. *Journal of Engineering Mechanics,* **138,** 263-275.

Liu, S. & Lok, T. M. H. Discrete Element Simulation of Particle Crushing in 1-D Compression. GeoShanghai International Conference, 2018. Springer, 140-147.

Maeda, K., Sakai, H., Kondo, A., Yamaguchi, T., Fukuma, M. & Nukudani, E. 2010. Stress-chain based micromechanics of sand with grain shape effect. *Granular Matter,* **12,** 499-505.

Manahiloh, K. N. & Muhunthan, B. 2012. Characterizing liquid phase fabric of unsaturated specimens from X-ray computed tomography images. *Unsaturated soils: Research and applications.* Springer.

Manahiloh, K. N., Muhunthan, B. & Likos, W. J. 2016. Microstructure-based effective stress formulation for unsaturated granular soils. *International Journal of Geomechanics,* **16,** D4016006.

Marri, A. 2010. *The mechanical behaviour of cemented granular materials at high pressures.* University of Nottingham.

Marri, A., Wanatowski, D. & Yu, H. 2012. Drained behaviour of cemented sand in high pressure triaxial compression tests. *Geomechanics and Geoengineering,* **7,** 159-174.

McConnachie, I. 1974. Fabric changes in consolidated kaolin. *Geotechnique,* **24,** 207-222.

McDowell, G. 2005. A physical justification for log e–log σ based on fractal crushing and particle kinematics. *Géotechnique,* **55,** 697-698.

Mcdowell, G. & Bolton, M. 1998. On the micromechanics of crushable aggregates.

McDowell, G., Bolton, M. & Robertson, D. 1996. The fractal crushing of granular materials. *Journal of the Mechanics and Physics of Solids,* **44,** 2079-2101.

McDowell, G. & Harireche, O. 2002a. Discrete element modelling of soil particle fracture. *Géotechnique,* **52,** 131-135.

McDowell, G. & Harireche, O. 2002b. Discrete element modelling of yielding and normal compression of sand. *Géotechnique,* **52,** 299-304.

Mehrabadi, M. M., Nemat-Nasser, S. & Oda, M. 1982. On statistical description of stress and fabric in granular materials. *International Journal for Numerical and Analytical Methods in Geomechanics,* **6,** 95-108.

Mitchell, J. 1976. Fundamentals of Soil Behaviour" John Wiley. *New York*.

Mitchell, J. K. & Soga, K. 2005. *Fundamentals of soil behavior*, John Wiley & Sons New York.

Muhunthan, B. 1991. Micromechanics of steady state, collapse and stress-strain modeling of soils. *PhD dissertation, Perdue University, West Lafayette.*

Murphy, D. J. 1987. Stress, degradation, and shear strength of granular material. *Geotech. Modeling and Applications, SM Sayed, Ed., Gulf Publishing Company, Houston, Tex***,** 181-211.

Nakata, Y., Hyodo, M., Hyde, A. F., Kato, Y. & Murata, H. 2001. Microscopic particle crushing of sand subjected to high pressure one-dimensional compression. *Soils and foundations,* **41,** 69-82.

Nova, R., Castellanza, R. & Tamagnini, C. 2003. A constitutive model for bonded geomaterials subject to mechanical and/or chemical degradation. *International Journal for Numerical and Analytical Methods in Geomechanics,* **27,** 705-732.

Obermayr, M., Dressler, K., Vrettos, C. & Eberhard, P. 2013. A bonded-particle model for cemented sand. *Computers and Geotechnics,* **49,** 299-313.

Oda, M. 1972a. Deformation mechanism of sand in triaxial compression tests. *Soils and Foundations,* **12,** 45-63.

Oda, M. 1972b. Initial fabrics and their relations to mechanical properties of granular material. *Soils and foundations,* **12,** 17-36.

Oda, M. 1972c. The mechanism of fabric changes during compressional deformation of sand. *Soils and foundations,* **12,** 1-18.

Oda, M. 1977. Fabrics and their effects on the deformation behaviors of sand. *埼玉大学工学部建設系研究報告*, p1-59.

Oda, M. 1993. Inherent and induced anisotropy in plasticity theory of granular soils. *Mechanics of Materials,* **16,** 35-45.

Oda, M. & Konishi, J. 1974. Microscopic deformation mechanism of granular material in simple shear. *Soils and foundations,* **14,** 25-38.

Oda, M. & Nakayama, H. 1989. Yield function for soil with anisotropic fabric. *Journal of Engineering Mechanics,* **115,** 89-104.

Oda, M., Nemat-Nasser, S. & Konishi, J. 1985. Stress-induced anisotropy in granular masses. *Soils and foundations,* **25,** 85-97.

Oda, M., Nemat-Nasser, S. & Mehrabadi, M. M. 1982. A statistical study of fabric in a random assembly of spherical granules. *International Journal for Numerical and analytical methods in Geomechanics,* **6,** 77-94.

Pekau, O. & Gocevski, V. 1989. Elasto-plastic model for cemented and pure sand deposits. *Computers and Geotechnics,* **7,** 155-187.

Razavi, M. R., Muhunthan, B. & Al Hattamleh, O. 2006. Representative elementary volume analysis of sands using X-ray computed tomography. *Geotechnical Testing Journal,* **30,** 212-219.

Rios, S., Da Fonseca, A. V. & Baudet, B. A. 2014. On the shearing behaviour of an artificially cemented soil. *Acta Geotechnica,* **9,** 215-226.

Robertson, D. 2000. *Computer simulations of crushable aggregates.* University of Cambridge.

Rotta, G., Consoli, N., Prietto, P., Coop, M. & Graham, J. 2003. Isotropic yielding in an artificially cemented soil cured under stress. *Geotechnique,* **53,** 493-501.

Santamarina, J. C., Klein, A. & Fam, M. A. 2001. Soils and waves: Particulate materials behavior, characterization and process monitoring. *Journal of Soils and Sediments,* **1,** 130-130.

Satake, M. & Jenkins, J. T. 2013. *Micromechanics of Granular Materials: Proceedings of the US/Japan Seminar on the Micromechanics of Granular Materials, Sendai-Zao, Japan, October 26-30, 1987*, Elsevier.

Schnaid, F., Prietto, P. D. & Consoli, N. C. 2001. Characterization of cemented sand in triaxial compression. *Journal of Geotechnical and Geoenvironmental Engineering,* **127,** 857-868.

Shen, Z., Jiang, M. & Thornton, C. 2016. DEM simulation of bonded granular material. Part I: contact model and application to cemented sand. *Computers and Geotechnics,* **75,** 192-209.

Soil, A. C. D.-o. & Rock 2004. *Standard test methods for one-dimensional consolidation properties of soils using incremental loading*, ASTM International.

Tagliaferri, F., Waller, J., Andò, E., Hall, S. A., Viggiani, G., Bésuelle, P. & DeJong, J. T. 2011. Observing strain localisation processes in bio-cemented sand using x-ray imaging. *Granular Matter,* **13,** 247-250.

Tengattini, A., Das, A. & Einav, I. 2016. A constitutive modelling framework predicting critical state in sand undergoing crushing and dilation. *Géotechnique,* **66,** 695-710.

Terzaghi, K. & Peck, R. 1948. Soil mechanics in engineering practice. *Soil mechanics in engineering practice.* J. Wiley and Sons.

Tordesillas, A. & Muthuswamy, M. 2009. On the modeling of confined buckling of force chains. *Journal of the Mechanics and Physics of Solids,* **57,** 706-727.

Utili, S. & Nova, R. 2008. DEM analysis of bonded granular geomaterials. *International Journal for Numerical and Analytical Methods in Geomechanics,* **32,** 1997-2031.

Wadell, H. 1935. Volume, shape, and roundness of quartz particles. *The Journal of Geology,* **43,** 250-280.

Wang, Y.-H. & Leung, S.-C. 2008. A particulate-scale investigation of cemented sand behavior. *Canadian Geotechnical Journal,* **45,** 29-44.

Wang, Z., Yang, X., Chen, Q., Zhang, Y. & Zhao, Y. Study of the contact forces and grain size distribution during grain crushing. Multimedia Technology (ICMT), 2011 International Conference on, 2011. IEEE, 2617-2622.

Wood, D. M. Geomaterials with changing grading: a route towards modelling. Int. Symp. on Geomechanics and Geotechnics of Particulate Media, IS-Yamaguchi, Ube, Japan, 12, 2006. 313-316.

Yamamuro, J. A., Bopp, P. A. & Lade, P. V. 1996. One-dimensional compression of sands at high pressures. *Journal of geotechnical engineering,* **122,** 147-154.

Yimsiri, S. & Soga, K. 2011. Effects of soil fabric on behaviors of granular soils: microscopic modeling. *Computers and Geotechnics,* **38,** 861-874.

Yu, H., Tan, S. & Schnaid, F. 2007. A critical state framework for modelling bonded geomaterials. *Geomechanics and Geoengineering,* **2,** 61-74.

Zhang, J., Wong, T.-F., Yanagidani, T. & Davis, D. M. 1990a. Pressure-induced microcracking and grain crushing in Berea and Boise sandstones: Acoustic emission and quantitative microscopy measurements. *Mechanics of Materials,* **9,** 1-15.

Zhang, J., Wong, T. F. & Davis, D. M. 1990b. Micromechanics of pressure-induced grain crushing in porous rocks. *Journal of Geophysical Research: Solid Earth,* **95,** 341-352.

Zhao, B., Wang, J., Coop, M., Viggiani, G. & Jiang, M. 2015. An investigation of single sand particle fracture using X-ray micro-tomography. *Géotechnique,* **65,** 625-641.

6 CONCEPTUAL FRAMEWORK FOR FABRIC STUDY OF CEMENTED SAND

6.1 Introduction

This study was intended to explore the behaviour of fabric of cemented sand undergoing high one-dimensional compression at grain-scale using X-Ray CT technology. To understand the influence of cementing on sand behaviour, the behaviour of the uncemented sand was investigated prior to investigating the cemented sand. As voids and sands/cement-sand matrix undergo changes with the increase of stress, it is essential to capture these changes and relate to the measurements taken at the boundary, which facilitates understanding the micromechanics. In this study for cemented sand, as specific microstructural component, the evolution of void fabric in terms of different scalar (sphericity, anisotropy) and directional (fabric anisotropy) parameters were analysed. This chapter is aimed at developing a conceptual framework to unify the globally measured parameters with those void fabric parameters based on the limited investigation carried out.

6.2 Second Order Fabric Tensor of Second Kind: A Clarification

In this study, Kanatani (1984)'s framework to quantify the 2nd and 4th order fabric tensors of the first, second and third kind for void long axis have been computed to express their distributions. These symmetric tensors numerically describe the anisotropy of any directional data of interest in a granular media. For 3D data, as 4th order tensors captures more details of the distribution, they have been presented in earlier chapters for uncemented and cemented sands. However, while comparing evolution of anisotropy with progressive stresses, 2^{nd} order fabric tensor of 2^{nd} kind was found not only sufficient (Li and Dafalias, 2011; Dafalias, 2016) for the samples studied here but also avoids unnecessary details as reflected in 4^{th} order distributions. Moreover, Fabric Anisotropy Variable ($FAVA$) (Li and Dafalias, 2011) presented in this study (further modified for this study by Dafalias, 2018) were computed from the 2^{nd} order fabric tensor of the second kind.

In this chapter, for representing the distribution of fabric tensor and computing Fabric Anisotropy Variable ($FAVA$) for the interparticle voids for uncemented and cemented sand (20% and 30% cemented sand), Kanatani (1984)'s 2^{nd} order fabric tensor of second kind have been used. However, due to insufficiency of data points as presented in chapter 5, 10% cemented sand is not considered here.

6.3 Brief Comparative Review of Void Fabric

In the earlier chapters, initial void fabric and their evolution with stresses on the of basis of scalar and directional parameters were presented and discussed separately for uncemented and cemented sand in chapter 4 and chapter 5 respectively. However,

prior to proposing a conceptual framework a brief comparative review of void fabric characteristics for uncemented and cemented sand are discussed briefly in the following sections.

6.3.1 Effect of cement content on e-logσ'_v behaviour

A gradual decrease of initial void ratio (e_o) (measured from X-ray CT images) of samples starting at 0.60 for uncemented sand to 0.17 for 20% cemented and 0.14 for 30% cemented sand was observed (Figure 6-1). The *e*-logσ'_v plot for uncemented sand shows a gradual change of slope up to 7 MPa, followed by a noticeable change, marked with a red arrow, as the yield stress (~14 MPa) obtained from the intersecting point of the two straight parts of the *e*-logσ'_v, due to the initiation of crushing of particles (Al Mahbub and Haque, 2016). The rapid decrease of void ratio in the post-yield stresses indicates a greater degree of particle crushing and noticeable collapse of voids, which is captured to some extent in the XZ sections of Figure 6-2(a). More details on changes of gradations resulting from the particle crushing with increased loading are available in chapter 4.

The *e*-logσ'_v plots for cemented sands (Figure 6-1) do not show any considerable change of void ratio until 14.1 MPa and 28.2 MPa for 20 and 30% cement contents, respectively. Moreover, the cemented sand samples show varying rates of change of void ratios, which reflect progressive bond breakage and collapse of voids (marked by light blue ellipses on Figure 6-2(b) and 6-2(c)). However, hardly any crushing of sand particles was observed from close inspections of 3-D greyscale images in Avizo software, as cementation had been reported to suppress crushing (Marri et al., 2012).

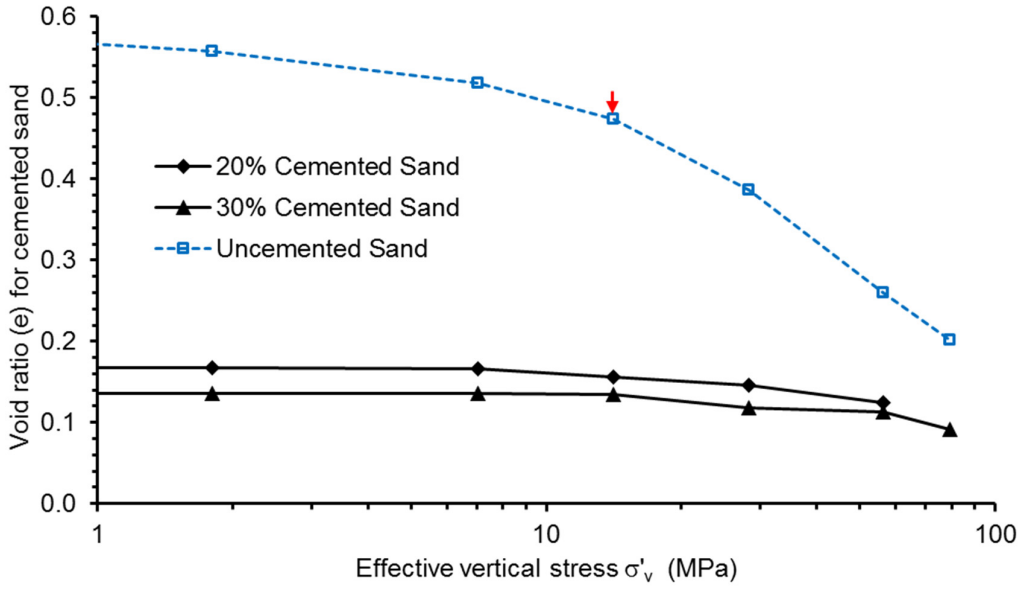

Figure 6-1: e-logσ'_v plot for uncemented and cemented sands

6.3.2 Effect of cement content on void morphology

For the uncemented sand, voids are highly interconnected (Figure 6-2(a)), whereas for cemented sands the accumulation of cement at particle contacts and inter-particle void throats results in isolated voids (Figure 6-2 (a) and (c)). The voids in cemented sand vary widely in size with the presence of more uniform-shaped smaller voids and large elongated inter-cluster voids with increased cement contents. The large voids may have developed from inhomogeneous mixing and/or segregation of cement during placement. The evolution of sphericity (defined as $\pi^{1/3}(6Vp)^{2/3}/Ap$, where Ap and Vp are surface area and volume of any particle, respectively) distribution of voids for all the samples with progressive loading are shown in Figure 6-3(a) to (c). In general, distribution curves are found to shift leftward indicating decrease of sphericity of voids with loading. However, for uncemented sand, increase of sphericity has been observed for voids with sphericity values above 0.4. The initial frequency distribution

of sphericity of cemented sand samples exhibits (Figure 6-4) a large shift towards right compared with its uncemented counterpart, indicating the presence of significantly higher volumes of spherical voids in cemented sand. Approximately 50% of voids with sphericity values of 0.40 for uncemented sand, and 40 and 60% of voids with sphericity of 0.80 for 20 and 30% cemented sand respectively were observed. The distribution of 20% cemented sand is slightly left-skewed, indicating the heterogeneity of the distribution of cement content due to the presence of more non-spherical shapes compared with 30% cemented sand.

For uncemented sand, the average sphericity of voids remains unchanged at 0.40 for stress up to 56.4 MPa. It is possible that the complex phenomena of particle crushing, grinding and reorientation of particles are still not at a stage to generate a wider range of particles, which may fill inter-particle spaces in such a way to give voids more regular or spherical shapes (Figure 6-2 (a), XZ sections). The rise of average sphericity to 0.44 at the final stress of 79.3 MPa may be a sign of the beginning of such an occurrence. For the 20% cemented sand, no significant change of average sphericity (0.80) from 14.1 MPa onwards was observed due to the rigid response of cemented material under the stress range investigated (Figure 6-2 (b), XZ sections). However, for the 30% cemented sand, slightly fluctuating values of average sphericity (0.66-0.72) were observed, possibly resulting from the partial closing or division of large voids (Figure 6-2 (c), XZ sections).

Anisotropy (defined as 1 minus the ratio of the smallest to the largest eigenvalue of the covariance matrix, FEI (2016)) can be hypothesized to increase with the increase of stress where voids are being progressively compressed. This has been reflected by the rightward shift of the anisotropy distribution curves with progressive loading, marginally for the uncemented sand and considerably for the cemented sand (Figure 6-3(d) to (f)). For uncemented sand, the average anisotropy increased from 0.73 under initial conditions to 0.75 at particle crushing stress (14.1 MPa) and thereafter remained almost constant (Figure 6-3(d), which is in line with the anisotropy distribution plot. However, for 20% cemented sand, it increased from 0.73 in the initial state to 0.78 at 14.1 MPa with no noticeable change thereafter (Figure 6-3(e)). On the other hand, for 30% cemented sand, the initial average anisotropy (0.57) was found to increase considerably to 0.71 at 14.1 MPa and thereafter showed slightly fluctuating values, which is clearly reflected in the anisotropy distributions (Figure 6-3(f)). The dynamics of void closures and divisions may have played a significant role here. In addition, the progressive breakage of cement bonds into small-sized particles below image resolution may be undetectable (Tagliaferri et al., 2011), and this may have affected the results.

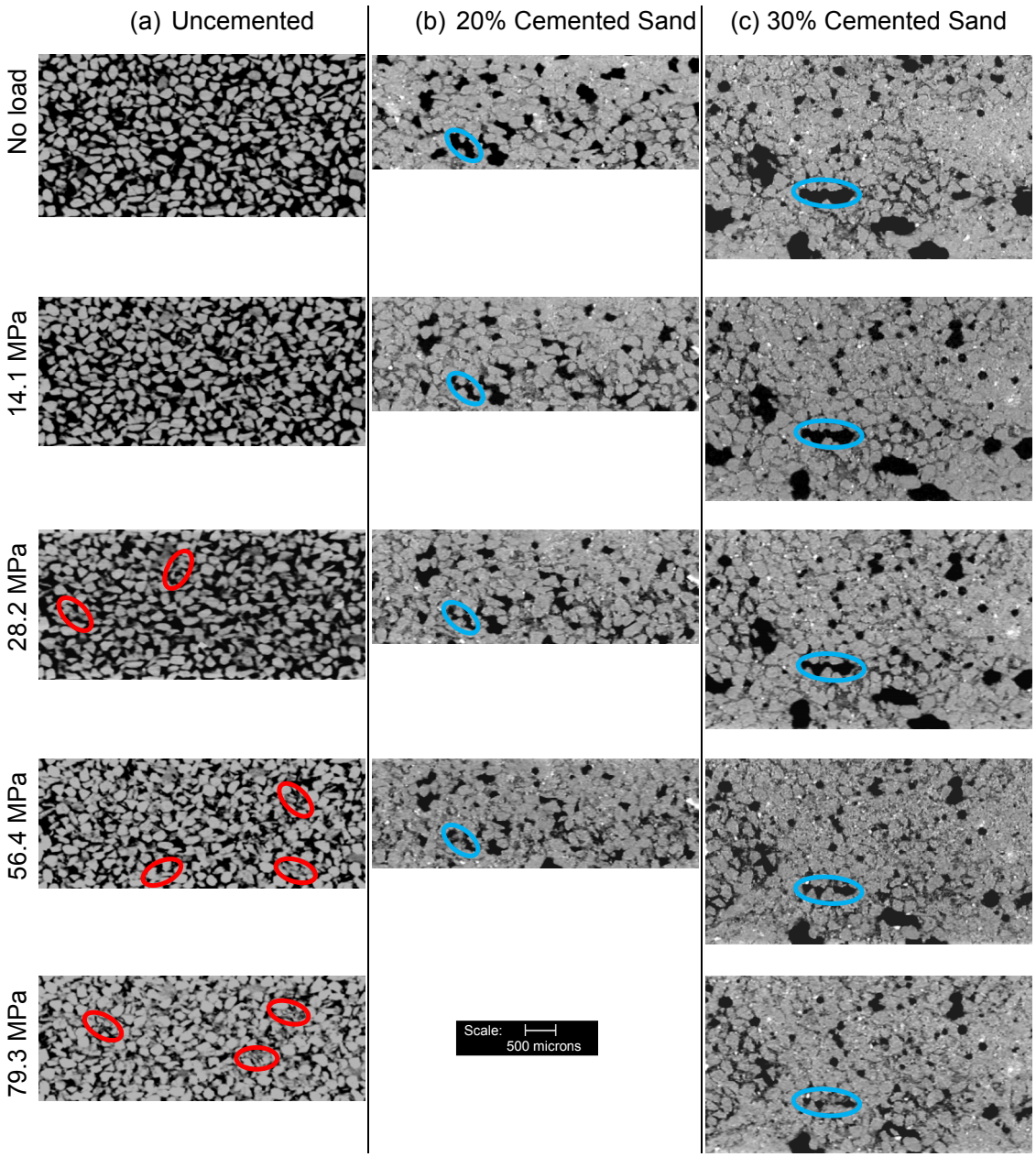

Figure 6-2: Vertical sections in XZ plane along the centre of (a) uncemented (b) 20% cemented and (c) 30% cemented samples with progressive loading.

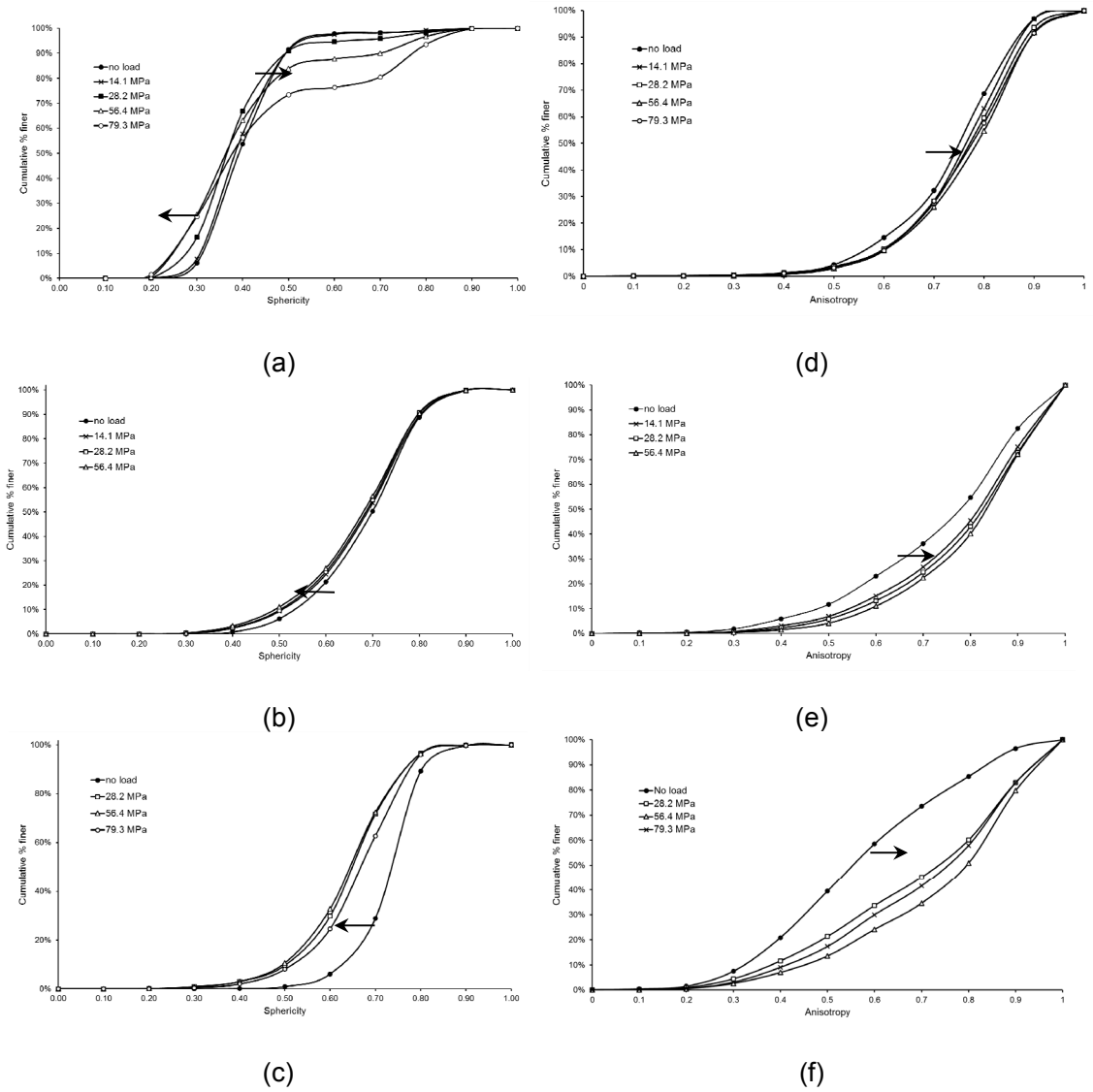

Figure 6-3: Evolution of sphericity and anisotropy: (a,d) uncemented sample, (b,e) 20% cemented sample and (c,f) 30% cemented sample

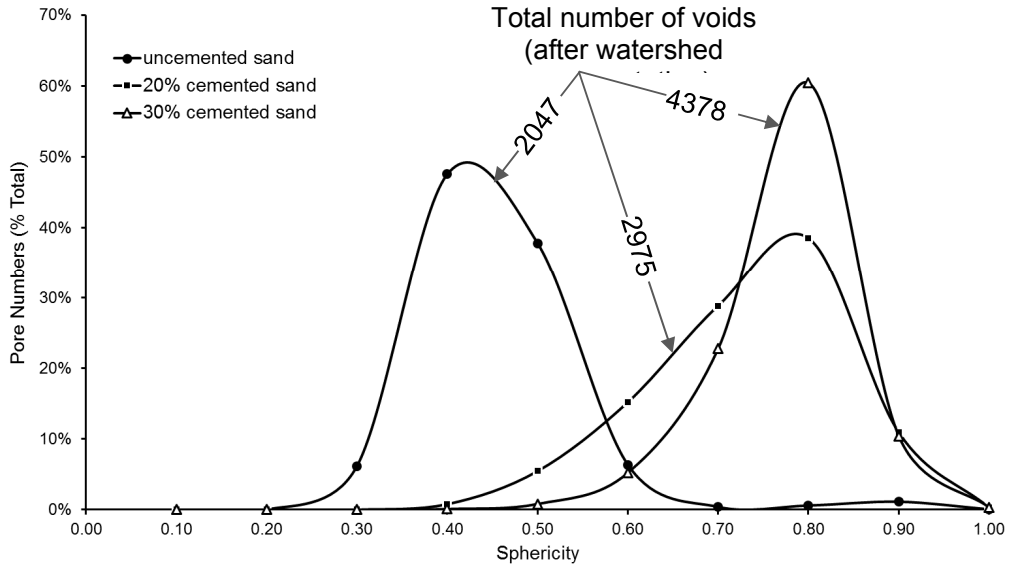

Figure 6-4: Distribution of sphericity of voids at initial condition

6.3.3 Effect of cement content on directional void fabric

The distribution of 3-D fabric tensors (top rows of Figure 6-5(a) to (c)) is represented by ellipsoidal surfaces, the shape of which in a specific direction gives an immediate indication of the preference of the voids' long axis. In contrast, the 2-D elliptic representation (shown in magenta in bottom rows of Figure 6-5(a)-(c)) indicates the preference of the void fabric on a planar view. In addition, the 2-D rose diagram (coloured cyan in bottom rows of Figure 6-5(a) to (c)) by summing the number of vectors of all slices within a particular angular range (15° in this case) was plotted. *FAV A* values are also presented in the middle row of Figure 6-5(a) to (c) for all loadings and cement contents.

The initial 3-D fabric tensors for all samples show transversely-isotropic distributions (i.e., rotational symmetry along the vertical loading axis) with an increase of 3-D *FAV*

A value from 0.45 for uncemented sand (Figure 6-5(a)) to 0.82 for 20% cemented sand (Figure 6-5(b)), indicating more bias in preferential orientation perpendicular to the loading direction. However, with increased cement content of 30%, the 3-D fabric tensors became almost spherical, indicating the absence of directional bias, as shown by the near-zero value of 3-D $FAV\ A$ (Figure 6-5(c)). The horizontally-biased orientation of voids for uncemented sands packed under gravity is to be expected, as is that of 20% cemented sand. However, the addition of more cement (30%) causes the formation of more uniform-shaped voids, as cement is increasingly present at the particle contacts and inter-particle void throats. Interestingly, the 2-D tensors and rose diagrams in the initial state for all the samples (Figure 6-5 (a) to (c)) represent the bias of fabric orientations sufficiently, as observed in the 3-D distributions.

For uncemented sand under progressive loading, the $FAV\ A$ (3-D) value is observed to increase marginally from 0.45 at no-load to 0.49 at 28.2 MPa then to 0.65 at 56.4 MPa, where significant crushing of particles (marked with red ellipses on Figure 6-2(a), XZ sections) occurs. The increase in $FAV\ A$ indicates the stronger horizontal preference of the void fabric. For 20% cemented sand, despite the rotational symmetry of the fabric in the initial state with $FAV\ A$ (3-D) of 0.82, fabric distributions with progressive loading show orthotropic distributions. These distributions were also captured by the 2-D fabric tensors and $FAV\ A$ (2-D) values (Figure 6-5(b)). The rotations of preferred fabric directions on the XY and YZ planes for 20% cemented sand are particularly interesting. On the other hand, the 3-D void tensors for 30% cemented sand, which started with an initial non-directional fabric ($FAV\ A$ (3-D)=0.07) state, changed to a

transverse isotropy at 14.1 MPa followed by repetitive and complex fabric distributions of orthotropic and transversely-isotropic types with increased loading up to 79.3 MPa. Similar to previous cases, 2-D fabric tensors and rose plots for all planes are capable of sufficiently describing the observed 3-D fabric distributions (Figure 6-5(c)) of 30% cemented sand with progressive loading.

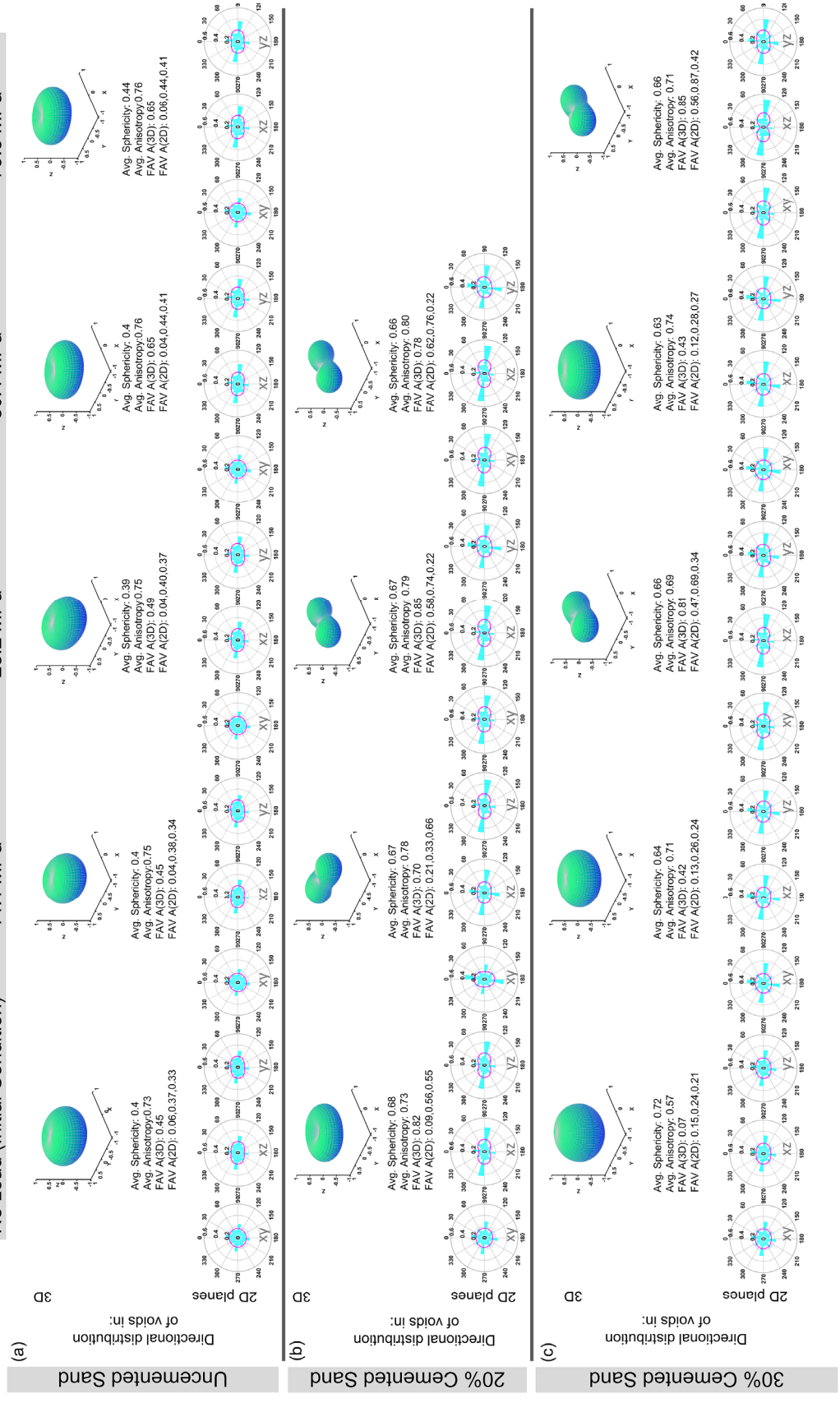

Figure 6-5:Evolution of void fabric under compression (a) uncemented sand (b) 20% cemented sand and (c) 30% cemented

6.4 Proposed Conceptual Framework for Cemented Sand

The above discussions on the evolution of scalar and directional parameters of voids reflect certain differences in the behaviour of uncemented and cemented sand under one-dimensional compression. To establish the observed behaviour as characteristics behaviour for cemented sand with the objective of using them in numerical modelling such as DEM, more studies need to be conducted. The author believes more such studies within a conceptual framework as proposed in Figure 6-6 will facilitate understanding and modelling global behaviour of cemented sand from microstructural point of view.

Under compression, although cemented sand shows stiffer (proportionate to cement content) response compared to its uncemented counterpart, global void ratio for both type of material reduces. However, the mechanics involved in the change of void ratio is different for two types of material. Under high compression, crushing of particles is the major contributing factor in uncemented sand for reduction of void ratio in the post yield region (Figure 6-6). However, for cemented sand, deformation of voids and breakage of bonds jointly contribute where noticeable change of void ratio were observed (Figure 6-6).

Evolution of average sphericity and average anisotropy - two void fabric parameters were observed (Figure 6-6) over the change of global void ratio. For uncemented sand, only noticeable change in value was 10% increase of average sphericity at the maximum applied stress, 79.3 MPa. No change in average anisotropy values was

noticed. However, $FAV\ A$ value shows gradual increase until the two final stresses where it stays stable. It is indicative of existence of some correlation between $FAV\ A$ and global void ratio and is worth investigating. Further study will be required to establish such relation, if any.

For 20% cemented sand, average sphericity values (Figure 6-6) show slightly decreasing trend with decreasing global void ratio whereas average anisotropy values show the opposite. This is perhaps reasonable for voids in cemented sands, which have more defined shape due to cementation and gradually deforms under compression. However, for 30% cemented sand, both these parameters show fluctuating values with decreasing void ratios. This may be attributed to complex behaviour of deforming, splitting or collapsing of voids. Interestingly, similar fluctuating values of $FAV\ A$ values with decreasing global void ratio were observed for both 20% and 30% cemented sand. However, despite fluctuating values, an overall increasing trend of $FAV\ A$ values for these samples can be noticed.

Thus, the framework attempts to illustrate differences in micromechanics between uncemented and cemented sand under compression. It is understandable that for this first-of-its-kind study, naturally there may be various external factors including the quality of sample, image processing etc. affecting the obtained results. However, what is important here is the study suggests a model platform for seeking insightful explanation of the global behaviour of cemented (including 0% cementation) sand in terms of fabric evolution.

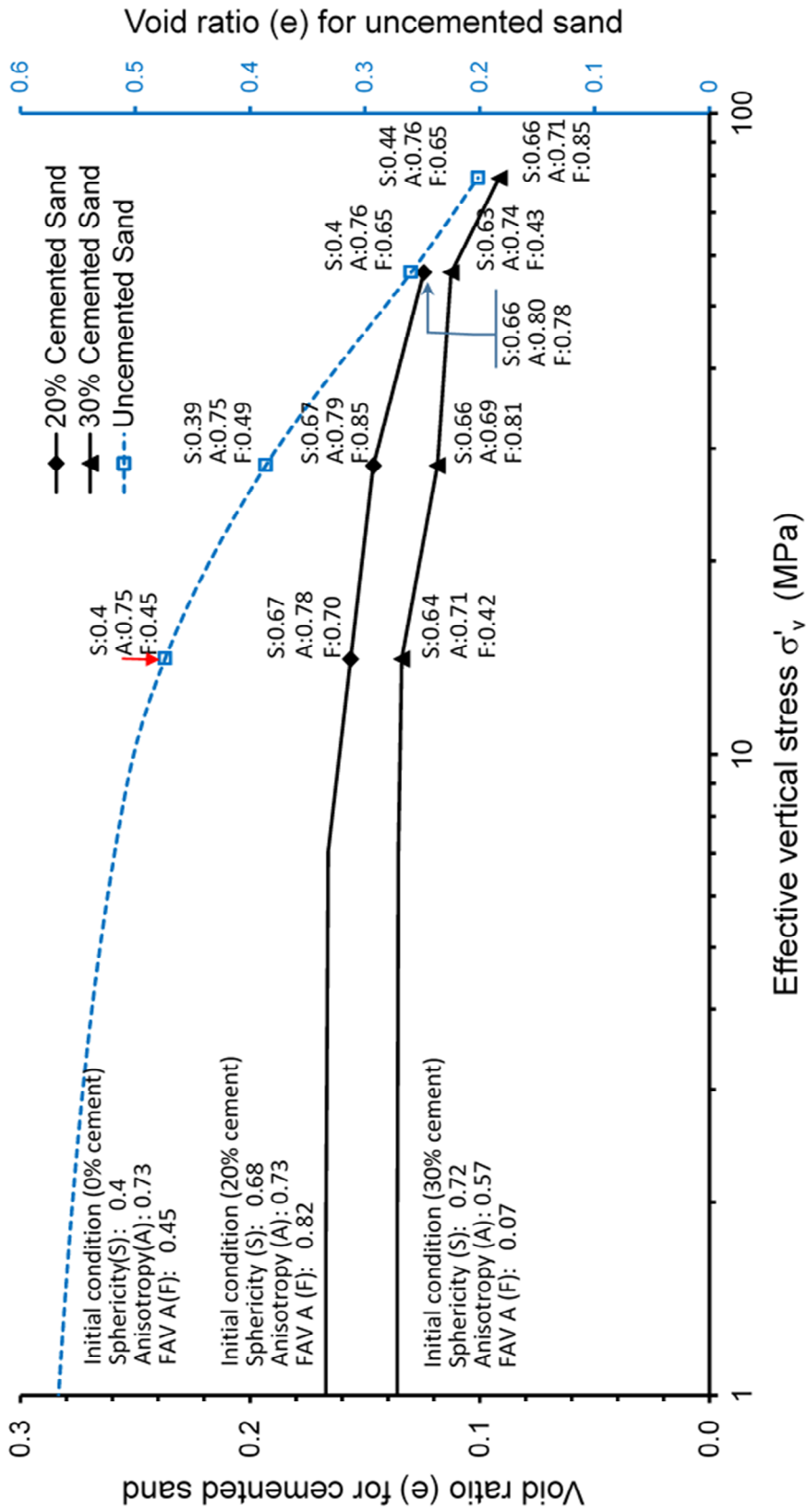

Figure 6-6: Conceptual Framework for cemented sand

6.5 Summary

A conceptual framework has been proposed in this chapter for fabric study of cemented sand based on the comparative study on evolution of void fabric for cemented and uncemented sand subjected to *insitu* X-ray CT imaging under one-dimensional loading. Pressure-void ratio plot (e-logσ'_v), for both uncemented and cemented sand shows initial stiffer response followed by gradual decrease in void ratio. Stiffness of overall material was observed to increase with cementation. Crushing of sand particles, which is observed for uncemented sand at post yield region was suppressed for cemented sand. Deformation of voids and breakage of bond were the mechanics behind reduction of void ration in cemented sand. Both 2D and 3D distributions of directional void fabric were analysed within Kanatani (1984)'s framework. The findings can be summarized as follows:

1. For uncemented sand, highly interconnected void structure was observed, however, for cemented sand, voids are isolated and becomes increasingly dispersed with increased cement content.
2. Voids for cemented sand are more regular in shape. Distribution of sphericity of voids at initial condition shifts significantly towards higher sphericity values with increased cementation. Compared to the uncemented sand, the average sphericity for 20% cemented sand increased by 70%. It further increased by 6% for 30% cemented sand.

However, with loading, hardly any change of average sphericity of voids were observed for uncemented and 20% cemented sand. Slightly fluctuating values of average sphericity for 30% cemented sand may be due to partial collapse or splitting of larger voids.

3. Average anisotropy of voids hardly show any noticeable change except for 30% cemented sand where it shows slightly fluctuating values with applied stresses.
4. The distribution of 3D void fabric tensors for all samples at the initial state show transversely isotropic distributions (i.e., rotational symmetry along the vertical loading axis). Higher $FAV\ A$ values for 20% cemented sand compared to the uncemented sand, indicates more bias in preferential orientation perpendicular to the loading direction. 30% cemented sand resulted in no-directional void fabric at the initial state.
5. With progressive loading, insignificant changes to void fabric distributions for uncemented sand were observed. However, a relatively complex fabric distributions comprising both transversely isotropic and orthotropic types were more appropriate to describe the evolution of fabric for cemented sands investigated here.
6. Distribution of 2D void fabric tensors and rose plots for all planes are capable of reasonably describing the observed 3D fabric distributions with progressive loading.

6.6 References

Al Mahbub, A. & Haque, A. 2016. X-ray computed tomography imaging of the microstructure of sand particles subjected to high pressure one-dimensional compression. *Materials,* **9,** 890.

Dafalias, Y. F. 2016. Must critical state theory be revisited to include fabric effects? *Acta Geotechnica,* **11,** 479-491.

Dafalias, Y. F. 2018. Thoughts on the proper choice of fabric tensor F within ACST. Personal communications, 1p.

FEI Visualizations Sciences Group. Avizo 9.1.1, FEI Visualizations Sciences Group: Hillsboro, OR, USA, 2016

Kanatani, K.-I. 1984. Distribution of directional data and fabric tensors. *International Journal of Engineering Science,* **22,** 149-164.

Li, X. S. & Dafalias, Y. F. 2011. Anisotropic critical state theory: role of fabric. *Journal of Engineering Mechanics,* **138,** 263-275.

Marri, A., Wanatowski, D. & Yu, H. 2012. Drained behaviour of cemented sand in high pressure triaxial compression tests. *Geomechanics and Geoengineering,* **7,** 159-174.

Tagliaferri, F., Waller, J., Andò, E., Hall, S. A., Viggiani, G., Bésuelle, P. & DeJong, J. T. 2011. Observing strain localisation processes in bio-cemented sand using x-ray imaging. *Granular Matter,* **13,** 247-250.

7 CONCLUSIONS AND RECOMMENDATIONS

7.1 Conclusions

Soil improvement by mixing cementitious additives (e.g., cement, lime, slag, fly ash) with soil is increasingly being used by geotechnical engineers in various infrastructure projects. Thus, improving the understanding of the behaviour of cemented soils has strong demand for geotechnical engineering applications. However, most of the earlier studies on cemented soils were based on their macroscale responses whereas microstructure has significant influences on their mechanical responses. On the other hand, existing microstructural studies based on phenomenological and discrete element methods are not sufficient to capture and understand the actual mechanics. State-of-the-art X-Ray CT technology offers wide opportunity to conduct grain-scale studies of soils. This study was intended to explore at grain-scale level the microstructural behaviour of cemented sand undergoing high one-dimensional compression using X-Ray CT technology and presented in this thesis. In the process of this study, a new cylindrical compression cell capable of withstanding high stress and suitable for high-resolution X-ray CT imaging was designed and fabricated. A

unique method for preparing such small scale cemented sample was improvised upon failure of several other methods. Based on trials, a standard test protocol was developed for the samples used in this study. In addition, as first ever image analysis based study in the department of civil engineering at Monash University, the author faced several challenges including making significant effort for few months in learning the sophisticated image analysis software, Avizo on his own without any sort of training or support. Two independent Matlab codes: one for 2D directional data and other for 3D directional data have been developed based on the Kanatani (1984)'s principle for 2^{nd} order (second kind) and 4^{th} order (2^{nd} and 3^{rd} kind) distribution of directional data. Matlab codes are presented in the appendix B.

Specific aims and objectives of the study and critical review of the earlier relevant studies are presented in chapter 1 and 2 respectively. Details on experimental setup and methodologies are explained in chapter 3. Chapter 4 and 5 presents findings of the microstructural studies for uncemented and cemented sand respectively, and finally a conceptual framework to correlate macro behaviour in terms of evolution of void fabric are presented in chapter 6. In this chapter, important microstructural observations, some of which could be conclusively related to the boundary measurement have been summarized. However, few other observations that will need further investigations to have a conclusive explanation, have also been presented.

7.2 Microstructural Behaviour of Uncemented Sand

High resolution X-Ray CT grain-scale images of uniformly graded sand particles subjected to high pressure one dimensional compression leading to particle crushing have been studied. The main outcomes of this study are summarised below:

- The small-scale 1D compression cell setup designed for X-Ray CT *insitu* imaging was found to produce comparable results for e-logσ'_v variations including the yield strength obtained from the lab-scale 1D compression test. The void ratios calculated for each load cases from the image analysis were in good agreement with the experimental data.
- Void ratio variations along the height of the sample showed a gradual decrease until the yield stress and thereafter a significant decrease instigated by marked particles crushing. The sinusoidal variation of void ratios along the height of the sample were found to gradually diminish with increased stresses.
- Uniform change of void ratios within sub-volumes located at peripheral positions were observed.
- The initial particle size distributions of sand particles obtained from mechanical sieve analysis and that obtained from image analysis using equivalent sphere diameter were in reasonably good agreement.
- From evolution of particle size distributions with increased stresses, specific size group of particles were found to be predominantly subjected to crushing. Moreover, size anisotropy of progressively generated finer particles from crushing showed decreasing values.

- Relative breakage parameter was found to increase at the onset of yielding and thereafter a linear variation with logarithm of vertical pressure could be approximated.
- Transverse isotropic distribution of voids shows preference in perpendicular to the loading direction. Intensity of the preference intensifies while the transverse isotropic distribution becomes more concentrated along two major axes (x and y) in yield and post yield stages.

7.3 Microstructural Behaviour of Cemented Sand

For cemented sand various scalar parameters (e.g. sphericity, void volume, anisotropy) and directional parameter (fabric anisotropy variable, $FAV\ A$) of interparticle void fabric have been investigated in relation to their evolution with progressive one-dimensional stresses. The findings are summarized below:

- More isolated, dispersed and increasingly smaller sized voids are generated in cemented sand samples with increasing cement content. Accumulation of cementing agents at particle contacts, throats and interparticle voids results in such void structure.
- For the similar reasons stated in the earlier point, higher cement quantity modifies void shape towards more spherical shape. This is reflected by the rightward shift of the sphericity distribution curve with increased cement quantity.
- Sphericity distribution curve for the sample with low (10%) cement content exhibits dual peaks with relatively wider spread compared to that for higher

cement content. Dual peaks indicate existence of two distinct group of voids in terms of their sphericity, which results either from insufficiency of cemente quantity or non-homogeneous mixture of cement. With increasing cement quantity (20 and 30%) the peaks gradually diminishes and distribution becomes narrower.

- With increased cement content, anisotropy of voids, a measure of their 3D symmetry, significantly decreases. However, with incremental stresses, anisotropy slightly increases. Larger voids, compared to smaller ones show much higher increase in anisotropy values.
- The 3D fabric tensors of voids for all samples at initial condition show transversely isotropic distributions (i.e., rotational symmetry along the vertical loading axis). For 20% cemented sand, strong biasness of fabric distribution perpendicular to the loading was observed whereas for 30% cemented sand, any directional biasness was absent.
- Under progressive loading, directional biasness of voids for 20% cemented sand intensified. However, orthotropic distributions with rotational shift in orthogonal directions were observed. This notion can be hypothesized with the closure and splitting of voids resulting rotational shift of long-axis. For 30% cemented sand, a relatively complex fabric distributions comprising alternating transversely isotropic and orthotropic types were observed. Interestingly, the 2D tensors and rose diagrams sufficiently represented the fabric orientations as observed in the 3D distributions. Fabric anisotropy variable ($FAV\ A$) were consistent with the graphical representation of the anisotropy.

7.4 Proposed Conceptual Framework for Cemented Sand

A conceptual framework incorporating globally observed behaviour of cemented sand under compression and evolution of its microstructural (void fabric in this study) parameters (scalar and directional) has been proposed. The proposed void-fabric based framework has the potential of depicting insightful explanation of the macro-scale behaviour of cemented sand subjected to 1D compression.

7.5 Recommendations for Future Research

3D image based quantitative analysis of microstructural behaviour of sand or cemented sand as conducted in this study was intensive. Moreover, many additional challenges as presented in chapter 3 had to be addressed. These difficulties have affected different aspects of the study which may have influenced the findings. Based on overall experience, the following recommendations are made for future studies:

- Number of samples used in this study was inadequate to make some of the conclusive remarks on characteristic behaviour of cemented sand. So, at least two samples for each cement content should be tested and analysed. In addition, more frequent cement contents: 15% and 25% can be used to map the gradual changes of microstructure. More frequent stress intervals can also facilitate the understanding of gradual changes of microstructure.
- Quality of the samples used in this study cannot be claimed to be of highest achievable quality. High resolution of images used in this study was capable of picking up apparently minor defects within the sample that may have affected the findings. To improve the method of sample preparation the following

aspects can be improved: machine mixing of sand and cement will improve homogeneity of the mix, larger size sample will reduce the defects originating from handling, preparing sample within the suitable compression cell will avoid unnecessary disturbances to the microstructure of the sample due to manual handling like laying, cutting, smoothening the surfaces.

- Segmentation of void is somewhat ambiguous. However, it can be enhanced if built-in Watershed segmentation method of Avizo is used in conjunction with in-house developed code which can identify a more acceptable point of segmentation. For directional anisotropy analysis, scan line method can be used.
- In addition to void fabric, particle fabric, bond, or contact planes (in the line of study by Dadda et al. (2017), Dadda et al. (2018a), Dadda et al. (2018b))can be analysed in terms of different scalar and directional parameters to explain the global behaviour of cemented sand. Similar conceptual framework as proposed in this study can be developed.
- Microstructural studies based on different other commonly used cementing agents such as lime, flyash, or even clay-cement mixture can be conducted. Other variation of sand in terms of shape (rounded, angular), size (medium or coarse graded), grading (well or gap graded) can be tested and analysed in future studies.
- Instead of 28 days curing time, samples with interim period of curing: 7, 14 and 21 days can be analysed to observe and measure the development of microstructure and their behaviour.

7.6 References

Dadda, A., Geindreau, C., Emeriault, F., du Roscoat, S. R., Filet, A. E. & Garandet, A. 2018a. Characterization of contact properties in biocemented sand using 3D X-ray micro-tomography. Acta Geotechnica, 1-17.

Dadda, A., Geindreau, C., Emeriault, F., du Roscoat, S. R., Garandet, A., Sapin, L. & Filet, A. E. 2017. Characterization of microstructural and physical properties changes in biocemented sand using 3D X-ray microtomography. Acta Geotechnica, 12, 955-970.

Dadda, A., Geindreau, C., Emeriault, F., Filet, A. E. & Garandet, A. 2018b. Influence of the microstructural properties of biocemented sand on its mechanical behavior. Int J Numerical Methods Geomech, 1, 10.

Kanatani, K.-I. 1984. Distribution of directional data and fabric tensors. International Journal of Engineering Science, 22, 149-164.

Appendix A

Thoughts on the proper choice of fabric tensor F within ACST

Thoughts on the proper choice of fabric tensor $\mathbf{F}$ within ACST

The "ideal" deviatoric fabric tensor $\mathbf{F}$ in ACST satisfies the following definition:

$$\mathbf{F}=F\mathbf{n}_F \qquad F=\sqrt{\mathbf{F}:\mathbf{F}} \qquad \mathbf{n}_F:\mathbf{n}_F=1 \qquad \text{At CS one must have } \mathbf{F}=\mathbf{n}_F=\mathbf{n} \qquad (1)$$

where $\mathbf{n}$ is the unit-norm deviatoric plastic strain rate direction at Critical State (CS), and the fabric tensor has been normalized by its CS norm, so that at CS $F=1$. Because both $\mathbf{n}_F$ and $\mathbf{n}$ are unit-norm deviatoric tensors, they must satisfy the conditions

$$tr\ \mathbf{n}_F=0 \qquad tr\ \mathbf{n}_F{}^2=\mathbf{n}_F:\mathbf{n}_F=1 \qquad \text{and} \qquad tr\ \mathbf{n}=0 \qquad tr\ \mathbf{n}^2=\mathbf{n}:\mathbf{n}=1 \qquad (2)$$

Transverse isotropy with direction 1 the axis of rotational symmetry and directions 2 and 3 on the plane of isotropy, implies for $\mathbf{F}$ that the sample has been prepared by correspondingly appropriate methods, e.g. pluviation along direction 1, while for $\mathbf{n}$ transverse isotropy implies triaxial type of deformation with the components 2 and 3 of the plastic strain rate tensor equal. In passing notice that if $\mathbf{F}$ is NOT transversely isotropic with its components 2 and 3 unequal, and one imposes a triaxial loading along direction 1, the induced $\mathbf{n}$ will NOT in general be transversely isotropic because the plastic strain rate tensor will NOT necessarily have its components 2 and 3 equal, because $\mathbf{F}$ does not. Thus, in transverse isotropy one has in conjunction with Eqs. (2):

$$n_{F1}=\pm\frac{2}{\sqrt{6}} \qquad n_{F2}=n_{F3}=\mp\frac{1}{\sqrt{6}} \qquad \text{and} \qquad n_1=\pm\frac{2}{\sqrt{6}} \qquad n_2=n_3=\mp\frac{1}{\sqrt{6}} \qquad (3)$$

where please notice that $\pm$ and $\mp$ are in that order necessarily between the components 1 and 2, 3 for each one of the $\mathbf{n}_F$ and $\mathbf{n}$, but they are NOT necessarily in the same order for $\mathbf{n}_F$ and $\mathbf{n}$.

This last observation in RED is very important when we must choose a fabric tensor from either DEM simulations or CT-X ray scan measurements and use it for application within ACST. The reason is that various fabric tensors behave differently not necessarily satisfying the last relation of Eq.(1). In fact it is easily seen that for a transversely isotropic sample subjected to triaxial compression as per above, one has two opposite outcomes when choosing as fabric tensor either the contact normal orientation based one and symbolized by $\mathbf{F}^c$, or the particle orientation based one and symbolized by $\mathbf{F}^p$. For the contact normal one will have at CS that $\mathbf{F}^c=\mathbf{n}_F^c=\mathbf{n}$ while for the particle orientation one will have $\mathbf{F}^p=\mathbf{n}_F^p=-\mathbf{n}$. In terms of numbers the choice of $\mathbf{F}^c$ will imply that the components of fabric and plastic strain rate direction tensors will have exactly the values shown in Eq. (3) in the same order, while the choice of $\mathbf{F}^p$ will imply that the components of fabric and plastic strain rate direction tensors will have the values of Eq. (3) in opposite order. The important conclusion is that at CS the very important Fabric Anisotropy Variable A, which defines the cardinal for ACST Dilatancy State Parameter (DSP) $\zeta=\psi-e_A(A-1)$ will be given at CS by either $A=\mathbf{F}^c:\mathbf{n}=\mathbf{n}:\mathbf{n}=1$ or $A=\mathbf{F}^p:\mathbf{n}=-\mathbf{n}:\mathbf{n}=-1$. This latter case is unacceptable within ACST because it yields a value $A=-1$ at CS that upsets the role of DSP ζ in the definition of dilatancy. Of course the culprit is the $\mathbf{F}^p=\mathbf{n}_F^p=-\mathbf{n}$ instead of $\mathbf{n}$.

The remedy is in this case VERY simple: Choose as fabric tensor the $-\mathbf{F}^p$.

Appendix B

Matlab codes developed for directional fabric analysis

%Code for 3D directional data distribution with 4th order fabric tensor of the third kind

```
s=load('C30-28D-14100kPa-voidForFabricStudy.mat');
fieldname=fieldnames(s)
m=s.Avizo_C30_28D_14100kPa_voidForFabricStudy_mat ;
sm=squeeze(m);
[L,num2] = bwlabeln(sm);

egnvctr=cell(num2,1); %prealocating cell/array
egnvls=cell(num2,1);  %prealocating cell/array

lngth=zeros(num2,3);
volm=zeros(num2,1);
sfcarea=zeros(num2,1);
sfcvolarea=zeros(num2,1);

n1=zeros(num2,1);
n2=zeros(num2,1);
n3=zeros(num2,1);

thn=zeros(num2,1);
phin=zeros(num2,1);
rn=zeros(num2,1);
thn2Deg=zeros(num2,1);
phin2Deg=zeros(num2,1);

for kk=1:num2
        stats=regionprops3((L==kk),"PrincipalAxisLength","EigenVectors","EigenValues","SurfaceAre
        a","Volume");
        egnvctr(kk,1)=stats.EigenVectors;
        egnvls(kk,:)=stats.EigenValues;
        lngth(kk,:)=stats.PrincipalAxisLength;
        volm(kk,1)=stats.Volume;
        sfcarea(kk,1)=stats.SurfaceArea;
        sfcvolarea(kk,1)=sfcarea(kk,1)./volm(kk,1);
end

egnvctrm=round(cell2mat(egnvctr),4); %Convert cell array to ordinary array
egnvlsm=cell2mat(egnvls);   %Convert cell array to ordinary array

for ii=1:num2
        n1(ii,1)=egnvctrm(ii+2*(ii-1),1);    % Separate each component of vectors in cartesian
coordinate
        n2(ii,1)=egnvctrm(ii+2*(ii-1)+1,1);
        n3(ii,1)=egnvctrm(ii+2*(ii-1)+2,1);
end

[N11,N12,N21,N22,N13,N31,N23,N32,N33]=deal(0);
[N1111,N1112,N1121,N1211,N1122,N1212,N1221,N1222,N2222,N2221,N2212,N2122,N2211,N2121
,N2112,N2111]=deal(0);
```

```
[N1113,N1131,N1311,N1133,N1313,N1331,N1333,N3333,N3331,N3313,N3133,N3311,N3131,N3113
,N3111]=deal(0);
[N2223,N2232,N2322,N2233,N2323,N2332,N2333,N3332,N3323,N3233,N3322,N3232,N3223,N3222
]=deal(0);
[N1123,N1132,N1231,N1213,N1312,N1321,N2113,N2131,N2311,N3121,N3211,N3112]=deal(0);
[N2213,N2231,N2132,N2123,N2321,N2312,N1223,N1232,N1322,N3212,N3122,N3221]=deal(0);
[N3321,N3312,N3213,N3231,N3132,N3123,N2331,N2313,N2133,N1323,N1233,N1332] = deal(0);

for tt=1:num2
        if (tt<num2)
           num3=1;
        else
          num3=num2;
end
% Fabric tensor of first kind of order 2

N11=(N11+n1(tt,1).*n1(tt,1))/num3;
N12=(N12+n1(tt,1).*n2(tt,1))/num3;
N21=(N21+n2(tt,1).*n1(tt,1))/num3;
N22=(N22+n2(tt,1).*n2(tt,1))/num3;
N13=(N13+n1(tt,1).*n3(tt,1))/num3;
N31=(N31+n3(tt,1).*n1(tt,1))/num3;
N33=(N33+n3(tt,1).*n3(tt,1))/num3;
N23=(N23+n2(tt,1).*n3(tt,1))/num3;
N32=(N32+n3(tt,1).*n2(tt,1))/num3;
end

% Fabric tensor of third kind of order 2

D11=15/2*(N11-1/3);
D12=15/2*N12;
D21=15/2*N21;
D22=15/2*(N22-1/3);

D13=15/2*N13;
D31=15/2*N31;
D33=15/2*(N33-1/3);

D23=15/2*N23;
D32=15/2*N32;

% FAV A calculation
F= [D11 D12 D13; D21 D22 D23; D31 D32 D33];
Fnorm=sqrt(D11^2+D22^2+D33^2+D12*D21+D23*D32+D13*D31);
nF=F/Fnorm;
nLV = [sqrt(2/3) 0 0; 0 -1/sqrt(6) 0; 0 0 -1/sqrt(6)]; % Loading vector
FAV= Fnorm*sum(sum(nF.*nLV))
FAV2=sum(sum(F.*nLV))

%Result writing
```

```
%FAV3D = table(D11,D22,D33,D12,D23,D13,Fnorm,FAV);
%filename = '3K3DUncemVoidResultsFAVA25May.xlsx';
%writetable(FAV3D,filename,'Sheet',1,'Range','A15');

% Fabric tensor of first kind of order 4

N1111=(N1111+n1(tt,1).*n1(tt,1).*n1(tt,1).*n1(tt,1))/num3;
N1112=(N1112+n1(tt,1).*n1(tt,1).*n1(tt,1).*n2(tt,1))/num3;
N1121=(N1121+n1(tt,1).*n1(tt,1).*n2(tt,1).*n1(tt,1))/num3;
N1211=(N1211+n1(tt,1).*n2(tt,1).*n1(tt,1).*n1(tt,1))/num3;
N1122=(N1122+n1(tt,1).*n1(tt,1).*n2(tt,1).*n2(tt,1))/num3;
N1212=(N1212+n1(tt,1).*n2(tt,1).*n1(tt,1).*n2(tt,1))/num3;
N1221=(N1221+n1(tt,1).*n2(tt,1).*n2(tt,1).*n1(tt,1))/num3;
N1222=(N1222+n1(tt,1).*n2(tt,1).*n2(tt,1).*n2(tt,1))/num3;
N2222=(N2222+n2(tt,1).*n2(tt,1).*n2(tt,1).*n2(tt,1))/num3;
N2221=(N2221+n2(tt,1).*n2(tt,1).*n2(tt,1).*n1(tt,1))/num3;
N2212=(N2212+n2(tt,1).*n2(tt,1).*n1(tt,1).*n2(tt,1))/num3;
N2122=(N2122+n2(tt,1).*n1(tt,1).*n2(tt,1).*n2(tt,1))/num3;
N2211=(N2211+n2(tt,1).*n2(tt,1).*n1(tt,1).*n1(tt,1))/num3;
N2121=(N2121+n2(tt,1).*n1(tt,1).*n2(tt,1).*n1(tt,1))/num3;
N2112=(N2112+n2(tt,1).*n1(tt,1).*n1(tt,1).*n2(tt,1))/num3;
N2111=(N2111+n2(tt,1).*n1(tt,1).*n1(tt,1).*n1(tt,1))/num3;
N1113=(N1113+n1(tt,1).*n1(tt,1).*n1(tt,1).*n3(tt,1))/num3;
N1131=(N1131+n1(tt,1).*n1(tt,1).*n3(tt,1).*n1(tt,1))/num3;
N1311=(N1311+n1(tt,1).*n3(tt,1).*n1(tt,1).*n1(tt,1))/num3;
N1133=(N1133+n1(tt,1).*n1(tt,1).*n3(tt,1).*n3(tt,1))/num3;
N1313=(N1313+n1(tt,1).*n3(tt,1).*n1(tt,1).*n3(tt,1))/num3;
N1331=(N1331+n1(tt,1).*n3(tt,1).*n3(tt,1).*n1(tt,1))/num3;
N1333=(N1333+n1(tt,1).*n3(tt,1).*n3(tt,1).*n3(tt,1))/num3;
N3333=(N3333+n3(tt,1).*n3(tt,1).*n3(tt,1).*n3(tt,1))/num3;
N3331=(N3331+n3(tt,1).*n3(tt,1).*n3(tt,1).*n1(tt,1))/num3;
N3313=(N3313+n3(tt,1).*n3(tt,1).*n1(tt,1).*n3(tt,1))/num3;
N3133=(N3133+n3(tt,1).*n1(tt,1).*n3(tt,1).*n3(tt,1))/num3;
N3311=(N3311+n3(tt,1).*n3(tt,1).*n1(tt,1).*n1(tt,1))/num3;
N3131=(N3131+n3(tt,1).*n1(tt,1).*n3(tt,1).*n1(tt,1))/num3;
N3113=(N3113+n3(tt,1).*n1(tt,1).*n1(tt,1).*n3(tt,1))/num3;
N3111=(N3111+n3(tt,1).*n1(tt,1).*n1(tt,1).*n1(tt,1))/num3;
N2223=(N2223+n2(tt,1).*n2(tt,1).*n2(tt,1).*n3(tt,1))/num3;
N2232=(N2232+n2(tt,1).*n2(tt,1).*n3(tt,1).*n2(tt,1))/num3;
N2322=(N2322+n2(tt,1).*n3(tt,1).*n2(tt,1).*n2(tt,1))/num3;
N2233=(N2233+n2(tt,1).*n2(tt,1).*n3(tt,1).*n3(tt,1))/num3;
N2323=(N2323+n2(tt,1).*n3(tt,1).*n2(tt,1).*n3(tt,1))/num3;
N2332=(N2332+n2(tt,1).*n3(tt,1).*n3(tt,1).*n2(tt,1))/num3;
N2333=(N2333+n2(tt,1).*n3(tt,1).*n3(tt,1).*n3(tt,1))/num3;
N3332=(N3332+n3(tt,1).*n3(tt,1).*n3(tt,1).*n2(tt,1))/num3;
N3323=(N3323+n3(tt,1).*n3(tt,1).*n2(tt,1).*n3(tt,1))/num3;
N3233=(N3233+n3(tt,1).*n2(tt,1).*n3(tt,1).*n3(tt,1))/num3;
N3322=(N3322+n3(tt,1).*n3(tt,1).*n2(tt,1).*n2(tt,1))/num3;
N3232=(N3232+n3(tt,1).*n2(tt,1).*n3(tt,1).*n2(tt,1))/num3;
N3223=(N3223+n3(tt,1).*n2(tt,1).*n2(tt,1).*n3(tt,1))/num3;
N3222=(N3222+n3(tt,1).*n2(tt,1).*n2(tt,1).*n2(tt,1))/num3;
```

```
N1123=(N1123+n1(tt,1).*n1(tt,1).*n2(tt,1).*n3(tt,1))/num3;
N1132=(N1132+n1(tt,1).*n1(tt,1).*n3(tt,1).*n2(tt,1))/num3;
N1231=(N1231+n1(tt,1).*n2(tt,1).*n3(tt,1).*n1(tt,1))/num3;
N1213=(N1213+n1(tt,1).*n2(tt,1).*n1(tt,1).*n3(tt,1))/num3;
N1312=(N1312+n1(tt,1).*n3(tt,1).*n1(tt,1).*n2(tt,1))/num3;
N1321=(N1321+n1(tt,1).*n3(tt,1).*n2(tt,1).*n1(tt,1))/num3;
N2113=(N2113+n2(tt,1).*n1(tt,1).*n1(tt,1).*n3(tt,1))/num3;
N2131=(N2131+n2(tt,1).*n1(tt,1).*n3(tt,1).*n1(tt,1))/num3;
N2311=(N2311+n2(tt,1).*n3(tt,1).*n1(tt,1).*n1(tt,1))/num3;
N3121=(N3121+n3(tt,1).*n1(tt,1).*n2(tt,1).*n1(tt,1))/num3;
N3211=(N3211+n3(tt,1).*n2(tt,1).*n1(tt,1).*n1(tt,1))/num3;
N3112=(N3112+n3(tt,1).*n1(tt,1).*n1(tt,1).*n2(tt,1))/num3;
N2213=(N2213+n2(tt,1).*n2(tt,1).*n1(tt,1).*n3(tt,1))/num3;
N2231=(N2231+n2(tt,1).*n2(tt,1).*n3(tt,1).*n1(tt,1))/num3;
N2132=(N2132+n2(tt,1).*n1(tt,1).*n3(tt,1).*n2(tt,1))/num3;
N2123=(N2123+n2(tt,1).*n1(tt,1).*n2(tt,1).*n3(tt,1))/num3;
N2321=(N2321+n2(tt,1).*n3(tt,1).*n2(tt,1).*n1(tt,1))/num3;
N2312=(N2312+n2(tt,1).*n3(tt,1).*n1(tt,1).*n2(tt,1))/num3;
N1223=(N1223+n1(tt,1).*n2(tt,1).*n2(tt,1).*n3(tt,1))/num3;
N1232=(N1232+n1(tt,1).*n2(tt,1).*n3(tt,1).*n2(tt,1))/num3;
N1322=(N1322+n1(tt,1).*n3(tt,1).*n2(tt,1).*n2(tt,1))/num3;
N3212=(N3212+n3(tt,1).*n2(tt,1).*n1(tt,1).*n2(tt,1))/num3;
N3122=(N3122+n3(tt,1).*n1(tt,1).*n2(tt,1).*n2(tt,1))/num3;
N3221=(N3221+n3(tt,1).*n2(tt,1).*n2(tt,1).*n1(tt,1))/num3;
N3321=(N3321+n3(tt,1).*n3(tt,1).*n2(tt,1).*n1(tt,1))/num3;
N3312=(N3312+n3(tt,1).*n3(tt,1).*n1(tt,1).*n2(tt,1))/num3;
N3213=(N3213+n3(tt,1).*n2(tt,1).*n1(tt,1).*n3(tt,1))/num3;
N3231=(N3231+n3(tt,1).*n2(tt,1).*n3(tt,1).*n1(tt,1))/num3;
N3132=(N3132+n3(tt,1).*n1(tt,1).*n3(tt,1).*n2(tt,1))/num3;
N3123=(N3123+n3(tt,1).*n1(tt,1).*n2(tt,1).*n3(tt,1))/num3;
N2331=(N2331+n2(tt,1).*n3(tt,1).*n3(tt,1).*n1(tt,1))/num3;
N2313=(N2313+n2(tt,1).*n3(tt,1).*n1(tt,1).*n3(tt,1))/num3;
N2133=(N2133+n2(tt,1).*n1(tt,1).*n3(tt,1).*n3(tt,1))/num3;
N1323=(N1323+n1(tt,1).*n3(tt,1).*n2(tt,1).*n3(tt,1))/num3;
N1233=(N1233+n1(tt,1).*n2(tt,1).*n3(tt,1).*n3(tt,1))/num3;
N1332=(N1332+n1(tt,1).*n3(tt,1).*n3(tt,1).*n2(tt,1))/num3;

end

% Fabric tensor of third kind of order 4

D1111=315/8*(N1111-6/7*N11+3/35);
D1122=315/8*(N1122-6/7*N22+3/35);
D1112=315/8*(N1112-6/7*N12);
D1121=315/8*(N1121-6/7*N21);
D1211=315/8*(N1211);
D1212=315/8*(N1212);
D1221=315/8*(N1221);
D1222=315/8*(N1222);
D2222=315/8*(N2222-6/7*N22+3/35);
D2211=315/8*(N2211-6/7*N11+3/35);
```

```
D2221=315/8*(N2221-6/7*N21);
D2212=315/8*(N2212-6/7*N12);
D2122=315/8*(N2122);
D2121=315/8*(N2121);
D2112=315/8*(N2112);
D2111=315/8*(N2111);
D1133=315/8*(N1133-6/7*N33+3/35);
D1113=315/8*(N1113-6/7*N13);
D1131=315/8*(N1131-6/7*N31);
D1311=315/8*(N1311);
D1313=315/8*(N1313);
D1331=315/8*(N1331);
D1333=315/8*(N1333);
D3333=315/8*(N3333-6/7*N33+3/35);
D3311=315/8*(N3311-6/7*N11+3/35);
D3331=315/8*(N3331-6/7*N31);
D3313=315/8*(N3313-6/7*N13);
D3133=315/8*(N3133);
D3131=315/8*(N3131);
D3113=315/8*(N3113);
D3111=315/8*(N3111);
D2233=315/8*(N2233-6/7*N33+3/35);
D2223=315/8*(N2223-6/7*N23);
D2232=315/8*(N2232-6/7*N32);
D2322=315/8*(N2322);
D2323=315/8*(N2323);
D2332=315/8*(N2332);
D2333=315/8*(N2333);
D3322=315/8*(N3322-6/7*N22+3/35);
D3332=315/8*(N3332-6/7*N32);
D3323=315/8*(N3323-6/7*N23);
D3233=315/8*(N3233);
D3232=315/8*(N3232);
D3223=315/8*(N3223);
D3222=315/8*(N3222);
D1123=315/8*(N1123-6/7*N23);
D1132=315/8*(N1132-6/7*N32);
D1231=315/8*(N1231);
D1213=315/8*(N1213);
D1312=315/8*(N1312);
D1321=315/8*(N1321);
D2113=315/8*(N2113);
D2131=315/8*(N2131);
D2311=315/8*(N2311);
D3121=315/8*(N3121);
D3211=315/8*(N3211);
D3112=315/8*(N3112);
D2213=315/8*(N2213-6/7*N13);
D2231=315/8*(N2231-6/7*N13);
D2132=315/8*N2132;
D2123=315/8*N2123;
```

```
D2321=315/8*N2321;
D2312=315/8*N2312;
D1223=315/8*N1223;
D1232=315/8*N1232;
D1322=315/8*N1322;
D3212=315/8*N3212;
D3122=315/8*N3122;
D3221=315/8*N3221;
D3321=315/8*(N3321-6/7*N21);
D3312=315/8*(N3312-6/7*N12);
D3213=315/8*N3213;
D3231=315/8*N3231;
D3132=315/8*N3132;
D3123=315/8*N3123;
D2331=315/8*N2331;
D2313=315/8*N2313;
D2133=315/8*N2133;
D1323=315/8*N1323;
D1233=315/8*N1233;
D1332=315/8*N1332;

tensor=[N11 N12 N13;N21 N22 N23; N31 N32 N33];
[EigDP,EigVP]=eigs(tensor);
[EigD,EigV]=sortem(EigDP,EigVP);          % confirm sorting in descending order
[Azim,Elev,r2]=cart2sph(EigD(1,1),EigD(2,1),EigD(3,1));
AzimDeg=rad2deg(Azim);
ElevDeg=rad2deg(Elev);

EigV1=EigV(1,1);
EigV2=EigV(2,2);
EigV3=EigV(3,3);

% use of surface

th=0:0.1:2*pi ;
fi=0:0.1:2*pi ;

XX = zeros(length(th),length(fi)) ;
YY = zeros(length(th),length(fi)) ;
ZZ = zeros(length(th),length(fi)) ;


for i = 1:length(th)
   for j = 1:length(fi)

fn=1/(4*pi)*(1+D11.*cos(th(i)).*cos(fi(j)).*cos(th(i)).*cos(fi(j))+(D12+D21).*cos(th(i)).*cos(fi(j)).*sin(t
h(i)).*cos(fi(j))+(D13+D31).*sin(fi(j)).*sin(fi(j))+(D23+D23).*sin(th(i)).*cos(fi(j)).*sin(fi(j))+D22.*sin(th(
i)).*cos(fi(j)).*sin(th(i)).*cos(fi(j))+D33.*sin(fi(j)).*sin(fi(j))+
D1111.*cos(th(i)).*cos(fi(j)).*cos(th(i)).*cos(fi(j)).*cos(th(i)).*cos(fi(j)).*cos(th(i)).*cos(fi(j))+(D1122+
D2211+D1221+D2112+D1212+D2121).*cos(th(i)).*cos(fi(j)).*cos(th(i)).*cos(fi(j)).*sin(th(i)).*cos(fi(j)).
*sin(th(i)).*cos(fi(j))+(D1112+D1121+D1211+D2111).*cos(th(i)).*cos(fi(j)).*cos(th(i)).*cos(fi(j)).*cos(t
```

```
h(i)).*cos(fi(j)).*sin(th(i)).*cos(fi(j))+(D1222+D2122+D2212+D2221).*cos(th(i)).*cos(fi(j)).*sin(th(i)).*
cos(fi(j)).*sin(th(i)).*cos(fi(j)).*sin(th(i)).*cos(fi(j))+D2222.*sin(th(i)).*cos(fi(j)).*sin(th(i)).*cos(fi(j)).*si
n(th(i)).*cos(fi(j)).*sin(th(i)).*cos(fi(j))+(D1133+D3311+D1331+D3113+D1313+D3131).*cos(th(i)).*co
s(fi(j)).*cos(th(i)).*cos(fi(j)).*sin(fi(j)).*sin(fi(j))+(D1113+D1131+D1311+D3111).*cos(th(i)).*cos(fi(j)).*
cos(th(i)).*cos(fi(j)).*cos(th(i)).*cos(fi(j)).*sin(fi(j))+(D1333+D3133+D3313+D3331).*cos(th(i)).*cos(fi(
j)).*sin(fi(j)).*sin(fi(j)).*sin(fi(j))+(D2233+D2323+D3322+D3232+D2332+D3223).*sin(th(i)).*cos(fi(j)).*
sin(th(i)).*cos(fi(j)).*sin(fi(j)).*sin(fi(j))+(D2223+D2232+D2322+D3222).*sin(th(i)).*cos(fi(j)).*sin(th(i))
.*cos(fi(j)).*sin(th(i)).*cos(fi(j)).*sin(fi(j))+(D2333+D3233+D3323+D3332).*sin(th(i)).*cos(fi(j)).*sin(fi(j
)).*sin(fi(j)).*sin(fi(j))+(D1123+D1132+D1231+D1213+D1312+D1321+D2113+D2131+D2311+D3121+
D3211+D3112).*cos(th(i)).*cos(fi(j)).*cos(th(i)).*cos(fi(j)).*sin(th(i)).*cos(fi(j)).*sin(fi(j))+(D2213+D22
31+D2132+D2123+D2321+D2312+D1223+D1232+D1322+D3212+D3122+D3221).*sin(th(i)).*cos(fi(j))
.*sin(th(i)).*cos(fi(j)).*cos(th(i)).*cos(fi(j)).*sin(fi(j))+(D3321+D3312+D3213+D3231+D3132+D3123+D
2331+D2313+D2133+D1323+D1233+D1332).*sin(fi(j)).*sin(fi(j))*sin(th(i)).*cos(fi(j)).*cos(th(i)).*cos(f
i(j))+D3333.*sin(fi(j)).*sin(fi(j)).*sin(fi(j)).*sin(fi(j)));

fnmax=fn;
if (fn[X,Y,Z] = sph2cart(th(i),fi(j),fn);
      %scatter3(X,Y,Z,'.');
      hold on;
      XX(i,j) = X ; YY(i,j) = Y ; ZZ(i,j) = Z ;
   end
end

surf(XX,YY,ZZ);

pbaspect([1 1 1]);
xlabel('X');
ylabel('Y');
zlabel('Z');

%Writing results in Excel file

%Data3Dsingle = table(EigV1,EigV2,EigV3,AzimDeg,ElevDeg,N11,N22,N33);
%Data3Dmultiple = table(lngth, volm, sfcarea, sfcvolarea);

%filename = '3K3D30CemVoidResults7May.xlsx';
%writetable(Data3Dsingle,filename,'Sheet',11,'Range','A1');
%writetable(Data3Dmultiple,filename,'Sheet',11,'Range','I1');
```

% Code for 3D directional data distribution with 2nd and 4th order fabric tensor of the second kind

```
s=load('C30-28D-noload-VoidForFabricStudy.mat');
fieldname=fieldnames(s)
m=s.Avizo_C30_28D_noload_VoidForFabricStudy_mat;
sm=squeeze(m);
[L,num2] = bwlabeln(sm);

%num2=10;
egnvctr=cell(num2,1); %prealocating cell/array
egnvls=cell(num2,1);  %prealocating cell/array

lngth=zeros(num2,3);
volm=zeros(num2,1);
sfcarea=zeros(num2,1);
sfcvolarea=zeros(num2,1);

n1=zeros(num2,1);
n2=zeros(num2,1);
n3=zeros(num2,1);

thn=zeros(num2,1);
phin=zeros(num2,1);
rn=zeros(num2,1);
thn2Deg=zeros(num2,1);
phin2Deg=zeros(num2,1);

for kk=1:num2
%stats=regionprops3((L==kk),"PrincipalAxisLength","EigenVectors","EigenValues","SurfaceArea","Vo
lume");
stats=regionprops3((L==kk),"EigenVectors","EigenValues");
egnvctr(kk,1)=stats.EigenVectors;
egnvls(kk,:)=stats.EigenValues;
%lngth(kk,:)=stats.PrincipalAxisLength;
%volm(kk,1)=stats.Volume;
%sfcarea(kk,1)=stats.SurfaceArea;
%sfcvolarea(kk,1)=sfcarea(kk,1)./volm(kk,1);
end

egnvctrm=round(cell2mat(egnvctr),4); %Convert cell array to ordinary array
egnvlsm=cell2mat(egnvls);   %Convert cell array to ordinary array

for ii=1:num2
        n1(ii,1)=egnvctrm(ii+2*(ii-1),1);    % Separate each component of vectors in cartesian
        coordinate
        n2(ii,1)=egnvctrm(ii+2*(ii-1)+1,1);
        n3(ii,1)=egnvctrm(ii+2*(ii-1)+2,1);
end

[N11,N12,N21,N22,N13,N31,N23,N32,N33]=deal(0);
```

```
[N1111,N1112,N1121,N1211,N1122,N1212,N1221,N1222,N2222,N2221,N2212,N2122,N2211,N2121
,N2112,N2111]=δεαλ(0);
[N1113,N1131,N1311,N1133,N1313,N1331,N1333,N3333,N3331,N3313,N3133,N3311,N3131,N3113
,N3111]=deal(0);
[N2223,N2232,N2322,N2233,N2323,N2332,N2333,N3332,N3323,N3233,N3322,N3232,N3223,N3222
]=deal(0);
[N1123,N1132,N1231,N1213,N1312,N1321,N2113,N2131,N2311,N3121,N3211,N3112]=deal(0);
[N2213,N2231,N2132,N2123,N2321,N2312,N1223,N1232,N1322,N3212,N3122,N3221]=deal(0);
[N3321,N3312,N3213,N3231,N3132,N3123,N2331,N2313,N2133,N1323,N1233,N1332] = deal(0);

for tt=1:num2

if (tt<num2)
    num3=1;
else
   num3=num2;
end

% Fabric tensor of first kind of order 2

N11=(N11+n1(tt,1).*n1(tt,1))/num3;
N12=(N12+n1(tt,1).*n2(tt,1))/num3;
N21=(N21+n2(tt,1).*n1(tt,1))/num3;
N22=(N22+n2(tt,1).*n2(tt,1))/num3;
N13=(N13+n1(tt,1).*n3(tt,1))/num3;
N31=(N31+n3(tt,1).*n1(tt,1))/num3;
N33=(N33+n3(tt,1).*n3(tt,1))/num3;
N23=(N23+n2(tt,1).*n3(tt,1))/num3;
N32=(N32+n3(tt,1).*n2(tt,1))/num3;


% Fabric tensor of first kind of order 4

N1111=(N1111+n1(tt,1).*n1(tt,1).*n1(tt,1).*n1(tt,1))/num3;
N1112=(N1112+n1(tt,1).*n1(tt,1).*n1(tt,1).*n2(tt,1))/num3;
N1121=(N1121+n1(tt,1).*n1(tt,1).*n2(tt,1).*n1(tt,1))/num3;
N1211=(N1211+n1(tt,1).*n2(tt,1).*n1(tt,1).*n1(tt,1))/num3;
N1122=(N1122+n1(tt,1).*n1(tt,1).*n2(tt,1).*n2(tt,1))/num3;
N1212=(N1212+n1(tt,1).*n2(tt,1).*n1(tt,1).*n2(tt,1))/num3;
N1221=(N1221+n1(tt,1).*n2(tt,1).*n2(tt,1).*n1(tt,1))/num3;
N1222=(N1222+n1(tt,1).*n2(tt,1).*n2(tt,1).*n2(tt,1))/num3;
N2222=(N2222+n2(tt,1).*n2(tt,1).*n2(tt,1).*n2(tt,1))/num3;
N2221=(N2221+n2(tt,1).*n2(tt,1).*n2(tt,1).*n1(tt,1))/num3;
N2212=(N2212+n2(tt,1).*n2(tt,1).*n1(tt,1).*n2(tt,1))/num3;
N2122=(N2122+n2(tt,1).*n1(tt,1).*n2(tt,1).*n2(tt,1))/num3;
N2211=(N2211+n2(tt,1).*n2(tt,1).*n1(tt,1).*n1(tt,1))/num3;
N2121=(N2121+n2(tt,1).*n1(tt,1).*n2(tt,1).*n1(tt,1))/num3;
N2112=(N2112+n2(tt,1).*n1(tt,1).*n1(tt,1).*n2(tt,1))/num3;
N2111=(N2111+n2(tt,1).*n1(tt,1).*n1(tt,1).*n1(tt,1))/num3;
N1113=(N1113+n1(tt,1).*n1(tt,1).*n1(tt,1).*n3(tt,1))/num3;
N1131=(N1131+n1(tt,1).*n1(tt,1).*n3(tt,1).*n1(tt,1))/num3;
```

```
N1311=(N1311+n1(tt,1).*n3(tt,1).*n1(tt,1).*n1(tt,1))/num3;
N1133=(N1133+n1(tt,1).*n1(tt,1).*n3(tt,1).*n3(tt,1))/num3;
N1313=(N1313+n1(tt,1).*n3(tt,1).*n1(tt,1).*n3(tt,1))/num3;
N1331=(N1331+n1(tt,1).*n3(tt,1).*n3(tt,1).*n1(tt,1))/num3;
N1333=(N1333+n1(tt,1).*n3(tt,1).*n3(tt,1).*n3(tt,1))/num3;
N3333=(N3333+n3(tt,1).*n3(tt,1).*n3(tt,1).*n3(tt,1))/num3;
N3331=(N3331+n3(tt,1).*n3(tt,1).*n3(tt,1).*n1(tt,1))/num3;
N3313=(N3313+n3(tt,1).*n3(tt,1).*n1(tt,1).*n3(tt,1))/num3;
N3133=(N3133+n3(tt,1).*n1(tt,1).*n3(tt,1).*n3(tt,1))/num3;
N3311=(N3311+n3(tt,1).*n3(tt,1).*n1(tt,1).*n1(tt,1))/num3;
N3131=(N3131+n3(tt,1).*n1(tt,1).*n3(tt,1).*n1(tt,1))/num3;
N3113=(N3113+n3(tt,1).*n1(tt,1).*n1(tt,1).*n3(tt,1))/num3;
N3111=(N3111+n3(tt,1).*n1(tt,1).*n1(tt,1).*n1(tt,1))/num3;
N2223=(N2223+n2(tt,1).*n2(tt,1).*n2(tt,1).*n3(tt,1))/num3;
N2232=(N2232+n2(tt,1).*n2(tt,1).*n3(tt,1).*n2(tt,1))/num3;
N2322=(N2322+n2(tt,1).*n3(tt,1).*n2(tt,1).*n2(tt,1))/num3;
N2233=(N2233+n2(tt,1).*n2(tt,1).*n3(tt,1).*n3(tt,1))/num3;
N2323=(N2323+n2(tt,1).*n3(tt,1).*n2(tt,1).*n3(tt,1))/num3;
N2332=(N2332+n2(tt,1).*n3(tt,1).*n3(tt,1).*n2(tt,1))/num3;
N2333=(N2333+n2(tt,1).*n3(tt,1).*n3(tt,1).*n3(tt,1))/num3;
N3332=(N3332+n3(tt,1).*n3(tt,1).*n3(tt,1).*n2(tt,1))/num3;
N3323=(N3323+n3(tt,1).*n3(tt,1).*n2(tt,1).*n3(tt,1))/num3;
N3233=(N3233+n3(tt,1).*n2(tt,1).*n3(tt,1).*n3(tt,1))/num3;
N3322=(N3322+n3(tt,1).*n3(tt,1).*n2(tt,1).*n2(tt,1))/num3;
N3232=(N3232+n3(tt,1).*n2(tt,1).*n3(tt,1).*n2(tt,1))/num3;
N3223=(N3223+n3(tt,1).*n2(tt,1).*n2(tt,1).*n3(tt,1))/num3;
N3222=(N3222+n3(tt,1).*n2(tt,1).*n2(tt,1).*n2(tt,1))/num3;
N1123=(N1123+n1(tt,1).*n1(tt,1).*n2(tt,1).*n3(tt,1))/num3;
N1132=(N1132+n1(tt,1).*n1(tt,1).*n3(tt,1).*n2(tt,1))/num3;
N1231=(N1231+n1(tt,1).*n2(tt,1).*n3(tt,1).*n1(tt,1))/num3;
N1213=(N1213+n1(tt,1).*n2(tt,1).*n1(tt,1).*n3(tt,1))/num3;
N1312=(N1312+n1(tt,1).*n3(tt,1).*n1(tt,1).*n2(tt,1))/num3;
N1321=(N1321+n1(tt,1).*n3(tt,1).*n2(tt,1).*n1(tt,1))/num3;
N2113=(N2113+n2(tt,1).*n1(tt,1).*n1(tt,1).*n3(tt,1))/num3;
N2131=(N2131+n2(tt,1).*n1(tt,1).*n3(tt,1).*n1(tt,1))/num3;
N2311=(N2311+n2(tt,1).*n3(tt,1).*n1(tt,1).*n1(tt,1))/num3;
N3121=(N3121+n3(tt,1).*n1(tt,1).*n2(tt,1).*n1(tt,1))/num3;
N3211=(N3211+n3(tt,1).*n2(tt,1).*n1(tt,1).*n1(tt,1))/num3;
N3112=(N3112+n3(tt,1).*n1(tt,1).*n1(tt,1).*n2(tt,1))/num3;
N2213=(N2213+n2(tt,1).*n2(tt,1).*n1(tt,1).*n3(tt,1))/num3;
N2231=(N2231+n2(tt,1).*n2(tt,1).*n3(tt,1).*n1(tt,1))/num3;
N2132=(N2132+n2(tt,1).*n1(tt,1).*n3(tt,1).*n2(tt,1))/num3;
N2123=(N2123+n2(tt,1).*n1(tt,1).*n2(tt,1).*n3(tt,1))/num3;
N2321=(N2321+n2(tt,1).*n3(tt,1).*n2(tt,1).*n1(tt,1))/num3;
N2312=(N2312+n2(tt,1).*n3(tt,1).*n1(tt,1).*n2(tt,1))/num3;
N1223=(N1223+n1(tt,1).*n2(tt,1).*n2(tt,1).*n3(tt,1))/num3;
N1232=(N1232+n1(tt,1).*n2(tt,1).*n3(tt,1).*n2(tt,1))/num3;
N1322=(N1322+n1(tt,1).*n3(tt,1).*n2(tt,1).*n2(tt,1))/num3;
N3212=(N3212+n3(tt,1).*n2(tt,1).*n1(tt,1).*n2(tt,1))/num3;
N3122=(N3122+n3(tt,1).*n1(tt,1).*n2(tt,1).*n2(tt,1))/num3;
N3221=(N3221+n3(tt,1).*n2(tt,1).*n2(tt,1).*n1(tt,1))/num3;
```

```
N3321=(N3321+n3(tt,1).*n3(tt,1).*n2(tt,1).*n1(tt,1))/num3;
N3312=(N3312+n3(tt,1).*n3(tt,1).*n1(tt,1).*n2(tt,1))/num3;
N3213=(N3213+n3(tt,1).*n2(tt,1).*n1(tt,1).*n3(tt,1))/num3;
N3231=(N3231+n3(tt,1).*n2(tt,1).*n3(tt,1).*n1(tt,1))/num3;
N3132=(N3132+n3(tt,1).*n1(tt,1).*n3(tt,1).*n2(tt,1))/num3;
N3123=(N3123+n3(tt,1).*n1(tt,1).*n2(tt,1).*n3(tt,1))/num3;
N2331=(N2331+n2(tt,1).*n3(tt,1).*n3(tt,1).*n1(tt,1))/num3;
N2313=(N2313+n2(tt,1).*n3(tt,1).*n1(tt,1).*n3(tt,1))/num3;
N2133=(N2133+n2(tt,1).*n1(tt,1).*n3(tt,1).*n3(tt,1))/num3;
N1323=(N1323+n1(tt,1).*n3(tt,1).*n2(tt,1).*n3(tt,1))/num3;
N1233=(N1233+n1(tt,1).*n2(tt,1).*n3(tt,1).*n3(tt,1))/num3;
N1332=(N1332+n1(tt,1).*n3(tt,1).*n3(tt,1).*n2(tt,1))/num3;

end

% Fabric tensor of second kind of order 2

F11=15/2*(N11-1/5);
F12=15/2*N12;
F21=15/2*N21;
F22=15/2*(N22-1/5);

F13=15/2*N13;
F31=15/2*N31;
F33=15/2*(N33-1/5);

F23=15/2*N23;
F32=15/2*N32;


%Fabric Anisotropic Variable (FAV)

p=1/3*(F11+F22+F33);
F= [(F11-p) F12 F13; F21 (F22-p) F23; F31 F32 (F33-p)];
Fnorm=sqrt((F11-p)^2+(F22-p)^2+(F33-p)^2+F12*F21+F23*F32+F13*F31);
nF=F/Fnorm; %the unit-norm deviatoric tensor-valued direction nF
nLV = [-1/sqrt(6) 0 0; 0 sqrt(2/3) 0; 0 0 -1/sqrt(6)]; % Loading vector
FAV= Fnorm*sum(sum(nF.*nLV))
FAV2=sum(sum(F.*nLV))

[V,D]=eig(F);

%Result writing

FAV3D = table(D11,D22,D33,D12,D23,D13,Fnorm,FAV);

filename = 'FAVOCT3.xlsx';
writetable(FAV3D,filename,'Sheet',1,'Range','A15');
```

```
% Fabric tensor of second kind of order 4

F1111=315/8*(N1111-2/3*N11+1/21);
F1122=315/8*(N1122-2/3*N22+1/21);
F1112=315/8*(N1112-2/3*N12);
F1121=315/8*(N1121-2/3*N21);
F1211=315/8*(N1211);
F1212=315/8*(N1212);
F1221=315/8*(N1221);
F1222=315/8*(N1222);

F2222=315/8*(N2222-2/3*N22+1/21);
F2211=315/8*(N2211-2/3*N11+1/21);
F2221=315/8*(N2221-2/3*N21);
F2212=315/8*(N2212-2/3*N12);
F2122=315/8*(N2122);
F2121=315/8*(N2121);
F2112=315/8*(N2112);
F2111=315/8*(N2111);

F1133=315/8*(N1133-2/3*N33+1/21);
F1113=315/8*(N1113-2/3*N13);
F1131=315/8*(N1131-2/3*N31);
F1311=315/8*(N1311);
F1313=315/8*(N1313);
F1331=315/8*(N1331);
F1333=315/8*(N1333);
F3333=315/8*(N3333-2/3*N33+1/21);
F3311=315/8*(N3311-2/3*N11+1/21);
F3331=315/8*(N3331-2/3*N31);
F3313=315/8*(N3313-2/3*N13);
F3133=315/8*(N3133);
F3131=315/8*(N3131);
F3113=315/8*(N3113);
F3111=315/8*(N3111);
F2233=315/8*(N2233-2/3*N33+1/21);
F2223=315/8*(N2223-2/3*N23);
F2232=315/8*(N2232-2/3*N32);
F2322=315/8*(N2322);
F2323=315/8*(N2323);
F2332=315/8*(N2332);
F2333=315/8*(N2333);
F3322=315/8*(N3322-2/3*N22+1/21);
F3332=315/8*(N3332-2/3*N32);
F3323=315/8*(N3323-2/3*N23);
F3233=315/8*(N3233);
F3232=315/8*(N3232);
F3223=315/8*(N3223);
F3222=315/8*(N3222);

F1123=315/8*(N1123-2/3*N23);
```

```
F1132=315/8*(N1132-2/3*N32);
F1231=315/8*(N1231);
F1213=315/8*(N1213);
F1312=315/8*(N1312);
F1321=315/8*(N1321);
F2113=315/8*(N2113);
F2131=315/8*(N2131);
F2311=315/8*(N2311);
F3121=315/8*(N3121);
F3211=315/8*(N3211);
F3112=315/8*(N3112);

F2213=315/8*(N2213-2/3*N13);
F2231=315/8*(N2231-2/3*N13);
F2132=315/8*N2132;
F2123=315/8*N2123;
F2321=315/8*N2321;
F2312=315/8*N2312;
F1223=315/8*N1223;
F1232=315/8*N1232;
F1322=315/8*N1322;
F3212=315/8*N3212;
F3122=315/8*N3122;
F3221=315/8*N3221;

F3321=315/8*(N3321-2/3*N21);
F3312=315/8*(N3312-2/3*N12);
F3213=315/8*N3213;
F3231=315/8*N3231;
F3132=315/8*N3132;
F3123=315/8*N3123;
F2331=315/8*N2331;
F2313=315/8*N2313;
F2133=315/8*N2133;
F1323=315/8*N1323;
F1233=315/8*N1233;
F1332=315/8*N1332;

tensor=[N11 N12 N13;N21 N22 N23; N31 N32 N33];
[EigDP,EigVP]=eigs(tensor);
[EigD,EigV]=sortem(EigDP,EigVP);          % confirm sorting in descending order
[Azim,Elev,r2]=cart2sph(EigD(1,1),EigD(2,1),EigD(3,1));

AzimDeg=rad2deg(Azim);
ElevDeg=rad2deg(Elev);

EigV1=EigV(1,1);
EigV2=EigV(2,2);
EigV3=EigV(3,3);

% use of surface
```

```
th=0:0.1:2*pi ;
fi=0:0.1:2*pi ;

XX = zeros(length(th),length(fi)) ;
YY = zeros(length(th),length(fi)) ;
ZZ = zeros(length(th),length(fi)) ;

fnmax=0;

for i = 1:length(th)
   for j = 1:length(fi)

%2nd kind 4th order
fn=1/(4*pi)*(F1111.*cos(th(i)).*cos(fi(j)).*cos(th(i)).*cos(fi(j)).*cos(th(i)).*cos(fi(j)).*cos(th(i)).*cos(fi(
j))+(F1122+F2211+F1221+F2112+F1212+F2121).*cos(th(i)).*cos(fi(j)).*cos(th(i)).*cos(fi(j)).*sin(th(i)).
*cos(fi(j)).*sin(th(i)).*cos(fi(j))+(F1112+F1121+F1211+F2111).*cos(th(i)).*cos(fi(j)).*cos(th(i)).*cos(fi(j
)).*cos(th(i)).*cos(fi(j)).*sin(th(i)).*cos(fi(j))+(F1222+F2122+F2212+F2221).*cos(th(i)).*cos(fi(j)).*sin(t
h(i)).*cos(fi(j)).*sin(th(i)).*cos(fi(j)).*sin(th(i)).*cos(fi(j))+F2222.*sin(th(i)).*cos(fi(j)).*sin(th(i)).*cos(fi(
j)).*sin(th(i)).*cos(fi(j)).*sin(th(i)).*cos(fi(j))+(F1133+F3311+F1331+F3113+F1313+F3131).*cos(th(i)).
*cos(fi(j)).*cos(th(i)).*cos(fi(j)).*sin(fi(j)).*sin(fi(j))+(F1113+F1131+F1311+F3111).*cos(th(i)).*cos(fi(j)
).*cos(th(i)).*cos(fi(j)).*cos(th(i)).*cos(fi(j)).*sin(fi(j))+(F1333+F3133+F3313+F3331).*cos(th(i)).*cos(fi
(j)).*sin(fi(j)).*sin(fi(j)).*sin(fi(j))+(F2233+F2323+F3322+F3232+F2332+F3223).*sin(th(i)).*cos(fi(j)).*si
n(th(i)).*cos(fi(j)).*sin(fi(j)).*sin(fi(j))+(F2223+F2232+F2322+F3222).*sin(th(i)).*cos(fi(j)).*sin(th(i)).*c
os(fi(j)).*sin(th(i)).*cos(fi(j)).*sin(fi(j))+(F2333+F3233+F3323+F3332).*sin(th(i)).*cos(fi(j)).*sin(fi(j)).*s
in(fi(j)).*sin(fi(j))+(F1123+F1132+F1231+F1213+F1312+F1321+F2113+F2131+F2311+F3121+F3211+F
3112).*cos(th(i)).*cos(fi(j)).*cos(th(i)).*cos(fi(j)).*sin(th(i)).*cos(fi(j)).*sin(fi(j))+(F2213+F2231+F2132
+F2123+F2321+F2312+F1223+F1232+F1322+F3212+F3122+F3221).*sin(th(i)).*cos(fi(j)).*sin(th(i)).*c
os(fi(j)).*cos(th(i)).*cos(fi(j)).*sin(fi(j))+(F3321+F3312+F3213+F3231+F3132+F3123+F2331+F2313+F2
133+F1323+F1233+F1332).*sin(fi(j)).*sin(fi(j))*sin(th(i)).*cos(fi(j)).*cos(th(i)).*cos(fi(j))+F3333.*sin(fi
(j)).*sin(fi(j)).*sin(fi(j)).*sin(fi(j)))

%2nd kind 2nd order

fn=1/(4*pi)*(F11.*cos(th(i)).*cos(fi(j)).*cos(th(i)).*cos(fi(j))+(F12+F21).*cos(th(i)).*cos(fi(j)).*sin(th(i)
).*cos(fi(j))+F22.*sin(th(i)).*cos(fi(j)).*sin(th(i)).*cos(fi(j))+(F13+F31).*cos(th(i)).*cos(fi(j)).*sin(fi(j))+(
F23+F32).*sin(th(i)).*cos(fi(j)).*sin(fi(j))+F33.*sin(fi(j)).*sin(fi(j)))

if(fn > fnmax)
   fnmax=fn;
   else
   fnmax=fnmax;
end

   end
end

for i = 1:length(th)
   for j = 1:length(fi)

%2nd kind 4th order
```

```
fn=1/(4*pi)*(F1111.*cos(th(i)).*cos(fi(j)).*cos(th(i)).*cos(fi(j)).*cos(th(i)).*cos(fi(j)).*cos(th(i)).*cos(fi(
j))+(F1122+F2211+F1221+F2112+F1212+F2121).*cos(th(i)).*cos(fi(j)).*cos(th(i)).*cos(fi(j)).*sin(th(i)).
*cos(fi(j)).*sin(th(i)).*cos(fi(j))+(F1112+F1121+F1211+F2111).*cos(th(i)).*cos(fi(j)).*cos(th(i)).*cos(fi(j
)).*cos(th(i)).*cos(fi(j)).*sin(th(i)).*cos(fi(j))+(F1222+F2122+F2212+F2221).*cos(th(i)).*cos(fi(j)).*sin(t
h(i)).*cos(fi(j)).*sin(th(i)).*cos(fi(j)).*sin(th(i)).*cos(fi(j))+F2222.*sin(th(i)).*cos(fi(j)).*sin(th(i)).*cos(fi(
j)).*sin(th(i)).*cos(fi(j)).*sin(th(i)).*cos(fi(j))+(F1133+F3311+F1331+F3113+F1313+F3131).*cos(th(i)).
*cos(fi(j)).*cos(th(i)).*cos(fi(j)).*sin(fi(j)).*sin(fi(j))+(F1113+F1131+F1311+F3111).*cos(th(i)).*cos(fi(j)
).*cos(th(i)).*cos(fi(j)).*cos(th(i)).*cos(fi(j)).*sin(fi(j))+(F1333+F3133+F3313+F3331).*cos(th(i)).*cos(fi
(j)).*sin(fi(j)).*sin(fi(j)).*sin(fi(j))+(F2233+F2323+F3322+F3232+F2332+F3223).*sin(th(i)).*cos(fi(j)).*si
n(th(i)).*cos(fi(j)).*sin(fi(j)).*sin(fi(j))+(F2223+F2232+F2322+F3222).*sin(th(i)).*cos(fi(j)).*sin(th(i)).*c
os(fi(j)).*sin(th(i)).*cos(fi(j)).*sin(fi(j))+(F2333+F3233+F3323+F3332).*sin(th(i)).*cos(fi(j)).*sin(fi(j)).*s
in(fi(j)).*sin(fi(j))+(F1123+F1132+F1231+F1213+F1312+F1321+F2113+F2131+F2311+F3121+F3211+F
3112).*cos(th(i)).*cos(fi(j)).*cos(th(i)).*cos(fi(j)).*sin(th(i)).*cos(fi(j)).*sin(fi(j))+(F2213+F2231+F2132
+F2123+F2321+F2312+F1223+F1232+F1322+F3212+F3122+F3221).*sin(th(i)).*cos(fi(j)).*sin(th(i)).*c
os(fi(j)).*cos(th(i)).*cos(fi(j)).*sin(fi(j))+(F3321+F3312+F3213+F3231+F3132+F3123+F2331+F2313+F2
133+F1323+F1233+F1332).*sin(fi(j)).*sin(fi(j))*sin(th(i)).*cos(fi(j)).*cos(th(i)).*cos(fi(j))+F3333.*sin(fi
(j)).*sin(fi(j)).*sin(fi(j)).*sin(fi(j)))

%2nd kind 2nd order
fn=1/(4*pi)*(F11.*cos(th(i)).*cos(fi(j)).*cos(th(i)).*cos(fi(j))+(F12+F21).*cos(th(i)).*cos(fi(j)).*sin(th(i)
).*cos(fi(j))+F22.*sin(th(i)).*cos(fi(j)).*sin(th(i)).*cos(fi(j))+(F13+F31).*cos(th(i)).*cos(fi(j)).*sin(fi(j))+(
F23+F32).*sin(th(i)).*cos(fi(j)).*sin(fi(j))+F33.*sin(fi(j)).*sin(fi(j)))

      [X,Y,Z] = sph2cart(th(i),fi(j),fn/fnmax);
      scatter3(X,Y,Z,'.r');
      hold on;
      XX(i,j) = X ; YY(i,j) = Y ; ZZ(i,j) = Z ;
   end
end

surf(XX,YY,ZZ);

pbaspect([1 1 1]);
xlabel('X');
ylabel('Y');
zlabel('Z');

%Writing results in Excel file

Data3Dsingle = table(EigV1,EigV2,EigV3,AzimDeg,ElevDeg,N11,N22,N33);
Data3Dmultiple = table(lngth, volm, sfcarea, sfcvolarea);

filename = '3K3DUnCemVoidResults7May.xlsx';
writetable(Data3Dsingle,filename,'Sheet',5,'Range','A1');
writetable(Data3Dmultiple,filename,'Sheet',5,'Range','I1');
```

%Code for 2D directional data distribution with 2nd and 4th order fabric tensor of the second kind

```
%"Index exceeds matrix dimensions." error means perhaps particle of only
% one voxel exists. Need to remove single particle for this program, bwareaopen function used for
that.

s=load('C30-28D-79300kPa-voidForFabricStudy.mat'); % load the image structure
fieldname=fieldnames(s)          % know the fieldname of the structure
m=s.Avizo_C30_28D_79300kPa_voidForFabricStudy_mat; % extract array from structure [x by y (i.e
column x row)] = 61 x 54)
sm=squeeze(m);                   % remove singleton dimension (row x column = 61 x 54)
sm = bwareaopen(sm,2,4);         % remove small objects from binary image of less than 2 pixel and
                        % connectivity of 4 (only 4 faces and not corners)
szdim=size(sm,3);                % returns the length of dimension dim.
slices=szdim;                    % number of slices that need to be analyzed
pieslice=25;                     % number of edges of polar histogram. It is number of divisions+1 of pie.
TbinVectorSum=zeros(1,pieslice-1);
indcs=zeros(size(sm,1),size(sm,2));
N11=zeros(slices,1);             %initialiaing coefficients of second order tensor
N12=zeros(slices,1);
N21=zeros(slices,1);
N22=zeros(slices,1);
N1111=zeros(slices,1);
N1122=zeros(slices,1);
N1112=zeros(slices,1);
N1121=zeros(slices,1);
N1211=zeros(slices,1);
N1212=zeros(slices,1);
N1221=zeros(slices,1);
N1222=zeros(slices,1);
N2222=zeros(slices,1);
N2221=zeros(slices,1);
N2212=zeros(slices,1);
N2122=zeros(slices,1);
N2211=zeros(slices,1);
N2121=zeros(slices,1);
N2112=zeros(slices,1);
N2111=zeros(slices,1);
F11=zeros(slices,1);
F12=zeros(slices,1);
F21=zeros(slices,1);
F22=zeros(slices,1);
F1111=zeros(slices,1);
F1122=zeros(slices,1);
F1112=zeros(slices,1);
F1121=zeros(slices,1);
F1211=zeros(slices,1);
F1212=zeros(slices,1);
F1221=zeros(slices,1);
F1222=zeros(slices,1);
F2222=zeros(slices,1);
```

```
F2211=zeros(slices,1);
F2221=zeros(slices,1);
F2212=zeros(slices,1);
F2122=zeros(slices,1);
F2121=zeros(slices,1);
F2112=zeros(slices,1);
F2111=zeros(slices,1);

porientdSlice=zeros(slices,1);
num=zeros(slices,1);      % number of objects in each slice

edges=zeros(1,pieslice);
NSlice1=zeros(slices,1);
NSlice2=zeros(slices,1);
deltaSlice=zeros(slices,1);
sumperea=zeros(slices,1);
pereaSlice=zeros(slices,1);

for jj=1:slices
   [L2,num(jj,1)] = bwlabel(sm(:,:,jj)); %label binary image and name it L2, count number of object in
of each slice

perip=zeros(num(jj,1),1);     % initialize perimeter of each object per slice
areap=zeros(num(jj,1),1);     % initialize area of each object per slice
perea=zeros(num(jj,1),1) ;    % initialize perimeter-area ratio of each object per slice

vector=zeros(num(jj,1),2);    % initialize vector of each object per slice
thetap=zeros(1,2.*num(jj,1));  % initialize alignment of each vector (with mirror) wrto y axis for each
slice


for ii=1:num(jj,1)           % find index of pixels for each object of each slice
   [r c]=find(L2==ii);      % Pick index (x,y) of each pixel of every object (ii) to (r,c) array
   indcs=[r c];             % name all pixels per slice and the (r,c) array
perio=regionprops((L2==ii),'perimeter'); %Find perimeter for each object(ii) of the image (transposing
                                                                                image makes no different)
perip(ii,1)=perio.Perimeter;           % perimeter of each object of  each slice
areao=regionprops((L2==ii),'area'); %Find area for each object(ii) of the image (transposing
image makes no different)
  areap(ii,1)=areao.Area;          % actual area of each object(ii) per slice (jj), Use when considering the
                                                                                    influence of area
perea(ii,1)=perip(ii,1)./areap(ii,1);% perimeter-area ratio of each object(ii) per slice (jj)
coeff=pca(indcs);       %perform pca (principal component analysis) for pixels of each object per slice
       vector(ii,1)=coeff(2,1);   %cos(theta), where theta is clockwise angle with +y axis.  %Store vector
                                                    coordinates of first principal component for each object(ii)
      vector(ii,2)=coeff(1,1);   %sin(theta), %To allign the coefficients against y (vertical) axis (as n1 is y
                                                    component of vector), position of the coefficients
                          %are interchanged to get the angle(theta) against %y axis. So, n1=vector(ii,1)
and n2=vector(ii,2).
sumperea(jj,1)=sumperea(jj,1)+perea(ii,1);% sum of perimeter-area ratios of all particles in each slice
```

```
end

pereaSlice(jj,1)=sumperea(jj,1)./num(jj); % average of area-perimeter ratios of all particles in each slice
                                % by dividing the sum of ratios of each slice by number of particles
vectord=[vector;-vector]; % mirror the points

for mm=1:2*num(jj,1)

   thetap(mm)=atan2d(vectord(mm,2),vectord(mm,1)); % find inclination of long axis of each object w r to vertical axis.
      if (thetap(mm) < 0)
         thetap(mm)=360+thetap(mm);
      else
         thetap(mm)=thetap(mm);
      end
end

for nn = 1:pieslice                    %define edges of polar histogram in radian
edges(1,nn)=(nn-1).*pi/((pieslice-1)./2);
end

hbin = histcounts(round(deg2rad(thetap),4),round(edges,4)); % hbin allocates bin number to each theta

TbinVectorSum= TbinVectorSum+hbin; % bin wise sum of vectors for all slices


% Find components of Kananti's fabric tensor of first kind (moment tensor).
% Here, N11, fabric tensor of first kind, is Average of sum of product of components(n1n1=cos(theta)*cos(theta))along vertical (y) axis and N22 is average of sum product of
% components (n2n2= sin(theta)*sin(theta)) along the horizontal (x) axis. So, larger value of N11 indicates particles are aligned mostly in vertical direction and vice versa.

% Slicewise Sum of of product of components order 2

for tt=1:2*num(jj,1)

N11(jj,1)=N11(jj,1)+vectord(tt,1).*vectord(tt,1);
N12(jj,1)=N12(jj,1)+vectord(tt,1).*vectord(tt,2);
N21(jj,1)=N21(jj,1)+vectord(tt,2).*vectord(tt,1);
N22(jj,1)=N22(jj,1)+vectord(tt,2).*vectord(tt,2);

% Slicewise Sum of product of components order 4

N1111(jj,1)=N1111(jj,1)+vectord(tt,1).*vectord(tt,1).*vectord(tt,1).*vectord(tt,1);
N1112(jj,1)=N1112(jj,1)+vectord(tt,1).*vectord(tt,1).*vectord(tt,1).*vectord(tt,2);
N1121(jj,1)=N1121(jj,1)+vectord(tt,1).*vectord(tt,1).*vectord(tt,2).*vectord(tt,1);
N1211(jj,1)=N1211(jj,1)+vectord(tt,1).*vectord(tt,2).*vectord(tt,1).*vectord(tt,1);
N1122(jj,1)=N1122(jj,1)+vectord(tt,1).*vectord(tt,1).*vectord(tt,2).*vectord(tt,2);
N1212(jj,1)=N1212(jj,1)+vectord(tt,1).*vectord(tt,2).*vectord(tt,1).*vectord(tt,2);
```

```
N1221(jj,1)=N1221(jj,1)+vectord(tt,1).*vectord(tt,2).*vectord(tt,2).*vectord(tt,1);
N1222(jj,1)=N1222(jj,1)+vectord(tt,1).*vectord(tt,2).*vectord(tt,2).*vectord(tt,2);
N2222(jj,1)=N2222(jj,1)+vectord(tt,2).*vectord(tt,2).*vectord(tt,2).*vectord(tt,2);
N2221(jj,1)=N2221(jj,1)+vectord(tt,2).*vectord(tt,2).*vectord(tt,2).*vectord(tt,1);
N2212(jj,1)=N2212(jj,1)+vectord(tt,2).*vectord(tt,2).*vectord(tt,1).*vectord(tt,2);
N2122(jj,1)=N2122(jj,1)+vectord(tt,2).*vectord(tt,1).*vectord(tt,2).*vectord(tt,2);
N2211(jj,1)=N2211(jj,1)+vectord(tt,2).*vectord(tt,2).*vectord(tt,1).*vectord(tt,1);
N2121(jj,1)=N2121(jj,1)+vectord(tt,2).*vectord(tt,1).*vectord(tt,2).*vectord(tt,1);
N2112(jj,1)=N2112(jj,1)+vectord(tt,2).*vectord(tt,1).*vectord(tt,1).*vectord(tt,2);
N2111(jj,1)=N2111(jj,1)+vectord(tt,2).*vectord(tt,1).*vectord(tt,1).*vectord(tt,1);
end

% Slicewise Fabric tensor of order 2 (average of sum of product of components order 2)

N11(jj,1)=N11(jj,1)./(2*num(jj,1));
N12(jj,1)=N12(jj,1)./(2*num(jj,1));
N21(jj,1)=N21(jj,1)./(2*num(jj,1));
N22(jj,1)=N22(jj,1)./(2*num(jj,1));

%Slicewise Fabric tensor of order 4 (average values of sum of product of components order 4)

N1111(jj,1)=N1111(jj,1)./(2*num(jj,1));
N1112(jj,1)=N1112(jj,1)./(2*num(jj,1));
N1121(jj,1)=N1121(jj,1)./(2*num(jj,1));
N1211(jj,1)=N1211(jj,1)./(2*num(jj,1));
N1122(jj,1)=N1122(jj,1)./(2*num(jj,1));
N1212(jj,1)=N1212(jj,1)./(2*num(jj,1));
N1221(jj,1)=N1221(jj,1)./(2*num(jj,1));
N1222(jj,1)=N1222(jj,1)./(2*num(jj,1));
N2222(jj,1)=N2222(jj,1)./(2*num(jj,1));
N2221(jj,1)=N2221(jj,1)./(2*num(jj,1));
N2212(jj,1)=N2212(jj,1)./(2*num(jj,1));
N2122(jj,1)=N2122(jj,1)./(2*num(jj,1));
N2211(jj,1)=N2211(jj,1)./(2*num(jj,1));
N2121(jj,1)=N2121(jj,1)./(2*num(jj,1));
N2112(jj,1)=N2112(jj,1)./(2*num(jj,1));
N2111(jj,1)=N2111(jj,1)./(2*num(jj,1));
% Slicewise Fabric tensor of second kind order 2
F11(jj,1)=4.*(N11(jj,1)-1/4);
F12(jj,1)=4.*N12(jj,1);
F21(jj,1)=4.*N21(jj,1);
F22(jj,1)=4.*(N22(jj,1)-1/4);


% Slicewise Fabric tensor of second kind order 4
F1111(jj,1)=16.*(N1111(jj,1)-3/4.*N11(jj,1)+1/16);
F1122(jj,1)=16.*(N1122(jj,1)-3/4.*N22(jj,1)+1/16);
F1112(jj,1)=16.*(N1112(jj,1)-3/4.*N12(jj,1));
F1121(jj,1)=16.*(N1121(jj,1)-3/4.*N21(jj,1));
F1211(jj,1)=16.*(N1211(jj,1));
F1212(jj,1)=16.*(N1212(jj,1));
```

```
F1221(jj,1)=16.*(N1221(jj,1));
F1222(jj,1)=16.*(N1222(jj,1));
F2222(jj,1)=16.*(N2222(jj,1)-3/4.*N22(jj,1)+1/16);
F2211(jj,1)=16.*(N2211(jj,1)-3/4.*N11(jj,1)+1/16);
F2221(jj,1)=16.*(N2221(jj,1)-3/4.*N21(jj,1));
F2212(jj,1)=16.*(N2212(jj,1)-3/4.*N12(jj,1));
F2122(jj,1)=16.*(N2122(jj,1));
F2121(jj,1)=16.*(N2121(jj,1));
F2112(jj,1)=16.*(N2112(jj,1));
F2111(jj,1)=16.*(N2111(jj,1));

% tensor, vector magnitude (delta), principal component values and directions for single slice

tensor=[N11(jj,1) N12(jj,1);N21(jj,1) N22(jj,1)];
deltaSlice(jj,1)=sqrt((N11(jj,1)-N22(jj,1)).^2+4.*(N12(jj,1)).^2);
[porientSlice,NSlice]=eigs(tensor); % eigs instead of eig gives sorted eigenvalues
porientdSlice(jj,1)=atan2d(porientSlice(2,1),porientSlice(1,1)); % from vertical y axis with clockwise
being positive
NSlice1(jj,1)=NSlice(1,1);
NSlice2(jj,1)=NSlice(2,2);
% tensor, vector magnitude (delta), principal component values and directions for single slice
for th=0:pi/180:2*pi

fn=1/(2*pi())*(F11(jj,1)*cos(th)*cos(th)+2*F12(jj,1)*sin(th)*cos(th)+F22(jj,1)*sin(th)*sin(th));
polarplot(th,fn,'.r');

%Distribution function with 4th order fabric tensor
fn4=1/(2*pi())*(F1111(jj,1)*cos(th)*cos(th)*cos(th)*cos(th)+F1122(jj,1)*cos(th)*cos(th)*sin(th)*sin(t
h)+F1112(jj,1)*cos(th)*cos(th)*cos(th)*sin(th)+F1121(jj,1)*cos(th)*cos(th)*sin(th)*cos(th)+F1211(jj,
1)*cos(th)*sin(th)*cos(th)*cos(th)+F1212(jj,1)*cos(th)*sin(th)*cos(th)*sin(th)+F1221(jj,1)*cos(th)*si
n(th)*sin(th)*cos(th)+F1222(jj,1)*cos(th)*sin(th)*sin(th)*sin(th)+F2222(jj,1)*sin(th)*sin(th)*sin(th)*s
in(th)+F2211(jj,1)*sin(th)*sin(th)*cos(th)*cos(th)+F2221(jj,1)*sin(th)*sin(th)*sin(th)*cos(th)+F2212(j
j,1)*sin(th)*sin(th)*cos(th)*sin(th)+F2122(jj,1)*sin(th)*cos(th)*sin(th)*sin(th)+F2121(jj,1)*sin(th)*co
s(th)*sin(th)*cos(th)+F2112(jj,1)*sin(th)*cos(th)*cos(th)*sin(th)+F2111(jj,1)*sin(th)*cos(th)*cos(th)*
cos(th));

polarplot(th,fn4,'.b');
hold on;
ax = gca;
d = ax.ThetaDir;
ax.ThetaDir = 'clockwise';
ax.ThetaZeroLocation = 'top';
ax.ThetaMinorGrid = 'on';
rlim([0 .06]);
end
end

% Average of perimeter-area ratio for all slices

pereaAvg=mean(pereaSlice);
```

```
% Average fabric tensors for all slices

% Average Fabric tensor of first kind order 2
N11Avg=mean(N11);
N12Avg=mean(N12);
N21Avg=mean(N21);
N22Avg=mean(N22);
% Average Fabric tensor of first kind order 4
N1111Avg=mean(N1111);
N1122Avg=mean(N1122);
N1112Avg=mean(N1112);
N1121Avg=mean(N1121);
N1211Avg=mean(N1211);
N1212Avg=mean(N1212);
N1221Avg=mean(N1221);
N1222Avg=mean(N1222);
N2222Avg=mean(N2222);
N2221Avg=mean(N2221);
N2212Avg=mean(N2212);
N2122Avg=mean(N2122);
N2211Avg=mean(N2211);
N2121Avg=mean(N2121);
N2112Avg=mean(N2112);
N2111Avg=mean(N2111);

% Average Fabric tensor of second kind order 2
F11Avg=4.*(N11Avg-1/4);
F12Avg=4.*N12Avg;
F21Avg=4.*N21Avg;
F22Avg=4.*(N22Avg-1/4);


D11Avg=4.*(N11Avg-1/2);
D12Avg=4.*N12Avg;
D21Avg=4.*N21Avg;
D22Avg=4.*(N22Avg-1/2);


% FAV A calculation
p=1/2*(F11Avg+F22Avg);
F= [(F11Avg-p) F12Avg; F21Avg (F22Avg-p)];

Fnorm=sqrt((F11Avg-p)^2+(F22Avg-p)^2+F12Avg*F21Avg);
nF=F/Fnorm;
nLV = [sqrt(2)/2 0 ; 0 -sqrt(2)/2]; % Loading vector
FAV= Fnorm*sum(sum(nF.*nLV))
FAV2=sum(sum(F.*nLV))

FAV3= Fnorm*sum(sum(nF.*nLV))
FAV4=sum(sum(F.*nLV))
```

```
%Result writing

FAV2D = table(F11Avg-p,F22Avg-p,F12Avg,F21Avg,Fnorm,FAV);

%filename = '2DXYC30VoidResultsFAVA25May.xlsx';
%writetable(FAV2D,filename,'Sheet',1,'Range','A27');

% Average Fabric tensor of second kind order 4
F1111Avg=16.*(N1111Avg-3/4.*N11Avg+1/16);
F1122Avg=16.*(N1122Avg-3/4.*N22Avg+1/16);
F1112Avg=16.*(N1112Avg-3/4.*N12Avg);
F1121Avg=16.*(N1121Avg-3/4.*N21Avg);
F1211Avg=16.*(N1211Avg);
F1212Avg=16.*(N1212Avg);
F1221Avg=16.*(N1221Avg);
F1222Avg=16.*(N1222Avg);
F2222Avg=16.*(N2222Avg-3/4.*N22Avg+1/16);
F2211Avg=16.*(N2211Avg-3/4.*N11Avg+1/16);
F2221Avg=16.*(N2221Avg-3/4.*N21Avg);
F2212Avg=16.*(N2212Avg-3/4.*N12Avg);
F2122Avg=16.*(N2122Avg);
F2121Avg=16.*(N2121Avg);
F2112Avg=16.*(N2112Avg);
F2111Avg=16.*(N2111Avg);

tensorAvg=[N11Avg N12Avg;N21Avg N22Avg];

deltaAvg=sqrt((N11Avg-N22Avg).^2+4.*(N12Avg).^2); % intensity of the preferred orientation of
particles

[porientAvg,NAvg]=eigs(tensorAvg);        % eigs instead of eig gives sorted eigenvalues

porientdAvg=atan2d(porientAvg(2,1),porientAvg(1,1)); % from vertial y axis with clockwise being
positive
NAvg1=NAvg(1,1);
NAvg2=NAvg(2,2);

% Histogram by summing binwise all vectors for all slices
pp=polarhistogram('BinEdges',edges,'BinCounts',TbinVectorSum,'Normalization','pdf','DisplayStyle','
stairs','EdgeColor','black','LineWidth',.75);
ax = gca;
d = ax.ThetaDir;
ax.ThetaDir = 'clockwise';
ax.ThetaZeroLocation = 'top';
ax.ThetaMinorGrid = 'off';
hold on;

for th=0:pi/180:2*pi

fn=1/(2*pi)*(F11Avg*cos(th)*cos(th)+(F12Avg+F21Avg)*sin(th)*cos(th)+F22Avg*sin(th)*sin(th));
```

```
polarplot(th,fn,'.b');

hold on;
fn4Avg=1/(2*pi)*(F1111Avg*cos(th)*cos(th)*cos(th)*cos(th)+(F1122Avg+F2211Avg+F1212Avg+F212
1Avg+F1221Avg+F2112Avg)*cos(th)*cos(th)*sin(th)*sin(th)+(F1112Avg+F1121Avg+F1211Avg+F2111
Avg)*cos(th)*cos(th)*cos(th)*sin(th)+(F1222Avg+F2122Avg+F2212Avg+F2221Avg)*cos(th)*sin(th)*si
n(th)*sin(th)+F2222Avg*sin(th)*sin(th)*sin(th)*sin(th));
polarplot(th,fn4Avg,'.r');
ax = gca;
d = ax.ThetaDir;
ax.ThetaDir = 'clockwise';
ax.ThetaZeroLocation = 'top';
ax.ThetaMinorGrid = 'off';

rlim([0 .06]);
end

%Writing results in Excel file%
DataAvg = table(deltaAvg,pereaAvg,porientdAvg,N11Avg,N12Avg,N22Avg,NAvg1,NAvg2);
DataSlice = table(deltaSlice,pereaSlice,porientdSlice,NSlice1, NSlice2);
filename = 'UncemVoidXZResults.xlsx';
writetable(DataAvg,filename,'Sheet',1,'Range','A1');
writetable(DataSlice,filename,'Sheet',1,'Range','I1');
```
